A Thesis Entitled

SYNTHESIS, PROPERTIES AND APPLICATIONS OF NANO METAL OXIDES AND NANO COMPOSITES

Submitted to Goa University for the Award of the Degree of

DOCTOR OF PHILOSOPHY

In

CHEMISTRY

By

Ms. PRATIBHA VINAYAK BAKRE

M. Sc.

Under the Guidance of

Prof. SANTOSH G. TILVE

Department of Chemistry

GOA UNIVERSITY

Taleigao Plateau, Goa 403206

INDIA

APRIL 2018

CERTIFICATE

This is to certify that the thesis entitled, "**Synthesis, Properties and Applications of Nano Metal Oxides and Nano Composites**" submitted by Ms. **PRATIBHA VINAYAK BAKRE**, is a record of research work carried out by the candidate during the period of study under my supervision and that it has not previously formed the basis for the award of any degree or diploma or other similar titles.

Goa University
April 2018

Prof. Santosh G. Tilve
Research Guide
Department of Chemistry
Goa University

DECLARATION

I hereby declare that the work embodied in the thesis entitled "**Synthesis, Properties and Applications of Nano Metal Oxides and Nano Composites**" is the result of investigations carried out by me under the guidance of **Prof. SANTOSH G. TILVE** at Department of Chemistry, Goa University and that it has not previously formed the basis for the award of any degree or diploma or other similar titles.

In keeping with the general practice of reporting scientific observations, due acknowledgement has been made wherever the work described is based on the findings of other investigators.

Goa University
April 2018

Ms. Pratibha V. Bakre
Ph.D. Student
Department of Chemistry
Goa University

ACKNOWLEDGEMENT

First and foremost, I would like to thank my supervisor, ***Prof. S. G. Tilve*** *(former Head, Department of Chemistry, Goa University) for giving me an opportunity to pursue my research work under his valuable guidance. The work presented in this thesis is a result of his able guidance, generous support and encouragement throughout my Ph.D. tenure. I express my deep gratitude for his constant motivation, innovative ideas, active discussions, constructive criticism and timely suggestions. I greatly admire his positive approach towards teaching, research and life and I will forever be grateful to him for understanding and helping me and also for the patience shown by him in these four years period. I also truly appreciate the independence fetched during this period for working in my area of interest, carrying out the experimental work and developing more interest in research.*

I would also like to express my kind gratitude to Goa University for giving me this opportunity. I am thankful to ***Prof. B. R. Srinivasan*** *(Head, Department of Chemistry, Goa University),* ***Prof. Gourish M. Naik*** *(Dean, Natural sciences, Goa University), the former deans,* ***Prof. J. B. Fernandes*** *and* ***Prof. A. V. Salker*** *for providing all the necessary facilities for my research work.*

I am thankful to my subject expert, ***Dr. J. B. Fernandes*** *and former subject expert,* ***Dr. Santosh G.*** *for their valuable suggestions and inputs.*

*I would like to thank University Grants Commission (****UGC****), New Delhi for the award of BSR Junior Research Fellowship and Senior Research fellowship.*

I am profoundly grateful to all my teachers, for all the knowledge I gained from them during my tenure at the University.

I deeply acknowledge all my colleagues and former Principal of Chowgule College of Arts & Science, Margao, for their constant motivation and support.

I thank ***IISc Bangalore, SAIF-IIT Mumbai, NCL Pune, IIT Madras, BITS Pilani, Goa Campus, Savitribai Phule University, Pune University, Abasaheb Garware College, Pune and Solapur University*** *for providing the instrumental facility.*

I would also like to thank all the non-teaching staff of the department and administrative staff of the University for their help time-to-time.

I express my wholehearted gratitude to all the research students, present and past, for helping me in instrumental analysis and related discussion throughout my PhD tenure. My special thanks go to all my lab mates for providing help in literature referencing and experimental work wherever needed.

I am greatly indebted to ***my parents, elder brother and sister, my husband and in-laws*** *for their selfless love and sacrifice. I also thank all my friends and family, for their valuable advice and moral support. I thank, who directly or indirectly encouraged and motivated me to step forward in this direction and built my mental strength to walk towards the end of this journey. I take this opportunity to thank all my well wishers who directly or indirectly supported me to walk towards the end of this journey.*

 *Finally, with silent words I thank GOD for granting me good health and strength*  *needed at every stage of my life.*

..... Pratibha V. Bakre

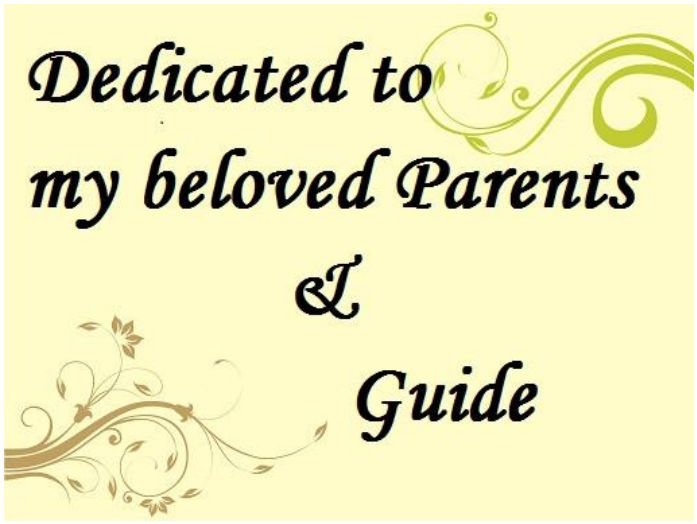
Dedicated to
my beloved Parents
&
Guide

TABLE OF CONTENT

	Abbreviations	*i*
	Abstract of thesis	*iii*
	Publications and conferences	*vii*
Chapter 1	***Background and General introduction***	***1-13***
1.1	*Introduction to nanomaterials and nanocomposites*	*1*
1.2	*Photocatalysis*	*3*
1.3	*Brief outline of various synthetic methods*	*4*
1.4	*Structural and surface properties*	*6*
1.5	*Brief introduction to characterization techniques*	*7*
	References	*12*
Chapter 2	***Template Assisted Synthesis of Mesoporous TiO_2***	***14-105***
2.1	*Introduction*	*14*
2.2	*General experimental procedure*	*24*
2.3	*Results and discussion*	
Section A	*Use of monocarboxylic acid templates*	*29*
Part 1	*Study of straight chain monocarboxylic acids as templates*	*30*
Part 2	*Study of sterically bulky monocarboxylic acids as templates*	*44*
Section B	*Study of dicarboxylic acids as templates*	*54*
Section C	*Study of amino acids as templates*	*69*
Section D	*In-*situ *formed imines as templates*	*84*
	LC-MS studies	*94*
	References	*98*
Chapter 3	***Synthesis of Modified TiO_2***	***106-196***
3.1	*Introduction*	*106*
3.2	*General experimental procedure*	*110*
3.3	*Results and discussion*	
Section A	*N-incorporated TiO_2*	*119*
Section B	*CuO-NiO-incorporated TiO_2*	*141*
Section C	*CuO-NiO-N-incorporated TiO_2*	*167*
	References	*186*

Chapter 4	***Synthesis and applications of mixed metal nano composites for hydrogen generation***	***197-225***
4.1	*Introduction*	*197*
3.2	*General experimental procedure*	*200*
3.3	*Results and discussion*	*203*
3.2	*References*	*219*

DEFINITION OF ABBREVIATIONS

General Abbreviations

g	Gram	eq.	Equation
mg	Milligram	rt	Retention time
mol	mole	wt.	Weight
mmol	Millimole	Å	Ångström
mL	Milliliter	°C	Degree Celcius
nm	Nanometre	K	Kelvin
max	Maximum	eV	Electron volt
h	Hour	%	Percentage
min	Minute	*p*	Para
ppm	Parts per million	*et al.*	Et alia (and others)
RT	Room temperature	*etc.*	et cetera (and the rest)
P/P_0	Relative pressure	*i.e.*	id est (that is)
S_{BET}	BET surface area	*e.g.*	exampli gratia (for example)
TLC	Thin layer chromatography	*viz*	videre licet (it is permitted to see)

Compound Abbreviations

TIP	Titanium isopropoxide	Cu $(CH_3COO)_4$	Anhydrous Copper acetate
IPA	Isopropyl alcohol	Ni $(CH_3COO)_2.4H_2O$	Nickel acetate tetrahydrate
MB	Methylene blue	$Fe(NO_3)_3.9H_2O$	Ferric Nitrate Nonahydrate
CG	Calmagite	$Ni(NO_3)_2.6H_2O$	Nickelous Nitrate Hexahydrate
RhB	Rhodamine B	$NaBH_4$	Sodium borohydride

AB	Ammonia borane	$(NH_4)_2SO_4$	Ammonium sulphate
THF	Tetrahydro furan	$BaSO_4$	Barium sulphate
DMSO	Dimethyl sulfoxide	TiO_2	Titanium dioxide

Spectroscopic Abbreviations

IR	Infrared	BET	Brunauer-Emmett-Teller
UV Vis	Ultra violet Visible	BJH	Barrett-Joyner-Halenda
DRS	Diffuse reflectance spectroscopy	XRD	X-ray diffraction
SEM	Scanning electron microscopy	XPS	X-ray photoelectron spectroscopy
TEM	Transmission electron microscopy	VSM	Vibrating sample magnetometer
SAED	Selected area electron diffraction	TG-DTA	Thermogravimetric analysis
HRTEM	High resolution transmission electron microscopy	NMR	Nuclear magnetic resonance
EDX	Energy-dispersive X-ray Spectroscopy	LC-MS	Liquid chromatography mass spectrometry
λ	Wavelength	M^+	Molecular ion
cm^{-1}	Frequency in wavenumber	*m/z*	Mass to charge ratio

ABSTRACT OF THESIS

TITLE: **SYNTHESIS, PROPERTIES AND APPLICATIONS OF NANO METAL OXIDES AND NANO COMPOSITES**

Various nano metal oxides and their nano composites are increasingly used in environmentally beneficial processes. Nano TiO_2 and doped TiO_2 have gained tremendous interest for photocatalytic and environmental cleaning processes like dye degradation, water splitting, CO_2 and NO_2 reduction, etc. Nano metal composites and nano alloys are more commonly studied for their applications in catalysis.

Development of synthetic strategies for such nano materials is an important aspect taken into consideration by many researchers. Thus, efforts have been made in developing newer strategies to prepare nano metal, metal oxide and their composites with enhanced properties. The thesis work deals with the synthesis of TiO_2 with improved catalytic properties by modifying synthetic methods, synthesis of nitrogen incorporated and copper oxide and nickel oxide incorporated TiO_2 for catalytic studies and synthesis of metal-metal boron composites for hydrogen generation from ammonia borane.

The thesis entitled is divided into 4 chapters.

Chapter 1: **Background and General introduction**

This chapter gives a brief introduction about nano materials, related literature work in this field. It also discusses in brief about the mechanism of photocatalytic processes and their importance for environmental remediation. A brief outline of various synthetic methods available for preparing nano materials is introduced. This is then followed by the properties of these nanomaterials and introduction to various characterization techniques.

Chapter 2: **Template Assisted Synthesis of Mesoporous TiO_2**

This chapter deals with synthesis TiO_2 as an effective photocatalytic material. The chapter is divided into 4 sections depending upon the type of precursor studied.

Section A – Study of monocarboxylic acid as templates

This section describes the use of aliphatic linear chain monocarboxylic acids as templates in the sol-gel synthesis of TiO_2. A detailed study on the effect of monocarboxylic acid chain length on the mesoporosity and other properties using the sol-gel method is carried out.

This section is further divided into two parts.

Part 1: **Study of straight chain monocarboxylic acids as templates**

Formic acid, acetic acid, butyric acid, octanoic acid and palmitic acid were used as aliphatic monocarboxylic acids for the study. Here titanium isopropoxide (TIP) was hydrolyzed in the presence of excess acid in water so that adequate control on hydrolysis, condensation and gel formation could be achieved. The gels obtained were then calcined to retain the porous structure and to get rid of the organic part. Further, the prepared catalysts were evaluated for photodegradation of methylene blue (MB), and compared with the rate of degradation caused by Degussa P25. The MB degradation was also subjected to LC-MS studies and the results of these studies are presented. The longer the chain of the monocarboxylic acid the higher was the surface area, smaller the size of the resultant catalyst and hence better was the photocatalytic activity.

Part 2 **– Study of sterically bulky monocarboxylic acids as templates**

In the second part of this section sterically bulky acids *viz.* phenyl acetic acid and pivalic acid as a precursor material were studied. Interesting results in terms of mesoporosity, size, pore diameter, phase selection and thereby enhanced photocatalytic activity was obtained. The probable participation of these acids in the final particulate synthesis is speculated and the results obtained are discussed. The bulkier acids were found to be good a substitute as lignads for long chain fatty acids. These acids are studied as ligands for the first time in synthesis of metal oxides.

Section B – Study of dicarboxyllic acids as templates

In this section dicarboxlyic acids as soft ligands were used in sol-gel synthesis. For this study, the series of dicarboxylic acids employed include, oxalic acid (2 carbons), malonic acid (3 carbons), succinic acid (4 carbons), glutaric acid (5 carbons), adipic acid (6 carbons), maleic acid (4 carbons, *cis*-double bond), fumaric acid (4 carbons, *trans*-double bond), malic acid (4 carbons with one additional hydroxyl group) and tartaric acid (4 carbons and 2 additional hydroxyl groups).

Sample prepared using glutaric acid showed the best photocatalytic activity due to pure anatase phase, higher pore volume and surface area, spherical morphology of macro-mesoporous nature with pore channels and having exceptionally broad pore size distribution. The use of different acids as a starting material induced an important modification in morphology due to preferential bridging mode. Catalyst obtained from acids with –OH functional group or *trans*-double bond gives anatase-rutile mixture and these samples showed least photo-degradation efficiency.

Section C – Study of amino acids as templates

This section covers the use of amino acids as smart templates in the preparation of mesoporous nano TiO_2 materials with desired structure and surface properties. The amino acids employed in this study were glycine, L-proline, β- alanine, DL- alanine, L- glutamic acid, DL- aspartic acid, DL- valine and DL- serine.

Formation of phase pure anatase nano particulate was observed in all cases except aspartic acid and serine. Among these acids, particles prepared from branched amino acids such as proline, valine and aspartic acid showed better photo-degradation in comparison with Degussa P25 by direct sunlight exposure of dyes methylene blue and calmagite. Aspartic acid was found to be the best templating agent. The smaller size of the particulate was found to be more important in determining the catalytic activity than the surface area and pore volume. Further, the IR studies suggested that the amino acids act as a template by acting as surfactant rather than the reactants. The surfactant activity was attributed to hydrogen bonding between surface hydroxyl groups of the colloid and the hydrogen of the ammonium group of the amino acids.

Section D – In situ formed imines as templates

In this section, the hydrolysis and condensation reaction of TIP was carried out in the presence of a mixture of aniline and anisaldehyde (4-methoxy benzaldehyde) in isopropanol. The ratio of the aniline:anisaldehyde was varied to make available initially with 4, 3 and 2 mole equivalents of water to TIP. The results of these studies indicated that the amount of water made available for the hydrolysis determines the phase selection and the amine and aldimine acts to direct the shape and the size of the material. Catalyst obtained from least amount *in situ* available water showed the maximum photo-activity.

Chapter 3: **Synthesis of modified TiO_2**

This chapter deals with modification of semiconductor TiO_2 material for enhancing its catalytic property by incorporating nitrogen, copper oxide and nickel oxide (co-doping) and nitrogen, copper oxide and nickel oxide (tri-doped system).

The chapter is divided into three sections.

Section A – N-incorporated TiO_2

This section deals with the modification of TiO_2 by incorporating nitrogen into it using decomposition method. Two different synthetic procedures were employed for obtaining this

material from varying starting precursor as a nitrogen source. Three different urea derivatives as nitrogen sources *viz.* urea, *N*,*N*-dimethyl urea and semicarbazide were selected for study. The catalyst obtained using semicarbazide showed the best photocatalytitc activity.

Section B – CuO-NiO- incorporated TiO_2

In this section transition metal incorporated TiO_2 systems with equivalent amount of copper and nickel as co-dopant metals were studied. The catalysts were synthesized by two different methods and their activity was compared for photocatalytic dye degradation with standard Degussa P25. The catalytic system with 0.05 wt % of the dopant showed the excellent photocatalytic activity. In addition to that, the catalysts with higher metal percentage were also studied for the reduction of aromatic nitro functionality. These catalytic materials also showed magnetic properties.

Section C- CuO-NiO-N- incorporated TiO_2

In continuation with the previous section the synergistic effect of the tri-doped system was studied in this section with a non-metal combination. In this section, we studied equivalent amount of CuO-NiO incorporation together with nitrogen into TiO_2. Till date no reports are found for this combination. We explored this material with varying percentage of the dopants with two different synthetic routes and studied its effectivity for photocatalytic dye degradation. The samples with 0.05 wt % of metal dopant showed the best photocatalytic activity.

Chapter 4: **Synthesis and applications of mixed metal nano composites for hydrogen generation**

This chapter mainly discusses about catalytic hydrogen generation from ammonia borane as a major hydrogen reservoir. Due to continuous demand of alternate energy source for traditional fossil fuels, hydrogen gas is thought and accepted to be a potential resource for future.

In this regard, the release of hydrogen from such reservoir sources is a major task taken by many researchers. In view of this, catalytic dehydrogenation of ammonia borane is reported mainly with some of the noble metal catalysts in literature. Looking at the cost effectiveness and recyclability, bimetallic alloys of first transition metals in combination with boron were selected for study. Here Fe-Ni-B catalyst with designed ratio was found to be more suitable for dehydrogenation of ammonia borane. Further kinetic studies were done by varying experimental conditions.

LIST OF PUBLICATIONS

List of publications:

Research Publication:

1. Influence of acid chain length on the properties of TiO_2 prepared by sol-gel method and LC-MS studies of methylene blue photodegradation.

Journal of Colloid and Interface Science 474 (2016) 58–67.

2. Dicarboxylic Acids as Soft Templates for the Sol-Gel Synthesis of Mesoporous Nano TiO_2 with Enhanced Photocatalytic Activity.

Chemistry Select (Materials Science inc. Nanomaterials & Polymers) 2 (2017) 7063–7072.

3. Investigation of amino acids as templates for the sol–gel synthesis of mesoporous nano TiO_2 for photocatalysis.

Monatsh. Chem. 149 (2018) 11–18.

4. Direct access to highly crystalline mesoporous nano TiO2 using sterically bulky organic acid templates.

Journal of Physics and Chemistry of Solids 116 (2018) 234–240.

Conference Attended and Presented:

1. Indo- UK International Workshop on Advanced Materials and Their Applications in Nanotechnology (AMAN 2014) organized and held at BITS Pilani, KK Birla Goa Campus.
2. National Symposium on Transcending Frontiers in Organic Chemistry (TFOC- 2014) held at CSIR – National Institute for Interdisciplinary Science and Technology, Trivandrum.
3. Poster presented titled: "Synthesis of TiO_2 nanoparticles *via* monocarboxylic acid templates and their comparison in the visible light photocatalytic degradation of methylene blue" at International Conference on Green Chemistry: Catalysis, Energy and Environment, (ICGC- 2015) organized by Department of Chemistry, Goa University.
4. Oral presentation titled: "Influence of acid chain length on the properties of TiO_2 prepared by sol-gel method and LC-MS studies of methylene blue photodegradation" at National Level Symposium on Materials Characterisation and Manufacturing (MCM – 2016) jointly organized by Department of Mechanical Engineering, Padre Conceicao College of Engineering and Department of Physics, Goa University.
5. Attended Royal Society of Chemistry (UK) West India Chapter Symposium on "Recent Advancements in Chemical Sciences and Research Scholars' Meet-2016" Organized at Birla Institute of Technology and Science Pilani, K K Birla Goa Campus.

6. Oral presentation titled: “Improved catalytic activity of dicarboxylic acid mediated TiO_2 for sunlight degradation of methylene blue” at National Conference on Innovative Research in Chemical Sciences (IRCS-2017), organized and held at Department Of Chemistry, Shivaji University, Kolhapur, Feb 1-2, 2017 and secured 3rd prize.

7. Poster presented titled: “Amino acid templates in the sol-gel synthesis of mesoporous nano-TiO_2 for enhanced photodegradation of dyes: Elucidating their role” at National Conference on New Frontiers in Chemistry (NFCFA-2017), organized and held at BITS-Pilani Goa Campus, Jan 28-29, 2017.

Chapter I – Background and General introduction

1.1. Introduction to nanomaterials and nanocomposites

Inorganic nanostructures including metal oxides, ceramics and composites have gained a worldwide research attention in the past two decades and tremendous efforts have been made on their synthetic aspects, characterization and applications. Among the various classes of nanomaterials, nano metal oxides are particularly attractive from the viewpoint of scientific and technological applications. They display unique physicochemical properties due to their restricted size and thus have application potential in fields like catalysis, sensors and environmental remediation [1].

Metals can form a large diversity of oxide compounds by employing various synthesis techniques. Metal oxide nanomaterials exhibit metallic, semiconductor, or insulator character due to the electronic structure difference. Semiconductors are materials whose valence and conduction bands are separated by an energy gap called as band-gap. When such materials absorb photons having energy equal or greater than its band-gap, it excites its electrons from the valence band to the conduction band, creating charge carriers.

Semiconductor metal oxides play a vital role in many areas of chemistry, physics, and material science. They are largely employed in a wide range of applications such as the fabrication of microelectronic circuits, sensors, piezoelectric devices, fuel cells, for coating against corrosion and as catalysts. The properties of metal oxides largely vary with the reduction of particle size in nano scale, which are either enhanced or completely display novel properties compared to their bulk materials. Thus, they are mainly prepared in the nanostructured form for improved properties and effectiveness [2-4].

The term nanomaterials embody a large variety of materials in the realm of nanometers. These include ceramics, metals and metal oxide nanoparticles with nanometer-sized microstructures.

By definition, a composite is considered to be any multiphase material that exhibits a significant proportion of the property of all constituent phases such that a better combination of properties is realized. Nanocomposite is a multiphase solid material in which at least one of the phases shows dimensions in the nanometre range, *i.e.* less than 100 nanometers. These include colloids, gels, porous media, copolymers and dendrimers. It is generally a solid combination of a bulk matrix and nano phase(s) material.

Some of the important classes of nanocomposites are as follows:

Ceramic-matrix nanocomposites

In this type of composites the main part of the volume is occupied by a chemical compound from the group of nitrides, borides, oxides, silicides, *etc.* In most cases, ceramic-matrix nanocomposites include a metal as the second component. Such ceramic-metal combinations were useful in improving their electrical, optical, magnetic, corrosion-resistance and other protective properties.

The concept of ceramic-matrix nanocomposites was also applied to thin films that are solid layers of a few nm to some tens of μm thickness deposited upon an underlying substrate that play an important role in the functionalization of technical surfaces.

Metal-matrix nanocomposites

Metal matrix nanocomposites are also referred as reinforced metal matrix composites. Boron nitride reinforced metal matrix composites, carbon nanotube metal matrix composites and carbon nitride metal matrix composites are the new research areas in metal matrix nanocomposites.

Another kind of nanocomposite is the energetic nanocomposite, generally as a hybrid sol-gel with a silica base, which, when combined with metal oxides and nano-scale aluminum powder, can form superthermite materials.

Polymer-matrix nanocomposites

In such type of nanocomposites a nano filler is added to a polymer and hence are also called as nanofilled polymer composites. If efficient dispersion of the filler is obtained in the polymer it can yield a high performance composite.

An example of this would be reinforcing a polymer matrix by much stiffer nanoparticles of ceramics, clays or carbon nanotubes.

In a recent study, polymeric nanocomposites were fabricated using various one-dimensional carbon nanostructures such as single- and multi- walled carbon nanotubes, as well as two-dimensional carbon and inorganic nanomaterials such as graphene platelets, graphene nanoribbon, single- and multi- walled graphene oxide nanoribbons, graphene oxide nanoplatelets and molybdenum disulphide nanoplatelets as reinforcing agents, to improve the mechanical properties of poly (propylene fumarate) nanocomposites, for bone tissue engineering applications.

Oxide nanomaterials are used in a new class of ceramics. Advanced ceramics with their larger strength, higher operating temperatures, improved toughness and tailorable properties

are used for applications such as chemical processing and environmental ceramics, engine components, computers and other electronic components, or cutting tools.

Nanoalloys

Bulk nano-crystalline alloys have attracted much attention due to their interesting mechanical and magnetic properties when compared with their fully amorphous and fully crystalline counterparts.

In material science, intermetallic compounds and alloys are prepared by mixing elements and the properties if such materials are studies. In certain examples, there is an improvement in specific properties after alloying. This is usually ascribed as synergistic effect of one element on the rest of composition. Myriad array of such alloys and compositions with different structures and properties have been prepared. Many of such alloys have found applications in catalysis, electronics and engineering. It is of great interest to fabricate materials with well defined, controllable properties and structures on the nanometer scale [5-8]. The bimetallic and trimetallic nanoclusters are called as alloy nanoclusters or nanoalloys.

1.2. Photocatalysis

The term photocatalysis means a photochemical reaction accelerated by a catalyst. In this process light, *i.e.* a photon is absorbed by a catalyst directly or *via* a dye on the surface. The adsorbed photon excites an electron in the catalyst. The excited electron travels from the valence band to the conduction band, leaving a hole in the valence band. The electrons and holes diffuse to the surface of the catalyst where they come in contact with the molecules of chemical adsorbed on it. The adsorbed chemical is the one on which we intend to have a photochemical reaction. The electrons can bring about the reduction of this chemical and the holes an oxidation. Such types of photo oxidations have a great ramification in the field of environmental cleansing. Dyes and other toxic chemicals can be broken down to benign or non-toxic molecules by such photo oxidation processes. The catalysts used for such processes are normally semiconductor materials.

The elimination of contaminants from waste effluents has become a primary issue due to the consequences to human health. Worldwide environmental problems associated with the textile industry are mainly due to water pollution caused by the discharge of untreated effluent and toxic chemicals especially during processing. The major contaminant includes dye waste from industrial effluents. Dyes usually have a complex aromatic molecular structure, which makes them more stable and difficult to biodegrade.

Many such organic dyes include Methylene blue, Rhodamine B, Malachite green, Calmagite, Methyl orange, *etc*. Methylene blue (MB) is a most commonly studied azo dye due to its complex aromatic structure and harmful intermediates [9-12].

Methylene blue (tetramethylthionine chloride, $C_{16}H_{18}ClN_3S$) is a heterocyclic aromatic dye, a member of thiazine dyes used for a number of different staining procedures, which includes colouring paper, dyeing cottons, wools, silk, leather and coating for paper stock. Although methylene blue is not strongly hazardous, it can cause some harmful effects, such as heartbeat increase, vomiting, shock, cyanosis, jaundice, quadriplegia and tissue necrosis in humans.

Calmagite ($C_{17}H_{14}N_2O_5S$), is a synthetic azo-dye widely used in textile industries, cosmetic, paper, drug and food processing industries in large quantities. Effluent of this dye is hard to treat and made of harmful organic and inorganic chemicals that exhibit toxic and carcinogenic effects toward biological systems.

Rhodamine B ($C_{28}H_{31}ClN_2O_3$) is another basic dye, which is an important representative of xanthene dyes, has two molecular forms of cationic and Zwitterionic form. Cationic dyes are considered as toxic colorants and can cause harmful effects such as allergic dermatitis, skin irritation, mutations and cancer. It is widely used in the manufacturing of textile, printing, paper, pharmaceutical and food products, and because of its high solubility in water, it constitutes an important source of environmental pollution reaching the atmosphere and ground waters.

To reduce the risk of environmental pollution from such effluents, it is extremely important to treat them before discharging. Photocatalytic degradation has enormous potential to control aqueous contaminants or pollutants [13-15].

Structures of these dyes are given below.

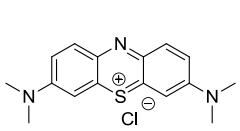

Methylene blue

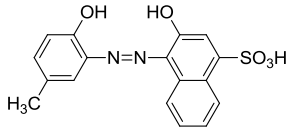

Calmagite

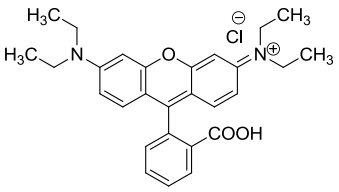

Rhodamine B

1.3. Brief outline of various synthetic methods

The properties of metal oxides can be altered based on many aspects. One of the most important aspects is by altering the synthetic method. Research on the controlled formation of nanocrystalline materials has reached to an enormous extent in recent years. Modification

in preparative strategies is done in empirical manner and rational approaches for the controlled formation of nanomaterials are available for a limited number of systems. This can be done by understanding the fundamental mechanism of nanocrystal formation.
Various synthetic approaches are available for the preparation of metal oxide based photocatalysts, and most popular are co-precipitation reactions, reduction synthesis, aqueous and non-aqueous sol-gel reactions, combustion method, decomposition method, hydrothermal and solvothermal approaches, *etc.* are adopted to prepare visible light active photocatalysts.

Co-precipitation is used for simultaneous precipitation of more than one component. Catalysts based on more than one component can be prepared easily by co-precipitation. The synthesis is generally carried out at room temperature and the properties of synthesized nanomaterial or nanoparticles are found to be dependent on initial reaction parameter such as pH values and reaction temperature. The precipitation process is used for preparation of bulk catalysts and support material such as Al_2O_3, SiO_2, TiO_2, ZrO_2, *etc.*

Hydrothermal method involves the thermal reaction (usually above 100 °C) of chemical/s in aqueous medium in a sealed vessel. Metal oxides with different shapes (flowers, rods, tubes, *etc*.) have been synthesized by using this method. It is a useful method for the preparation of hydroxides, oxyhydroxide and oxides. It can also be used for non-oxide metals (for instance nitrides, chalcoginides, *etc.*).

Solvothermal method is a chemical reaction in a closed system in the presence of a solvent (aqueous and non-aqueous solution) at a temperature higher than that of the boiling point of such a solvent. Solvothermal reactions have been mainly used for preparing micro or nanoparticles with different morphologies for applications such as sensors, separation and catalysis, molecular devices and spintronics.

Combustion synthesis is a low-cost method used for the production of various industrial materials. The process involves an exothermic reaction accompanied by evolution of heat and light. For any combustion synthesis, fuel and oxidizer are necessary ingredients. In this synthesis method, the metallic precursor gets decomposed by the heat generated by the violent reaction between the fuel the oxidizer.

The thermal decomposition method, also called as thermolysis is used to produce tunable and highly crystalline products. It involves decomposition of some precursor in the presence of a surfactant dissolved in a high boiling point, non-reacting solvent. The reaction is usually endothermic in this process and heat is essential to break chemical bonds in the compound enduring decomposition.

Template/surface-mediated synthesis is generally based on the construction of the needed nanomaterial within the pores or channels of a nanoporous template. Various synthetic techniques such as electrochemical, sol-gel, chemical polymerization and chemical vapor deposition are the major strategies employed in this type of fabrication. Nanomaterial with desired morphologies such as fibrils, rods, and tubules can be synthesized by using different template materials. The method is mainly used to obtain highly monodispersed mesoporous nanomaterials with uniform shape and a high specific surface area.

The sol-gel method is a homogeneous process wherein there is a continuous transformation of a solution into a hydrated solid precursor (hydrogel). The method involves hydrolysis and gelation of appropriate precursors in alcoholic solution. The advantages associated with sol-gel process include synthesis of nanosize materials of high purity and of uniform size, low reaction temperature, controlling the reaction process by stoichiometric addition of reagents, and synthesis of composite nano materials. These advantages have made the sol-gel method very popular for the synthesis of TiO_2-based photocatalysts [16-17].

1.4. Structural and surface properties

Mesoporous materials are materials having pore sizes in the range of 2–50 nm. Due to the combination of porous structure and high surface area these materials are expected to have improved catalytic properties, owing to which they have received much interest in the field of catalysis and nanomaterials.

According to the IUPAC, a mesoporous material can be disordered or ordered in a mesostructure. In crystalline inorganic materials, mesoporous structure restricts the number of lattice units, and thus alters the properties of the material.

Optical Properties

The main mechanism of light absorption in pure semiconductors is direct inter-band electron transitions. This absorption is observed to be smaller in indirect semiconductors, *e.g.*, TiO_2,

where the direct electron transitions between the band centers are prohibited by the crystal symmetry.

Whereas direct semiconductor, possess comparatively higher absorption coefficient and most of the sunlight is absorbed within a small range beneath the surface.

Magnetic Properties

Semiconductor materials can be readily transformed into a magnetic semiconductor material by adding some foreign impurities having magnetic properties. Since the magnetic element concentration is relatively low (dilute), the resultant material is termed as dilute magnetic semiconductor (DMS). These materials have gained much interest due to their semiconductor properties associated with magnetic properties. The ferromagnetism shown at room temperature on introducing small quantities of magnetic impurity into the non-magnetic material is generally termed as room temperature ferromagnetism (RTFM).

Most of the late transition metals, mainly of the first transition series, are added as dopant to semiconductor metal oxides so as to prepare DMS materials and hence to show RTFM. Commonly reported systems include, Cu, Co, Ni, Fe doped TiO_2, ZnO, SnO_2, *etc.*

1.5. Brief introduction to characterization techniques

Physicochemical characterization is a major aspect to understand the detailed properties of a material. Some basic properties, such as crystallinity, crystallite size, nature of active sites, morphology, particle size, phase structure, optical properties, surface structure, textural properties, *etc.* are characteristic features of any materials to be studied. A brief introduction to some important characterisation techniques employed for the present research work is summarized here with their basic principles.

X-ray Diffraction Properties of TiO_2 Nanomaterials

XRD is an essential technique used in the determination of structural properties such as phase identification and unit cell dimensions of the nanocrystalline material. It gives information about the crystal structure and the crystallinity, lattice parameter and crystallite size, which is estimated using Scherrer equation - $D = K\lambda / \beta \cos\theta$, where K is a dimensionless constant, 2θ is the diffraction angle, λ is the wavelength of the X-ray radiation, and β is the full width at half-maximum (FWHM) of the diffraction peak. Crystallite size is inversely related to the FWHM of an individual peak and is determined by measuring the broadening of a particular

peak in a diffraction pattern associated with a particular planar reflection from within the crystal unit cell.

Diffraction patterns of the nanomaterials are recorded with an X-ray diffractometer using Cu Kα radiation (λ =1.5418 Å). By investigative diffraction pattern, the crystalline phase of nanomaterial, can be identified. It was discovered by Laue in 1912 to determine long range order of crystalline phases, in which crystalline substances act as three-dimensional diffraction gratings for X-ray wavelengths similar to the spacing of planes in a crystal lattice. It is now a commonly used technique for the study of crystal structures and atomic spacing.

In this technique, the monochromatic beam of X-ray is made to incident on the analyte at various angles (θ). After the striking analyte it diffracts producing constructive diffraction patterns for certain angles corresponding to particular planes (h,k,l) to satisfy Bragg's diffraction condition, which is given by $2d\sin\theta = n\lambda$, where d is the interplanar distance between diffracting planes, θ is the angle of incidence of X-Ray, λ is the wavelength of the incident X-Ray and n is in an integer.

The widths of the diffraction peaks are closely related to the size, size distribution, defects and strain in the nanocrystals.

Scanning electron microscopy (SEM)

This technique allows direct observation of topography and morphological features with the help of signals produced by the interaction of electrons with atoms in the sample. The shape and morphology of nanostructured materials can be preliminarily determined by SEM. It produces images of the sample by scanning the surface with a focused beam of electrons. When an incident electron beam interact with specimen surface, secondary electrons with energies typically smaller than 50 eV evolve from the surface, whose emission efficiency depends upon the surface geometry, surface chemical characteristics and bulk chemical composition.

Transmission electron microscopy (TEM)

The technique is used for atomic mapping of the crystal. It is a high spatial resolution structural and chemical characterization technique. In this a thin specimen is illuminated with uniform and high intensity electrons and the forward transmitted beam is analyzed. TEM can be used to characterize metal oxide nanomaterials to determine particle size, shape, crystallinity and inter-particle interaction.

High resolution-transmission electron microscopy (HR-TEM) is a further advancement of this technique which is used to provide atomic resolution images of catalytic active sites under controlled environments (<10 torr). Hansen and co-workers have further expanded such studies to a wide range of catalytic materials and reaction conditions.

Selected area electron diffraction (SAED) is a crystallographic technique performed inside TEM, in which angular distribution of scattering can be viewed in the form of diffraction patterns. It is used to identify crystal structures and examine crystal defects and is mostly useful in polycrystalline specimens.

UV-Vis diffuse reflectance spectroscopy

UV-visible diffuse reflectance spectroscopy is one of the simplest techniques useful for studying optical and electronic properties of nanomaterials, which was discovered in 1970s and was mainly used for metal oxide catalytic materials. Weber extended these findings for quantitative determination of band-gap, *e.g.*, of a metal oxide. The basic operating principle of this spectroscopic technique is a measurement of light absorption due to electronic transitions in nanomaterials. It uses light in both the UV and visible region of the electromagnetic spectrum for electronic transition.

Diffuse reflectance spectroscopy (DRS) is a technique closely related to UV-Vis spectroscopy in which valence electron is excited to an empty orbital and the relative change in the amount of light being reflected off from a source is measured. It is used to study the band gap of a semiconductor material which is calculated by using equation - $E = h*C/\lambda$, where, h = Planck's constant = 6.626 x 10-34 Joules sec, C = Speed of light = 3.0 x 10^8 meter/sec and λ = Cut off wavelength

Fourier transforms infrared spectroscopy (FT-IR)

Infrared is a common vibrational spectroscopy technique useful for characterizing structural properties such as vibrational frequencies of molecules and phonons for identification of functional groups of the sample. It also provides information about chemisorbed molecules on oxide surfaces. However, it is lacking the fundamental molecular structural information about the metal oxide catalytic active sites on surfaces. Thus, it is used to study bonding modes of inorganic and organic materials. It is based on the measurement of transmitted IR light through a sample.

In this technique, the sample is illuminated with IR radiation which leads to excitation of vibrational modes in the chemically bonded functional groups. For nanoparticles, IR

spectrum measures the phonon mode. Interaction between the surface molecules or ions with nanoparticles usually causes a change in the vibrational or phonon frequencies. Hence the changes in frequencies measured in IR spectrum can give information about the interaction between the nanoparticles and surface molecules. The necessary condition to spectrum to appear is vibrations amongst bonded atoms should produce the change in the permanent dipole moment of the molecule. It is considered that the more polar bond gives intense signals.

Thermal Analysis [Thermo-Gravimetric/Differential Thermal Analysis (TGA/DTA)]

Thermo-gravimetric analysis (TGA) studies change in mass of a sample with an imposed change in the temperature. The changes that occur on heating include melting, phase transition, sublimation, and decomposition. TGA measures mass changes in a material as a function of temperature (or time) under a controlled atmosphere. Its principal uses include measurement of thermal stability and composition of a material. TGA is most useful to study for dehydration, decomposition, desorption, and oxidation processes. In Differential Thermal Analysis **(**DTA), the temperature of a sample is compared with that of an inert reference material during a programmed change of temperature. Changes in the sample, either exothermic or endothermic, can be detected relative to the inert reference. Thus, a DTA curve provides data on the transformations that have occurred, such as glass transitions, crystallization, melting and sublimation. The area under a DTA peak is the enthalpy change and is not affected by the heat capacity of the sample.

Brunauer-Emmett-Teller (BET) surface area

The specific surface area of a material is evaluated by this analysis by nitrogen multilayer adsorption measured as a function of relative pressure. This technique covers the external area and pore area evaluations to determine the total specific surface area in m^2/g of macroporous and mesoporous materials, along with pore volume and pore size distributions that characterise porosity of a material. Standard BET analysis is conducted at the boiling point of liquid nitrogen (77 K).

Barrett-Joyner-Halenda (BJH) analysis can also be employed to determine pore area and specific pore volume using adsorption and desorption techniques. This technique characterises pore size distribution independent of external area due to particle size of the sample [19-20].

Vibrating Sample Magnetometry (VSM)

It is a technique used to measure the magnetic properties of a material. It is based on Faraday's law of induction in which the vibrating component causes a change in the magnetic field of the sample, which generates an electric field in a coil. The sample is placed within suitably placed sensing coil and held at desirable angle and is mechanically vibrated. The magnetic field appears around the sample and magnetization of the sample is analysed as the vibration begins. This generates hysteresis loop which shows the nature of magnetization and is a characteristic of a material [21-22].

X-ray photoelectron spectroscopy (XPS)

XPS is a surface sensitive quantitative spectroscopic technique, essentially used for measuring elemental composition, empirical formula, chemical state and electronic state of the element within the material. It is mainly used to study the binding energy of core electron in an atom. XPS is based on the principle of measurement of the kinetic energy of photoelectrons generated when the sample is illuminated with soft X-ray radiation in the ultrahigh vacuum.

The energy of the photoelectrons thus leaving the sample is determined and this gives a spectrum for intensity as a function of binding energy. The binding energies of the peaks are characteristic of each element. Hence, XPS can also provide chemical binding information. For catalytic study, it was first developed by Siegbahn in the late 1950s and 1960s, to allow determination of the surface region of catalytic materials [23].

References

1. J. L.G. Fierro, Metal Oxides: Chemistry and Applications, CRC Press, Florida, 2006.
2. A.R. José, F.-G. Marcos, Synthesis, Properties, and Applications of Oxide Nanomaterials, Willey, New Jersey, 2007.
3. D.W. Goodman, Chemical and Spectroscopic Studies of Metal Oxide Surfaces, J. Vac. Sci. Technol. A 14 (1996) 1526-1531.
4. G. Oskam, Metal Oxide Nanoparticles: Synthesis, Characterization and Application, J. Sol-Gel Sci. Technol. 37 (2006) 161-164.
5. P.H.C. Camargo, K.G. Satyanarayana, F. Wypych, Nanocomposites: Synthesis, Structure, Properties and New Application Opportunities, Mater. Res. 12 (2009) 1-39.
6. F.E. Kruis, H. Fissan, A. Peled, Synthesis of Nanoparticles in the Gas Phase for Electronic, Optical and Magnetic Applications-A Review, J. Aerosol Sci. 29 (1998) 511-535.
7. S. Zhang, D. Sun, Y. Fu, H. Du, Recent Advances of Superhard Nanocomposite Coatings: A Review, Surf. Coat. Technol. 167 (2003) 113-119.
8. W.S. Khan, N.N. Hamadneh, W.A. Khan, Polymer Nanocomposites – Synthesis Techniques, Classification and Properties, P.D. Sia (Ed), Science and applications of Tailored Nanostructures, One Central Press, (2017) 50-67.
9. R. Saravanan, F. Gracia, A. Stephen, Basic Principles, Mechanism, and Challenges of Photocatalysis, M.M. Khan *et al*. (Eds.), Nanocomposites for Visible Light-induced Photocatalysis, Springer International Publishing (2017) 19-40.
10. A. Ajmal, I. Majeed, R.N. Malik, H. Idriss, M.A. Nadeem, Principles and Mechanisms of Photocatalytic Dye Degradation on TiO_2 Based Photocatalysts: A Comparative Overview, RSC Adv. 4 (2014) 37003-37026.
11. M. Rochkind, S. Pasternak, Y. Paz, Using Dyes for Evaluating Photocatalytic Properties: A Critical Review, Molecules 20 (2015) 88-110.
12. N.M. Julkapli, S. Bagheri, S.B.A. Hamid, Recent Advances in Heterogeneous Photocatalytic Decolorization of Synthetic Dyes, Sci. World J. 2014 (2014) 1- 25.
13. W.-K. Jo, R.J. Tayade, Recent Developments In Photocatalytic Dye Degradation Upon Irradiation with Energy-Efficient Light Emitting Diodes, Chin. J. Catal. 35 (2014) 1781-1792.
14. A. Gnanaprakasam, V.M. Sivakumar, M. Thirumarimurugan, Influencing Parameters in the Photocatalytic Degradation of Organic Effluent *via* Nanometal Oxide Catalyst: A Review, Indian J. Mater. Sci. 2015 (2015) 1-16.

15. M.P. Reddy, A.Venugopal, M. Subrahmanyam, Hydroxyapatite Photocatalytic Degradation of Calmagite (an Azo Dye) in Aqueous Suspension, Appl. Catal. B 69 (2007) 164-170.
16. S. Stankic, S. Suman, F. Haque, J. Vidic, Pure and Multi Metal Oxide Nanoparticles: Synthesis, Antibacterial and Cytotoxic Properties, J. Nanobiotechnol. 14 (2016) 73:1-20.
17. B. Kim, J. Kim, H. Baik, K. Lee, Large-scale One Pot Synthesis of Metal Oxide Nanoparticles by Decomposition of Metal Carbonates or Nitrates, CrystEngComm, 17 (2015) 4977-4981.
18. S. Suresh, Semiconductor Nanomaterials, Methods and Applications: A Review, Nanosci. Nanotechnol. 3 (2013) 62-74.
19. R. Srivastava, Synthesis and Characterization Techniques of Nanomaterials, Int. J. Green Nanotechnol. 4 (2012) 17-27.
20. M. Joshi, A. Bhattacharyya, S.W. Ali, Characterization Techniques for Nanotechnology Applications in Textiles, Indian J. Fibre Text. Res. 33 (2008) 304-317.
21. W. Burgei, M.J. Pechan, H. Jaeger, A Simple Vibrating Sample Magnetometer For Use in a Materials Physics Course, Am. J. Phys. 71 (2003) 825-828.
22. W.E. Case, R.D. Harrington, Calibration of Vibrating-Sample Magnetometers, J. Res. Natl. Bur. Stand. Sec. C 70C (1966) 255-262.
23. T.A. Carlson, Photoelectron and Auger Spectroscopy, Plenum Press, New York, 1976.

Chapter 2 – Template Assisted Synthesis of Mesoporous TiO_2

2.1. Introduction

TiO_2 based photocatalytic systems have been utilized in various environmental applications for removing contaminants from air and water and decomposition of unwanted and toxic organic compounds. It is found to be an ideal photocatalyst because of its non-toxic nature, water insolubility, resistance to corrosion, low cost and photo-stability in solutions [1-3]. TiO_2-based photocatalysis is exhaustively researched all over the world for heterogeneous photocatalytic reactions and other environmental cleanup applications. However, it has a major drawback of wide band-gap energy and many investigations on decreasing the band-gap value and enhancement of the photocatalytic activity in either or both the ultraviolet or visible region has been carried out for past few years.

TiO_2 structure and properties

Titanium dioxide exhibits polymorphism and the different polymorphs of it in nature are known. Till date 13 polymorphs are reported, among which the commonly known are anatase (β-TiO_2) (tetragonal), brookite (α-TiO_2) (orthorhombic) and rutile (γ-TiO_2) (tetragonal). The other polymorphs include, bronze (TiO_2 (B)) (monoclinic), hollandite (TiO_2 (H)) and ramsdellite (TiO_2 (R)), all of which are low pressure phases. Some of the high pressure phases include, columbite (α-PbO_2-type, TiO_2-II), baddeleyite, cotunnite, fluorite, pyrite, modified fluorite and hexagonal Fe_2P-type, which can be synthesized from rutile phase [4].

Of these, far more studied are brookite, anatase and rutile and rutile is known to be a most stable polymorph. All these three polymorphs can be readily synthesized in the laboratory. The metastable anatase and brookite can be transformed into the thermodynamically stable rutile phase by calcining at temperature above 600 °C [5-6]. In all three forms, TiO_6 octahedra are formed by titanium (Ti^{4+}) atoms co-ordinating to six oxygen (O^{2-}) atoms [7]. Both anatase and rutile polymorphs adopts a tetragonal structure, but the difference between the two is that, four edges are shared per octahedron with no corner sharing in anatase, while in rutile the two opposite edges of octahedron are shared to form linear chains, which are joined through corner connections. In case of brookite with an orthorhombic structure, octahedra share three edges and also corners [8-9].

Titanium dioxide is an n-type semiconductor in its sub-stoicheometric form TiO_{2-x}, due to oxygen deficiency created because of intrinsic defect [10]. The typical band-gap for rutile is

3.0 eV, while for anatase it is 3.4 and brookite 3.3 eV [11]. The key properties of these three phases are summarized below (Table 1).

Table 1- Key properties of the three phases of TiO_2

Property	Anatase	Rutile	Brookite
Light absorption (nm)	< 390	< 415	
Mohr's (Mohs) Hardness	5.5	6.5 – 7.0	5.5-6.0
Refractive index	2.55	2.75	>2.5
Dielectric constant	31	114	
Crystal structure	Tetragonal	Tetragonal	Orthorhombic
	a = 3.78	a = 4.59	a = 5.4558
	b = 9.1819		
	c = 9.52	c = 2.96	c = 5.1429
Density (g/cm^3)	3.79	4.13	3.99
Ti–O bond length (Å)	1.94 (4) 1.97 (2)	1.95 (4)	1.98 (2)
Specific gravity	3.9	4.2	4.08-4.18
Band-gap	3.2	3.0	3.3

Importance of TiO_2

TiO_2 first caught the eye of the scientific community in 1972, when Fujishima and Honda reported the water splitting photochemically, using TiO_2 as an anode [12]. Subsequently, in 1977, Frank and Band reported photo-reduction of CN^- in water [13-14]. This was the beginning of remediation of environmental pollutants by using TiO_2 as a photocatalyst. Both this breakthroughs brought about immense interest in TiO_2 because of its potential for treatment of water and air pollution using "free" solar energy. Further, Wang *et al.* disclosed excellent antifogging and self-cleaning ability of the photo-excited TiO_2 surface by its super hydrophilic properties [15]. Graetzel and O'Regan in 1991 announced the utility of nano TiO_2 in efficient dye sensitized solar cells (DSSC) [16]. This led to research in the area of confining the size of TiO_2 to nano level for improving photocatalytic efficiency of TiO_2. Various strategies were explored for controlling the size, morphology, surface area and porosity.

TiO_2 is claimed to show maximum light scattering ability with virtually no absorption. Mechanistic steps involved in heterogeneous photocatalytic processes are excitation, bulk diffusion and surface transfer of photo-excited electrons and holes. Apparently, the reactivity of photocatalyst is affected by surface atomic structures. Hence the worldwide interest has emerged in tuning of photocatalysts in order to optimize the photocatalytic reactivity [17].

As described in the literature, visible light activity of the three phases of TiO_2 follows the order, anatase > brookite > rutile. The higher photocatalytic activity of anatase phase in

comparison to rutile is described to be due to the higher Fermi level of anatase, which is responsible for longer photo-excited electron-hole lifetime and higher electron mobility [18-19]. Due to higher photocatalytic activity and high surface area, anatase titania has received much attention in past three decades.

Literature studies are also available with the observation that, the combination of anatase and rutile phases show better photocatalytic activity, may be due to enhanced separation of photo-generated electron-hole pairs [20]. Synergistic effect between anatase and rutile is responsible for excellent activity, for example Degussa P25, which is considered as a benchmark photocatalyst [21].

Methods of preparation

Sol-gel is a most commonly used and highly versatile soft chemical technique, applied for synthesizing metal-oxide in its nano structured form by a relatively simple route. It involves controlled hydrolysis of metallo-organic compounds (alkoxides), which is especially beneficial in the formation of mesoporuos TiO_2 with hierarchical nanostructures. It offers the unique advantage of producing highly pure homogeneous precursor powder, having better control over stoichiometric composition, particle morphology and size. Sol-gel chemistry is primarily originated with the hydrolysis and condensation of metal alkoxides and therefore tailoring of various types of nanoparticles is possible. The synthesis parameters can be altered by using different metal alkoxides precursors, such as titanium tetraisopropoxide, titanium tetraethoxide, titanium tetrabutoxide or titanium tetrachloride [22. The uncontrolled hydrolysis and condensation, results in TiO_2 particles with poor control over the size and properties. Moreover, it requires calcination process to obtain final product, which causes agglomeration of the particles. Hence efforts are made to control the hydrolysis and condensation process during gelling. The size, shape and properties can be controlled by adding modifier during the hydrolysis process. Changing the properties of the hydrolysis media or introducing an acid group as a surfactant or template material is also attempted in this context [23-24]. The new strategy of employing some of the organic ligands as surfactants or capping agents is found beneficial for obtaining small nanoparticles with a perfect control over the size and morphology and high dispersibility. Various organic compounds such as thiols, carboxylic acids, beta-diketones like acetylacetonate (acac) and amines have been used effectively as metal oxide modifiers [25-30]. These compounds act as ligands or surfactants, controlling the hydrolysis and condensation reactions, thus resulting in affecting morphology of nanoparticles.

a. Aqueous sol-gel method

In this method, the starting metal precursors, usually metal alkoxides, are converted to inorganic solid by inorganic polymerization mediated by water. In the first step, the metal precursors are hydrolyzed by water to metal hydroxide. This process is accelerated by addition of acid or base. This results in a homogeneous solution. In the second step, condensation (oxolation) takes place to form M-O-M bond. This is referred to as inorganic polymerization and the process is the aging process. In this process colloidal particle starts appearing which further slowly forms a gel. The gel is rigid, porous in an interconnected network in water. This process is called sol-gel transition. The gel is then usually dried by evaporating water. The resultant powder obtained is amorphous in nature. Further calcinations results in crystalline powder.

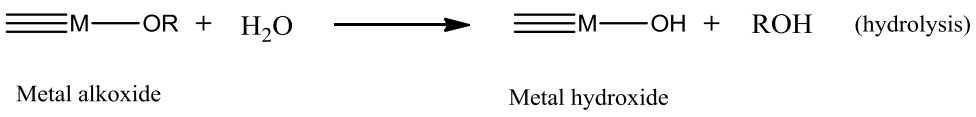

Metal alkoxide

Metal hydroxide

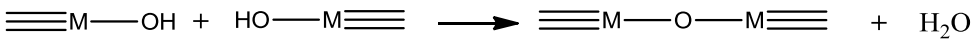

(oxolation)

(condensation and polymemrization)

During hydrolysis step the quantity of water added, way of addition and the pH of the medium are important factors. If the hydrolysis is incomplete, oligomeric intermediate species are formed. This process is called as alkoxolation.

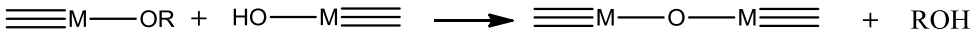

(alkoxolation)

b. Non-aqueous sol-gel method

In this method, the metal precursors are placed in an organic solvent in absence of water. In addition to metal alkoxide and metal salts, which are used in aqueous sol-gel method, metal acetates and metal acetylacetonates are also employed. Here the oxygen of the metal oxide comes from organic ligand, which differs from aqueous sol-gel method where it originates from water. The metal-oxygen-metal bond, the basic structure arises from mostly simple organic reactions. The schematic representations of these organic reactions are shown below.

i) Alkyl halide elimination

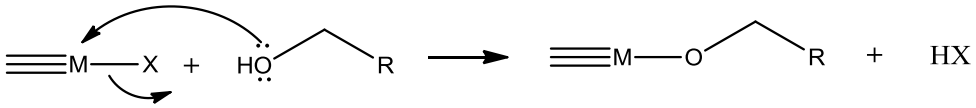

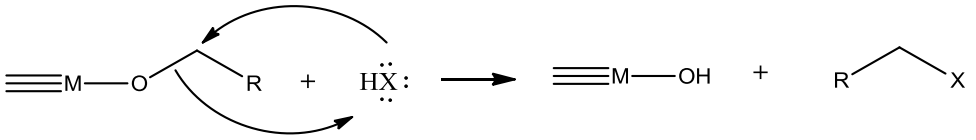

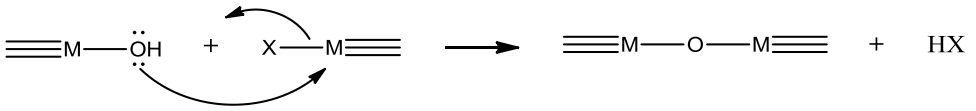

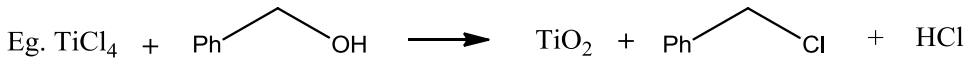

ii) Esterification and hydrolysis

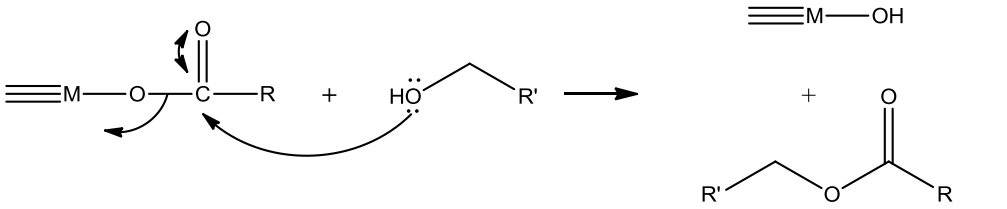

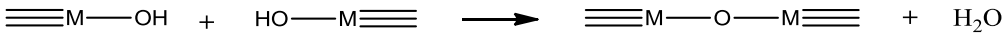

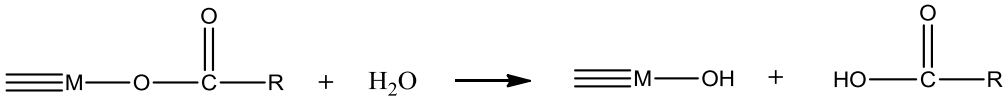

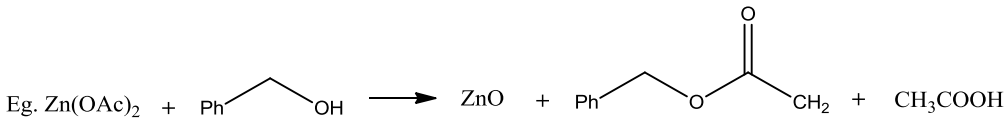

iii) Amidation and/or hydrolysis

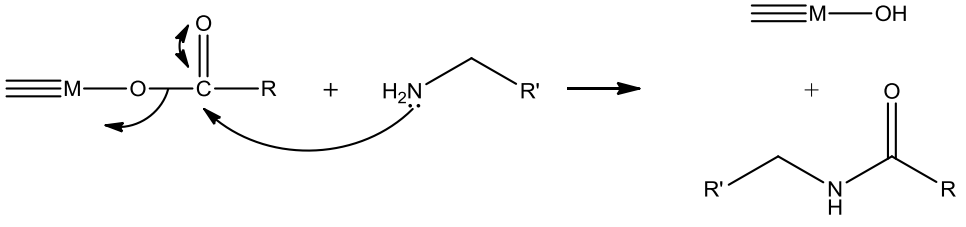

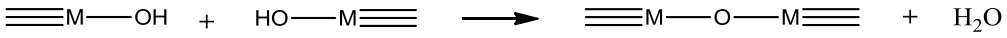

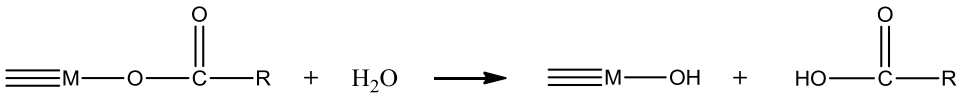

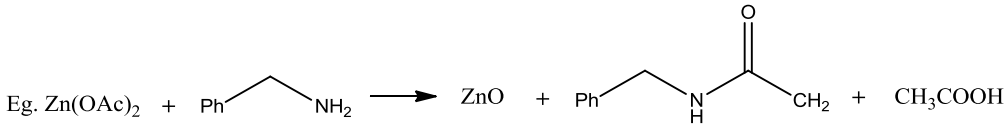

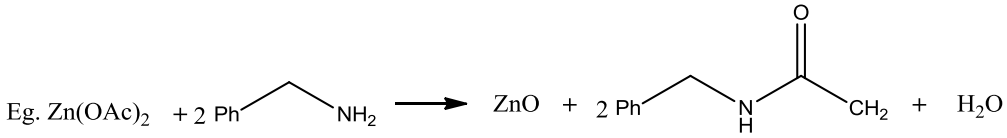

iv) Ligand exchange, esterification and hydrolysis

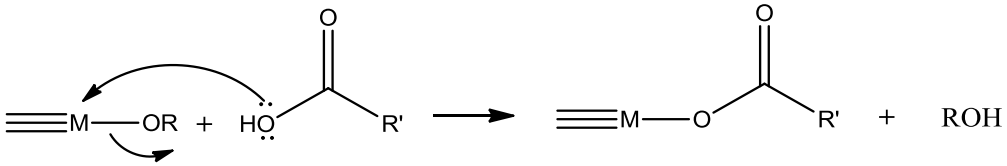

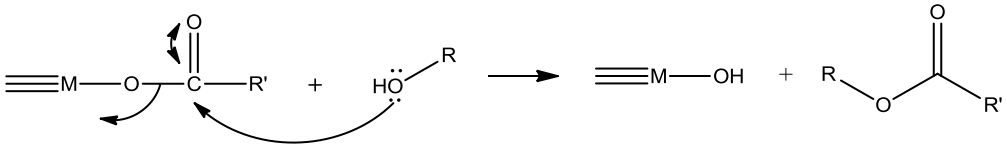

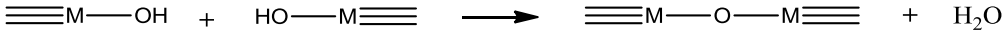

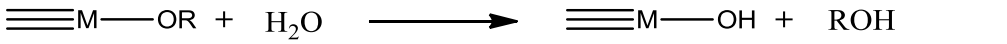

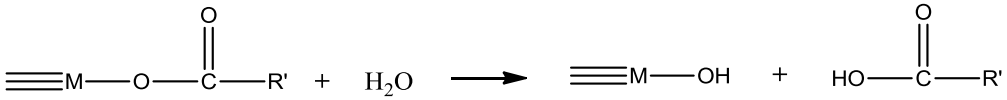

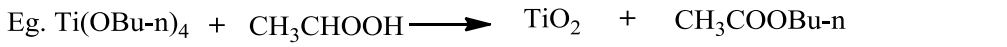

v) Etherification and hydrolysis

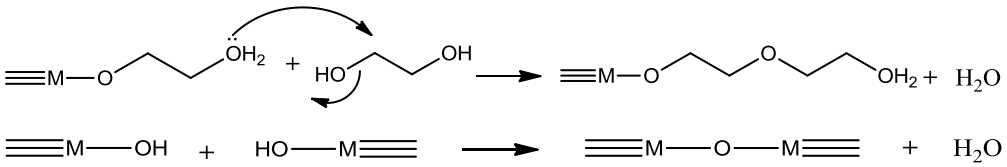

Eg. $Ti(OiPr)_4$ + $HOCH_2CH_3OH$ ⟶ TiO_2 + iPrOH + $HOCH_2CH_2OCH_2CH_2OH$

v) Condensation and hydrolysis

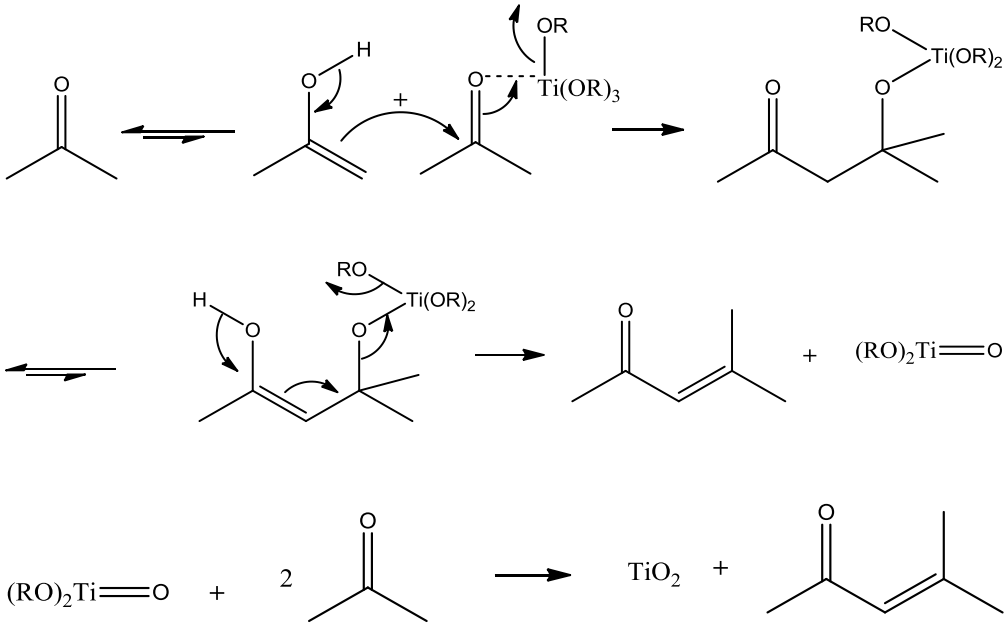

Eg. $Ti(OiPr)_4$ + 4 CH_3COCH_3 ⟶ TiO_2 + 4 iPrOH + 2 $CH_3COCH{=}C(CH_3)_2$

vi) C-C bond formation between benzylic alcohols and alkoxides

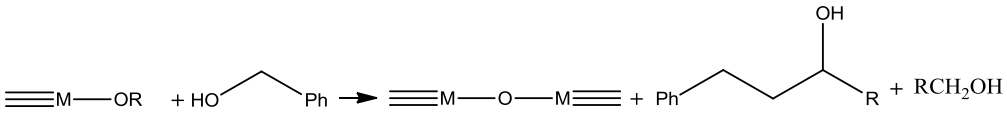

(Mechanism of this reaction is not clearly understood)

Eg. $Ti(OBu)_4$ + $PhCH_2OH$ ⟶ TiO_2 + $PhCH_2CH_2CHOHPr$ + BuOH

Applications in environmental remediation

Solar energy is the most important alternative energy source in the future and has an advantage of free availability and abundance in nature; therefore, it is required to select a material which efficiently absorbs the solar radiations. Current research in the field of photocatalysis is devoted to develop a photo-active material which could effectively utilize the maximum part of solar energy. However, the photocatalytic efficiency of these materials is influenced by their optical properties. For titanium dioxide, the photo-efficiency is limited by its large intrinsic band-gap. Thus the required modification in this wide band-gap semiconductor TiO_2 is in high demand. With the help of DFT calculations brookite and rutile are proved to have direct fundamental band-gap, while that of anatase possesses indirect band-gap [31].

Recombination is another major issue which results from electron and hole pairs generated by photon energy when the material is exposed to light. These species play a significant role in surface photocatalytic processes. However, due to a slow mobility of electrons, they tend to recombine with the corresponding holes generated and thus are less available near the surface which in turn results in the decreased photocatalytic activity of the material. Particle size reduction while retaining high crystallinity is an important approach to prevent recombination, since the smaller particle size with high crystallinity helps for faster diffusion of charge carriers to the surface without charge recombination [32].

The mesoporous titania material is of special interest in recent years, since it displays the good photocatalytic activity due to fast diffusion of charge carriers to the surface. In this regard attempts have been made to synthesize mesoporous titania by using various surfactants and template materials.

In addition to being a good photocatalytic semiconductor under solar light illumination, titania nanoparticles are known to be an effective adsorbent. Adsorption of the different chemicals onto calcined material and its kinetics is studied by many researchers.

Thus, it can be said that crystallinty, surface properties and morphologies are the important factors which affect the photocatalytic activity of the semiconductor material. In view of this, mesoporous TiO_2 of anatase phase with high crystallinity and large surface area has received much attention principally in the field of photocatalysis, due to its 3D connected pore network favoring diffusion of reactants and products and also providing more active sites. The uniform mesopore channels in this material increases the density of active sites with high accessibility leading to high surface area and pore volume providing enhanced dye loading capability and pollutant adsorption [33-34].

The concept of mesoporous TiO_2 was first taken up by Antonelli and Ying in 1995 [35]. Since then much effort has been made in this field for further improving mesoporosity. Generally, the synthesis of ordered mesoporous TiO_2 can be performed by using soft or hard templates, which act as structure directing agents to form mesoporous networks. This includes some of the cationic/ anionic surfactants, phosphates or amines as soft templates or porous silica/ alumina which are used in hard templating agents.

Mesoporous TiO_2 structure development basically includes three steps, firstly preparing ordered mesoporous TiO_2 followed by enlarging pore sizes which then results in semi-crystalline to highly crystalline frameworks.

It is well known that highly crystalline frameworks are obtained at high calcination temperatures. However, it leads to collapse of mesoporous structures on heating at high temperatures. In addition, the phase change from anatase to rutile is also obvious at high calcination temperature. Thus, it is required to choose an appropriate synthetic method for preparing such material with all these desired properties. Synthesizing mesoporous titania using various surfactants is a major challenge accepted by many researchers in recent years.

Other than cationic/ anionic surfactants, phosphates or amines, organic acids as templates or surfactants are usually employed due to their benefit of easy removal during the calcination process. They act as directing templates by coordinating with the sol by different mechanisms. However, systematic study regarding use of organic acids as templates depending on the size, nature and the role they could play during polymerization was lacking. Therefore, it was thought worthwhile to study organic acids as soft templates for the preparation of mesoporous nano TiO_2 by the sol-gel method.

Carboxylic acids are successfully used as such modifiers in solvothermal synthesis, with a coordination of carboxylic groups (-COOH) to the surface Ti atoms [36-37]. They play an important role in improving the quality of the catalyst when used as a template material. Particularly long chain carboxylic acids, such as decanoic acid, oleic acid and linoleic acid are very effective.

During hydrolysis and condensation (polymerization) reaction of $Ti(O\textit{i}Pr)_4$ in water leading to a gel with three dimensional network of Ti-O-Ti bonds, two processes can occur simultaneously. In the first process, complete hydrolysis of $Ti(O\textit{i}Pr)_4$ to $Ti(OH)_4$ can take place and in the second process, partial hydrolysis to form $Ti[(OH)(O\textit{i}Pr)_4]$ can take place. This then undergoes polymerization and in the second case polymerization and hydrolysis, as depicted in Scheme 1.

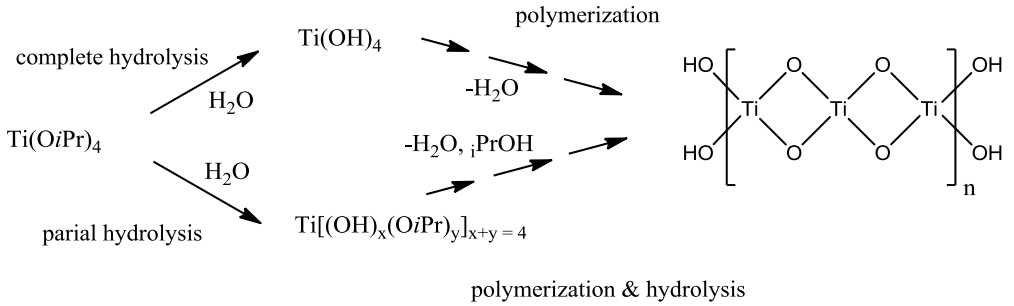

Scheme 1

In the presence of organic acids, three more processes can compete as shown in Scheme 2. The other three processes are expected to slow down the polymerization leading to some control in the final network of the gel.

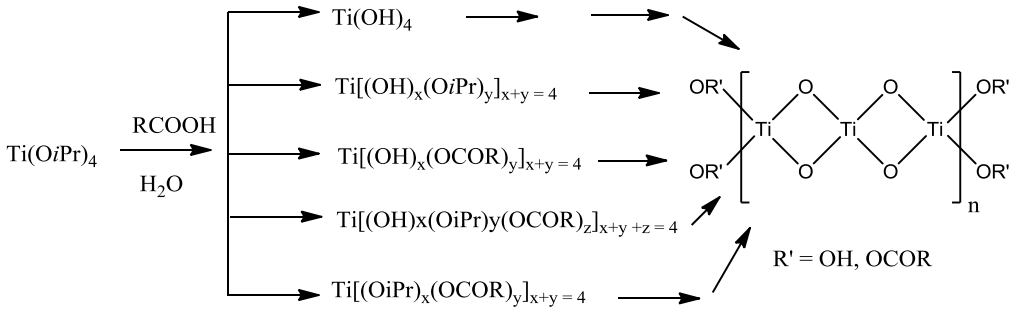

Scheme 2

A typical polymerization process by which an acid can control the formation of TiO_2 is depicted in Scheme 3. Here one can see capping with the carboxylate bond of the oligomers, is responsible for the control.

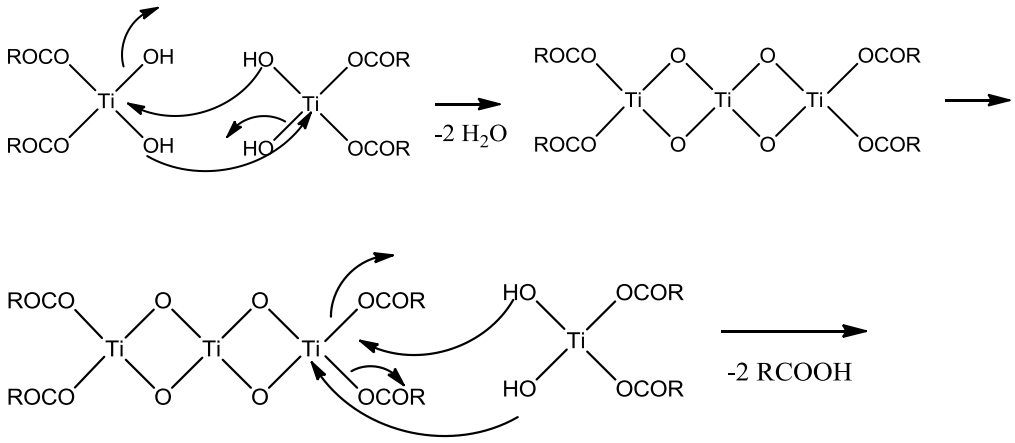

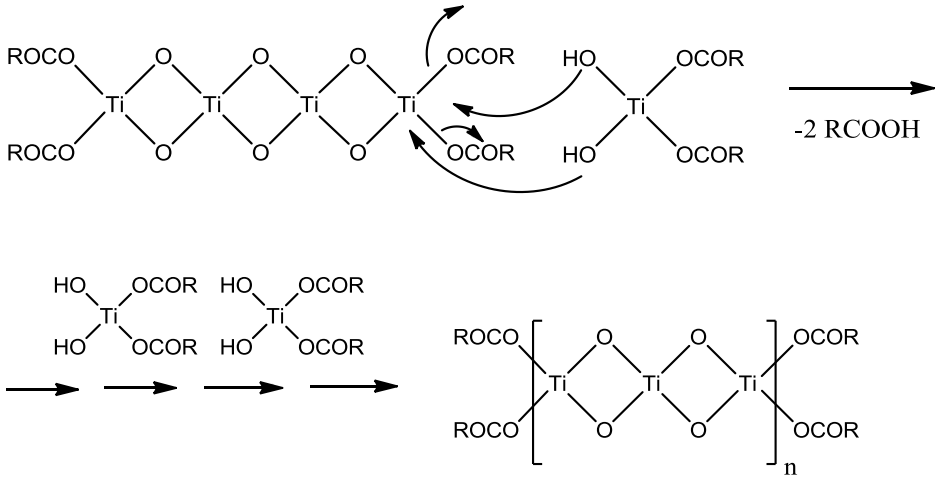

Scheme 3

Literature search indicated that the sol-gel method using carboxylic acids is not well studied. So we thought of studying various types of organic acids for the sol-gel synthesis of TiO_2. At first, a systematic study of the effect of chain length of monocarboxylic acid templates on the properties of synthesized TiO_2 was undertaken. We then replaced straight chain acids with hindered acids, dicarboxylic acids and amino acids as starting precursor and studied their effect on properties of resultant catalysts. We also then explored a new non-aqueous route to make TiO_2 with tailored properties. All this work is described in this chapter. This chapter is divided into four sections. The first section covers the importance of catalytic TiO_2 nanoparticles prepared from series of mono-carboxylic acids as precursor materials. This is further divided into straight chain and branched chain acid precursors. In the second section the importance of catalytic TiO_2 nanoparticles prepared from a series of di-carboxylic acids as precursor materials are covered. The third section deals with the importance of catalytic TiO_2 nanoparticles prepared from series of amino acids as precursor materials. The fourth section is about the catalyst prepared by organic precursors mediated imination reaction.

All these catalytic materials obtained were further evaluated for photocatalytic degradation of methylene blue, which is considered as one of the model compound in the field of environmental pollution. The detailed degradation procedure of this compound was studied by using LC-MS technique and the same is discussed at the end of this chapter.

2.2. General experimental procedure

Materials

Titanium tetraisopropoxide (TIP, reagent grade, 97%), carboxylic acids, *viz.*, formic acid, acetic acid, butyric acid, octanoic acid, palmitic acid, pivalic acid, phenoxyacetic acid, oxalic acid, malonic acid, succinic acid, glutaric acid, adipic acid, maleic acid, fumaric acid, malic

acid and tartaric acid; amino acids, *viz.*, glycine, DL-alanine, β-alanine, DL-valine, L-proline, DL-serine, DL-aspartic acid, L-glutamic acid; and, aniline and anisaldehyde were used as template materials, which were purchased from Spectrochem, methylene blue (MB) from Merck and calmagite (CG) from Thomas Baker. Isopropyl alcohol (IPA) supplied by Loba Chemicals was used as a solvent and deionized water was used as a medium. All the reagents were used without any further treatment.

Synthetic procedure

a. By using aqueous sol-gel route

In a typical synthesis, the predetermined amount of acid precursor was first dissolved completely in a definite quantity of water (200 mL) to make a homogeneous mixture. In case of phenoxyacetic acid and palmitic acid, an appropriate amount of ammonia solution was added for complete dissolution. To this acid solution, titanium (IV) isopropoxide (16.4 mmol), previously mixed with isopropanol (50 mL), was added drop wise with constant stirring. The reaction mixture was stirred vigorously. White colloidal gel started to develop in about 2 h. The complete gelation occurred after 12 h constant stirring. A white colloidal gel obtained was dried at 100°C to yield a powder. This amorphous powder was further calcined at 500 °C for 3 h to obtain crystalline nano-sized TiO_2 powder. The ratio of TIP:acid was maintained as 1:4 for series 1 and 3 and 1:3 for series 2. The catalysts obtained were coded according to precursor acid used and are categorized into three different series (Table 2, 3, 4 and 5 respectively).

Table 2 – Sample labelling for series 1a

Precursor acid	Label
Formic acid	A1
Acetic acid	A2
Butyric acid	A3
Octanoic acid	A4
Palmitic acid	A5

Table 3 – Sample labelling for series 1b

Precursor acid	Label
Pivalic acid	P1
Phenoxyacetic acid	P2

Table 4 – Sample labelling for series 2

Precursor acid	Label
Oxalic acid	B1
Malonic acid	B2
Succinic acid	B3
Glutaric acid	B4
Adipic acid	B5
Maleic acid	B6
Fumaric acid	B7
Malic acid	B8
Tartaric acid	B9

Table 5 – Sample labelling for series 3

Precursor acid	Label
Glycine	C1
L-proline	C2
β-alanine	C3
DL-alanine	C4
L-glutamic acid	C5
DL-aspartic acid	C6
DL-valine	C7
DL-serine	C8

b. By using non-aqueous route.

Mesoporous nanocrystalline titania was prepared under controlled hydrolysis conditions by a sol-gel process in non-aqueous medium. Titanium isopropoxide was hydrolyzed through the imination reaction of anisaldehyde in isopropanol solvent medium. All the experimental operations were carried out in the dry and anhydrous medium.

In a typical synthesis, aniline (8 mL, 87.62 mmol) was mixed with isopropanol (50 mL) and to this mixture titanium (IV) isopropoxide (5 mL, 16.48 mmol) diluted with isopropanol (30 mL) was added with constant stirring. Anisaldehyde (8 mL, 65.81 mmol) in isopropanol (20 mL) was then added drop wise with constant stirring. The entire mixture was allowed to stir for further 2 h, which resulted in a white homogeneous colloidal solution. The reaction mixture was continued to stir for further 12 h for gelation. The gel was centrifuged at 5000 rpm. The residue was washed with isopropanol 3 times to remove the excess aniline and the imine. The resulted semisolid material was dried at 100 °C to get a precursor powder, and was further calcined at 500 °C for 3 h to produce the desired TiO_2 nanopowders. The resultant catalysts were coded according to the varied ratio of precursors. The molar ratio of TIP: aniline: anisaldehyde was maintained here as 1:5:4.

Further, the ratio was varied to 1:4:3, by mixing aniline (6 mL, 65.94 mmol), anisaldehyde (6 mL, 49.45 mmol) and 1:3:2, by mixing aniline (4 mL, 49.54 mmol), anisaldehyde (4 mL, 32.97 mmol) in isopropanol solution with the same procedure as above. The same volume of TIP was maintained throughout the reaction.

The samples coded according to the varied ratio of precursors are given in Table 6.

Table 6 – Sample labelling for series 4

TIP: aniline: anisaldehyde ratio	Label
1 : 5 : 4	O1
1 : 4 : 3	O2
1 : 3 : 2	O3

Characterization of TiO_2 nanoparticles

The crystal phase composition and crystallite size of TiO_2 nanoparticles were recorded using Bruker D8 ADVANCE X-ray diffractometer with Cu Kα radiation (1.5406 Å) in the 2θ scan range of 10-80°. The average crystallite size for the series of TiO_2 nanopowders were estimated according to the Scherrer's equation-

$$D = K\lambda / \beta \cos\theta \quad \text{- (eq. } \mathbf{1}\text{)}$$

Where, K is the Scherrer constant, λ is the X-ray wavelength, β is the peak width at half maximum and θ is the Bragg's diffraction angle.

The percentage of anatase phase in the respective samples was calculated using the equation

$$\% A = 100 / (1 + 1.33 [I(R) / I(A)]) \quad \text{- (eq. } \mathbf{2}\text{)}$$

Where, I(A) and I(R) are the intensities of the major anatase (101) and rutile (110) peaks respectively.

Morphology of the sample was investigated by using Zeiss Avo18 scanning electron microscopy (SEM), which was further confirmed and also determined the particle size of the sample, by using transmission electron microscopy (TEM). Bright field and high resolution TEM and selective area electron diffraction (SAED) patterns were obtained by using TECHNAI F30 and PHILIPS CM 200 field emission transmission electron microscope operating at 200 kV. The TEM samples were prepared by sonicating nanopowders in methanol for 5 min before placing the sample on a formvar-coated copper grid.

The surface area (S_{BET}) of the samples was analyzed by a multipoint Brunauer-Emmett-Teller (BET) method using nitrogen adsorption/desorption isotherm measurements on a Quantachrome ASiQwin (ASIQC0100-4) and TriStar 3000 V6.08 instruments. Before the

analysis, samples were degassed at 150-300 °C for 0.5-12 h with continuous flow of nitrogen gas.

Optical properties of all the samples were studied using UV-Vis diffuse reflectance spectroscopy (UV-DRS) (Shimadzu UV-2450) with $BaSO_4$ as a reference. Spectra were recorded at room temperature in the wavelength range of 200-800 nm. The minimum wavelength required to promote an electron depends upon the band-gap energy (E_g, eV) of the photocatalyst and can be estimated by determining the absorption wavelength (λ_{max}, nm) of each UV-Visible absorbance spectrum and calculating by the known relationship between the absorption band edge and the band-gap

$$E_g = 1239.8 / \lambda_{max} \quad \text{- (eq. 3)}$$

Where, E_g is the band-gap (eV) and λ (nm) is the wavelength of the absorption edges in the spectrum.

The IR studies were carried out on a Shimadzu IR Prestige-21 FTIR in the range of 4000-400 cm^{-1}. Thermogravimetric analysis (TG-DTA) was carried out in air up to 800 °C at the heating rate of 10 °C min^{-1} using STA 409 PC Luxx simultaneous TG-DTA analyzer (Netzsch, Germany).

Photocatalytic activity testing

The photocatalytic activity of these samples was measured in terms of dye degradation under direct sunlight and also using 125 W Hg lamp. Methylene blue and calmagite dyes were selected due to their toxic effect when released in water from various industries. The catalytic activity of these samples was compared with the commercial Degussa P25, since it is well a known reference material with mixed anatase and rutile phase, for photo-degradation of various dyes and other organic materials.

The experiment was carried out in bright sunlight for 120 min between 10:00 am to 12:00 noon. In a typical experiment, dye stock solutions (0.010 g/L – methylene blue and 0.020 g/L – calmagite) were prepared in deionized water. A given amount of the catalyst (10 mg) was added to 25 mL of a dye solution. The contents of the solution were allowed to equilibrate for a given time (usually 15–30 min) in the dark before irradiation and then were exposed to sunlight irradiation for the duration of the experiment under intermittent swirling. The prepared catalysts were also tested for their activities by irradiating the reaction mixtures with a 125 W Hg lamp in case of series A.

After every 20 min interval, 2 mL aliquots were pipetted out, centrifuged and the absorbance of the clear supernatants was recorded at the wavelength 660 nm for MB and at 540 nm for

CG, against the appropriate blanks. The experiment was repeated for three times and the average of three readings was considered. The extent of photo-degradation of dye was calculated using a calibrated relationship between the measured absorbance and concentration. The recyclability studies were also done for three cycles. The kinetic studies of the same were carried out from which the rate of dye degradation was determined.

2.3. Results and discussion

Section A – Use of monocarboxylic acid templates

This section describes the use of aliphatic linear chain monocarboxylic acids as templates. In literature, some small chain and long chain acids are reported for controlling hydrolysis and as surfactant materials in the synthesis of TiO_2. Smaller chain organic acids have been used to control the hydrolysis of titanium alkoxide by converting it to alkoxycarboxy titanates [38-44]. Longer chain acids are mostly used as surfactants in the hydrothermal synthesis due to their affinity for various surfaces along with additives like amines to make tailor made shapes of nano TiO_2 [23, 45-50]. However, the systematic study of the effect of chain length of the acid on the properties of catalysts prepared was lacking in this field. As the properties of TiO_2 are known to depend on the templating agent, here we have carried out a detailed study of the effect of monocarboxylic acid chain length on the mesoporosity and other properties using the sol-gel method.

This section was divided into two parts.

Part 1 – Study of straight chain monocarboxylic acids as templates

Introduction

Here we chose formic acid, acetic acid, butyric acid, octanoic acid and palmitic acid for our study (Table 2). The structures of theses acids are given in Fig. 1. It was planned to hydrolyze titanium isopropoxide (TIP) in the presence of excess acid in water so that adequate control on hydrolysis, condensation and gel formation could be achieved. The gel can then be calcined to retain the porous structure and to get rid of the organic part. During the condensation process, one acid molecule can bond or two acid molecules can bond (I and II, Scheme 4) with the condensate to control the polymerization by breaking the chain in the gel structure. During the calcination, a nonhydrolytic route to final particulate was expected. The metal carboxylates formed were expected to decompose to metal oxide and volatile organic fragments at 500 °C. The carboxylate I (Scheme 5) would undergo elimination of an acid, while the carboxylate II an acid molecule, carbon monoxide and an alkene fraction or an acid and a ketene (scheme 6). In the case of formic acid, the carboxylate II would eliminate one molecule of formic acid and carbon monoxide (Scheme 7). It was also of interest to study whether the sol-gel method could control the shape of the particulates. Further, the prepared catalysts were to be evaluated for photo-degradation of methylene blue (MB), a dye usually used to test the photocatalytic activity of a catalyst.

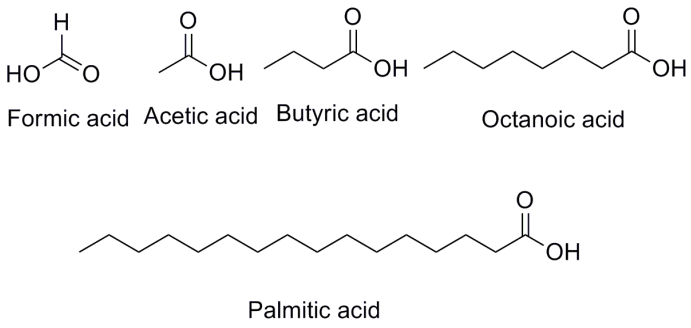

Fig. 1 – *Structures of the precursor acids used for series 1a*

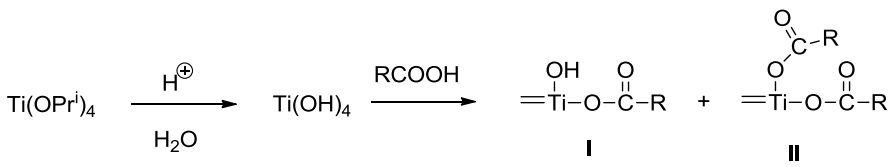

Scheme 4

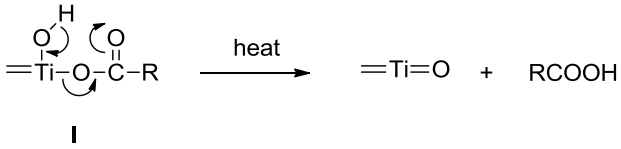

I

Scheme 5

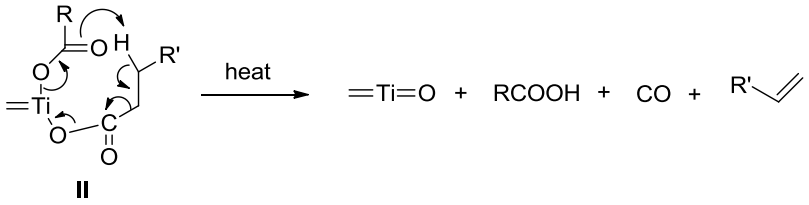

II

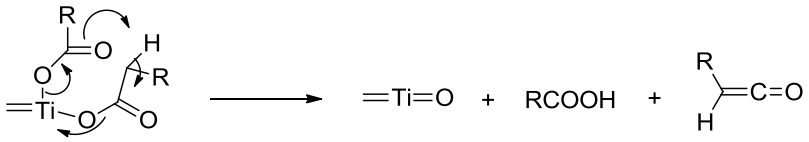

II

Scheme 6

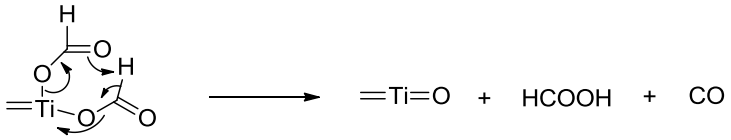

II

Scheme 7

Surface, structural and optical properties

Powder X-ray studies

The phase purity and the crystallite size of the prepared TiO_2 samples were evaluated by the X-ray powder diffraction analysis (Fig. 2). Sharp and well-defined peaks indicated the highly crystalline nature of the prepared samples. All the peak positions can be indexed to the TiO_2 anatase phase [51]. Their peak positions and relative intensities are consistent with the standard powder diffraction patterns of anatase TiO_2 (JCPDS card # 21-1272), with the main peak at 25.27° corresponding to the (101) plane.

The average particle size as determined from (101) diffraction peak (the most predominant highest intensity peak) using Scherrer's equation (eq. **1**), is found to be in the range of 12-18 nm (Table 7). It can be observed that the crystallite size, as expected, goes on decreasing with the increase in chain length of the acid. Moreover, the synthesized samples were found to be smaller in size as compared to Degussa P25 [52].

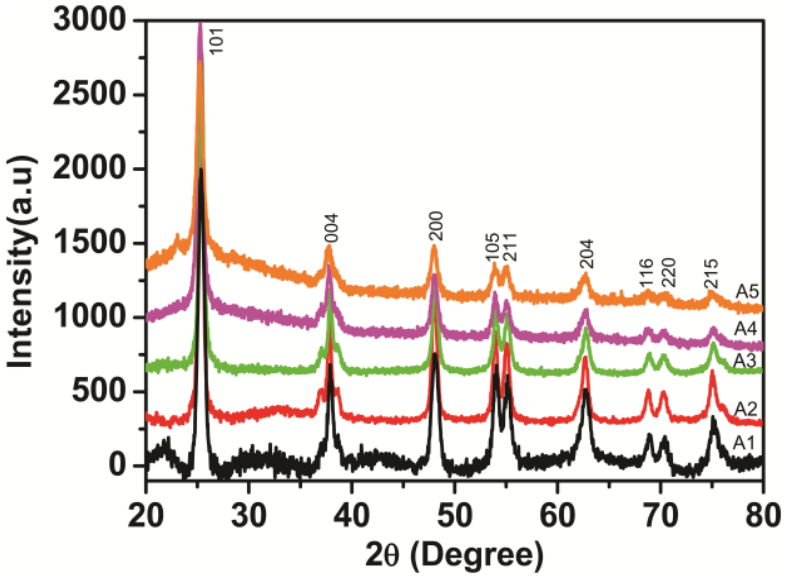

Fig. 2—*XRD plots for calcined samples*

Table 7 – Crystallite sizes

Sample	Crystallite size (nm)
A1	17.4
A2	16.4
A3	18.4
A4	14.7
A5	12.2
P25	25.0

UV-DRS studies

Optical studies of the samples are carried out by diffuse reflectance spectroscopy (Fig. 3). From the spectral plot, it is observed that samples A4 and A5 have better light absorbance than Degussa P25, which display shift in absorption edges to a longer wavelength. The observed red shift of this type can be attributed to the charge transfer transition.

The band-gap energies of these samples calculated using eq. **3**, are found to vary over a range of 3.2-3.3 eV (Table 8). Thus, it can be seen that sample A3 (prepared from butyric acid) is slightly blue shifted, having higher band-gap energy than the other samples. As expected, this sample shows poor photocatalytic activity (discussed later) than the Degussa, while samples A4 and A5, observed with an extended absorption spectrum in the visible region, shows enhanced photocatalytic activity then Degussa. These results conclude that the photocatalytic activity of these samples is strongly correlated with the optical properties.

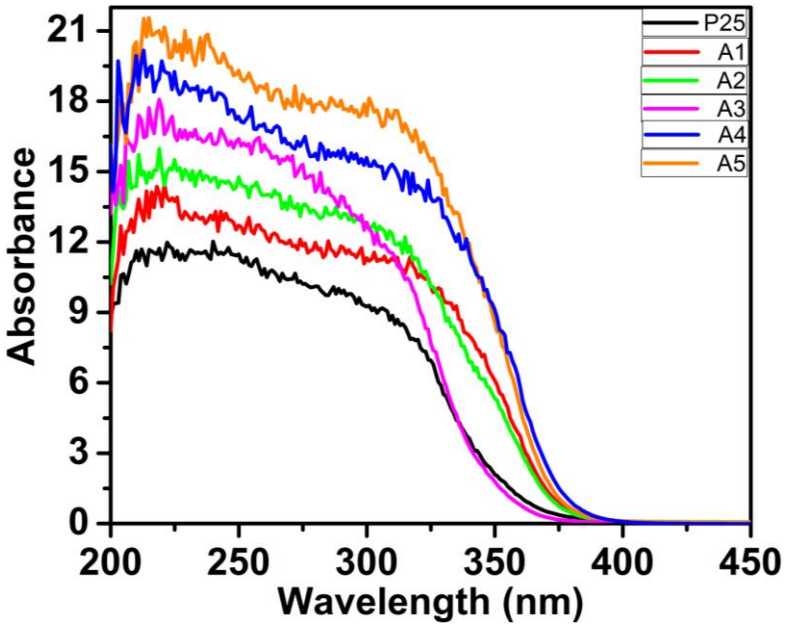

Fig. 3—*UV-DRS spectra of calcined samples*

Table 8 – Band-gap energies

Sample	Band-gap (eV)
A1	3.34
A2	3.24
A3	3.45
A4	3.23
A5	3.21
P25	3.35

BET analysis

The surface area analysis is carried out by using N_2 adsorption-desorption studies. The typical isotherm plot with pore size distribution curves (inset) is shown in Fig. 4. According to IUPAC classification, the isotherm curves are seen to be of the type IV, indicating the typical nature of mesoporous materials [53].

The Hysteresis loops in the BJH adsorption analysis are observed to be of H3-type for samples A2 and A4, which shows that the catalysts consist of the aggregates of cube-like particles forming pores of non-uniform size and shape. Whereas for samples A1 and A5, the nature of the loop is observed to be intermediate of H2- and H3-type, which is a characteristic of the nanoparticles with slit shaped pores. While for sample B3, a narrow hysteresis loop between H1- and H3-type is seen, which is consistent with the rigid pore structure of the sample. A relatively narrow pore size distribution with an average pore diameter less than 20 nm further confirms the presence of mesopores in these samples.

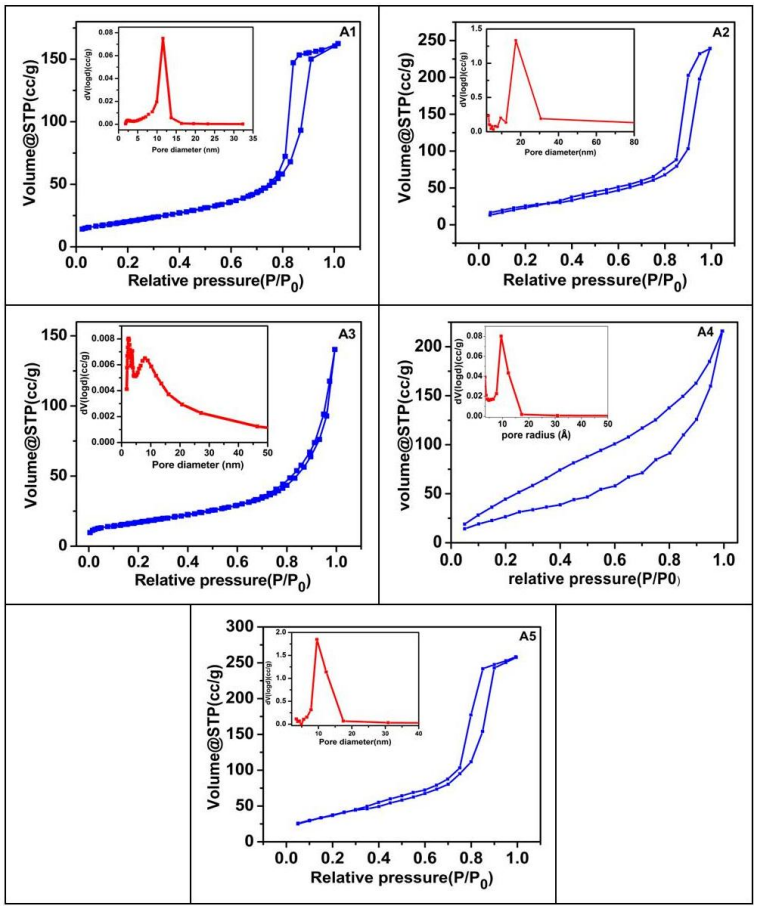

Fig. 4—*Nitrogen adsorption-desorption isotherms and pore size distribution (inset) of TiO_2 nanoparticles*

The least pore diameter of 7.6 nm is found for sample A5, which shows highest photocatalytic activity. The bimodal nature of pore size distribution is seen for sample A3 with a narrow peak in the micropore region, may be because of the slightly amorphous nature of this sample. The rigid pore structure of this sample probably results in its poor photocatalytic activity.

Surface area values of all the samples are given in Table 9 and are found to be higher than that of commercial Degussa P25. As postulated earlier, the surface area increases as the length of the precursor acid increase, but a corresponding decrease in pore radius is not observed. This could be probably due to the irregular shapes of the pores. The surface area for the sample prepared from acetic acid was found to be 99.1 m^2/g, which is slightly less than that, reported value of 116 m^2/g for acetic acid, water and pluronic P123 [39]. Similarly, for palmitic acid it was found to be 205.5 m^2/g, which is much higher than the reported using oleic acid and oleylamine combinations [54]. The high porosity of samples prepared from palmitic acid could be the result of evaporation of palmitic acid during heating, causing cavities in the solid arrangement of the Ti-O-Ti framework and the exit pathway.

Table 9 – Surface properties

Sample	BJH surface area (m^2/g)	Average pore diamater (nm)
A1	98.4	9.9
A2	99.1	15.4
A3	69.2	12.6
A4	127.1	8.8
A5	205.5	7.6
P25	56.0	17.5

TEM analysis

Morphology and the particle sizes of these nanoparticles were characterized by using TEM micrographs (Fig. 5 (a, d, g, j and m)).

It is seen from the TEM images that most of the nanoparticles crystallize in a cubic morphology and are randomly packed with pore channels formed between the particle packing. Slight agglomeration is observed as can be seen from shadow regions in the picture. The average particle sizes of these samples were found to be over a range of 10-18 nm, which is smaller than that of Degussa. The particle size values are in close agreement with the crystallite sizes obtained from XRD and are found to be decreasing with the increase in chain length of acids. It is observed that the smallest particle size is obtained for the samples (A4 and A5) showing better catalytic activity than P25 (Table 4). The average particle size obtained of A2 (from acetic acid) was found to be 16 nm and is smaller to the reported value of 25-30 nm [44]. For the sample A5 (from palmitic acid) the size obtained is matching with that of the reported value for sample prepared using oleic acid *via* hydrothermal method (10 nm) [49].

HR-TEM studies

For the detailed crystalline information such as, lattice fringes and interface information, high-resolution TEM images were recorded and are shown in Fig. 5(b, e, h, k, n and inset for magnified image). A large number of crystalline grains are observed appearing in the structured matrix indicating the well crystalline nature of TiO_2 nanoparticles.

The clear lattice fringes can be indexed to anatase phase, which can be evaluated from the distance between the adjacent lattice fringes by assigning the lattice plane on the nanoparticles. The lattice d-spacing of about 0.35 nm corresponds to (101) plane of anatase

TiO_2, matching with the highest intensity peak in XRD pattern and d-spacing of 0.26 nm corresponds to (004) plane.

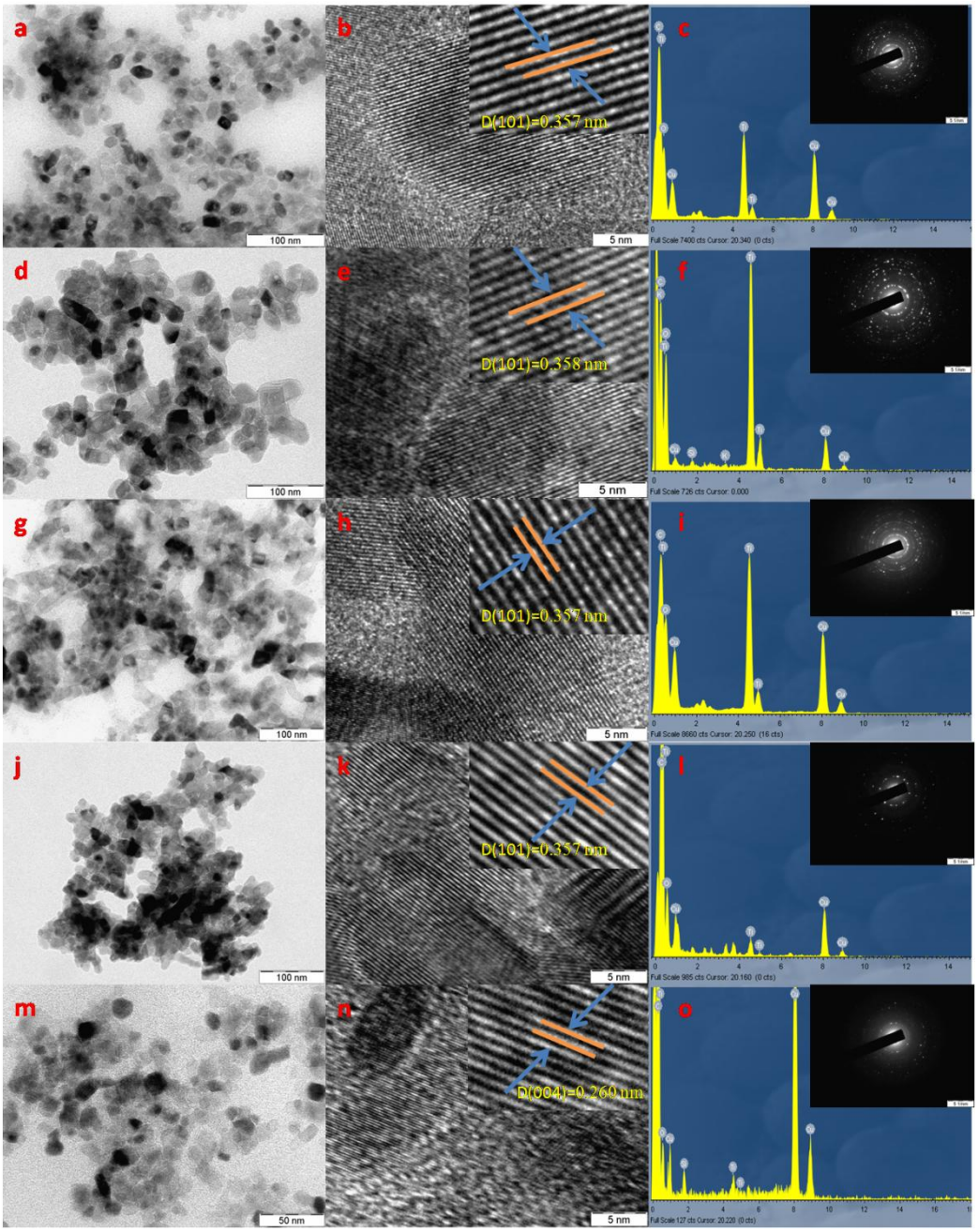

Fig. 5—*TEM images of TiO_2 nanoparticles- sample A1 (a), sample A2 (d), sample A3 (g), sample A4 (j), sample A5 (m); corresponding HRTEM images and lattice fringes- magnified images (inset) (b), (e), (h), (k), (n); corresponding EDX images and SAED patterns (inset) (c), (f), (i), (l), (o).*

Table 10 – Particle sizes

Sample	Particle size (nm)
A1	17.0
A2	16.0
A3	18.0

A4	10.8
A5	10.0
P25	21.0

Thus, it can be said that, pure phase anatase TiO_2 nanostructures are obtained using the current procedures with this series of acid templates. The presence of anatase phase is further confirmed by the electron diffraction pattern. The SAED patterns, as shown in the inset of Fig. 5(c, f, i, l, o), reveals the apparent ring diffraction patterns with concentric circles of small spots indicating the polycrystalline nature of the particles and the diffraction spots for pure anatase TiO_2. The corresponding d-spacings are assigned as (101), (004), (200), (211), (204), (220), (215), matching with the XRD results.

EDX studies

The chemical composition of the prepared nanoparticles was detected by using Energy-dispersive X-ray Spectroscopy (EDX) (Fig. 5 (c, f, i, l, o)). The presence of Ti, O, Cu, C, and Si elements is clearly seen from EDX images, of which Cu, C and Si signals are due to the TEM grid used for the imaging.

From the morphological analysis, it is concluded that all the acids used resulted in similar shape particulates suggesting lack of control of the acid in directing the shape of the particulate. This could be due to the hybrid hydrolytic nonhydrolytic pathway followed in the present studies. This implies that for obtaining tailor made shapes of the particulate, sol-gel method appears to be non suitable [48]. However the particle sizes of the samples has a definite effect on the catalytic properties.

IR studies

The IR spectra of the calcined TiO_2 samples shows a typical absorption band for Ti-O-Ti network as a strong, broad band around 600 cm^{-1}. A slightly less strong, broad band is seen at around 3300-3500 cm^{-1} (O-H stretching mode) and weak bands at ~1633 cm^{-1} is due to physically adsorbed water on the surface of TiO_2 and/or surface hydroxyl groups (Fig. 6a).

In the spectra of precursor (uncalcined) samples (Fig. 6b), broad peak at 3500-2500 cm^{-1} (Ti-OH stretching and unreacted R-COOH) and 800-450 cm^{-1} (Ti-O stretching) are seen in for all samples. The sample A1 (formic acid) displays two peaks at 1622 cm^{-1} and 1347 cm^{-1} ($\Delta\nu$=275 cm^{-1}) for the unsymmetrical and symmetrical stretching of the metal carboxylate. Similar peaks for A2 (acetic acid) at 1541, 1447 cm^{-1} ($\Delta\nu$=94 cm^{-1}), A3 (butyric acid) at 1540, 1429 cm^{-1} ($\Delta\nu$=111 cm^{-1}), and A4 (octanoic acid) at 1551, 1428 cm^{-1} ($\Delta\nu$=123 cm^{-1}),

were observed. However, in the case of sample A5 (palmitic acid) no distinct carboxylate peaks were observed, rather peaks of palmitic acid and $Ti(OH)_4$ were observed.

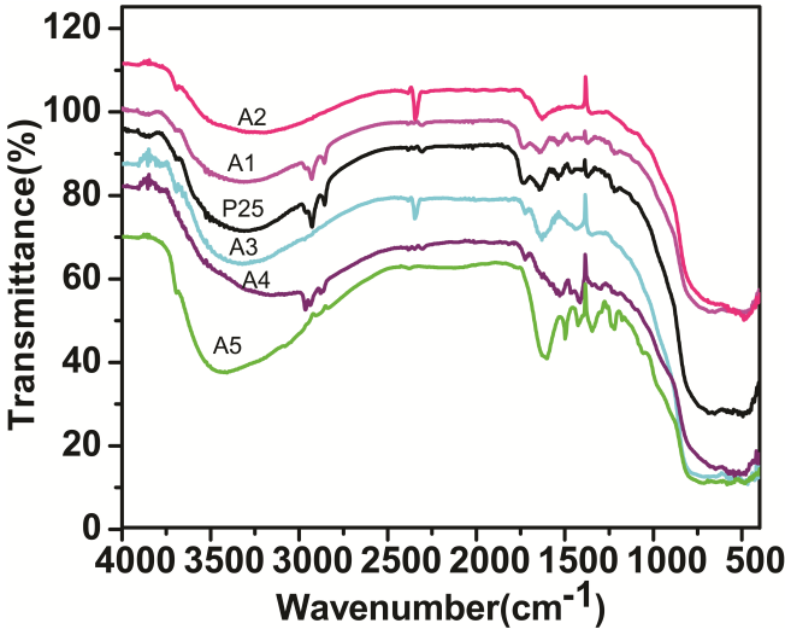

Fig. 6a—*IR spectra of calcined samples*

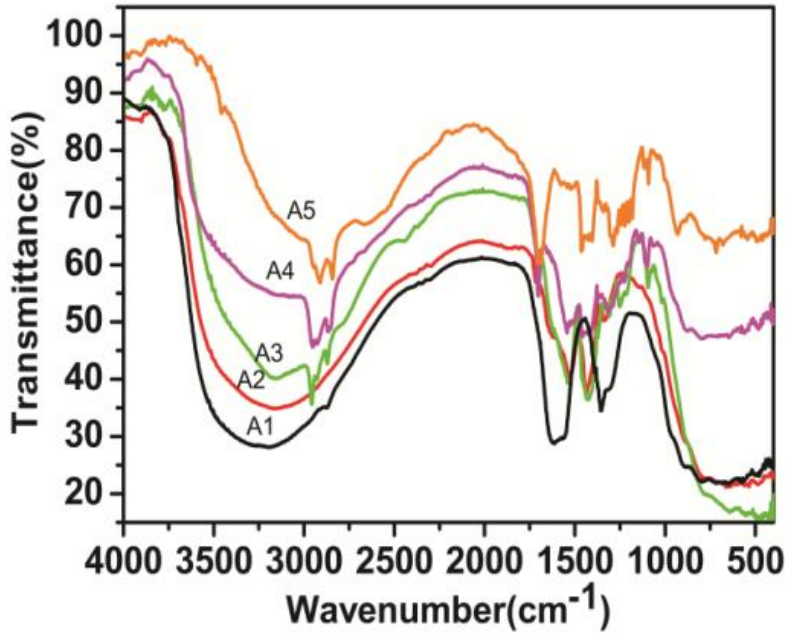

Fig. 6b– *IR spectra of precursor samples*

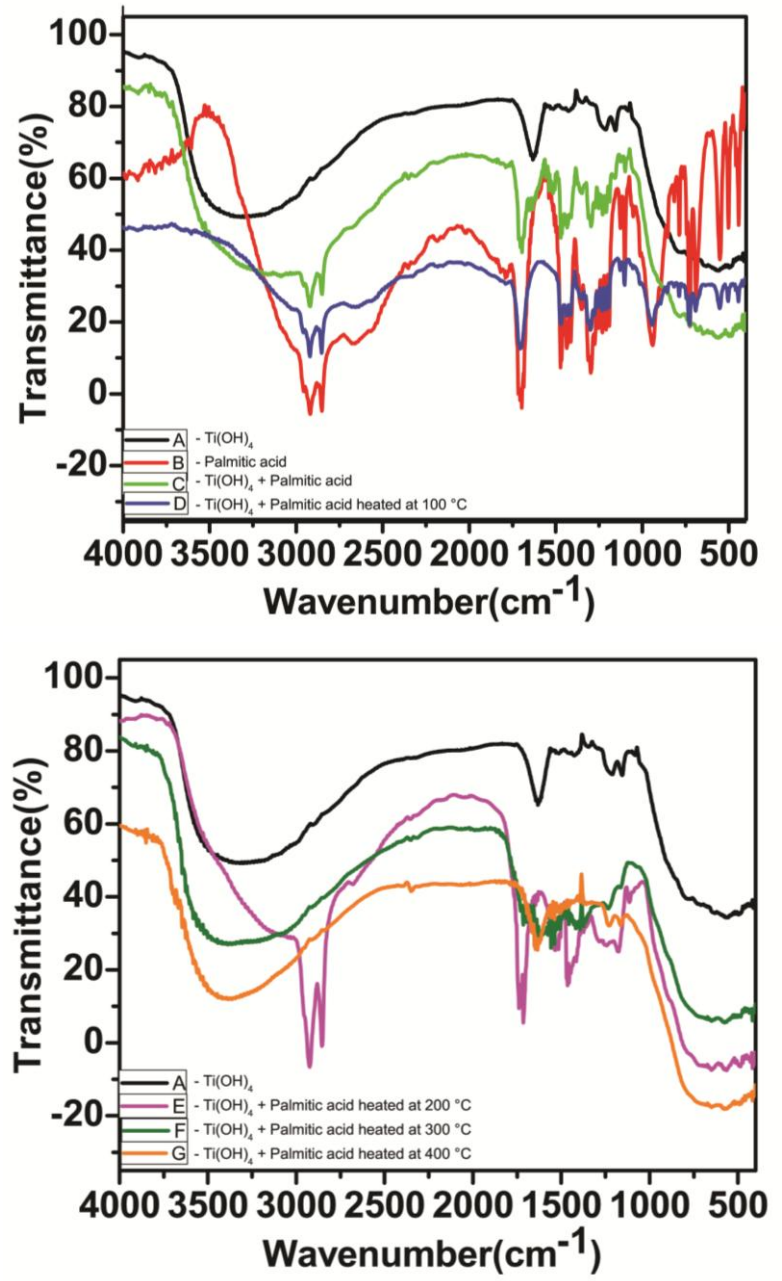

Fig. 6c—*IR spectra of $Ti(OH)_4$ + Palmitic acid*

To further confirm if metal carboxylate was formed, palmitic acid was mixed with $Ti(OH)_4$ and heated at 100 °C, 200 °C, 300 °C and 400 °C for one hour each. In none of the cases, corresponding carboxylate peaks were seen (Fig. 6c). In the sample prepared by heating at 400 °C, peaks due to palmitic acid also disappeared. Similar mixing of acetic acid with $Ti(OH)_4$ and heating at 100 °C showed distinct metal carboxylate peaks (Fig. 6d). This suggested that in case of palmitic acid experiment, TiO_2 is formed from the direct condensation of $Ti(OH)_4$ and not *via* the corresponding metal carboxylate. In this case, the palmitic acid must have acted as a surfactant alone, whereas in the remaining cases, the acid

used, acts also as a ligand. This observation regarding palmitic acid differs from the earlier reports using long chain acids like oleic acid, lauric acid, *etc.* [45-50], wherein the corresponding carboxylate bands were reported.

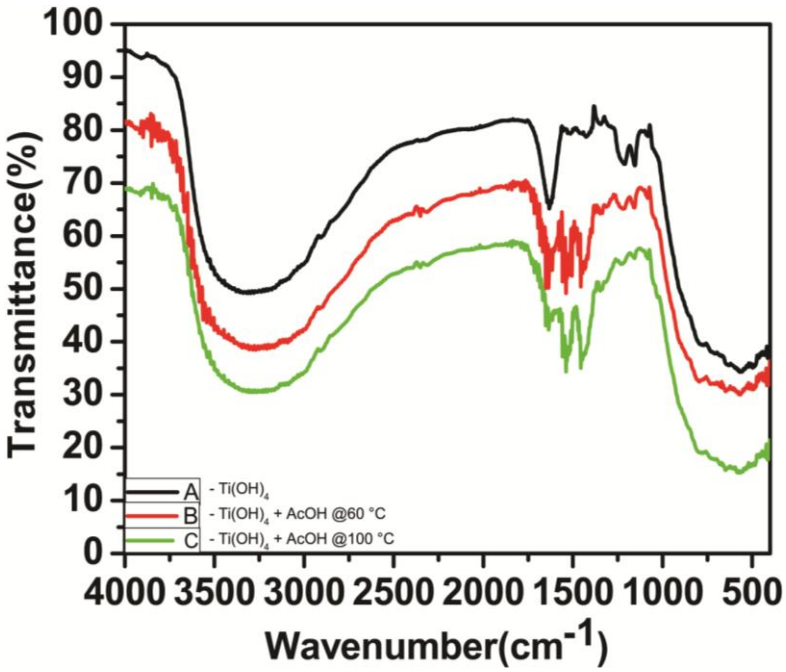

Fig. 6d —*IR spectra of $Ti(OH)_4$ + Acetic acid*

Photocatalytic activity studies in direct sunlight

The photocatalytic activity was compared with Degussa P25 for the degradation of methylene blue in direct sunlight. The results obtained are displayed in graphical form below (Fig. 7a). It can be clearly seen that the rapid degradation is observed for samples A4 and A5 (obtained from long chain acid precursor) than Degussa P25.

From the degradation studies, it is observed that the small chain acid precursor *viz.* formic acid, acetic acid and butyric acid resulted in the catalyst with inferior activity compared to Degussa P25, while that of catalysts prepared from bulkier acids like octanoic acid and palmitic acid display appreciable activity. This is basically a result of their small size, narrow pore radius, higher surface area and lesser band-gap energy. The sample A3 obtained using butyric acid was found to show least activity, which is due of its low surface area, larger size and higher band-gap energy. Although, samples A1, A2 and A3 have higher surface area than that of Degussa P25, the high activity of the latter owes to the presence of a mixture of anatase and rutile phases.

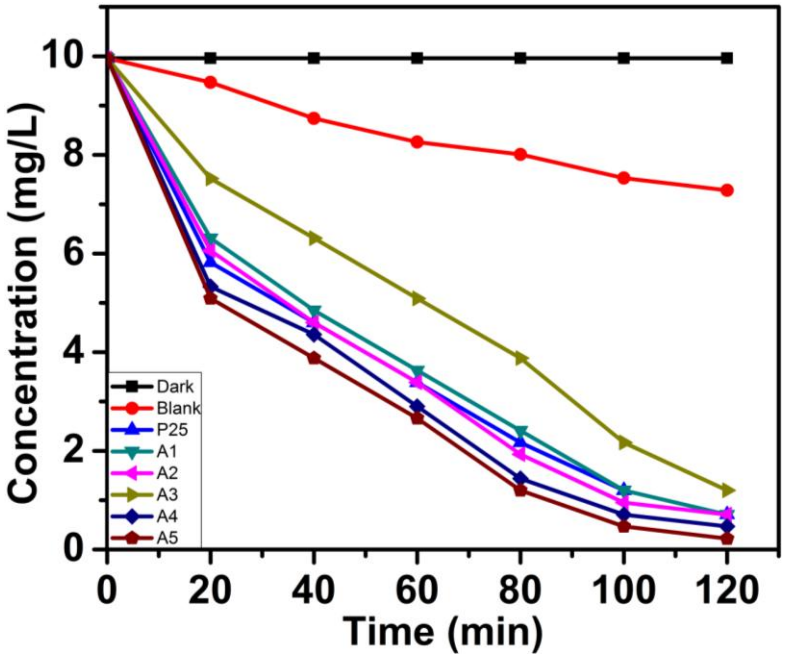

Fig. 7a—*Degradation plots in sunlight*

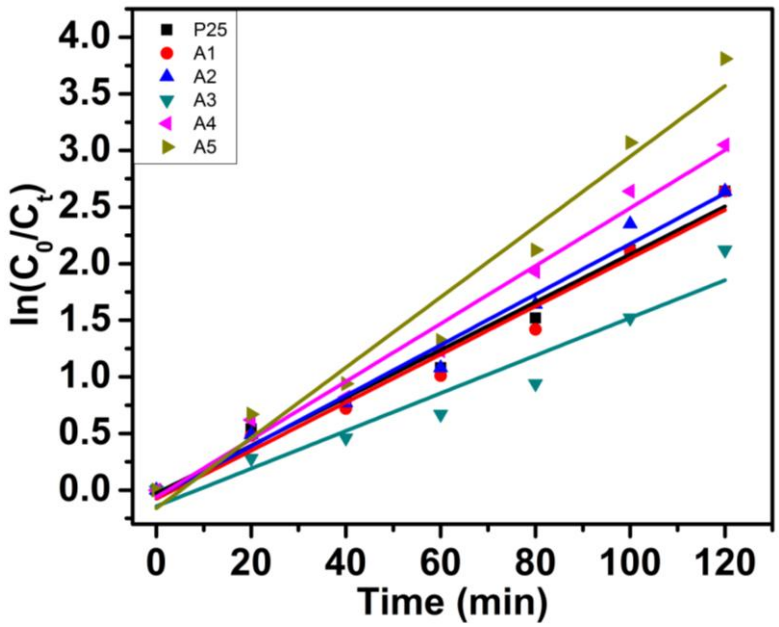

Fig. 7b—*Kinetics of MB degradation.*

A plot of ln (C_0/C_t) versus time (Fig. 7b) represents a straight line which indicates the photocatalytic degradation follows a pseudo first order kinetics. The rate constants derived from the plot are given in Table 11, which is in accordance with the other results.

Recyclability studies for the samples showing better results were carried out for three cycles, after separating the catalyst by centrifugation and the results were compared with Degussa (Fig. 7c). All the samples could be reused for degradation with negligible loss in activity.

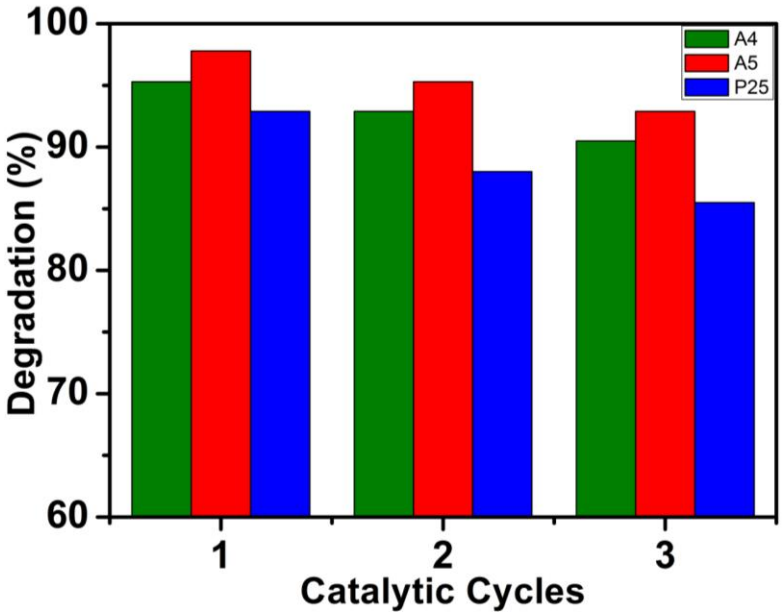

Fig. 7c—*Recyclability studies for samples showing better results.*

Photocatalytic activity studies using 125 W mercury lamp

Photocatalytic activity was also compared by employing a 125 W mercury lamp and the similar trend was observed (Fig. 7c). However, the rate of degradation was found to be slower than direct sunlight.

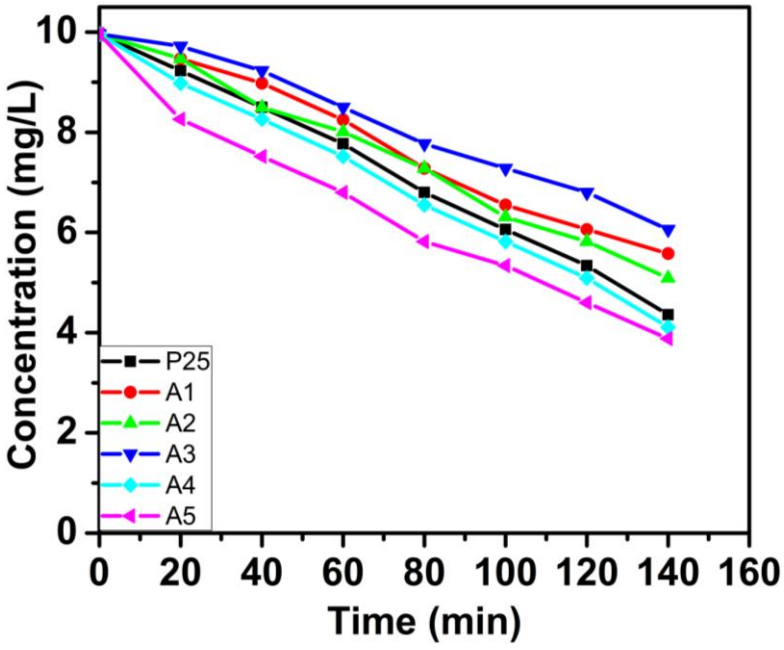

Fig. 7d— *Degradation plots using Hg 125 W bulb*

Table 11 – Rate constants

Sample	Rate constant k (min^{-1})
A1	0.0212
A2	0.0223
A3	0.0166
A4	0.0255
A5	0.0311
P25	0.0211

Summary and conclusion

Sol-gel method was used to study the effect of chain length of the monocarboxylic acids on the properties of TiO_2. The IR studies of the precursor samples suggest that, the formation of metal oxide follows a hybrid of hydrolytic and non-hydrolytic pathway except for palmitic acid. All the acids used acts as ligands and surfactants except palmitic acid, which acts as surfactant only.

Analysis by different characterization techniques (XRD, TEM, BET, *etc.*) indicates that the prepared TiO_2 catalysts are of pure anatase phase of nano-size with a good crystallinity and cubic morphology. The properties of catalysts are summarized in Table 12.

Table 12 – Summary of the properties of TiO_2 nanoparticles.

Sample	Crystallite size (nm)	Particle size (nm)	BJH surface area (m^2/g)	Av. Pore dia. (nm)	Rate constant k (min^{-1})
A1	17.4	17.0	98.4	9.9	0.0212
A2	16.4	16.0	99.1	15.4	0.0223
A3	18.4	18.0	69.2	12.6	0.0166
A4	14.7	10.8	127.1	8.8	0.0255
A5	12.2	10.0	205.5	7.6	0.0311
P25	25.0	21.0	56.0	17.5	0.0211

Part 2 – Study of sterically bulky monocarboxylic acids as templates

Introduction

In the earlier half part of this section, straight chain acids were studied as precursor material for the synthesis of TiO_2 photocatalytic material. The results showed that long chain acids give better photocatalyst for direct sunlight degradation of methylene blue.

We speculated that instead of long chain acids if we use sterically bulky acids, similar or better results in terms of mesoporosity, size, pore diameter, phase selection and thereby the better photocatalytic activity could be obtained. Presence of free hydroxyl groups on the surface of a catalyst is known to provide better photocatalytic activity due to better adsorption of the pollutant [54]. Here we used pivalic acid and phenoxyacetic acid as precursor materials. The sterically bulky pivalic acid and phenoxyacetic acid were not only expected to control the hydrolysis and condensation by ligating as carboxylate ligands to form small particulates, but also to provide surface hydroxyl groups during calcination by a non-hydrolytic pathway as shown in Scheme 8. The structures of these acids are shown in Fig. 8.

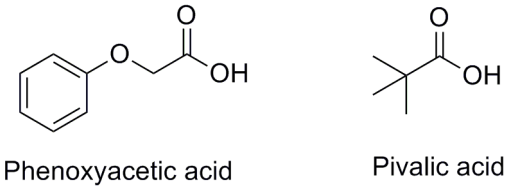

Fig. 8 - *Structures of the precursor acids used for series 1b*

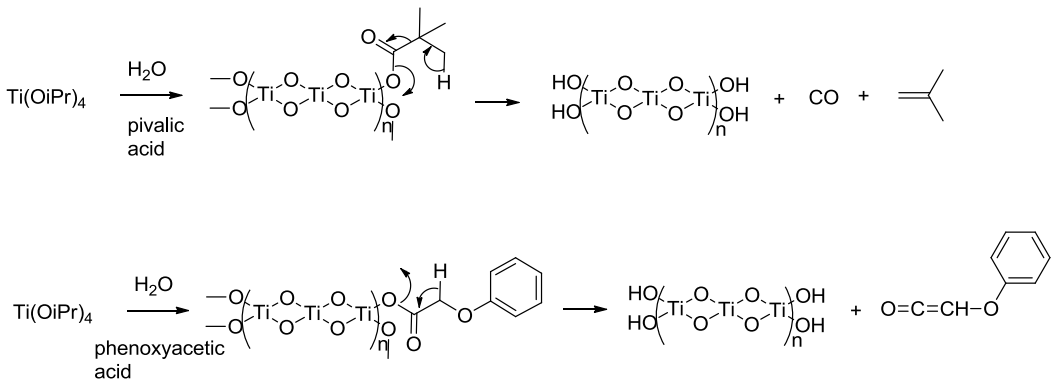

Scheme 8

Structural and morphological properties

Powder X-ray studies

The phase composition, crystal structure and the crystallite size of the prepared TiO_2 samples were evaluated by X-ray powder diffraction analysis. The XRD plots (Fig. 9) display the patterns with characteristic peaks of anatase TiO_2 at (101), (004), (200), (105), (211), (204),

(116), (220) and (215), matching with the JCPDS card # 21-1272. The sharp and well-defined peaks indicated pure crystalline nature of the samples. The consistency in the peaks suggested the purity of the phase [51].

The crystallite size as obtained from the Scherrer's equation (eq. **1**) is found to be 10 and 11 nm respectively for samples P1 and P2 (Table 13).

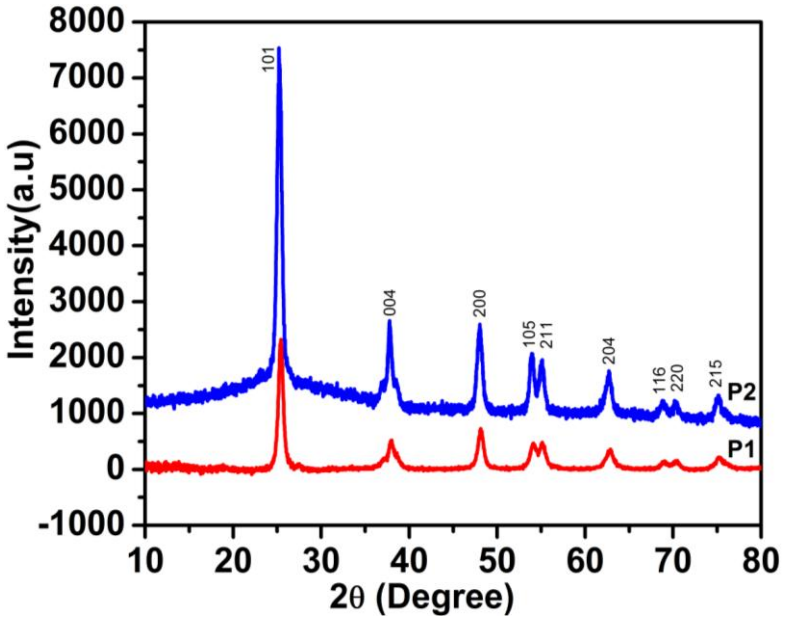

Fig. 9—*XRD plots for calcined samples*

Table 13 – Crystallite sizes

Sample	Crystallite size (nm)
P1	10.8
P2	11.5
P25	25.0

UV studies

The absorption coefficient and optical band-gap of a material plays a key role in controlling a photocatalytic reaction. The absorption spectra of prepared TiO_2 nanostructures as a function of wavelength are shown in Fig. 10.

The prepared samples exhibited strong absorption in UV-Vis range. The absorption band edges were found to be at 378 and 375 nm for samples P1 and P2 respectively. A slight red shift is observed in the band-gap transition for both the samples in comparison to Degussa, for which absorption wavelength is observed to be at 370 nm. For a semiconductor material, the band-gap is closely related to the wavelength range absorbed. A red shift in the

absorption increases the absorption of visible light and significantly reduces the band-gap, which is beneficial for improving the photocatalytic activity.

The band-gap values as calculated using eq. **3** were found to be 3.23 and 3.26 eV (Table 14) respectively for samples P1 and P2. Values of 2.86 to 3.34 eV are reported for anatase phase TiO_2 in the literature. The minute difference in E_g values may be due to size reduction of nanoparticles [55] which can be attributed to the use of different templates as a precursor material.

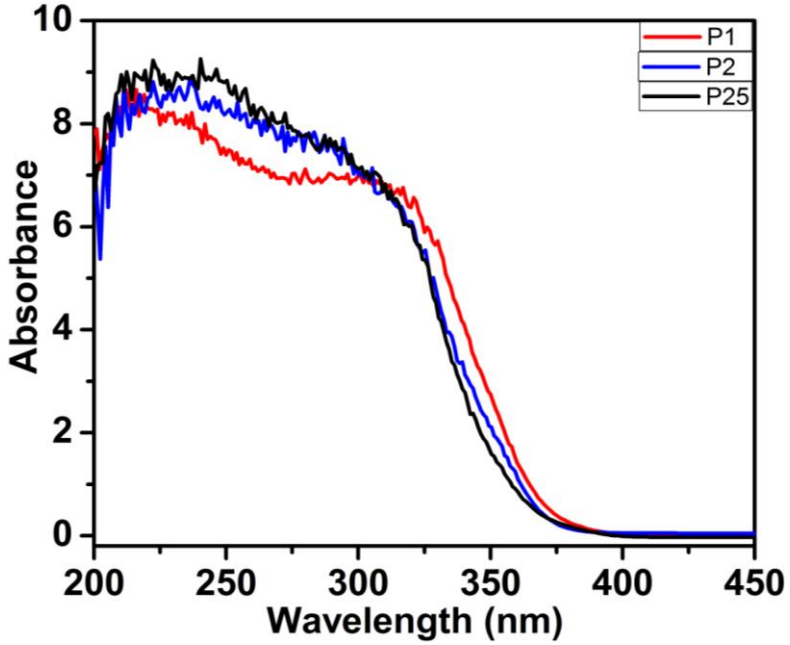

Fig. 10—*UV-DRS spectra of calcined samples*

Table 14 – Band-gap energies

Sample	Band-gap (eV)
P1	3.23
P2	3.26
P25	3.35

BET analysis

It is generally believed that photocatalytic activities are dependent on the specific surface area of the catalysts. The typical plot of N_2-sorption isotherms at 77 K and corresponding pore size distribution curves of the samples are displayed in Fig. 11. Classical type IV isotherms are observed for both the samples, showing hysteresis loops with limiting uptake over a range of high P/P_0 reaching up to 1, which is associated with capillary condensation taking place within mesopores. It also implies the presence of highly correlated structures with independent porous units wherein adsorption and desorption occur in the same way. The

broad hysteresis loop suggests the high degree of mesoporosity and the loop starting from the lower range of P/P_0 (<0.2), may be due to residual microporosity, probably caused by non-uniform pore size, which indicate the multi-scale mesoporosity of these samples [53, 56].

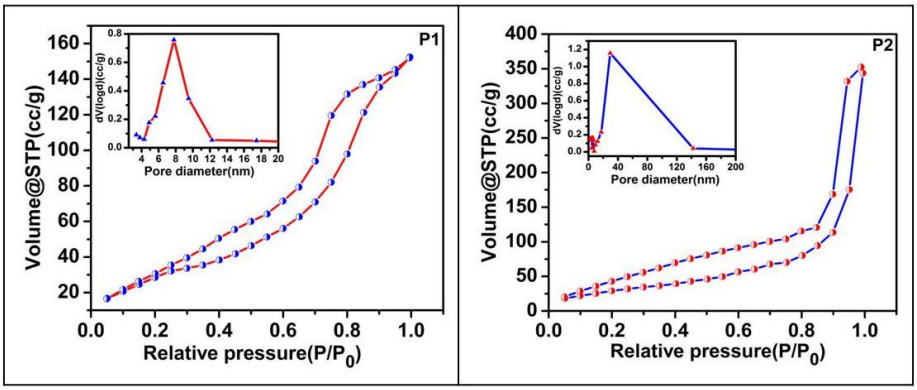

Fig. 11—*Nitrogen adsorption-desorption isotherms and pore size distribution curves (inset) of TiO_2 nanoparticles- samples P1 and P2.*

The hysteresis loop for sample P1, is of somewhat H2-type, indicating that the sample is mainly mesoporous and contain a small number of micropores. Such type of hysteresis loop is associated with pore-blocking with large size distribution of neck widths. This is also seen by relatively narrow pore size distribution from 4-12 nm, with an average pore diameter of 7.6 nm.

For sample P2, the hysteresis loop is observed to be of H3-type, suggesting the presence of aggregates of cube-like particles forming slit-like pores of non-uniform size and shape. The high adsorption at a relatively high pressure (P/P_0) in isotherm with H3-type hysteresis loop also indicates the formation of large mesopores and macropores, which is furter confirmed from the wide pore size distribution from 7.7-142 nm. In addition, bimodal nature is observed in this sample with a small sharp peak in the range 4.8-7.7 nm, indicating the presence of slight amorphous nature.

The overall BET surface area of both the samples is observed to be 122 m^2/g (Table 15), which is much higher than that of Degussa (56 m^2/g). Such a large specific surface area and a high degree of mesoporosity favor the adsorption of dye on the catalyst surface and this seems to be responsible for the better photoactivity of the catalysts.

Table 15 – Surface properties

Sample	BJH surface area (m^2/g)	Average pore diamater (nm)
P1	121.8	7.6
P2	122.8	14.8
P25	56.0	17.5

SEM analysis

Scanning electron microscopy (SEM) of the nanocrystalline TiO_2 was carried out to study the surface morphology (Fig. 12a). As shown in the figure, both the samples display a densely packed arrangement of spherical particles fused together forming small aggregates. The agglomeration seen may be occurring during the calcination of samples due to their mesoporous nature.

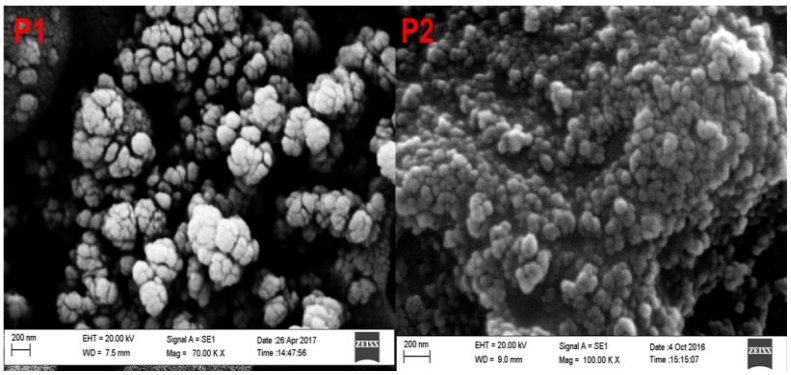

Fig. 12a—*SEM images of TiO_2 nanoparticles P1 and P2*

TEM analysis

Morphology was further confirmed by TEM images, wherein, spherical particles in fused form arranged on one another are observed with a small degree of agglomeration. TEM images are in accordance with that of SEM observation, which clearly shows that the samples are composed of tiny particles grouped in the form of clusters. The micrographs of these samples are shown in Fig. 12b (a, d). The average particle size of TiO_2 nanoparticles was found to be in the range of 9-10 nm (Table 16).

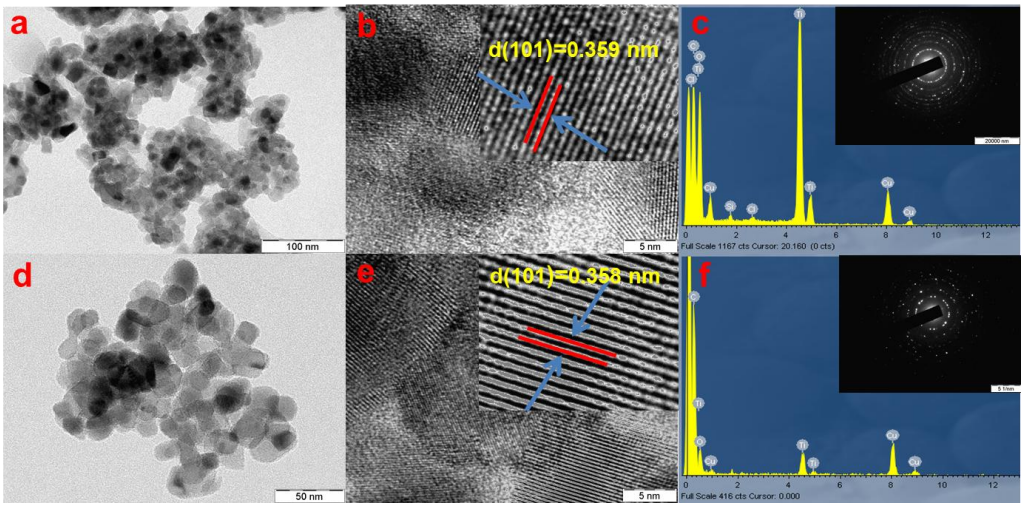

Fig. 12b—*TEM images of TiO_2 nanoparticles- **sample P1** (a), **sample P2** (d); corresponding HRTEM images and lattice fringes- magnified images (inset) (b), (e); corresponding EDX images and SAED patterns (inset) (c), (f).*

HR-TEM studies

High resolution TEM images were recorded to investigate lattice fringes, crystalline patterns and interface information, as shown in Fig. 12b (b, e and inset for magnified image). The clear lattice fringes indicate the well crystalline nature of TiO_2 nanoparticles. From the distance between the adjacent lattice fringes, we can assign the lattice plane on the nanoparticles. The value of lattice d-spacing of 0.35 nm corresponding to (101) plane of anatase TiO_2 indicates the anatase phase of nanostructures.

SAED patterns further confirmed the phase purity and crystallinity of these samples. As seen from the inset of Fig. 12b(c, f), the apparent ring diffraction patterns with concentric circles of small spots indicated the polycrystalline nature of the samples. The corresponding d-spacings are assigned as (101), (004), (200), (211), (204), (220), and (215) of anatase phase and are matched with the XRD results.

EDX studies

The elements Ti, O, Cu, C, and Si are detected by EDX pattern, confirming the chemical composition of the prepared nanoparticles (Fig. 12b (c, f)). The Cu, C and Si signals are due to the TEM grid used for the imaging.

Table 16 – Particle sizes

Sample	Particle size (nm)
P1	9.0
P2	10.0
P25	21.0

IR studies

The IR spectra of all calcined TiO_2 samples show a strong broad band at ~ 600 cm^{-1} typical of Ti-O-Ti network. Another broad band at ~ 3300 cm^{-1} and a weak band at ~ 1633 cm^{-1} indicated the presence of surface hydroxyl groups and adsorbed water on the surface of TiO_2 (Fig. 13a).

The precursor samples displayed typical bands of Ti-OH stretching and unreacted acids at 2500-3500 cm^{-1} and at ~ 1700 cm^{-1} for the free -COOH groups. In addition to this, the bands at 1552 cm^{-1} and 1382 cm^{-1} for pivalic acid sample and at 1582 cm^{-1} and 1438 cm^{-1} for the phenoxacetic acid sample were seen (Fig. 13b). These bands were assigned to the unsymmetrical and symmetrical vibrations of the metal carboxylate bonds. The presence of these bands indicates that the condensation of the sol is controlled by the organic acids by the

formation of the metal carboxylate bonds. The bands at 800-450 cm^{-1} were attributed to the Ti-O stretching mode. These observations suggested that the formation of TiO_2 is taking place by both hydrolytic and non-hydrolytic pathway.

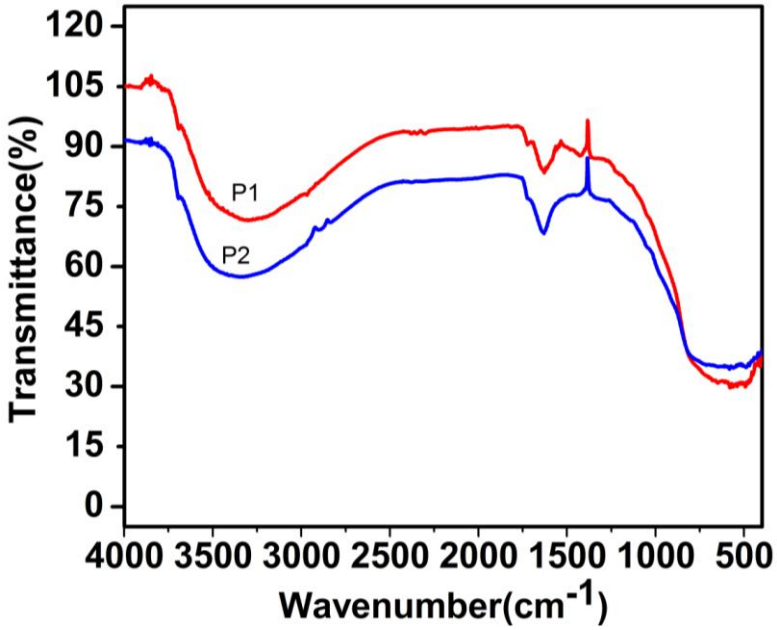

Fig. 13a—*IR spectra of calcined samples*

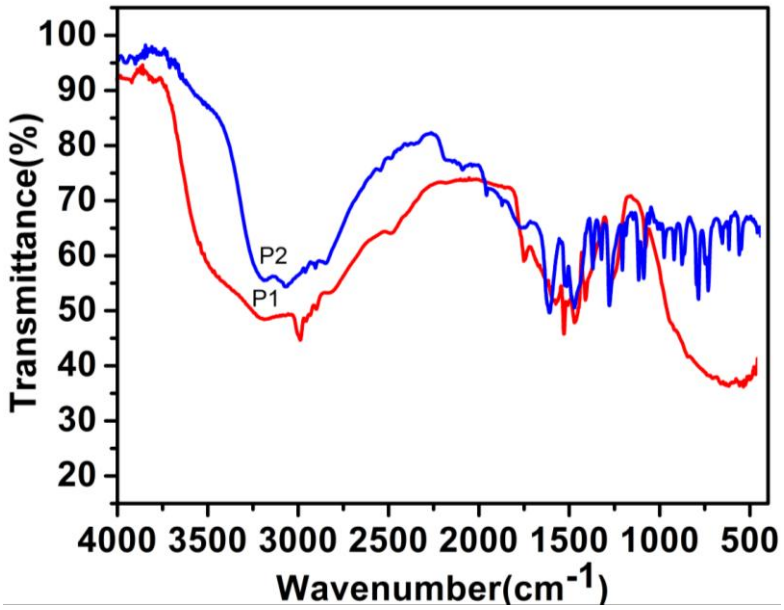

Fig. 13b– *IR spectra of precursor samples*

Photocatalytic activity testing

The photocatalytic activity was studied by degradation of methylene blue under direct sunlight in comparison with the commercial Degussa P25 (Fig. 14a). Degradation pattern reveals that both the samples show rapid degradation than the Degussa P25 and the sample P1 (prepared from pivalic acid precursor) was found to be the better photocatalyst of the two.

The studies were also carried out in the absence of sunlight (dark reaction) and without catalyst (blank), which showed almost nil degradation in both the cases.

The kinetic studies shown by plot of ln (C_0/C_t) versus time (Fig. 14b), represents a straight line which indicates the photocatalytic degradation follows a pseudo first order kinetics. The rate constant derived from the plot is given in Table 17, which is in accordance with the other results.

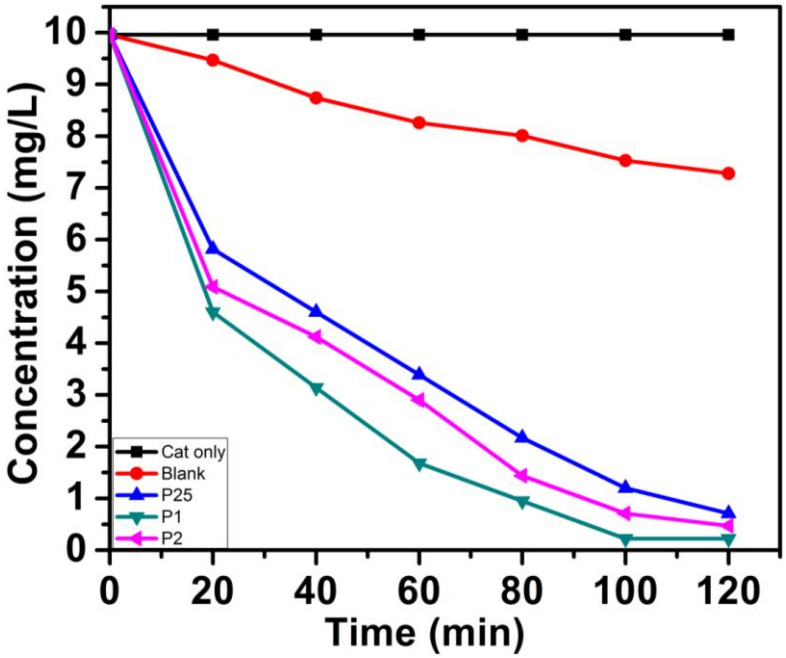

Fig. 14a—*Sunlight degradation plots for methylene blue*

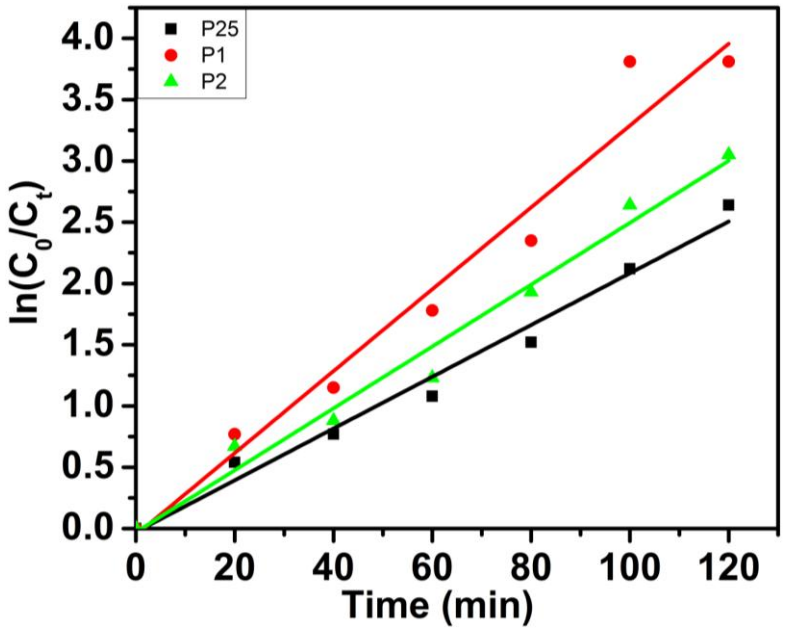

Fig. 14b—*Kinetic studies*

From the data, it is observed that the sample P1 shows higher degradation rate constant (0.0334) which is almost 1.6 times higher than the P25 and is also more than the sample P2. This can be correlated with the other properties (Table 18). For instance, highly crystalline and pure anatase nature is always advantageous for photocatalytic activity. Moreover, smaller particle size and pore diameter in combination with higher surface area allows better absorption of the dye molecules on the catalyst surface and thus improving better penetration through the channels of the catalyst, which is responsible for faster degradation process. The shift in absorption wavelength to higher value (i.e lower band-gap) also plays a crucial role in photo-activity of the catalyst.

However sample P2, though having a similar surface area and higher pore volume, shows slightly lower degradation rate. This could be due to higher pore diameter, particle size and higher band-gap of sample P2 than P1. It may also have been affected due to the slight amorphous nature of the sample as seen in the pore size distribution curve.

Recyclability studies were done for three cycles for these samples after separating the catalyst by centrifugation. Both the samples showed good reusability for degradation in comparison with Degussa (Fig. 14c).

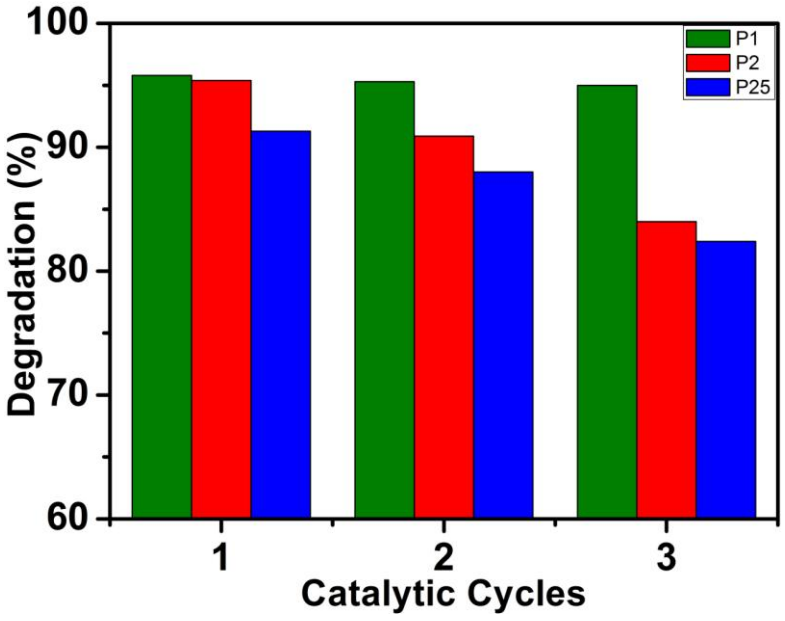

Fig. 14c—*Recyclability studies*

Table 17 – Kinetic studies

Sample	Rate constant k (min^{-1})
P1	0.0334
P2	0.0252
P25	0.0211

Summary and Conclusion

Sterically hindered monocarboxylic- pivalic and phenoxyacetic acids were examined as templates for the sol-gel synthesis of TiO_2. Both the acids acted as templates as well as surfactant during the sol-gel synthesis. Pure anatase phase was obtained for both the acid precursors. The catalyst prepared displayed better photocatalytic activity for degradation of methylene blue than the commercial Degussa P25 and the catalyst obtained using pivalic acid was found to be better photoactive among the two. Thus, sterically bulky acids can be effective replacement for long chain fatty acids as templates for synthesis of metal oxides. The properties of the catalysts are summarized in Table 18.

Table 18 – Summary of the properties of TiO_2 nanoparticles.

Sample	**Particle size (nm)**	**BJH surface area (m^2/g)**	**Ave. pore dia. (nm)**	**λ_{max} (nm)**	**Rate const. k (min^{-1})**
P1	9	121.8	7.6	378	0.0334
P2	10	122.8	14.8	375	0.0252
P25	21	56.0	17.5	370	0.0211

Section B – Study of dicarboxylic acids as templates

Introduction

In the previous section of this chapter, the experimentation on the synthesis of nano-TiO_2 mesoporous materials using different mono-carboxylic acids was carried out. The effect of long chain acids and sterically hindered acids on the properties of the catalysts prepared was found to have a beneficial effect.

In continuation with this ligation approach of the organic acids to improve the catalyst properties, we decided to study use of dicarboxylic acids as soft ligands in sol-gel synthesis. Oxalic acid has been studied for the sol-gel synthesis [57] of TiO_2 however, very little is known about the use of other dicarboxylic acids. Some of the dicarboxylic acids such as succinic, maleic, itaconic, etc., have been used as modifiers for the hydrothermal synthesis of the catalyst [24, 58-63]. Lack of data on sol-gel synthesis using dicarboxylic acids prompted us to undertake this study.

In hydrothermal products partly acid remains attached to the surface of the particle as carboxylate linkage and are detrimental for the photocatalyic activity though helps in shape selectivity. While in sol-gel method during calcination the carboxylate linkage gets removed by a non-hydrolytic pathway leading to pristine TiO_2.

We envisaged that dicarboxylic acids may act as a better template due to the possibility of attachment of two -COOH groups onto the Ti surface. The ligation can take place either in an intermolecular fashion **1**, wherein one acid function ligates with one Ti atom or both the acid functionality attaches to one Ti atom **2** or a hybrid of these two modes **3** as shown below (Scheme 9), depending on the structure of the acid. For example fumaric acid can bridge only in mode **1** fashion while maleic acid can bridge only in mode **2**. It was expected that these bridges formed by the dicraboxylic acid during calcination *via* non-hydrolytic pathway will collapse, leaving a trace which will define the pore size, pore volume, the porosity and the phase and size of the resultant TiO_2 catalyst. For this study, we chose following nine dicarboxylic acids. Oxalic acid (2 carbons), malonic acid (3 carbons), succinic acid (4 carbons), glutaric acid (5 carbons), adipic acid (6 carbons), maleic acid (4 carbons, *cis*-double bond), fumaric acid (4 carbons, *trans*-double bond), malic acid (4 carbons with one additional hydroxyl group) and tartaric acid (4 carbons and 2 additional hydroxyl groups). The structures of these acids are shown in Fig. 15. It was expected that due to the geometrical rotational barrier malic acid, tartaric acid and fumaric acid would bind preferably in intermolecular fashion **1** while the other acids would bridge by intramolecuar fashion **2**. The

intramolecular ligation **2** was expected to be stronger than the intermolecular **1** and this could result in getting some mixed phases during calcination for bridging **1**.

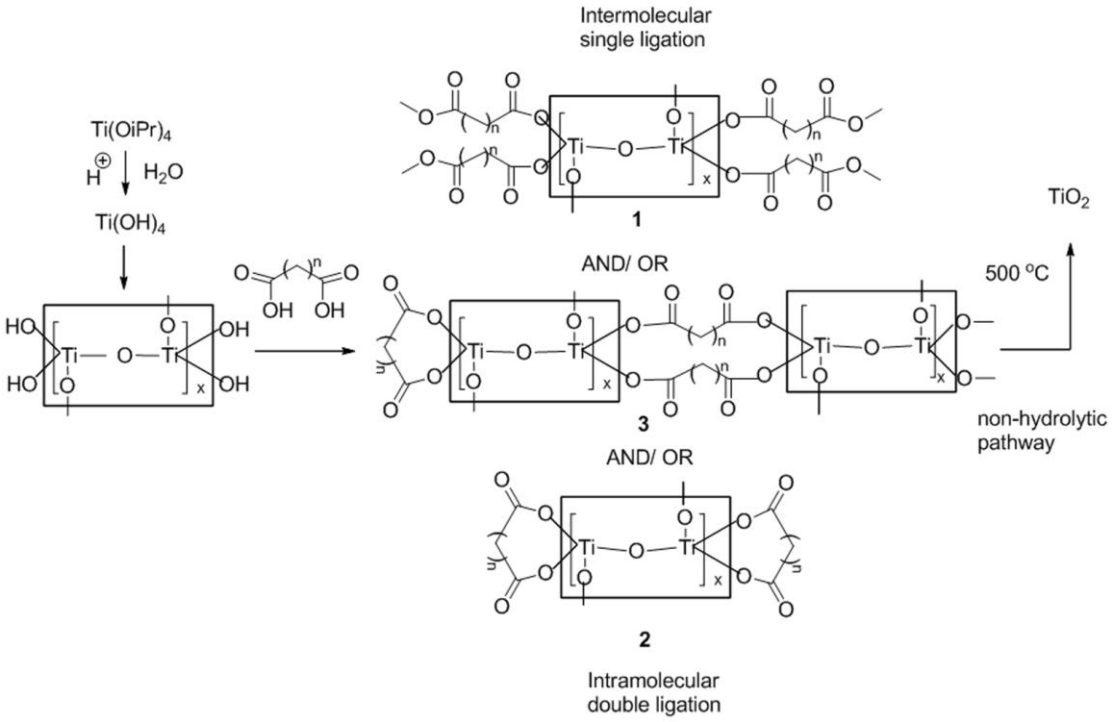

Scheme 9

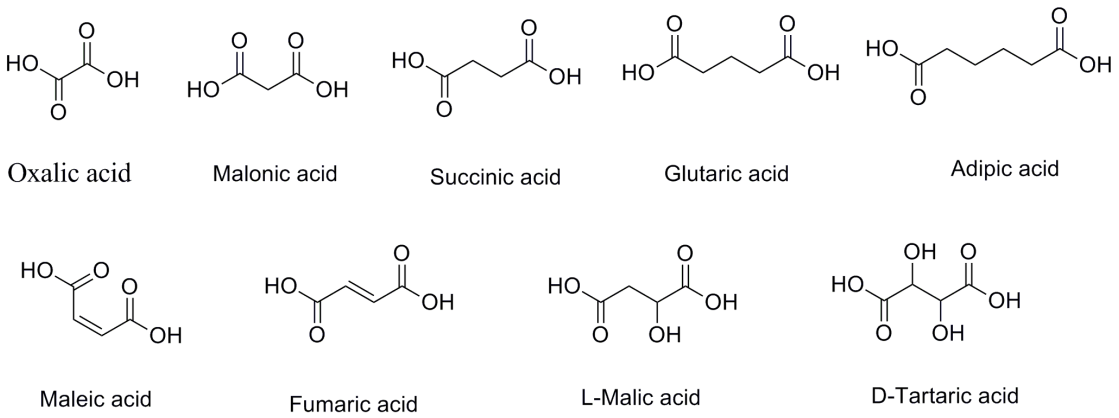

Fig. 15 - *Structures of the precursor acids used for series 2*

Structural, optical and morphological analysis

Powder X-ray studies

X-ray powder diffraction analysis is used to study the phase composition and the crystallite size of the samples. From XRD patterns (Fig. 16), it is observed that the catalysts crystallize in major anatase phase with highest intensity peak (101).

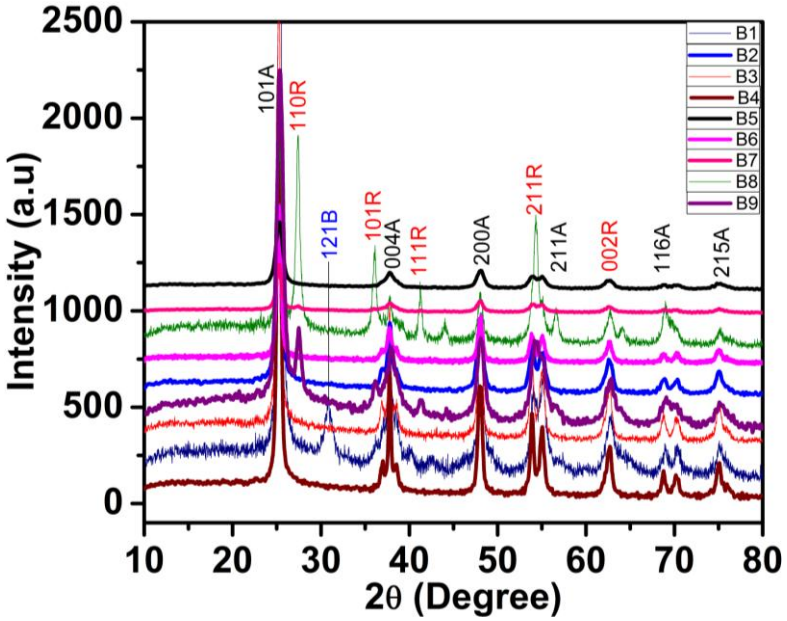

Fig. 16—*XRD plots for calcined samples*

However the mixture of rutile and brookite is observed in few samples. The difference in crystal structures could be attributed to the structural variation in the precursor acid used as template material. The sharpness of the peaks indicated the high crystallinity of the catalysts.

As shown in the figure, for sample B1, with oxalic acid as a precursor, the product was mainly anatase and also contained a very small amount of brookite phase (denoted as B). This could be due to the tight ligation of oxalic acid with the colloid. With the increase in carbon number in precursor acids, *i.e.*, the products from malonic, succinic, glutaric and adipic acids, pure anatase phase TiO_2 was obtained. Further variation in carbon chain with 4 carbon atoms (succinic acid), with various functional groups (malic and tartaric acid) or double bond (maleic and fumaric acid), some change in phases were expected. Out of these four samples, samples obtained from malic, tartaric and fumaric acid precursor had varied amount of rutile along with anatase, while maleic acid gave a pure anatase sample. The malic, tartaric and fumaric acid may be getting loosely bound with the colloid resulting in some rutile phase. The anatase phase was confirmed by JCPDS card # 21-1272, while rutile phase by JCPDS card # 21-1276 and brookite phase by JCPDS card # 29-1360.

The percentage of rutile phase in the respective samples was calculated using eq. **2**.

For the samples B7 6.37 % rutile is observed, while for B9 it was 15.76 %. However, for the sample B8, anatase-rutile mixture is obtained in almost equal quantity and distinct diffraction peak at 2θ of 27.5° for the rutile (110) plane is obtained in 49.09 %.

The above observation regarding the phases obtained suggest that the acids like oxalic acid, malonic acid, succinic acid, glutaric acid and adipic acid, which do not have any functional groups and the maleic acid, which has a *cis*-geometry, may have preferentially ligated in an

intramolecular fashion to form a cyclic bridge structure **2** and delivered anatase or anatase/brookite form. Whereas the malic acid and tartaric acid, containing additional hydroxyl groups and fumaric acid having a *trans*-double bond, gave mixed anatase/rutile phases, due to preferential intermolecular ligation **1**, because of their geometrical rotational restriction as envisioned in Scheme 9. The stronger bridging by oxalic acid had resulted in some brookite phase.

The phase content and average crystallite size of these samples calculated from the line broadening of the highest intensity anatase (101) diffraction peak, by using the Scherrer's equation (eq. **1**) are given in Table 19. The crystallite sizes are found to be in the range of 8-14 nm.

Table 19 – Crystallite sizes

Sample	Crystallite size (nm)	Phase
B1	13.7	A + B
B2	10.0	A
B3	13.7	A
B4	14.2	A
B5	8.0	A
B6	13.1	A
B7	10.7	A + R
B8	12.0	A + R
B9	8.3	A + R
P25	25.0	A + R

UV studies

The absorption spectra of these samples (Fig. 17) reveal that the band edges are in the range 367 to 406 nm. It is observed that the absorption wavelength for samples B1-B7 is in the range of ~367-386 nm, and originates from the inherent property of the anatase TiO_2 phase, while the absorption wavelength of the samples B8 and B9 is extended to 405 and 396 nm respectively, due to the inherent property of the rutile TiO_2 phase. A slight blue shift was observed for samples B4 (glutaric acid precursor) and B3 (malonic acid precursor) which showed better photocatlytic activity than the other samples, while for the sample B8, prepared from malic acid, the single -OH group present in precursor acid influenced the absorbance value and correspondingly the shift in absorbance value to longer wavelength up to 405 nm is observed. This can also be correlated with the XRD results, which shows almost equal percentage of anatase-rutile mixture in this sample.

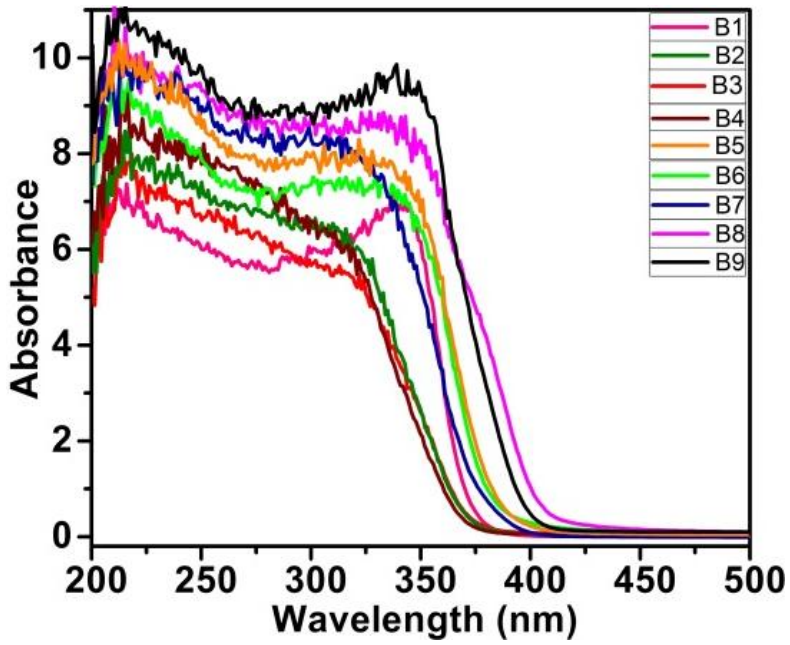

Fig. 17—*UV-DRS spectra of calcined samples*

Table 20 – Band-gap energies

Sample	Band-gap (eV)
B1	3.32
B2	3.34
B3	3.32
B4	3.38
B5	3.21
B6	3.24
B7	3.26
B8	3.06
B9	3.13
P25	3.35

The band-gap energies for all the samples, as calculated using eq. **3**, are given in Table 20 and are found to vary over a range of 3.05 to 3.38 eV. The comparatively lower value of band-gap is observed for the samples with a mixture of anatase and rutile phase than that of pure anatase samples. The band-gap results are in good agreement with the crystalline phase identified by XRD.

BET analysis

The gas adsorption experiments were carried out to study the surface properties of the prepared nanoparticles. The typical plot of N_2 adsorption-desorption isotherm and pore size distribution curves of all the samples are shown in Fig. 18. Isotherm curves for all the

samples can be classified as type IV, characteristic of mesoporous materials, according to IUPAC classification.

The hysteresis loops of samples B1 (anatase:brookite), B8 and B9 (anatase:rutile) are observed to be of an intermediate between typical H1- and H2-type starting with a slightly lower value of relative pressure ~0.45 and extending up to P/P_0 value close to unity. This pronounced hysteresis loop suggests the existence of large mesopores within the samples, with a cage like pore structure connected by windows of smaller size. Also the bimodal nature of pore size distribution, with a small sharp peak in the range 3-4 nm, for these samples indicate the presence of slight amorphous nature. For samples B8 and B9 narrow pore size distribution of 4-11 and 3-8 nm respectively is observed, whereas slightly broader range of 5-30 nm is observed for sample B1.

A similar type of hysteresis loop is also observed for samples B5 and B6 (anatase), with loop starting at $P/P_0 = 0.59$ and closing at a slightly lower P/P_0 value of 0.87, may be due to longer chain length (of 6C) in case of B5 and the presence of *cis*- double bond in the precursor, in case of B6. A monomodal nature of pore size distribution is observed at a narrow range of 3-8.5 for B5 and 3-11 for B6.

However, for the sample B7, H3-type hysteresis loop starting slightly at higher P/P_0 value of 0.52 and closing at 0.94 is observed. This change in behaviour from other two rutile samples is also observed in SEM images, but has no significant effect on photocatalytic properties. A bimodal pore size distribution is observed in this sample in the range 3-29 nm with a small peak due to some amorphous nature.

For samples B2, B3 and B4, with pure anatase phase and smaller carbon chain acid precursors, H3-type hysteresis loop is observed at relatively higher P/P_0 range of ~0.75-0.99, indicating the presence of large interparticulate mesoporosity in these samples. This sharp increase can be ascribed to the capillary condensation of N_2 molecules into the mesopores indicating the small pore size of these samples with large pore channels. Also such type of hysteresis loop is associated with mesopores present in aggregates of plate-like particles, giving rise to slit-like pores [53, 56]. Hysteresis loop approaching to a relatively higher value of $P/P_0 = 1$, also indicates the presence of some macroporosity (>50 nm) in the samples.

A nearly broad pore size distribution from 5 to 30 nm, for samples B2 and B3, corresponding to the half the part of mesoporous region (2-50 nm), while for sample B4, exceptionally broad peak ranging from 11 nm up to 182 nm is observed, which can be ascribed to the interspaces between the TiO_2 nanoparticles. Also the collapsed mesoporous structure and thus formation of some of the macropores may be attributed from this nature.

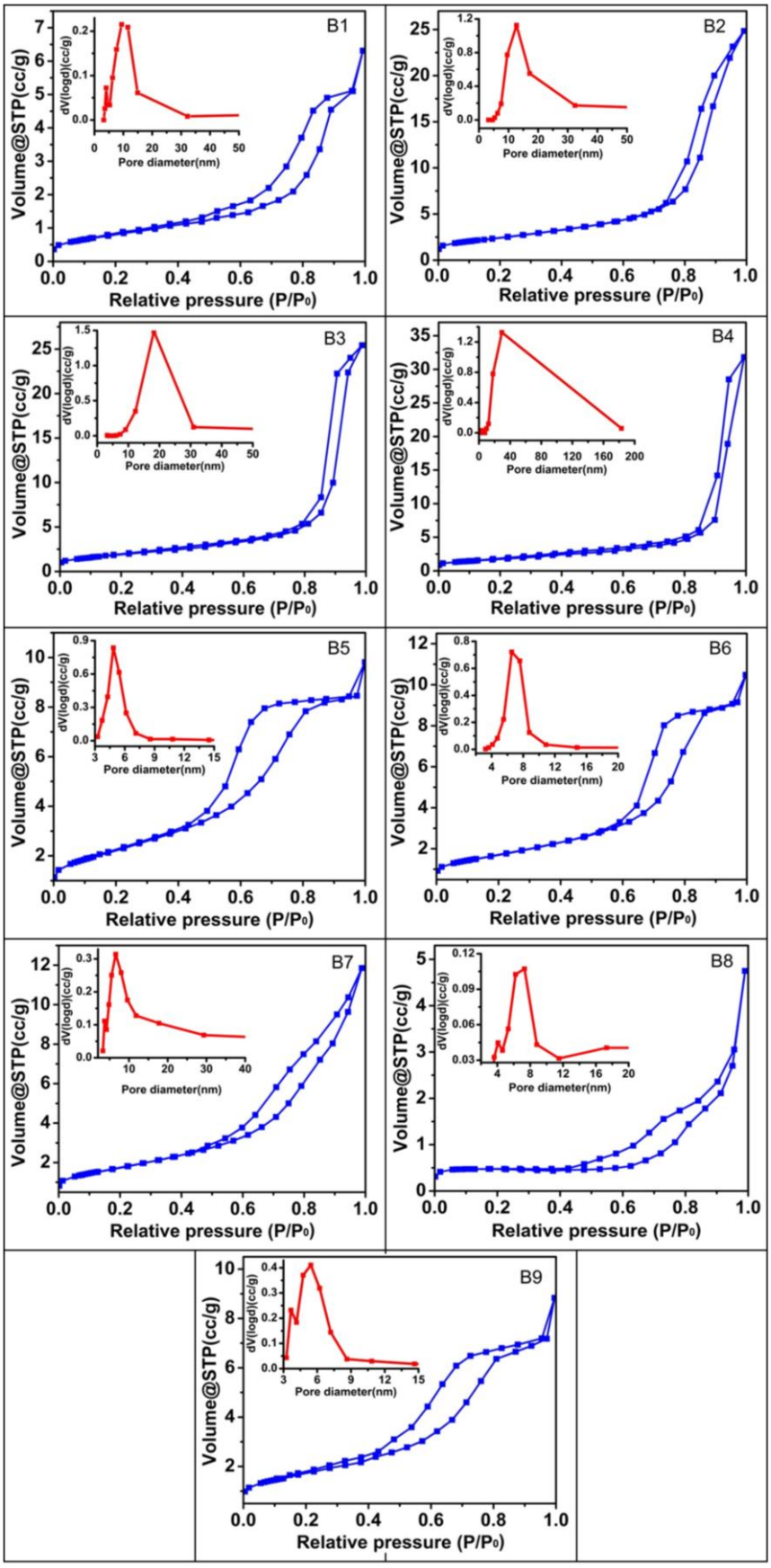

Fig. 18—*Nitrogen adsorption-desorption isotherms and pore size distribution (inset) of TiO_2 nanoparticles for sample B1 to B9.*

The values of surface area, pore volume and pore diameter are summarized in Table 21. Sample B4 exhibit a higher value of surface area (297 m^2/g) and pore volume (1.24 cc/g), followed by sample B2 (254 m^2/g, 0.77 cc/g), which can be attributed to the presence of inner pore channels in these materials and also to the contribution of macropores and larger interparticulate mesoporous structure.

Table 21 – Surface properties

Sample	BJH surface area (m^2/g)	Average pore diamater (nm)	Pore volume (cc/g)
B1	43.05	13.17	0.10
B2	253.8	17.27	0.77
B3	91.04	22.73	0.39
B4	297.0	30.94	1.24
B5	109.5	74.52	0.14
B6	77.55	10.36	0.14
B7	77.84	11.40	0.16
B8	25.15	24.01	0.08
B9	97.78	15.23	0.13
P25	56.00	17.50	0.25

SEM analysis

Scanning electron microscopy (SEM) of the nanocrystalline TiO_2 was carried out to study the surface morphology. From the SEM images (Fig. 19a) it can be seen that, most of the nanoparticles are well separated, although some of them are partially aggregated. Different micro structural features are distinguished among the particles.

For the samples B2 and B4-B7, the titania particles are composed of very tiny well defined spherical nanoparticles with almost uniform size. The clusters composed of these particles tend to fuse together to form small aggregates. Among these, monodispersed mesoporous nanoparticles with small pore channels are obtained for samples B2 and B7, while somewhat densely packed arrangement of such particles with lesser channels are observed in case of the samples B5 and B6, which is also shown by their pore size distribution. Whereas for sample B4, macro-mesoporous network of well-defined interconnected mesopores with small pore channels is observed as can be seen from its broad pore size distribution. For sample B1, mostly cubic nanoparticles in the highly agglomerated form are observed. Sample B3 shows nanoporous networks composed of embedded TiO_2 particles forming larger agglomerates. For samples B8 and B9, irregular nanometric particles can be seen agglomerating into larger, block like irregular particles at the micrometric scale with slightly amorphous mixture, which

is shown by narrow pore size distribution and also an extra small sharp peak observed along with it, in its BET data.

Thus out of nine samples, the cubic shape is observed for the sample B1, formed with the mixture of brookite and anatase, and somewhat irregular shapes are observed in the case of samples B5 and B9, consisting of rutile phase and with -OH functional group present in the template used. Whereas well dispersed spherical nanoparticles are observed for fumaric acid template (B7) sample. All other samples with pure anatase phase showed spherical morphology with pore channels.

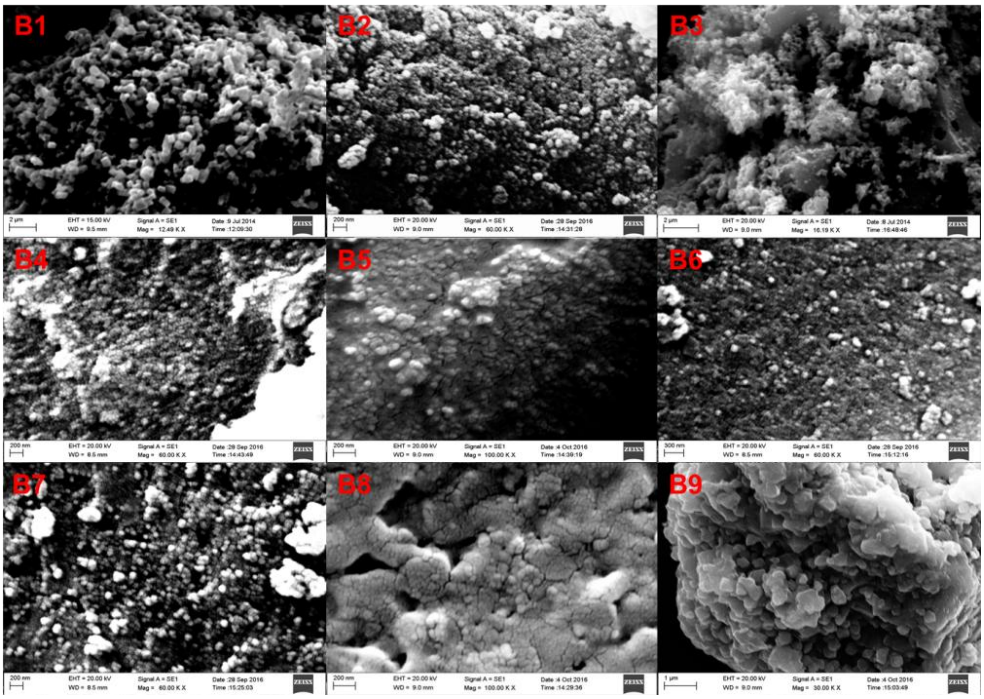

Fig. 19a—*SEM images of TiO_2 nanoparticles B1-B9*

TEM analysis

The B2 and B4 samples which displayed higher photocatalytic activity and showed perfect spherical morphology with small pore channels and mesoporosity in SEM images were further investigated with TEM analysis. TEM micrographs (Fig. 19b) displayed tiny spherical nanoparticles agglomerated to bigger particles with small pore channels through the nano spheres indicating macro-mesoporous nature of these samples. Shadow regions in the picture indicate the agglomeration in particles. The average particle sizes of TiO_2 nanoparticles were observed to be in the range of 12-13 nm. These values are consistent with XRD results.

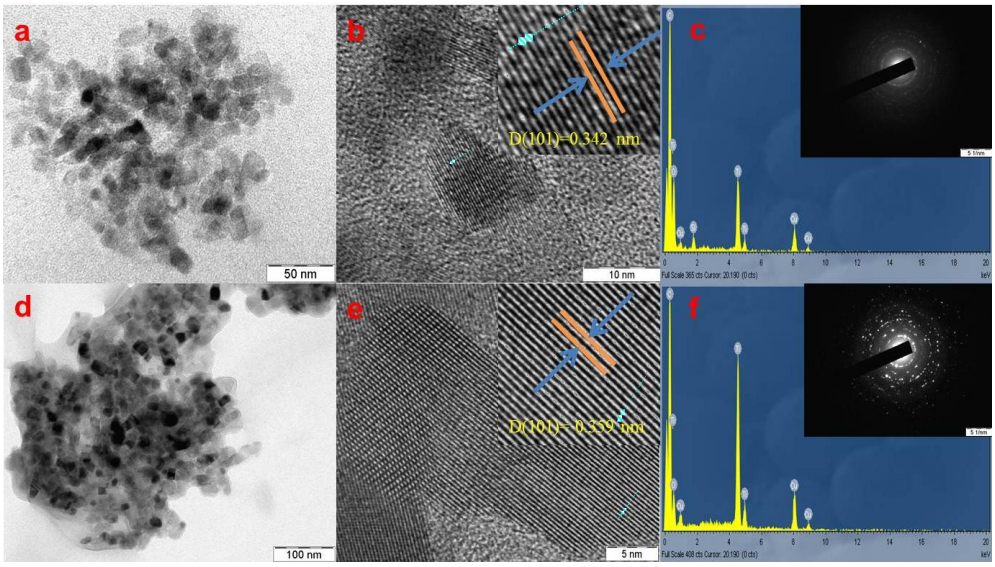

Fig. 19b—*TEM images of TiO_2 nanoparticles-* ***sample B2*** *(a),* ***sample B4*** *(d); corresponding HRTEM images & lattice fringes- magnified images (inset) (b), (e); corresponding EDX images & SAED patterns (inset) (c), (f).*

HR-TEM studies

Further the detailed study of lattice fringes and interface information was done using high resolution TEM images (Fig. 19b (b, e and inset for magnified image)). Well-structured matrix of lattice fringes indicates the highly crystalline nature of TiO_2 nanoparticles. The lattice d-spacing with distances close to 0.35 nm in HRTEM image corresponded to (101) plane of anatase phase (highest intensity peak in XRD pattern). The polycrystalline nature of these samples was further confirmed from concentric ring patterns of small spots in SAED images (inset of Fig. 19b (c, f)). The observed patterns are consistent with Bragg's reflections observed in XRD pattern. The corresponding interplanar spacings that could be indexed according to anatase TiO_2 are assigned as (101), (004), (200), (211), (204), (220), (215), and are matching with the XRD results (JCPDF no. 21-1272).

EDX studies

The chemical composition was confirmed using the Energy-dispersive X-ray Spectroscopy (EDX), which show the expected primary metal element signals (Ti, O) along with Cu, C, and Si elements as shown in Fig. 19b (c, f). The Cu, C and Si signals are due to the TEM grid used for the imaging. It confirms here that the inorganic walls consist of predominantly metal-oxygen networks.

IR studies

The IR spectra of all calcined TiO_2 samples shows a typical absorption band for Ti-O-Ti network as a broad band around 600 cm^{-1}. Absorption bands due to -OH stretching of adsorbed water and the free -OH groups on the surface of TiO_2 were seen at 3540-3150 cm^{-1} and at around 1635 cm^{-1} for the bending vibrations (Fig. 20a).

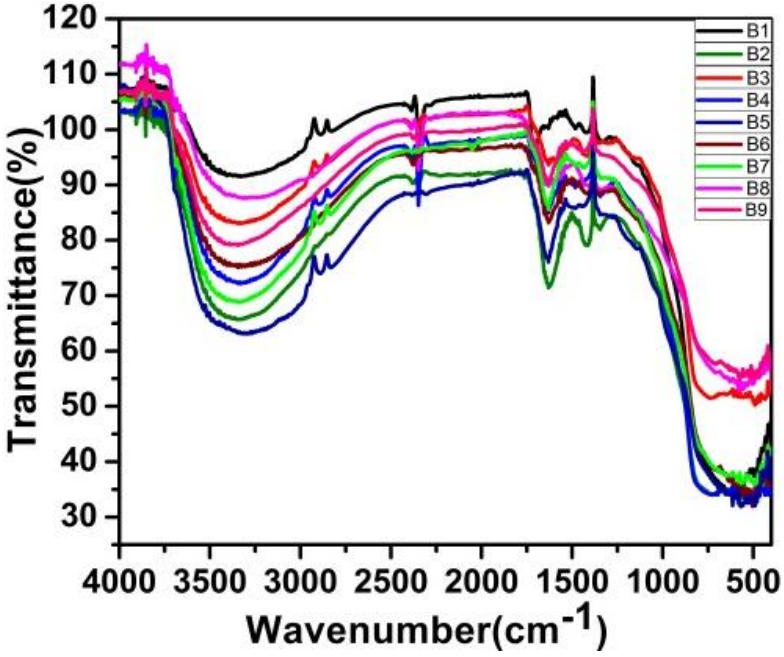

Fig. 20a—*IR spectra of calcined samples*

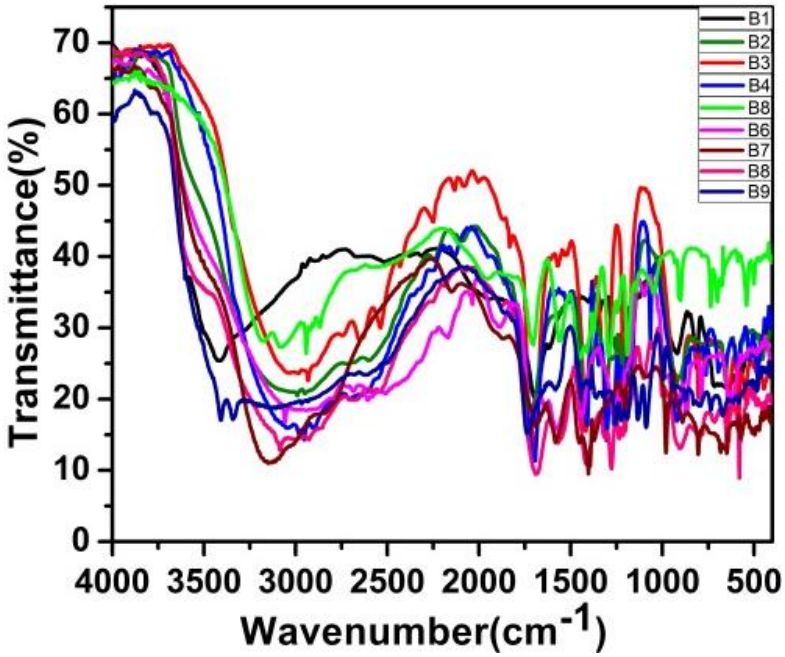

Fig. 20b– *IR spectra of precursor samples*

Absence of other bands due to organic acids indicated the complete removal of organic templates. The spectra of precursor samples were complex because of free unreacted acids (Fig. 20b). Typical bands around 2500-3400 (br), ≈ 1700 cm^{-1} (str) due to the presence of -COOH groups of unreacted acids were found. The other two sharp peaks in the range of 1550 to 1450 cm^{-1} for symmetric and unsymmetric stretching carbonyl of the carboxylate were seen in addition to C-O stretching frequencies at around 1250 cm^{-1}. The presence of these additional peaks of symmetric and unsymmetric carbonyl frequencies confirmed the formation of carboxylate bridging between the titanium atoms.

Photocatalytic activity testing

The photocatalytic performance of TiO_2 nanoparticles was evaluated by degradation of methylene blue as a model compound. The activities are compared with Degussa P25, since it is the most widely used as standard reference material among currently available commercial TiO_2 photocatalysts. Fig. 21a shows the degradation plots of the MB aqueous solution in sunlight and corresponding kinetics are shown in Fig. 21b. The tested TiO_2 powders have shown unequal photocatalytic activities towards the degradation of MB.

The experimental results showed that out of nine samples, B2 and B4 can effectively degrade MB solution and exhibited higher photocatalytic activities than commercial Degussa P25 under sunlight irradiation. The relatively poor activities of the samples B7-B9 are probably related to their rutile dominant phase components. Sample B4 shows highest photocatalytic activity among all the tested samples as a result of its higher surface area, pore volume, broad pore size distribution and its meso-macroporous nature.

The observed degradation patterns can be correlated with the structural and morphological properties of the catalysts. It can be seen that the increase of pore volume and surface area (S_{BET}) can result in an increase of photocatalytic activity. This is because; the higher pore volume and S_{BET} allow more MB to enter into TiO_2 spheres, so as to increase the photocatalytic activity. In addition, the spherical morphologies of these nanoparticles (B2 and B4) with pore channels can also increase the light scattering during the photocatalytic reaction, and can effectively make use of sunlight which leads to increase the photocatalytic activity. Sample B7, though, has a spherical morphology with pore channels showed poor activity due to the mixed anatase-rutile phase.

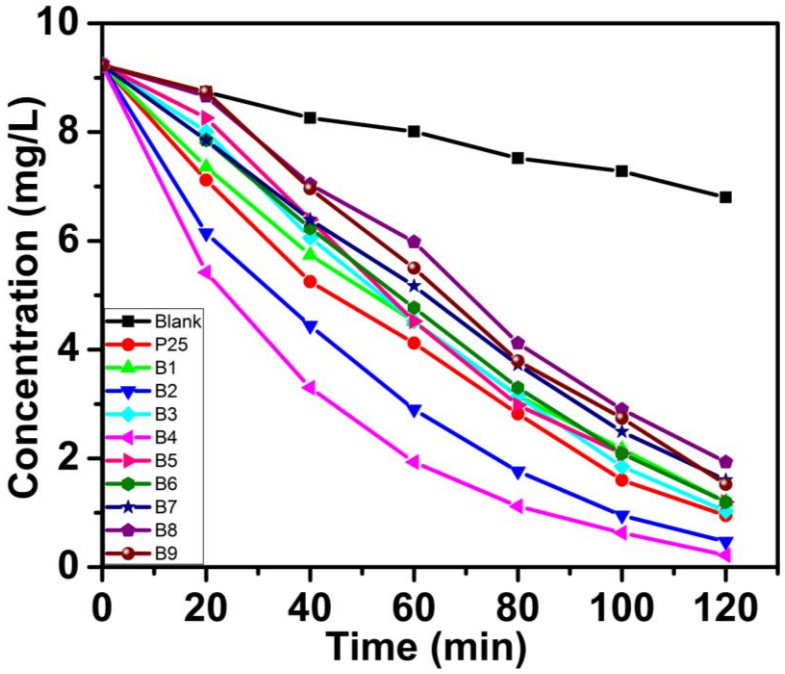

Fig. 21a—*Sunlight degradation plots for methylene blue*

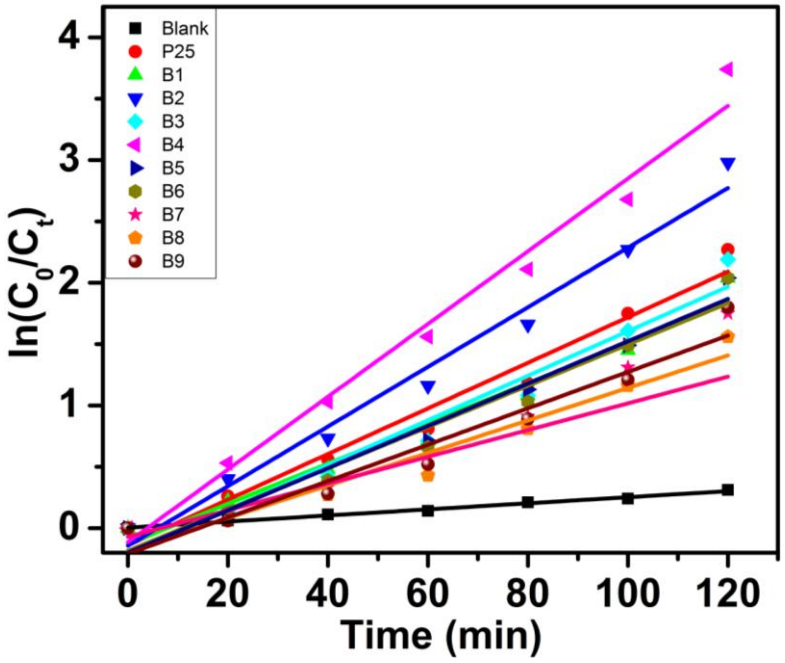

Fig. 21b—*Kinetic studies*

The photocatalytic degradation of MB aqueous solution can be regarded as a pseudo first order reaction, as indicated by a straight line plot of ln (C_0/C_t) versus time. The rate constant values derived from the plot are listed in Table 22. It can be seen that the sample B4 exhibits the highest k value of 0.03 min^{-1}, which is almost twice as that of P25 (k = 0.018 min^{-1}).

Recyclability studies for the samples showing better results were carried out for three cycles, after separating the catalyst by centrifugation and the results were compared with Degussa (Fig. 21c). All the samples could be reused for degradation with negligible loss in activity.

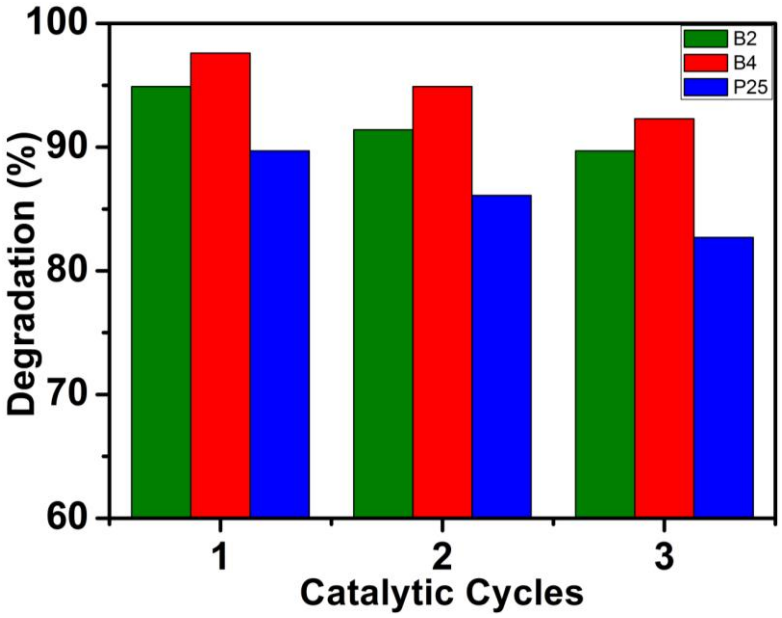

Fig. 21c—*Recyclability studies for the samples showing better results*

Table 22 – Kinetic studies

Sample	Rate constant k (min^{-1})
B1	0.016
B2	0.024
B3	0.018
B4	0.030
B5	0.017
B6	0.017
B7	0.011
B8	0.013
B9	0.015
P25	0.018

Summary and Conclusion

Titania materials with different morphologies and textural properties were systematically studied by employing different dicarboxylic acids with increasing carbon chain and also with varying functional groups, as templating materials in the sol-gel synthesis. Sample prepared using glutaric acid shows the best photocatalytic activity due to pure anatase phase, higher pore volume, surface area, spherical morphology of macro-mesoporous nature with pore channels and having exceptionally broad pore size distribution. The use of different acids as a starting material induced an important modification in morphology due to preferential

bridging mode. Catalyst obtained from acids with -OH functional group or *trans*-double bond gives anatase-rutile mixture and these samples showed least photo-degradation efficiency. Also it is found that sample showing slight blue shift (B4) is observed to be better photocatalyst rather than the sample which showed a red shift (B8). This may be again due to the presence of rutile content in sample B8, and pure anatase phase of sample B4. The tightly bound and more acidic oxalic acid gave brookite-anatase mixture. Thus, it can be concluded here that phase and structural features of the catalyst is determined by the precursor dicarboxylic acid and the photocatalytic activity is determined by the phase, size and the porosity of the catalyst. The properties of catalysts are summarized in Table 23.

Table 23– Summary of the properties of TiO_2 nanoparticles.

Sample	**Cryst. size (nm) & (phases)**	**BJH surface area (m^2/g)**	**Pore vol. (cc/g)**	**Av. pore dia. (nm)**	**λ_{max} (nm)**	**Rate const. k (min^{-1})**
B1	13.7 (A+B)	43.05	0.10	13.17	373	0.016
B2	10.0 (A)	253.80	0.77	17.27	371	0.024
B3	13.7 (A)	91.04	0.38	22.73	373	0.018
B4	14.2 (A)	297.00	1.24	30.94	367	0.030
B5	8.0 (A)	109.50	0.14	74.52	386	0.017
B6	13.1 (A)	77.55	0.14	10.36	383	0.017
B7	10.7 (A+R)	77.84	0.16	11.40	380	0.011
B8	12.0 (A+R)	25.15	0.08	24.01	405	0.013
B9	8.3 (A+R)	97.78	0.13	15.23	396	0.015
P25	25.0 (A+R)	56.00	0.25	17.50	370	0.018

Section C – Study of amino acids as templates

Introduction

In the previous sections, monocarboxylic and dicarboxylic acid templates were shown to have a significant effect on the size, phase and the mesoporosity of the TiO_2 catalyst during sol-gel synthesis.

Moving further on in this direction, it was thought that amino acids, the natural building units of proteins, could serve as a smart template in the preparation of mesoporous nano TiO_2 materials with desired structure and surface properties.

Amino acids have been routinely used in the combustion and solvothermal synthesis of TiO_2 [64-77]. However, a direct comparison of the amino acids for the sol-gel synthesis of nano TiO_2 was lacking. Amino acids exist in zwitterionic forms and they are expected to behave differently than the other organic acids. Organic acids in general react with surface hydroxyl of the inorganic materials and form a metal carboxylate bond. However, the same is not studied in detail about the amino acids. Some of the reports suggested that amino acids act as a template by reacting with surface hydroxyl group and forms, metal carboxylates [78-80], while one report suggested adsorption of an amino group on the surface of TiO_2 [81]. We were also interested to know the role of amino acids in controlling the size of the particulate in the sol-gel synthesis of TiO_2 and thereby their effect on the photocatalytic properties of the catalyst formed. The amino acids employed as precursor materials in this study were glycine, L-proline, β- alanine, DL- alanine, L- glutamic acid, DL- aspartic acid, DL- valine and DL-serine (Table 5). The structures of these acids are shown in Fig. 22.

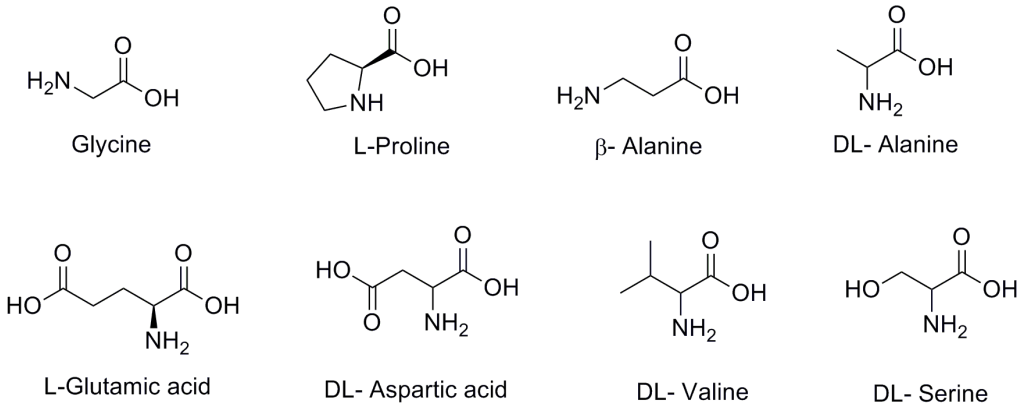

Fig. 22 - *Structures of the precursor acids used for series 3*

Structural, optical and morphological properties

Powder X-ray studies

In order to establish the crystallinity, crystalline phase and the crystallite size of the pure titania nanoparticles, the analysis of the calcined nanoparticles was carried out by X-Ray powder diffraction patterns (XRD).

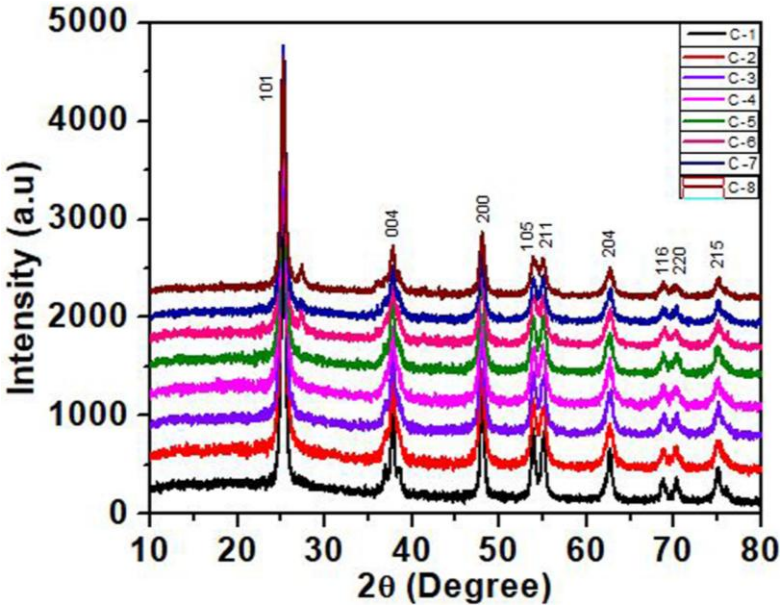

Fig. 23—*XRD plots for calcined samples*

Sharp and well resolved peaks are seen from the XRD patterns (Fig. 23), indicating high crystallinity and the presence of small sized nanocrystals. The peak positions can be assigned to anatase TiO_2 with characteristic values, (101), (004), (200), (105), (211), (204), (116), (220) and (215), (JCPDS card # 21-1272). For the samples C1-C5 and C7, a pure anatase phase is obtained and no peak attributable to other TiO_2 crystalline phases is observed, suggesting the high purity of the samples [51]. However, the samples C6 (aspartic acid) and C8 (serine) show the presence of very small amounts (~8 %) of rutile phase as calculated using eq. **2**.

The average crystallite size for the series of TiO_2 nano powders was determined from (101) diffraction peak (the most predominant highest intensity peak), using Scherrer's eq. **1**.

It is found to be in the range of 11-18 nm (Table 24). The smallest crystallite size is observed for sample C6 (aspartic acid) of 12 nm and the largest for sample C1 (glycine) of 18.9 nm. The synthesized samples were found to be smaller in size as compared to Degussa P25 [52]. Thus we can say that, in general, branched amino acids gave samples with smaller crystallite size.

Table 24 – Crystallite sizes

Sample	Crystallite size (nm)
C1	18.9
C2	13.7
C3	13.6
C4	12.4
C5	12.4
C6	12.0
C7	14.2
C8	15.1
P25	25.0

UV-DRS studies

The optical properties of TiO_2 nanoparticles were investigated by UV-Vis diffuse reflectance spectroscopy, as shown in Fig. 24.

From the absorption spectra, it is observed that the samples absorb in the UV region, confirming their wide band-gap, as calculated using eq. **3**, which is in the range between 3.1 to 3.3 eV (Table 25). The band-gap values are observed to be lower than that of Degussa. The slight shift in the absorption edge is observed for samples C3 and C5, though it has no significant effect on the photo-degradation studies.

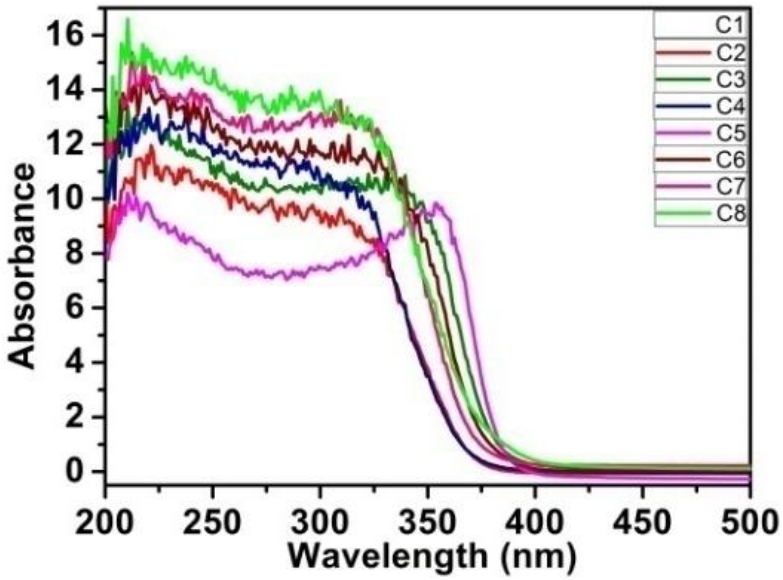

Fig. 24—*UV-DRS spectra of calcined samples*

Table 25 – Band-gap energies

Sample	Band-gap (eV)
C1	3.12
C2	3.25
C3	3.15
C4	3.27
C5	3.15
C6	3.22
C7	3.22
C8	3.22
P25	3.35

BET analysis

Fig. 25 illustrates the nitrogen adsorption-desorption isotherms and corresponding pore size distribution curves (inset) of these samples. The isotherm patterns exhibited the typical of IUPAC type IV with H3-type hysteresis loop. This hysteresis loop behavior can be attributed to the existence of mesopores in the size range 2-50 nm. In addition the observed hysteresis loops shifts to the higher relative pressure region, which shows the capillary condensation is associated with large pore channels [53]. The sharp decline in desorption curve is indicative of mesoporosity while slightly broader hysteresis between the two curves for samples C1, C3 and C6 demonstrates that there is a diffusion bottle-neck, possibly caused by non-uniform pore size. The pore size distribution up to 20 nm further confirms the mesoporous nature of these samples. Whereas for samples C2, C4, C7 and C8, a very narrow hysteresis loop is observed, suggesting the existence of more uniformly shaped pores. Corresponding narrow range of pore size distribution with a sharp peak in the lower region reveals the presence of some micropores in these samples. A bimodal nature of pore size distribution extending up to 40 nm is observed for sample C2, in addition to a sharp narrow peak. For sample C5, the intermediate of H2- and H3-type hysteresis loop is observed, indicating the non-rigid structure of pores. The pore size distribution from 5 to 15 nm, with an additional peak in the lower region is seen, may be attributed to the slight amorphous nature of this sample.

This observed variation in the shapes of hysteresis loops does not show significant effect on the properties of the catalysts. The specific surface area calculated from the BJH desorption plot and the pore diameter of all investigated photocatalysts is summarized in Table 26. The maximum surface area of 95.3 m^2/g, was observed for the sample C6 obtained from aspartic acid and a minimum of 24.6 m^2/g for the sample C7 (valine). These results are difficult to

correlate with the hydrophobic carbon chain length of the amino acids and may have to do with the affinity of each amino acid to the various surfaces of the particulate.

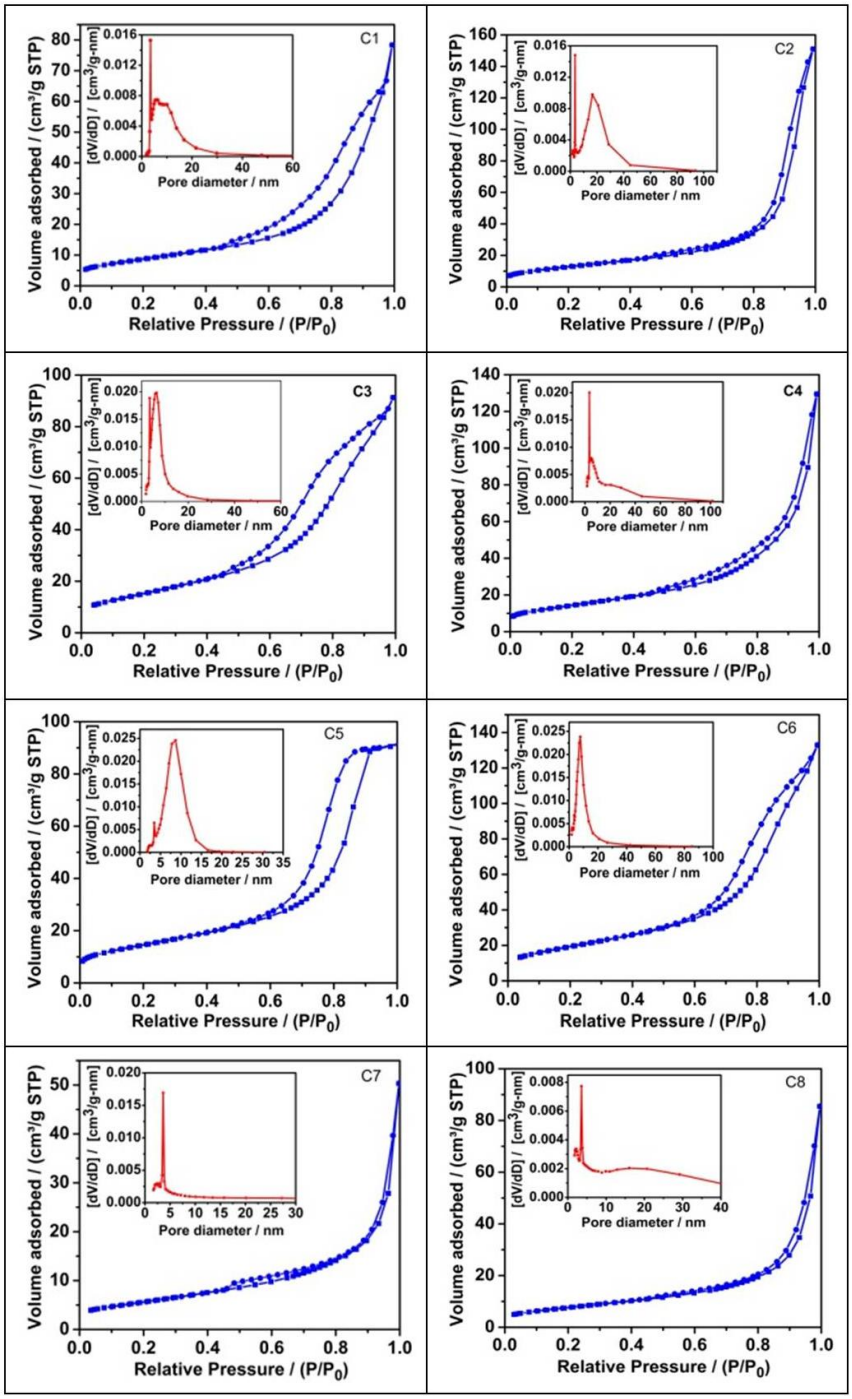

Fig. 25—*Nitrogen adsorption-desorption isotherms and pore size distribution (inset) of TiO_2 nanoparticles for samples C1-C8.*

Table 26 – Surface properties

Sample	BJH surface area (m^2/g)	Average pore diamater (nm)
C1	47.6	10.2
C2	60.4	15.5
C3	81.8	7.0
C4	67.1	12.0
C5	72.0	7.8
C5	95.3	8.7
C5	24.6	12.7
C5	33.2	16.0
P25	56.0	17.5

TEM analysis

The exact microstructure and the particle size of the prepared TiO_2 catalysts were studied by TEM micrographs. The TEM images as shown in Fig. 26 indicate largely cubical shape of particles with non-uniform size. Some weak aggregation among the particles is also seen from these micrographs. The average particle size was estimated to be about 10-15 nm (Table 27), corresponding closely to the size estimated by XRD analysis.

To further investigate the detailed structure and crystallinity of TiO_2 nanoparticles, the SAED patterns are obtained as shown in the inset of Fig. 26. A set of diffraction rings is observed in SAED patterns due to the randomly oriented TiO_2 nanoparticle, which are indexed as the anatase phase of TiO_2, and this is consistent with the XRD results. Detailed analysis indicates that the first diffraction circle in the pattern corresponds to the (101) plane of anatase TiO_2. The corresponding d-spacings are assigned as (101), (004), (200), (211), (204), (220), (215), matching with the XRD results (JCPDS no. 21-1272). Thus, it is reasonable to believe that the TiO_2 nanoparticles are well crystallized particles.

Table 27 – Particle sizes

Sample	Particle size (nm)
C1	15.2
C2	10.8
C3	11.7
C4	11.7
C5	13.0
C6	10.4
C7	11.2
C8	15.2
P25	21.0

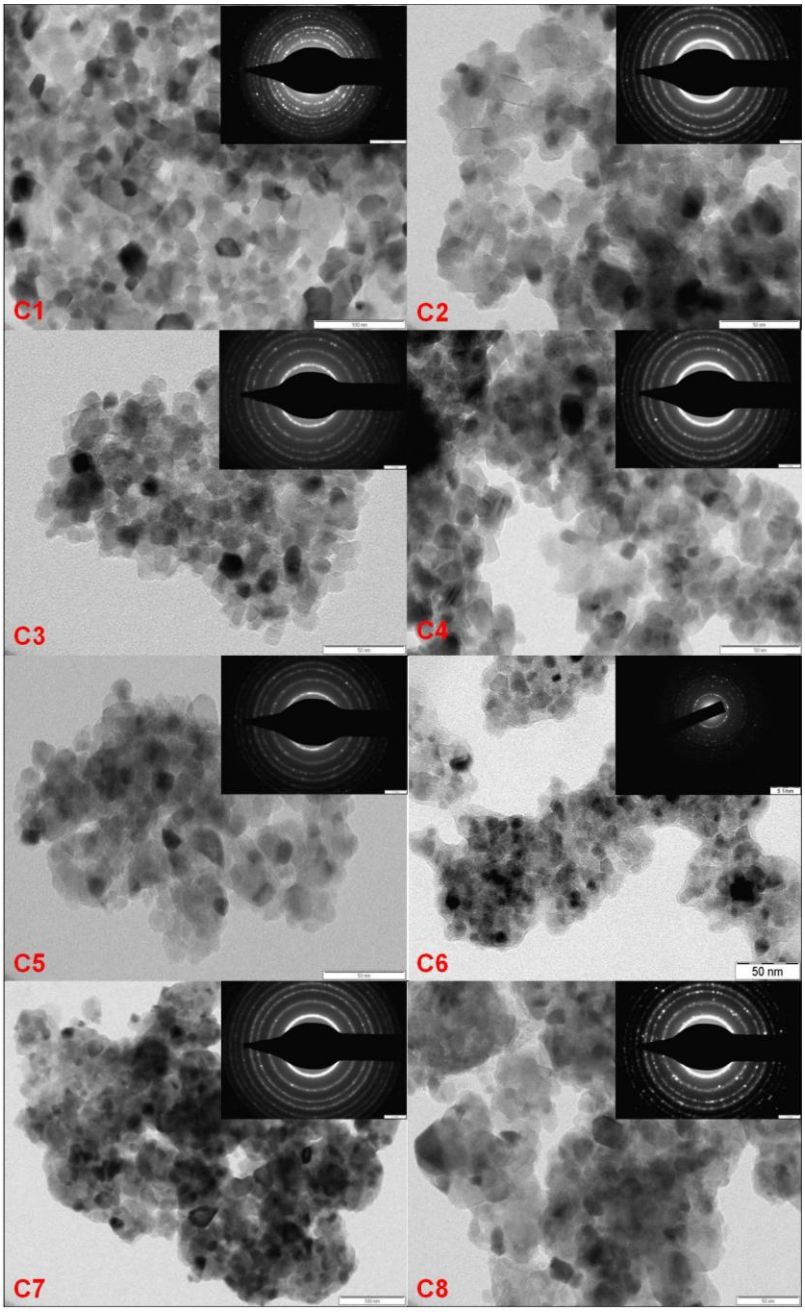

Fig. 26—*TEM images of TiO_2 nanoparticles and corresponding SAED patterns (inset) for samples C1-C8.*

IR studies

The IR spectra of all the calcined TiO_2 samples show a typical absorption band for Ti-O-Ti network as a strong, broad band around 600 cm^{-1}. A slightly less strong, broad band at 3300-3500 cm^{-1} (-OH stretching mode) and weak bands at ~1633 cm^{-1} seen were due to physically adsorbed water on the surface of TiO_2 and surface hydroxyl groups (Fig. 27a). In the spectra of precursor samples (Fig. 27b), the strong, broad band between 2500-3500 cm^{-1} (R-COOH) and four typical strong bands between 1400-1600 cm^{-1} (C=$O_{(s,un)}$, -NH_3^+,-CH_2), suggested the

presence of unreacted amino acids. The close resembles of these spectra with the starting amino acids' spectra with no significant change in the region between 1400-1600 cm^{-1} suggested absence of metal carboxylates bonds [68]. Such a metal carboxylate bond is usually formed when organic acids are heated with $Ti(OH)_4$. This was further confirmed by mixing $Ti(OH)_4$ and glycine and heating at 100 °C which displayed a similar IR spectrum. This was also further studied by heating the precursor sample of glycine at different temperatures viz. 200, 300 & 400 °C (Fig. 27c). The IR spectra of the sample heated at 200 °C did not show any remarkable change, while the sample heated at 300 °C showed the presence of a strong band at 1683 cm^{-1}, which could be due to the presence of the free carboxylic acid group (Scheme 10).

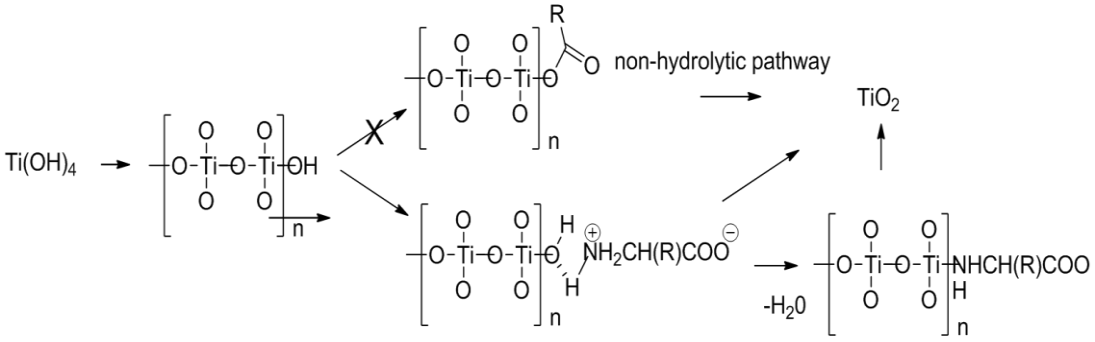

Scheme 10

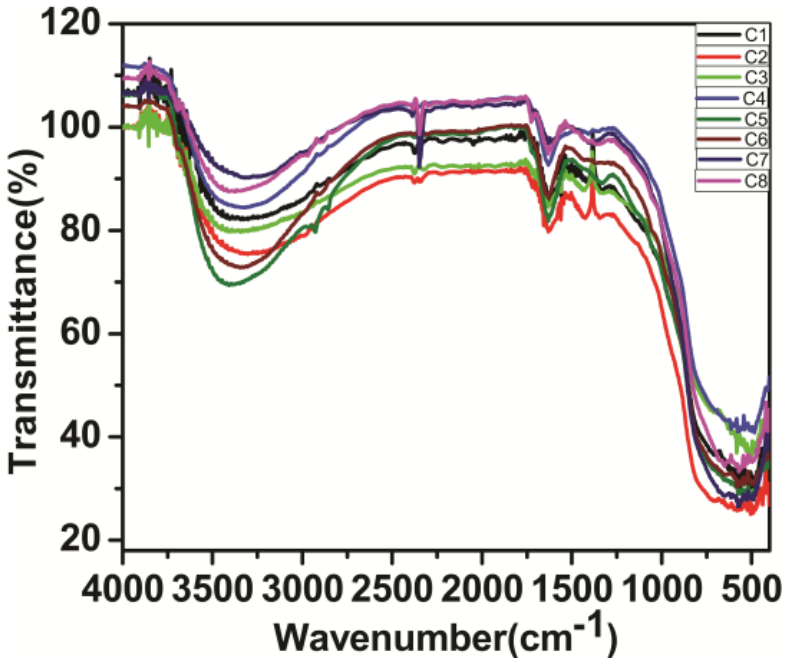

Fig. 27a—*IR spectra of calcined samples*

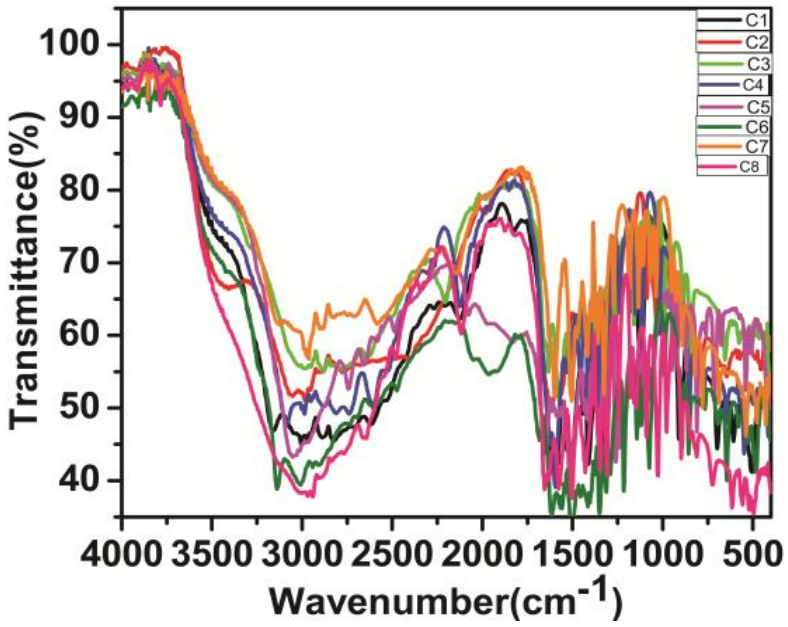

Fig. 27b– *IR spectra of precursor samples*

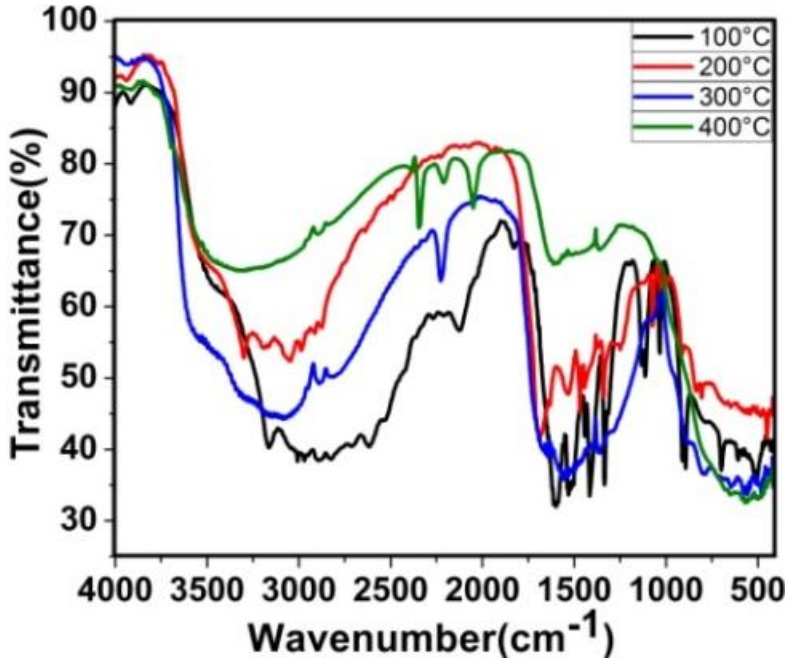

Fig. 27c—*IR spectra of precursor samples heated at different temperature*

The IR spectrum of the sample heated at 400 °C was matching with the calcined sample C1. TG-DTA of the precursor sample (Fig. 27d) also showed similarity with the reported TG-DTA of glycine [82] confirming our observation that amino acids are more probably acting as surfactants and not as reactants [81]. Also, precursor sample of C1 when washed with water did not show any residual carbonyl functionality while precursor sample prepared from acetic acid did show the unsymmetrical and symmetrical stretching of the carbonyl

functionality in their IR spectra [54]. This result could also explain why amino acids fail to functionalize TiO_2 while N-Boc amino acid could [83].

During the condensation of the $Ti(OH)_4$ to form nano TiO_2, the hydrogen of the ammonium group of the protonated amino acid forms hydrogen bonding with the free surface -OH groups of the particulate as shown in Scheme 10 to control the polymerization. The same phenomenon perhaps can be used to explain the adsorption behaviour of the amino acids on the surface of TiO_2 [84].

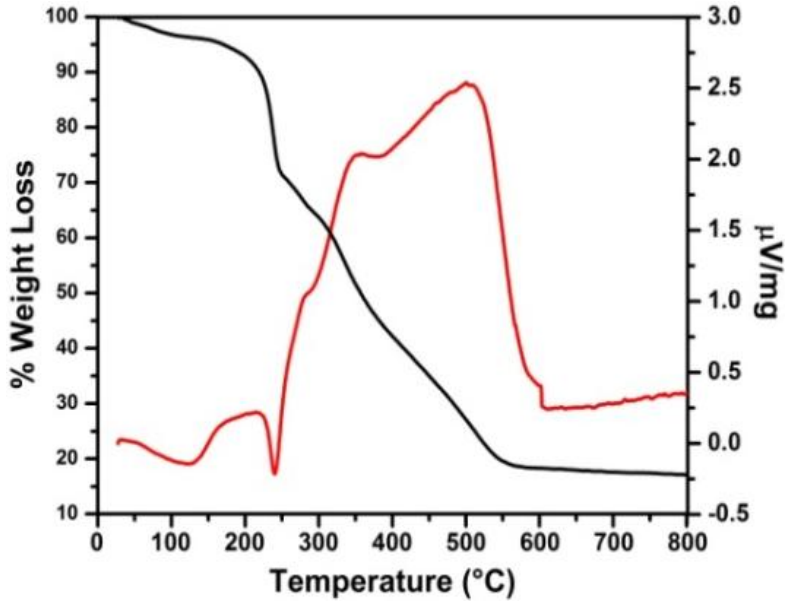

Fig. 27d– *TG-DTA spectra of precursor sample of glycine*

Photocatalytic activity testing

The photocatalytic activity of the samples was evaluated by their ability to degrade MB in aqueous suspensions under direct sunlight irradiation at room temperature. Direct sunlight degradation of toxic chemicals is very relevant to environmental cleansing. Fig. 28a shows the concentration plots during sunlight irradiation over a time for the average results of three readings and corresponding kinetic studies are shown in Fig. 28b. Sample C6 shows better degradation efficiency by decreasing the concentration of MB at a faster rate with time, followed by sample C2 and C7, in comparison with Degussa P25.

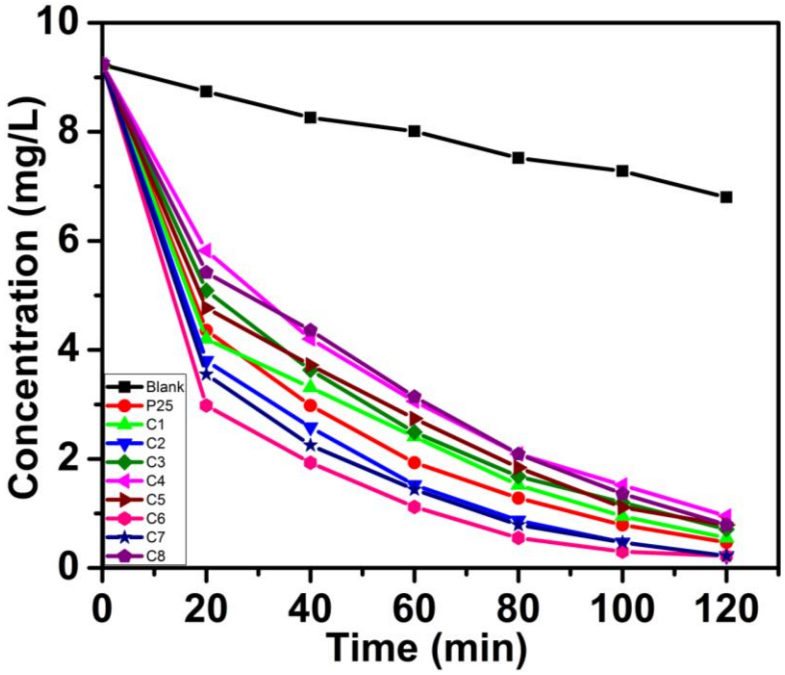

Fig. 28a—*Degradation plots for methylene blue*

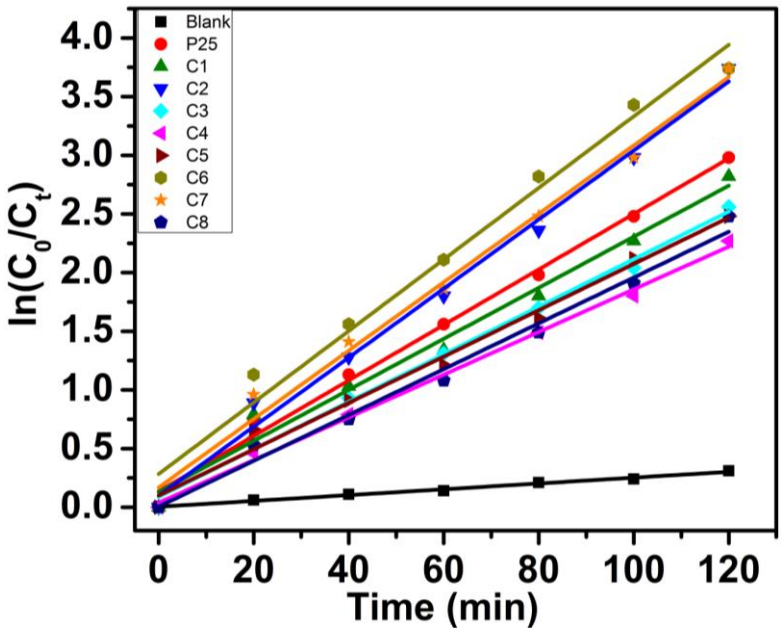

Fig. 28b—K*inetic studies for MB degradation*

The results were further supported by degradation of another dye, calmagite (2-hydroxy-1-(2-hydroxy-5-methylphenylazo)-4-naphthalenesulfonic acid), an anionic azo dye, where the same trend was observed. The concentration plots during sunlight irradiation of this dye are shown in Fig. 28c with corresponding kinetic studies (Fig. 28d).

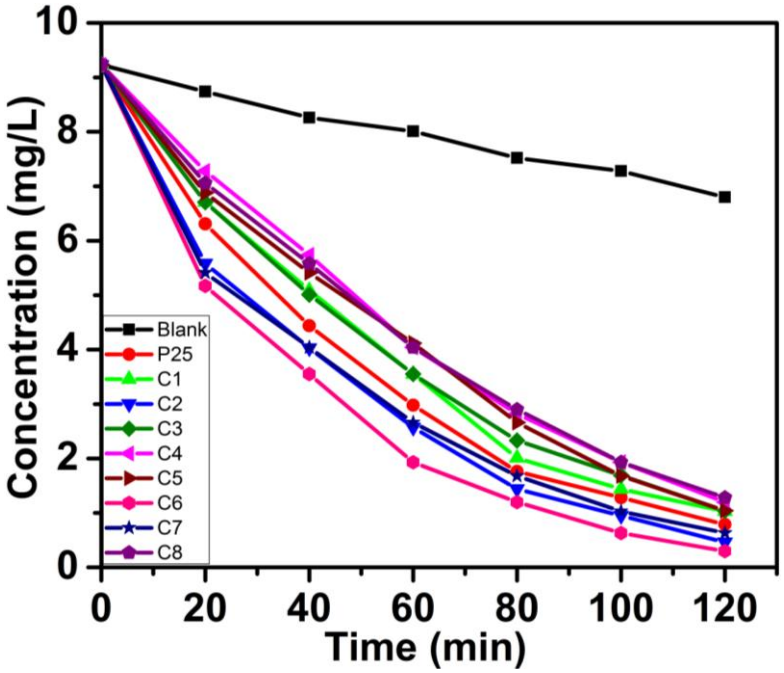

Fig. 28c—*Degradation plots for calmagite*

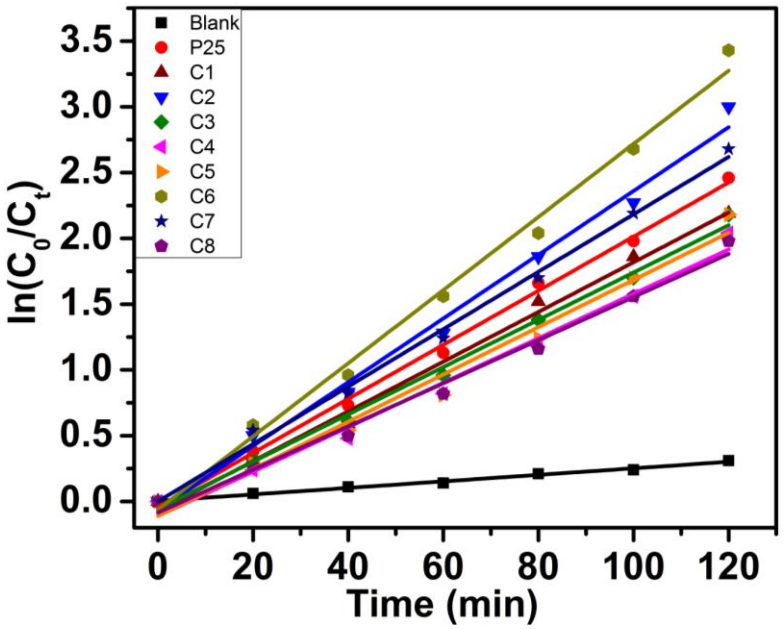

Fig. 28d—K*inetic studies for CG degradation*

The kinetics of the photocatalytic degradation reaction were studied under optimized conditions and hence calculated the rate constants by using Langmuir–Hinshelwood kinetic model- $\ln (C_0/C_t) = kt$, where C_0 is the initial concentration of dye solution at time t = 0, C is the concentration of dye solution after different time interval of photocatalytic reaction and slope k is the apparent rate constant.

A plot of $\ln (C_0/C_t)$ versus time for both the dyes (Fig. 28b & 28d) represents a straight line, which indicates the photocatalytic degradation follows a pseudo first order kinetics. Linear

relationships for all the photocatalysts is seen from which it can be observed that the apparent reaction rate constant is highest for sample C6. The rate constant k for both the dyes is given in Table 28, which is in accordance with the other results.

Thus, it is concluded here that the degradation rate depends on precursor amino acids used as a starting material. Among the acids tested, it is observed that branched amino acids give better catalyst than the straight chain compound. However, glutamic acid though have a maximum chain length of non-polar hydrocarbon chain does not give expected results and this could be due to the difference of affinity of glutamic acid, compared to aspartic acid towards the surface of TiO_2 [78]. The little percentage of rutile phase in two samples has also not shown any significant contribution in photocatalytic activity.

Recyclability studies for the samples showing better results for both the dyes were carried out for three cycles, after separating the catalyst by centrifugation. The results were compared with Degussa and are displayed in Fig. 28e for MB degradation and Fig. 28f for CG degradation. All the prepared samples could be reused for degradation with negligible loss in activity.

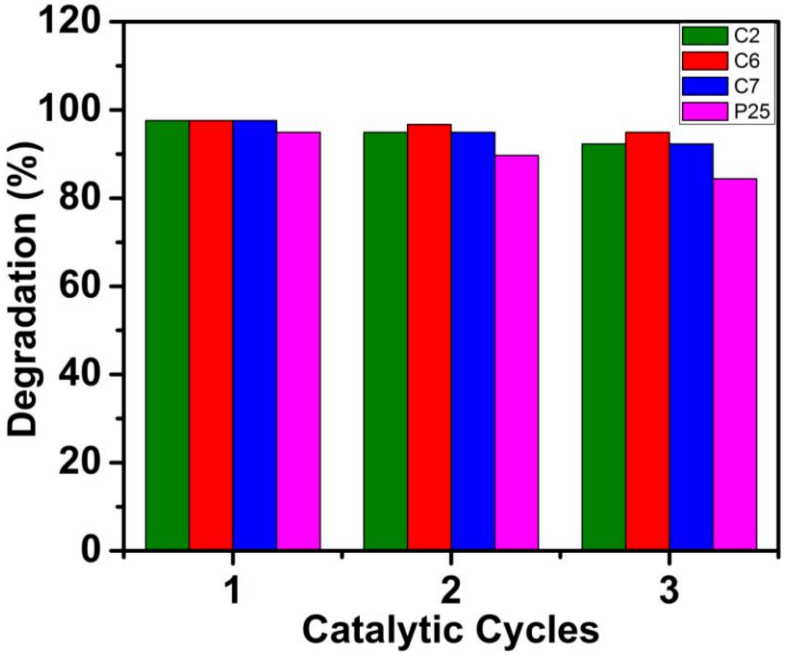

Fig. 28e—*Recyclability studies for the samples showing better results for MB*

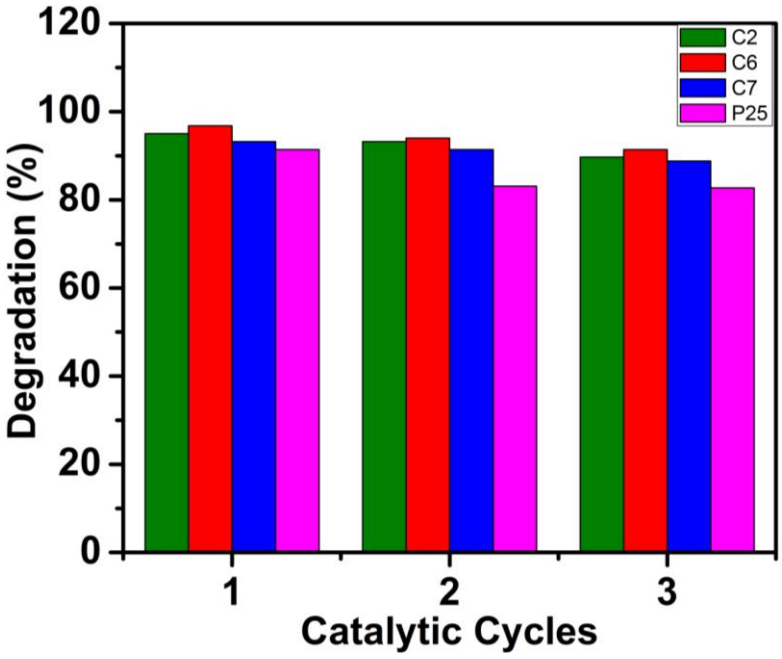

Fig. 28f—*Recyclability studies for the samples showing better results for CG*

Table 28 – Degradation kinetic studies

Sample	Rate constant k (min^{-1})	
	MB	CG
C1	0.022	0.019
C2	0.029	0.024
C3	0.020	0.018
C4	0.018	0.017
C5	0.020	0.018
C6	0.030	0.028
C7	0.029	0.022
C8	0.020	0.016
P25	0.024	0.020

Summary and Conclusions

Eight amino acids, glycine, DL-alanine, β-alanine, DL-valine, L-proline, DL-serine, DL-aspartic acid and L-glutamic acid were compared as templates for sol-gel synthesis of TiO_2. Formation of phase pure anatase nano particulate was observed in all cases except aspartic acid and serine. Among these acids, particles prepared from the branched amino acids (proline, valine and aspartic acid), showed better photo-degradation in comparison with Degussa P25 by direct sunlight exposure of dyes, MB and CG. Aspartic acid was found to be the best templating agent. The smaller size of the particulate was found to be more important in determining the catalytic activity than the surface area and pore volume. Further, the IR studies suggested that the amino acids act as a template by acting as surfactant rather than as a reactant. The

surfactant activity was attributed to hydrogen bonding between surface hydroxyl groups of the colloid and the hydrogen of the ammonium group of the protonated amino acid. The properties of the catalysts are summarized in Table 29.

Table 29 – Summary of the properties of TiO_2 nanoparticles.

Sample	Cryst. size (nm)	Particle size (nm)	Av. pore dia. (nm)	BJH surface area (m^2/g)	Rate constant k (min^{-1}) for MB	CG
C1	18.9	15.2	10.2	47.6	0.022	0.019
C2	13.7	10.8	15.5	60.4	0.029	0.024
C3	13.6	11.7	7.0	81.8	0.020	0.018
C4	12.4	11.7	12.0	67.1	0.018	0.017
C5	12.4	13.0	7.8	72.0	0.020	0.018
C6	12.0	10.4	8.7	95.3	0.030	0.028
C7	14.2	11.2	12.7	24.6	0.029	0.022
C8	15.1	15.2	16.0	33.2	0.020	0.016
P25	25.0	21.0	17.5	56.0	0.024	0.020

Section D – In-*situ* formed imines as templates

Introduction

All the previous sections (1-3) deal with the effect of different class of organic acids acting as ligands and surfactants in presence of a large excess of water. In this section a slightly different approach is followed. In this approach, the hydrolysis and condensation reaction was taking place in the presence of excess of aniline and anisaldehyde (4-methyl benzaldehyde). It was expected that aniline would react with anisaldehyde to generate water, which would then hydrolyze the TIP. The hydrolysis reaction was to be controlled by the presence of water available which could either result into complete hydrolysis or partial hydrolysis as shown below in Scheme 11. The ratios of the aniline:anisaldehyde was varied to make available initially 4, 3 and 2 moles of water respectively.

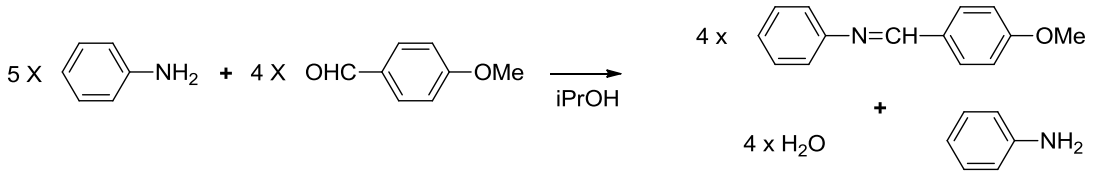

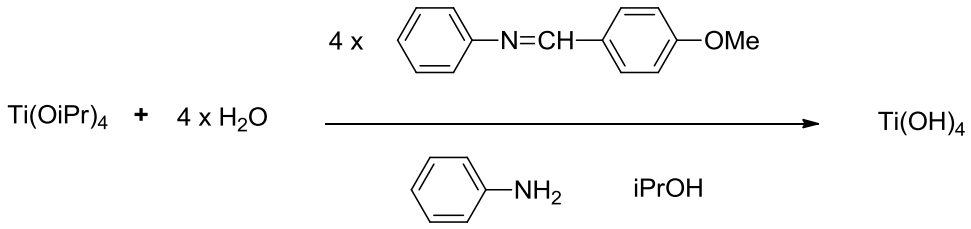

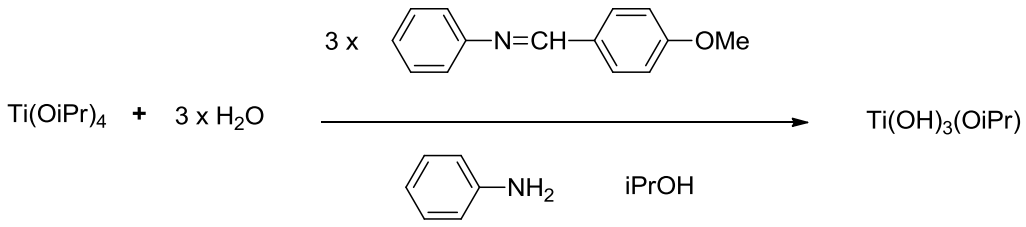

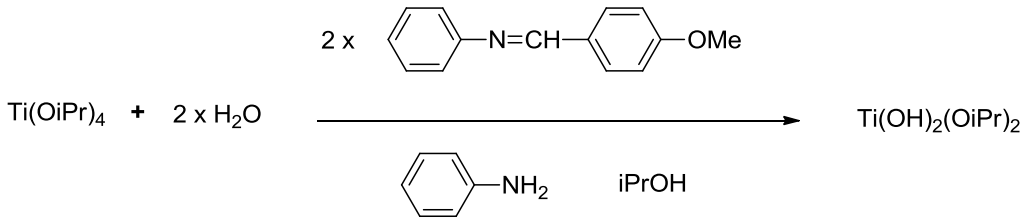

Scheme 11

So, it was expected that, the restricted supply of water would lead to partial hydrolysis and polymerization sequence to form the gel. During the formation of gel, the imine and primary amine (aniline) would serve as a directing ligand. There are a few recent reports from M. Salvato-Nisari's group about imine (Schiff base) and amines as ligands in hydrothermal synthesis of TiO_2. For instance *N,N'*-buthylenebis(acetylacetone iminato) dianion (Acacbn), triethanolamine (TEOA), $H_2[H_2Salen]$, $H_2[H_2Salpn]$ and $H_2[H_2Salophen]$ were found to be effective to control the shape, size and optical properties [25, 26, 85-88].

In the present approach the precursor powders were calcined at 500 °C for 3 h. It was presumed that, as the number of water molecules released by the imination reaction decrease, the rate of hydrolysis will slow down. This would then have unexpectedly reduced powerful dye with enhanced photocatalytic activity.

Structural, optical and surface properties

Powder X-ray studies

Fig. 29 shows the powder XRD patterns of these samples. It is seen that the peaks are very sharp indicating the highly crystalline nature of all three samples. The major patterns for all the samples could be indexed to anatase phase of TiO_2 with 101 peak of highest intensity. The sample O1 is seen to have a pure anatase phase with no peaks of other phases of TiO_2. The sample O2 displayed mixed anatase-rutile phase with about 3.9 % of rutile phase (as calculated using eq. **2** and marked as * in Fig. 29). While the sample O3 has 5.5 % rutile phase. From this observation it is found that with a diminishing amount of water available for the hydrolysis of TIP the percentage of rutile phase increase in the anatase-rutile mix phase samples.

Further crystallite size was calculated using Scherrer's formula (eq. **1**) and was found to be in the range of 12-15 nm (Table 30). Slight increase in crystallite grain size is observed may be due to formation of rutile phase for samples O2 and O3.

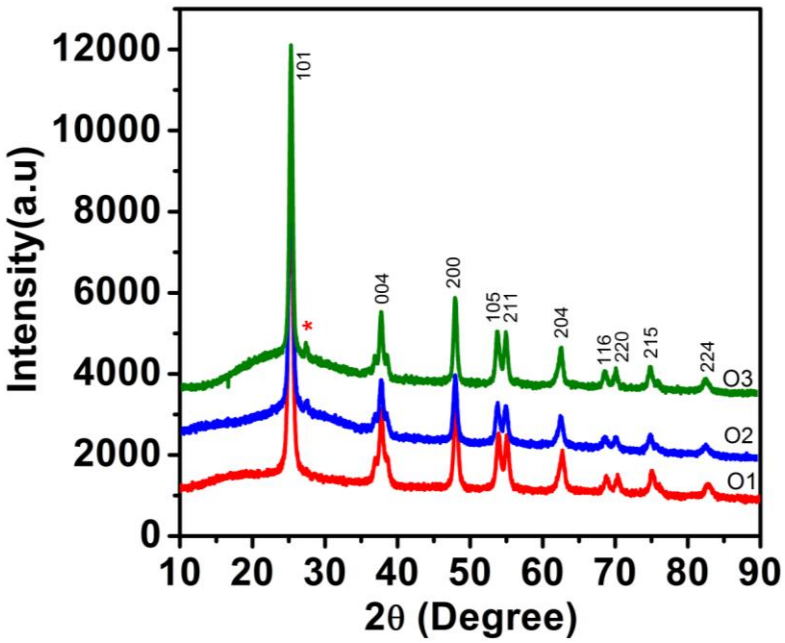

Fig. 29—*XRD plots for - calcined samples*

Table 30 – Crystallite sizes

Sample	Crystallite size (nm)
O1	12.9
O2	13.4
O3	15.3
P25	25.0

UV-DRS studies

Optical studies were carried out with the help of UV-Vis diffuse reflectance spectroscopy. From Fig. 30, a steep decrease in the absorption at wavelengths longer than 380 nm is observed, which can be assigned to the intrinsic band-gap absorption of pure anatase TiO_2. A distinct red shift in absorption edge is observed as we move from sample O1 to O3 which could be due to increase in rutile percentage in the samples. However, a huge difference in absorption wavelength is observed in comparison to Degussa, which explains perhaps the better photocatalytic activity of these samples.

The band-gap energies for these samples were calculated from the obtained λ_{max} values using eq. **3** and are found to vary over a narrow range of 3.11 to 3.16 eV, which are lower than that of Degussa (Table 31).

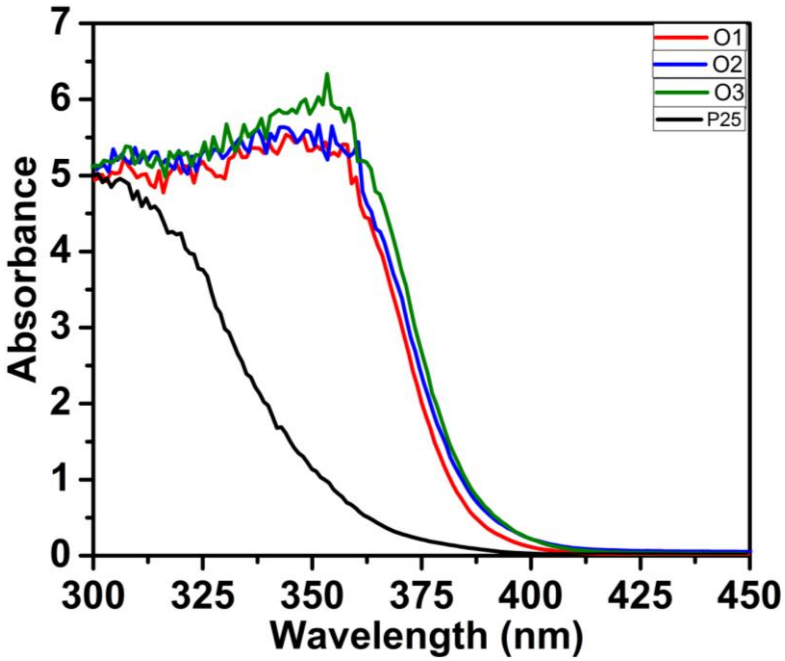

Fig. 30—*UV-DRS spectra of calcined samples*

Table 31 – Band-gap energies

Sample	Band-gap (eV)
O1	3.16
O2	3.13
O3	3.11
P25	3.35

BET analysis

The surface studies of the prepared catalysts are carried out by using BET analysis. Fig. 31 illustrates the nitrogen adsorption-desorption isotherms and corresponding pore size distribution curves (inset) of the synthesized TiO_2 photocatalysts. The isotherms of these samples exhibited type IV pattern typical of mesoporous materials. Slightly broader hysteresis loops, intermediate between H2- and H3-type are observed. The loops, closing at lower relative pressure and extending up to unity is indicative of the presence of mesoporosity and non-rigid structure of pores. Mesoporous nature is also seen from the broad pore size distribution of these samples ranging from 20-80 nm. In addition, the observed shift in hysteresis loops to the higher relative pressure region is also indicative of the capillary condensation associated with large pore channels [53]. The lower value of specific surface area and pore volume of sample O2 and O3 (Table 32) can be attributed to

the presence of a slight rutile phase in the samples and also due to the presence of some of the particles in hexagonal and/or rod shaped.

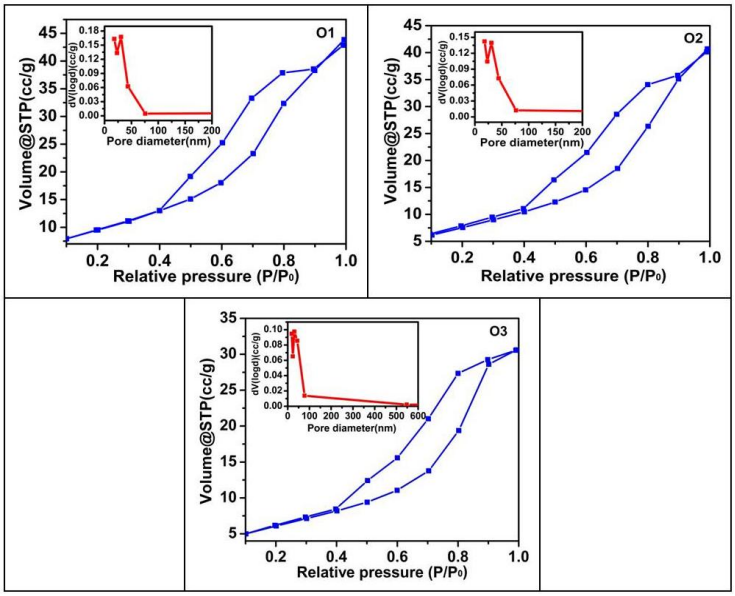

Fig. 31—*isotherm curves for TiO_2 nanoparticles O1, O2 and O3 and corresponding pore size distribution curves (inset)*

Table 32 – Surface properties

Sample	BJH surface area (m^2/g)	Pore volume (cc/g)
O1	50.0	0.073
O2	44.5	0.068
O3	33.3	0.051
P25	56.0	0.250

SEM analysis

The SEM micrograph of TiO_2 nanoparticles are displayed in Fig. 32a.

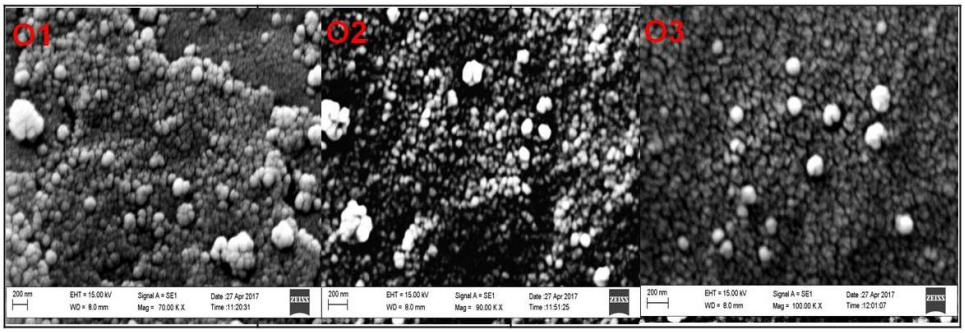

Fig. 32a—*SEM images of TiO_2 nanoparticles O1, O2 and O3*

Well-defined densely packed tiny nanoparticles of spherical shapes are observed from the SEM pictures for all the three samples. Slight agglomeration is observed for samples O2 and

O3 which may be due to the lower calcination temperature. Comparatively higher degree of agglomeration is seen for the sample O1, which differentiate it from the other two samples. This difference is reflected in the photocatalytic activity and other characteristic properties of these samples.

TEM analysis

Representative TEM images are shown in Fig. 32b. The spherical shape of particles is confirmed from the TEM micrographs. In addition to the spherical particles a few hexagonal and rod shaped particles are seen in O2 and O3 samples, respectively (Fig. 32b inset, left corner bottom), which contain slight rutile phase. The spherical particles could be due the anatase phase and the hexagonal and rod shaped could be of rutile phase as observed by Liu *et al.* [89]. Slight agglomeration among the particles is also observed here. The average particle size was estimated to be about 8-11 nm (Table 33).

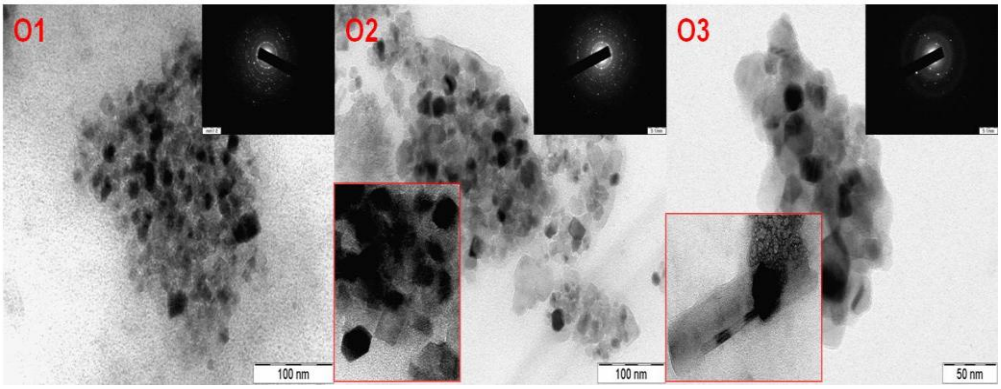

Fig. 32b— *TEM images of TiO_2 nanoparticles O1, O2 and O3 with corresponding SAED images (inset right corner top) and magnified images for samples O2 and O3 (inset left corner bottom).*

Table 33 – Particle sizes

Sample	Particle size (nm)
O1	11.4
O2	10.3
O3	8.6
P25	21.0

The SAED patterns are shown in the inset of Fig. 32b (right corner top). A set of diffraction rings is observed in SAED pattern indicating the polycrystalline nature of the catalysts prepared. The ring patterns could be indexed to anatase phase TiO_2, which is in accordance with the peaks obtained in the XRD pattern with highest intensity peak (101). The slight

rutile phase is not reflected in SAED pattern. The hexagonal and rod shape of some of the particles could be the result of availability of water molecules for the hydrolysis.

IR studies

The prepared catalysts were studied by FTIR analysis. The IR spectra of all the calcined samples are shown below (Fig. 33). Broad band at 3500-3000 cm^{-1} (-OH stretching) and at ~1630 cm^{-1} (-OH banding) were seen for the surface hydroxyl and/or the adsorbed water. Strong band seen at 800-450 cm^{-1} was assigned for Ti-O stretching.

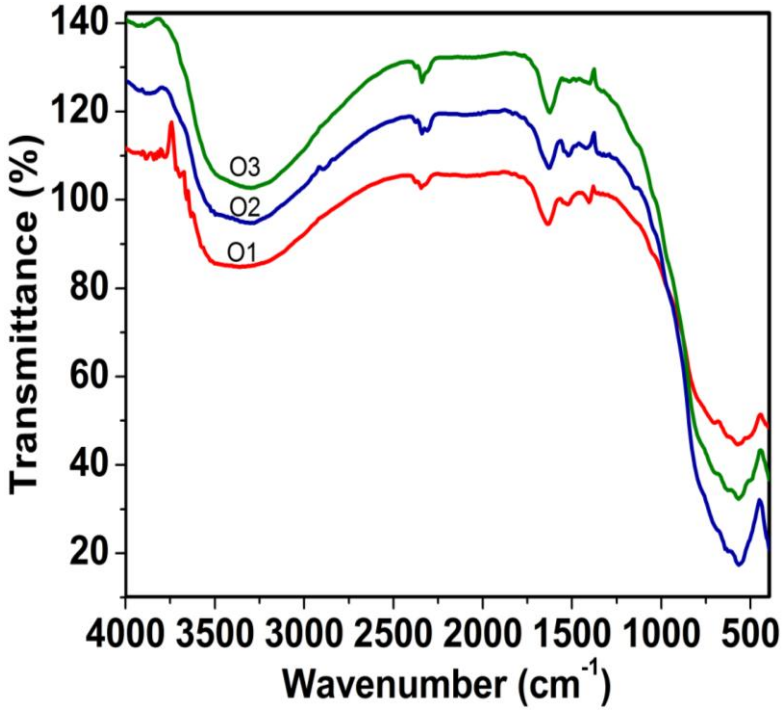

Fig. 33—*IR spectra of calcined samples*

Photocatalytic activity testing

To evaluate the photocatalytic activity of the prepared TiO_2 nanoparticles, the activity of these samples was compared with that of the commercial TiO_2 catalyst for the photo-degradation of methylene blue under direct sunlight. Blank experiments were carried out to show that the photo-degradation reaction did not proceed effectively without the presence of a catalyst. The intensity of degraded dye is measured by using a colorimeter.

It is found that all three samples show better photocatalytic activity in comparison to commercial Degussa P25 (Fig. 34a). Further, the results indicate that the samples having anatase-rutile mixture (O2 and O3) shows better photo-activity than the sample with pure anatase phase (O1). Amongst the catalyst prepared, sample O3 shows the best activity. The obtained results are in accordance with the higher shift in absorption wavelength and smaller

size of these samples. Moreover, the improved photocatalytic activity of the samples O2 and O3 suggest that there is better utilization of the direct sunlight by catalyst having a slight rutile phase.

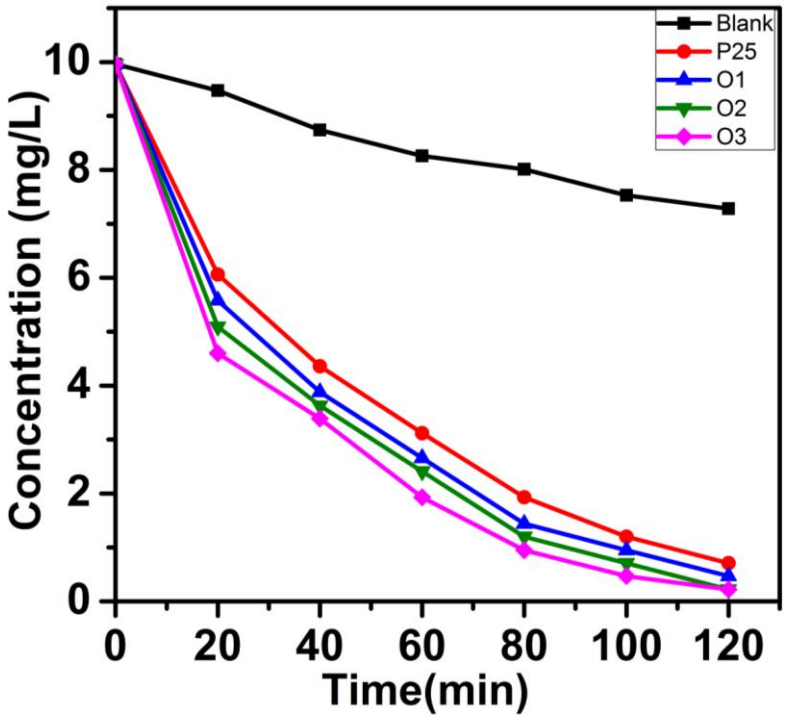

Fig. 34a—*Sunlight degradation plots for methylene blue*

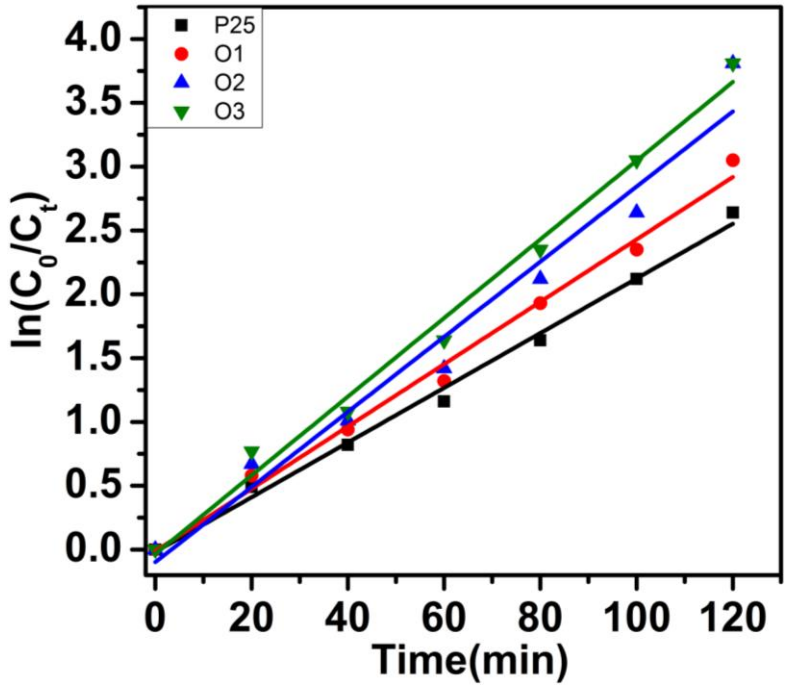

Fig. 34b—*Kinetic studies for MB degradation*

Further the kinetics of the dye degradation was studied to determine the rate of degradation. A plot of ln (C_0/C_t) versus time (Fig. 34b) represents a straight line which indicates the

photocatalytic degradation follows a pseudo first order kinetics. Linear relationships for all the photocatalysts is seen from which it can be observed that the apparent reaction rate constant is highest for sample O3. The rate constant k for all three samples is defined by ln (C_0/C_t) = kt and is given in Table 34, which is in accordance with the other results. Recyclability studies for these samples were carried out for three cycles, after separating the catalysts by centrifugation. The results were compared with Degussa and are displayed in Fig. 34c. All the prepared samples could be reused for degradation with negligible loss in activity.

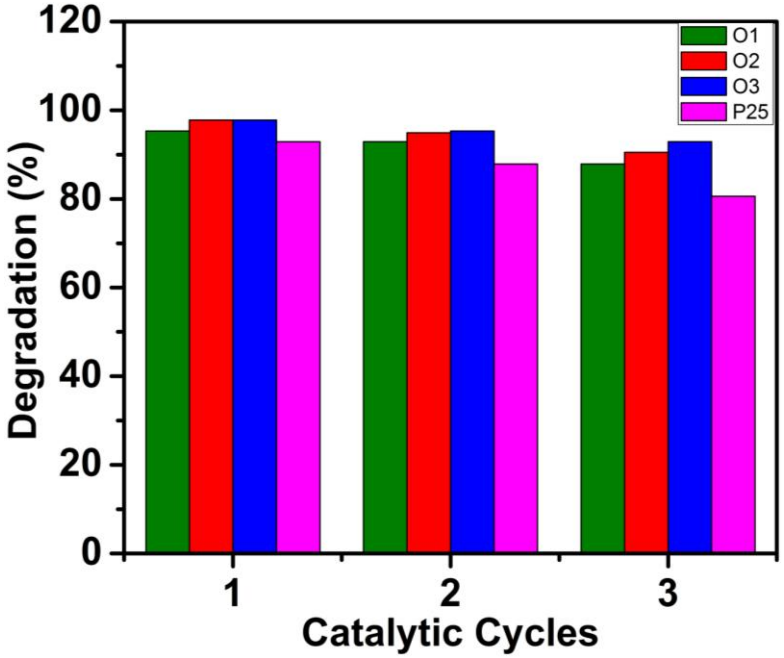

Fig. 34c—*Recyclability studies*

Table 34 – Kinetic studies

Sample	Rate constant k (min^{-1})
O1	0.0244
O2	0.0294
O3	0.0308
P25	0.0214

Summary and Conclusion

In summary, a simple method to develop TiO_2 nanoparticles *via* a non-aqueous sol-gel route by controlled release of water is reported. Anatase or mixed anatase-rutile phase can be controlled by varying the amount of release of water in the imination process. The excess used amine, aniline and the *in-situ* formed corresponding Schiff base acts as directing agents to control the size and shape of the particulates. The photo-degradation results indicate that all the catalyst prepared by the present non-aqueous route shows better activity compared to

the commercial Degussa P25 catalyst. Among the catalyst synthesized, the one obtained *via* the least amount of water released during the imination reaction had the best photocatalytic activity and had mixed anatase-rutile phase. The properties of the catalysts are summarized in Table 35.

Table 35 – Summary of the properties of TiO_2 nanoparticles.

Sample	**Particle size (nm)**	**BJH surface area (m^2/g)**	**Pore vol. (cc/g)**	**λ_{max} (nm)**	**Rate const. k (min^{-1})**
O1	11.4	50.0	0.073	392	0.0244
O2	10.3	44.5	0.068	396	0.0294
O3	8.6	33.3	0.051	398	0.0308
P25	21.0	56.0	0.250	370	0.0214

LC-MS studies

In addition to delineate the photo-degradation pathway for methylene blue, tandem liquid chromatography mass spectrometry (LC-MS) study was used, as most of the reported degradation studies have postulated pathways without isolating any intermediates.

The chromatography experiments with LC-MS were carried out on LC-DGU-20ASR liquid chromatography (Shimadzu, Japan) using a binary solvent gradient pump and an automatic injector. The dye degradation products were separated by using VP-ODS column 150 X 2 mm packed with 4.6 µm particle size. The detection system was a UV detector set at 254 nm. The signal acquired from the detector was recorded using Labsolutions software. The mobile phase consisted of two solutions, namely, A and B. Solution A was made from 0.01 M ammonium acetate and acetic acid (pH 5.3), whereas solution B was acetonitrile. The gradient elution was from 10% to 90% in 32 min, the flow rate was 0.4 mL/min and the injector volume was 2 µL. The gradient HPLC separation was coupled with a single quad mass spectrometer (Shimadzu LC-MS-2020). The mass spectrometer was equipped with an electrospray ionization source and operated in positive and negative polarity. The ESI conditions were as follows at corona needle at 4.5 kV, the nebulizer pressure was 1.5 L/min, drying gas flow was 15 L/ min and drying temperature was 400 °C. The mass range was from 100-500 m/z.

3.3 Analysis and identification of photo-degradation products using LC-MS

The aliquots were subjected to LC-MS analysis after every 20 min. Initially, the MB solution (Fig. 35a) displayed two peaks at retention time (rt) 7.954 (M+ = 270, self degradation) and 8.214 (M+ = 284, molecular ion). With time, the peak due to MB decreased in intensity and after complete decolorization of the solution, no peak was observed both in HPLC and mass (positive and negative mode) when 4 µL of the sample was injected. These results are in agreement with most of the literature reports; where in complete mineralization of the dye is suggested. To get more insight into the degradation process, 50 mL of photo-degraded (after 120 min of degradation) MB solution was filtered and concentrated to 1 mL. Then, 40 µL of this was injected on LC-MS and analyzed by both positive and negative modes. HPLC indicated one major peak at retention time 19.431 min (Fig. 35b) which corresponds only in negative mode at m/z = 288.05 (M-1) in the MS (Fig. 35c).

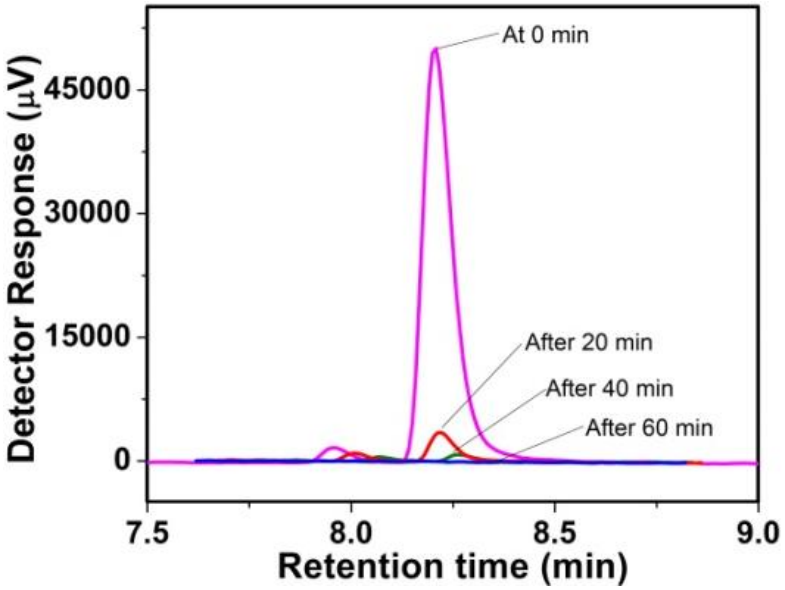

Fig. 35a—*LC data during photo-degradation of methylene blue*

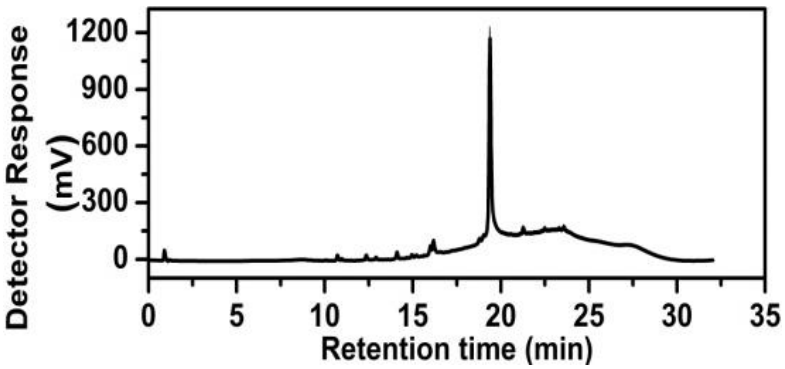

Fig. 35b—*LC data of photo-degraded methylene blue*

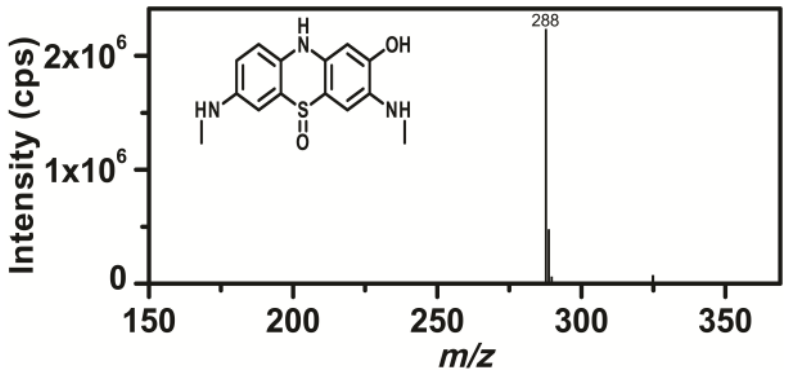

Fig. 35c—*M-1 peak of probable intermediate in MS*

The other significant ions observed in positive mode being at m/z 272, 279, 281, 320, 321, 322, 350 and 362, while those in negative mode are at m/z 119, 198.75, 199.85, 265, 288, and 343. The probable structures of some of these ions are given in Fig. 35d. The self degradation product seen at retention time 7.954 (M+ = 270) might be due to the N-demethylation of the dye due to aerial oxidation process. However, during the photochemical

degradation studies, the intensity of this peak neither increased nor decreased corresponding to continuous decrease in intensity of MB peak (retention time 8.214 min, Fig. 35a). This suggests that the N-demethylation route does not form the major degradation pathway.

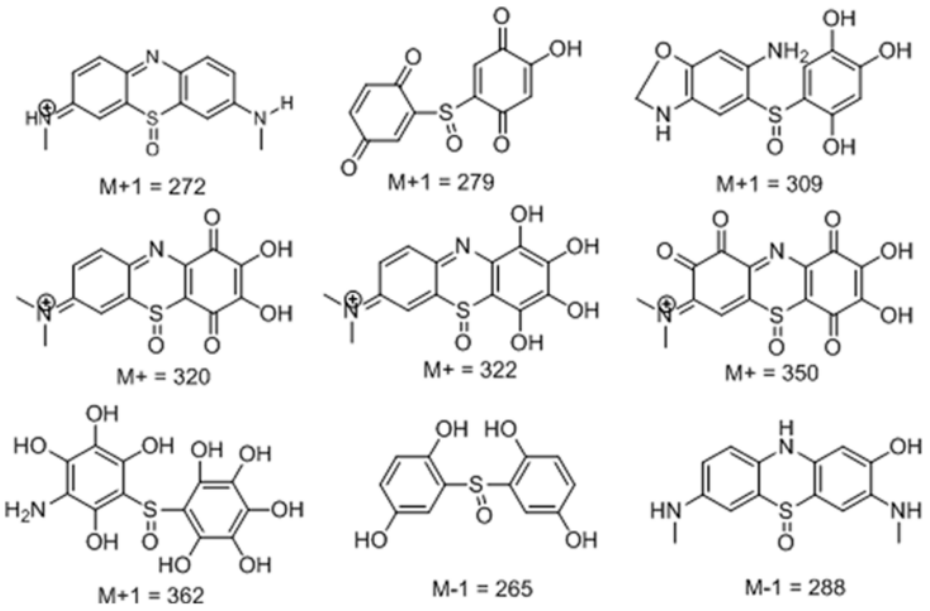

Fig. 35d - *Probable degradation intermediates of methylene blue displayed in MS*

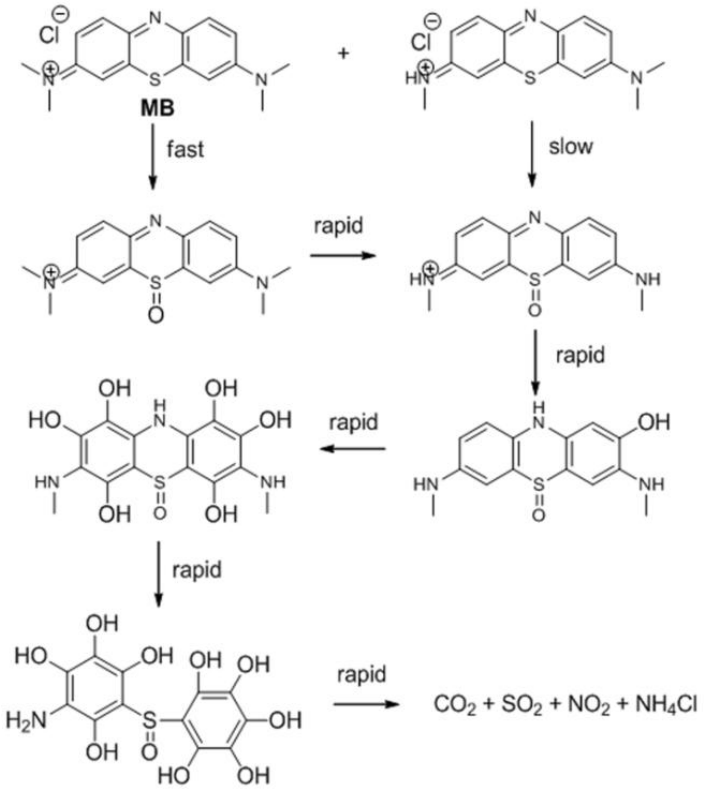

Scheme 12 - *Probable photo-mineralisation route of MB*

The detection of only one intense peak at retention time 19.4 min corresponding to M-1 = 288 in the degraded sample solution suggests that the major route (Scheme 12) may have

traversed initially through the oxidation of sulfur to sulfone followed by N-demethylation, hydroxylation, and ultimately to complete demineralization.

The probable course of photo-degradation of MB is depicted in Fig. 36. The MB molecules adsorbed on the surface of TiO_2 absorb a photon from the visible light. The photon energy is passed to TiO_2 wherein the surface h (hole) reacts with water to produce H^+ and ·OH. While the released electrons react with O2 to form $O2^{\cdot -}$. The $O2^{\cdot -}$ ion combines with H^+ to form H_2O_2, which oxidizes sulfur to sulfone. The fact that sunlight or TiO_2 alone under the experimental conditions do not decolorize the MB solution, suggest that the first adsorption of MB on TiO_2 followed by photon absorption takes place. The absence of the leuco MB in LC-MS studies confirm that the decolorization takes place due to oxidative degradation of MB. It is interesting to note here is that this is a first report on identifying degradation intermediate by LC-MS of reaction mixture containing MB.

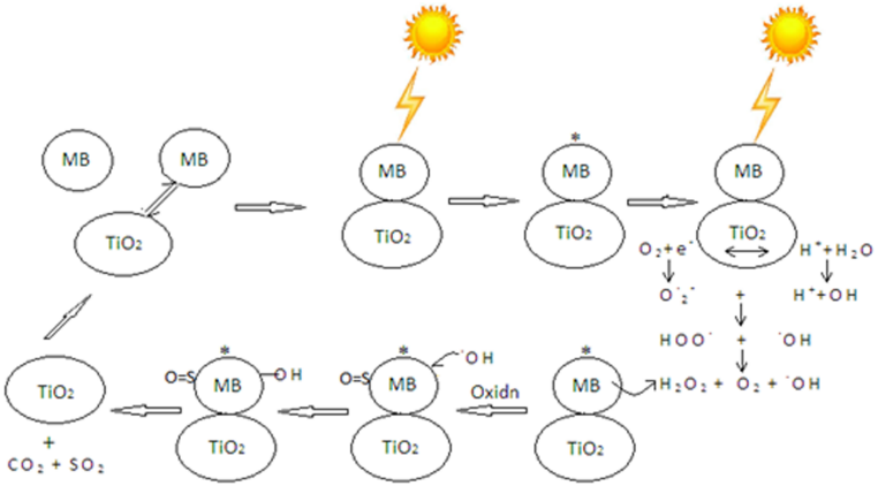

Fig. 36 - *Probable route for MB photo-degradation.*

To conclude with, the LC-MS studies of the photocatalytic degradation of MB suggest that, along with demethyation, oxidation of sulfur, ring hydroxylation and hydrolysis of the iminium ion takes place. Furthermore, a new intermediate is detected for the first time during these studies.

References

1. X. Chen, S.S. Mao, Titanium Dioxide Nanomaterials: Synthesis, Properties, Modifications, and Applications, Chem. Rev. 107 (2007) 2891-2959.
2. M.R. Hoffmann, S.T. Martin, W. Choi, D.W. Bahnemann, Environmental Applications of Semiconductor Photocatalysis, Chem. Rev. 95 (1995) 69-96.
3. M.A. Fox, M.T. Dulay, Heterogeneous Photocatalysis, Chem. Rev. 93 (1993) 341-357.
4. Q.-J. Liu, Z. Ran, F.-S. Liu, Z.-T. Liu, Phase Transitions and Mechanical Stability of TiO_2 Polymorphs under High Pressure, J. Alloys Compd. 631 (2015) 192-201.
5. N.T. Nolan, M.K. Seery, S.C. Pillai, Spectroscopic Investigation of the Anatase-to-Rutile Transformation of Sol-Gel-Synthesized TiO_2 Photocatalysts, J. Phys. Chem. C 113 (2009) 16151-16157.
6. Y.-F. Chen, C.-Y. Lee, M.-Y. Yang, H.-T. Chiu, The Effect of Calcination Temperature on the Crystallinity of TiO_2 Nanopowders, J. Cryst. Growth 247 (2003) 363-370.
7. D. Nicholls, Complexes and First-Row Transition Elements, MacMillan Education, Hong Kong, 1974.
8. S.M. Gupta, M. Tripathi, A review of TiO_2 nanoparticles, Chinese Sci. Bull. 56 (2011) 1639-1657.
9. X.-Q. Gong, A. Selloni, First-Principles Study of the Structures and Energetics of Stoichiometric Brookite TiO_2 Surfaces, Phys. Rev. B 76 (2007) 235307:1-11.
10. B.J. Morgan, G.W. Watson, Intrinsic n-type Defect Formation in TiO_2: A Comparison of Rutile and Anatase from GGA+U Calculations, J. Phys. Chem. C 114 (2010) 2321–2328.
11. M. Landmann, E. Rauls, W.G. Schmidt, The Electronic Structure and Optical Response of Rutile, Anatase and Brookite TiO_2, J. Phys. Condens. Matter. 24 (2012) 195503:1-6.
12. A. Fujishima, K. Honda, Electrochemical Photolysis of Water at a Semiconductor Electrode, Nature, 238 (1972) 37-38.
13. S.N. Frank, A.J. Bard, Heterogeneous Photocatalytic Oxidation of Cyanide Ion in Aqueous Solutions at Titanium Dioxide Powder, J. Am. Chem. Soc. 99 (1977) 303-304.
14. S.N. Frank, A.J. Bard, Heterogeneous Photocatalytic Oxidation of Cyanide and Sulfite in Aqueous Solutions at Semiconductor Powders, J. Phys. Chem. 81 (1977) 1484-1488.
15. R. Wang, K. Hashimoto, A. Fujishima, M. Chikuni, E. Kojima, A. Kitamura, M. Shimohigoshi, T. Watanabe, Light-induced Amphiphilic Surfaces, Nature 388 (1997) 431-432.
16. B. O'Regan, M. Grätzel, A Low-Cost, High-Efficiency Solar Cell Based On Dye-Sensitized Colloidal TiO_2 Films, Nature 353 (1991) 737-740.

17. O. Carp, C. L. Huisman, A. Reller, Photoinduced Reactivity of Titanium Dioxide, Prog. Solid State Chem. 32 (2004) 33-177.
18. S. Banerjee, J. Gopal, P. Muraleedharan, A.K. Tyagi, B. Rai, Physics and Chemistry of Photocatalytic Titanium Dioxide: Visualization of Bactericidal Activity Using Atomic Force Microscopy, Curr. Sci. India 90 (2006) 1378-1383.
19. M.C. Xu, Y.K. Gao, E.M. Moreno, M. Kunst, M. Muhler, Y.M. Wang, H. Idriss, C. Woll, Photocatalytic Activity of Bulk TiO_2 Anatase and Rutile Single Crystals Using Infrared Absorption Spectroscopy, Phys. Rev. Lett. 106 (2011) 138302:1-4.
20. R.J. Tayade, R.G. Kulkarni, R.V. Jasra, Photocatalytic Degradation of Aqueous Nitrobenzene by Nanocrystalline TiO_2, Ind. Eng. Chem. Res. 45 (2006) 922-927.
21. Z. Xiong, H. Wu, L. Zhang, Y. Gu, X.S. Zhao, Synthesis of TiO_2 with Controllable Ratio of Anatase to Rutile, J. Mater. Chem. A 2 (2014) 9291-9297.
22. A.E. Danks, S.R. Hall, Z. Schnepp, The Evolution of 'Sol–Gel' Chemistry as a Technique for Materials Synthesis, Mater. Horiz. 3 (2016) 91-112.
23. P.D. Cozzoli, A. Kornowski, H. Weller, Low-Temperature Synthesis of Soluble and Processable Organic-Capped Anatase TiO_2 Nanorods, J. Am. Chem. Soc. 125 (2003) 14539-14548.
24. B.-P. Jiang, H.-B. Yin, T.-S. Jiang, J. Yan, Z. Fan, C.-S. Li, J. Wu, Y. Wada, Size-Controlled Synthesis of Anatase TiO_2 Nanoparticles by Carboxylic Acid Group-Containing Organics, Mater. Chem. Phys. 92 (2005) 595-599.
25. N. Mir, M. Salavati-Nissari, Photovoltaic Properties of Corresponding Dye Sensitized Solar Cells: Effect of Active Sites of Growth Controller on TiO_2 Nanostructures, Sol. Energy 86 (2012) 3397-3404.
26. N. Mir, M. Salavati-Nissari, Preparation of TiO_2 Nanoparticles by using Tripodal Tetraamine Ligands as Complexing Agent *via* Two-Step Sol–Gel Method and Their Application in Dye-Sensitized Solar Cells, Mater. Res. Bull. 48 (2013) 1660-1667.
27. N. Nakayama, T. Hayashi, Preparation of TiO_2 Nanoparticles Surface-Modified by Both Carboxylic Acid and Amine: Dispersibility and Stabilization in Organic Solvents, Colloids Surf., A 317 (2008) 543-550.
28. A.S. Attar, M.S. Ghamsari, F. Hajiemaeilbaigi, S. Mirdamadi, Modifier Ligands Effects on the Synthesized TiO_2 Nanocrystals, J. Mater Sci. 43 (2008) 1723-1729.
29. M.-A. Neouze, U. Schubert, Surface Modification and Functionalization of Metal and Metal Oxide Nanoparticles by Organic Ligands, Monatsh Chem. 139 (2008) 183-195.

30. U. Schubert, Chemical Modification of Titanium Alkoxides for Sol–Gel Processing, J. Mater. Chem. 15 (2005) 3701-3715.
31. Y. Liao, W. Que, Q. Jia, Y. He, J. Zhang, P. Zhong, Controllable Synthesis of Brookite/Anatase/Rutile TiO_2 Nanocomposites and Single-Crystalline Rutile Nanorods Array, J. Mater. Chem. 22 (2012) 7937-7944.
32. M. Pelaez, N.T. Nolan, S.C. Pillai, M.K. Seery, P. Falaras, A.G. Kontos, P.S.M. Dunlop, J.W.J. Jeremy, J.A. Byrne, K. O'Shea, M.H. Entezari, D.D. Dionysiou, A Review on the Visible Light Active Titanium Dioxide Photocatalysts for Environmental Applications, Appl. Catal., B 125 (2012) 331-349.
33. P. Yang, D. Zhao, D.I. Margolese, B.F. Chmelka, G.D. Stucky, Generalized Syntheses of Large-Pore Mesoporous Metal Oxides with Semicrystalline Frameworks, Nature 396 (1998) 152-155.
34. L. Robben, A.A. Ismail, S.J. Lohmeier, A. Feldhoff, D.W. Bahnemann, J. Buhl, Facile Synthesis of Highly Ordered Mesoporous and Well Crystalline TiO_2: Impact of Different Gas Atmosphere and Calcination Temperatures on Structural Properties, Chem. Mater. 24 (2012) 1268-1275.
35. D.M. Antonelli, J.Y. Ying, Synthesis of Hexagonally Packed Mesoporous TiO_2, by a Modified Sol-Gel Method, Angew. Chem. Int. Ed. Engl. 34 (1995) 2014-2017.
36. C.M. Liu, H. Sun, S.H. Yang, From Nanorods to Atomically Thin Wires of Anatase TiO_2: Nonhydrolytic Synthesis and Characterization, Chem. Eur. J. 16 (2010) 4381-4393.
37. Q.Y. Qu, H.W. Geng, R.C. Peng, Q. Cui, X.H. Gu, F.Q. Li, Chemically Binding Carboxylic Acids onto TiO_2 Nanoparticles with Adjustable Coverage by Solvothermal Strategy, Langmuir 26 (2010) 9539-9546.
38. T.J. Boyle, T.M. Alam, C.J. Tafoya, B.L. Scott, Formic Acid Modified $Ti(OCHMe_2)_4$. Syntheses, Characterization and X-ray Structures of $Ti_4(\mu_4\text{-}O)(\mu\text{-}O)(OFc)_2(\mu\text{-}OR)_4(OR)_6$ and $Ti_6(\mu_3\text{-}O)_6(OFc)_6(OR)_6$ (OFc) O_2CH; OR) $OCHMe_2$), Inorg. Chem. 37 (1998) 5588-5594.
39. J. Liu, T. An, G. Li, N. Bao, G. Shreng, J. Fu, Preparation and Characterization of Highly Active Mesoporous TiO_2 Photocatalysts by Hydrothermal Synthesis Under Weak Acid Conditions, Microporous Mesoporous Mater. 124 (2009) 197-203.
40. P.A. Venz, J.T. Kloprrogge, R.L. Frost, Chemically Modified Titania Hydrolysates: Physical Properties, Langmuir 16 (2000) 4962-4968.

41. R. Campostrini, M. Ischia, L. Palmisano, Pyrolysis Study of Sol–Gel Derived TiO_2 Powders Part III. TiO_2-Anatase Prepared by Reacting Titanium (IV) Isopropoxide with Acetic Acid, J. Therm. Anal. Calorim. 75 (2004) 13-24.
42. M. Ischia, R. Campostrini, L. Lutterotti, Synthesis, Characterization and Photocatalytic Activity of TiO_2 Powders Prepared Under Different Gelling and Pressure Conditions, Sol-Gel Sci. Technol. 33 (2005) 201-213.
43. O. Muniz-Serrato, J. Serrato-Rodriguez, Nanostructuring Anatase Through the Addition of Acetic Acid by the Sol–Gel Low Temperature Aqueous Processing, Ceram. Int. 40 (2014) 8631-8635.
44. R. Parra, M.S. Castro, E. Longo, P.R. Bueno, J.A. Varela, Reaction Pathway to the Synthesis of Anatase *via* the Chemical Modification of Titanium Isopropoxide with Acetic Acid, Chem. Mater. 20 (2008) 143-150.
45. B.H. Wu, G.Y. Guo, N.F. Zheng, Z.X. Xie, G.D. Stucky, Nonaqueous Production of Nanostructured Anatase with High-Energy Facets, J. Am. Chem. Soc. 130 (2008) 17563-17567.
46. B. Hao, Y. Li, S. Wang, Synthesis and Structural Characterization of Surface-Modified TiO_2, Adv. Mat. Res. 129-131 (2010) 154-158.
47. Y.-W. Jun, M.F. Casula, J.-H Sim, S.Y. Kim, Surfactant-Assisted Elimination of a High Energy Facet as a Means of Controlling the Shapes of TiO_2 Nanocrystals, J. Cheon, A.P. Alvisators, J. Am. Chem. Soc. 125 (2003) 15981-15985.
48. R.J. Wilkerson, T. Elder, O. Sowinski, J.I. Fostvedt, J.D. Hoefelmeyer, Phase Transfer of Oleic Acid Stabilized Rod-shaped Anatase TiO_2 Nanocrystals, Surf. Sci. 648 (2016) 333-338.
49. B. Mukherjee, C. Karthik, N. Ravishankar, Hybrid Sol-Gel Combustion Synthesis of Nanoporous Anatase, J. Phys. Chem. C 113 (2009) 18204-18211.
50. C.-T. Dinh, T.-D. Nguyen, F. Kleitz, T.-O. Do, Shape-Controlled Synthesis of Highly Crystalline Titania Nanocrystals, ACS Nano 3 (2009) 3737-3743.
51. K. Thamaphat, P. Limsuwan, B. Ngotawornchai, Phase Characterization of TiO_2 Powder by XRD and TEM, Kasetsart J. Nat. Sci. 42 (2008) 357-361.
52. K.J. Anthony Raj, B. Vishwanathan, Effect of Surface Area, Pore Volume and Particle Size of P25 Titania on the Phase Transformation of Anatase to Rutile, Indian J. Chem. 48A (2009) 1378-1382.
53. G. Leofanti, M. Padovan, G. Tozzola, B. Venturelli, Surface Area and Pore Texture of Catalysts, Catal. Today 41 (1998) 207-219.

54. P.V. Bakre, P.S. Volvoikar, A.A. Vernekar, S.G. Tilve, Influence of Acid Chain Length on the Properties of TiO_2 Prepared by Sol-Gel Method and LC-MS Studies of Methylene Blue Photodegradation, J. Colloid Interface Sci. 474 (2016) 58-67.
55. T.S. Natrajan, H.C. Bajaj, R.J. Tayade, Preferential Adsorption Behavior of Methylene Blue Dye onto Surface Hydroxyl Group Enriched TiO_2 Nanotube and its Photocatalytic Regeneration, J. Colloid Interface Sci. 433 (2014) 104-114.
56. M. Thommes, K. Kaneko, A.V. Neimark, J.P. Olivier, F.R.-Reinoso, J. Rouquerol, K.S.W. Sing Physisorption of Gases, with Special Reference to the Evaluation of Surface Area and Pore Size Distribution (IUPAC Technical Report), Pure Appl. Chem. 87 (2015) 1051-1069.
57. R. Campostrini, M. Ischia, L. Palmisano, Pyrolysis Study of Sol–Gel Derived TiO_2 Powders Part II. TiO_2-Anatase Prepared by Reacting Titanium (IV) Isopropoxide with Oxalic Acid, J. Therm. Anal. Calorim. 71 (2003) 1011-1022.
58. M. Kobayashi, K. Tomita, V. Petrykin, S. Yin, T. Sato, M.O. Yoshimura, M. Kakihana, Hydrothermal Synthesis of Nanosized Titania Photocatalysts Using Novel Water-soluble Titanium Complexes, Solid State Phenom. 124-126 (2007) 723-726.
59. P. Wang, K. Kobiro, Ultimately Simple One-pot Synthesis of Spherical Mesoporous TiO_2 Nanoparticles in Supercritical Methanol, Chem. Lett. 41 (2012) 264-266.
60. K. Tomita, M. Kobayashi, V. Petrykin, S. Yin, T. Sato, M. Yoshimura, M. Kakihana, Hydrothermal Synthesis of TiO_2 Nano-particles Using Novel Watersoluble Titanium Complexs, J. Mater. Sci. 43 (2008) 2217-2221.
61. J.A. Gonzalez-Calderon, J. Vallejo-Montesinos, J.M. Mata-Padilla, E. Pérez, A. Almendarez-Camarillo, Effective Method for the Synthesis of Pimelic Acid/TiO_2 Nanoparticles with a High Capacity to Nucleate β-Crystals in Isotactic Polypropylene Nanocomposites, J. Mater. Sci. 50 (2015) 7998-8006.
62. S.-J. Liu, X.-X. Wu, B. Wu, J.-Y. Gong, S.-H. Yu, Novel Anatase TiO_2 Boxes and Tree-like Structures Assembled by Hollow Tubes: D,L-Malic Acid-Assisted Hydrothermal Synthesis, Growth Mechanism, and Photocatalytic Properties, Cryst. Growth Des. 9 (2009) 1511-1518.
63. Y. Jiang, H. Yin, Y. Sun, H. Liu, L. Lei, K. Chen, Y. Wada, Effects of Organic Acids on the Size-Controlled Synthesis of Rutile TiO_2 Nanorods, Appl. Surf. Sci. 253 (2007) 9277-9282.
64. K. Kanie, T. Sugimoto, Shape Control of Anatase TiO_2 Nanoparticles by Amino Acids in a Gel-Sol System, Chem Commun (2004) 1584-1585.

65. K. Nagaveni, M. Hegde, N. Ravishankar, G.N. Subbanna, G. Madras, Synthesis and Structure of Nanocrystalline TiO_2 with Lower Band Gap Showing High Photocatalytic Activity, Langmuir 20 (2004) 2900-2907.
66. C.M. Wang, H. Wu, S.L. Chung, Optimization of Experimental Conditions Based on Taguchi Robust Design for the Preparation of Nano-Sized TiO_2 Particles by Solution Combustion Method, J. Porous Mater. 13 (2006) 307-314.
67. O. Durupthy, J. Bill, F. Aldinger, Bioinspired Synthesis of Crystalline TiO_2: Effect of Amino Acids on Nanoparticles Structure and Shape, Cryst. Growth Des. 7 (2007) 2696-2704.
68. T.V. Anuradha, S. Ranganathan, Nanocrystalline TiO_2 by Three Different Synthetic Approaches: A Comparison, Bull. Mater. Sci. 30 (2007) 263-269.
69. M. Kobayashi, V. Petrykin, K. Tomita, M. Kakihana, New Water-Soluble Complexes of Titanium with Amino Acids and their Application for Synthesis of TiO_2 Nanoparticles, J. Ceram. Soc. Jpn. 116 (2008) 578-583.
70. H. Jia, W.-J. Xiao, L. Zhang, Z. Zheng, H. Zhang, F. Deng, *In S**itu* L-Hydroxyproline Functionalization and Enhanced Photocatalytic Activity of TiO_2 Nanorods, J. Phys. Chem. C 112 (2008) 11379-11384.
71. Y. Hayami, Y. Suzuki, T. Sagawa, S. Yoshikawa, TiO_2 Rutile Nanorod Arrays Grown on FTO Substrate Using Amino Acid at a Low Temperature, J. Nano Sci. Nano technol. 10 (2010) 2284-2291.
72. A. Sedghi, S. Baghshahi, N.R. Nouri, M. Barkhordari, Synthesis of Titanium Oxide Nano Powder by a Novel Gel Combustion Method, Digest J. Nanomater. Biostruct. 6 (2011)1457-1462.
73. S. Ding, F. Huang, X. Mou, J. Wu, X. Lü, Mesoporous Hollow TiO_2 Microspheres with Enhanced Photoluminescence Prepared by a Smart Amino Acid Template, J. Mater. Chem. 21 (2011) 4888-4892.
74. Y. Tao, Y. Xu, J. Pan, H. Gu, C. Qin, P. Zhou, Glycine Assisted Synthesis of Flower-Like TiO_2 Hierarchical Spheres and its Application in Photocatalysis, Mater. Sci. Eng. B 177 (2012) 1664-1671.
75. A.D. Mani, B.R. Raju, N. Xanthopoulos, P. Ghosal, B. Sreedhar, C. Subrahmanyam, Effect of Fuels on Combustion Synthesis of TiO_2 – Towards Efficient Photocatalysts for Methylene Blue Oxidation and Cr (VI) Reduction Under Natural Sunlight, Chem. Eng. J. 228 (2013) 545-553.

76. M. Senna, N. Myers, A. Aimable, V. Laporte, C. Pulgarin, O. Baghriche, P. Bowen, Modification of Titania Nanoparticles for Photocatalytic Antibacterial Activity *via* a Colloidal Route with Glycine and Subsequent Annealing, J. Mater. Res. 28 (2013) 354-361.
77. Y. Chang, X. Liu, A. Cai, S. Xing, Z. Ma, Glycine-Assisted Synthesis of Mesoporous TiO_2 Nanostructures with Improved Photocatalytic Activity, Ceram. Int. 40 (2014) 14765-14768.
78. A.D. Roddick-Lanzilotta, A.J. McQuillan, An *in situ* Infrared Spectroscopic Study of Glutamic Acid and of Aspartic Acid Adsorbed on TiO_2: Implications for the Biocompatibility of Titanium, J. Colloid Interface Sci. 227 (2000) 48-54.
79. M. Schmidt, X-ray Photoelectron Spectroscopy Studies on Adsorption of Amino Acids from Aqueous Solutions onto Oxidised Titanium Surfaces, Arch. Orthop. Trauma Surg. 121 (2001) 403-410.
80. M. Schmidt, S.G. Steinmann, XPS Studies of Amino Acids Adsorbed on Titanium Dioxide Surfaces, Fresenius J. Anal. Chem. 341 (1991) 412-415.
81. R. Chu, J. Yan, S. Lian, Y. Wang, F. Yan, D. Chen, Shape-Controlled Synthesis of Nanocrystalline Titania at Low Temperature, Solid State Commun. 130 (2004) 789-792.
82. C. Yogambal, R.E. Vizhi, D.R. Babu, Effect of Cesium Chloride Addition on Crystal Growth, Structural, Thermal and Optical Properties of γ -Glycine Single Crystal, Cryst. Res. Technol. 50 (2015) 22-27.
83. R.W. Cheyne, T.A.D. Smith, L. Trembleau, A.C. Mclaughlin, Synthesis and Characterisation of Biologically Compatible TiO_2 Nanoparticles, Nanoscale Res. Lett. 6 (2011) 423:1-6.
84. E. Carla, M. Giacomelli, J. Avena, C.P. De Pauli, Aspartic Acid Adsorption onto TiO_2 Particles Surface Experimental Data and Model Calculations, Langmuir 11 (1996) 3483-3490.
85. E. Noori, N. Mir, M. Salavati-Niasari, T. Gholami, M. Masjedi-Arani, Shape Control of Nanostructured TiO_2 Using a Schiff Base Ligand *via* Sol–Gel Hydrothermal Method, J. Sol-Gel Sci. Technol. 69 (2014) 544-552.
86. N. Mir, M. Salavati-Niasari, Effect of Tertiary Amines on the Synthesis and Photovoltaic Properties of TiO_2 Nanoparticles in Dye Sensitized Solar Cells, Electrochim. Acta. 102 (2013) 274-281.

87. M. Masjedi, N. Mir, E. Noori, T. Gholami, M. Salavati-Niasari, Effect of Schiff Base Ligand on the Size and the Optical Properties of TiO_2 nanoparticles, Superlattices Microstruct. 62 (2013) 30-38.
88. T. Gholami, N. Mir, M. Masjedi-Arani, E. Noori, M. Salavati-Niasari, Investigating the Role of a Schiff-base Ligand in the Characteristics of TiO_2 Nano-particles: Particle Size, Optical Properties, and Photo-voltaic Performance of Dye-sensitised Solar Cells, Mater. Sci. Semicond. Process. 22 (2014) 101-108.
89. X. Liu, Y. Li, D. Deng, A One-Step Nonaqueous Sol–Gel Route to Mixed Phase TiO_2 with Enhanced Photocatalytic Degradation of Rhodamine B under Visible Light, CrystEngComm 18 (2016) 1964-1975.

Chapter 3 – Synthesis of Modified TiO_2

3.1. Introduction

Titanium dioxide because of its wide applications and excellent chemical and physical properties is prominently researched semiconductor material all over the world. It is potentially best suited for tapping direct sunlight because of its stability in water and non-toxic nature. It can be used for environmental cleansing by utilizing direct sunlight to destroy toxic chemicals. This can be done by using the process of photochemical oxidation. To become an ideal catalyst for photochemical oxidation, the catalytic material has to utilize a maximum percentage of direct sunlight by absorbing it. However, TiO_2 because of its wide band-gap of 3.2 eV is able to utilize only UV component of sunlight, which is about 4 %. Hence, to increase effectiveness of TiO_2 different strategies are adopted. For example, sensitization, wherein a visible light active dye is applied over a catalyst and then adsorbed light is harnessed. However the drawback of this strategy is that the most of the times the dye gets degraded.

The second approach is to increase the surface area so that more of the pollutant gets adsorbed on the surface of the catalyst, thereby it can be degraded faster. This can be achieved by decreasing the size of the catalyst in the nano range and increase the mesoporosity. In this context, we have used various organic acids as templates which are described in the first chapter. An alternate approach to this could be capping, which helps to decrease the size, prevent agglomeration and also functionalize the nano particle to have interaction with the pollutant to get more adsorbed.

The third approach could be of coupling, wherein TiO_2 can be coupled with other materials like graphene which have more surface area and hence more absorbent power.

The fourth approach is to improve photo-response of the TiO_2 to visible range by band-gap engineering. This is achieved by modifying the catalyst surface by foreign elements, *i.e.* adding metal/s or non-metal/s during the synthesis of catalyst to get incorporated in it or adding it to the surface to modify the surface. This causes band-gap narrowing resulting in red shift in the absorption edge. Frequently, they may or may not get incorporated in the lattice structure of TiO_2.

A large number of metals and non-metals are used in doping. Non-metal dopants are shown to possess the ability to improve the morphology of the material. In addition to improving the photo-response to visible light, the dopants have to be effective to improve the trapping of electrons and inhibit the electron-hole recombination.

The prime intention of non-metal doping is for band-gap narrowing. First non-metal used as a dopant for TiO_2 is nitrogen, introduced by S. Sato in 1986 [1]. However, N-TiO_2 systems gained much interest only in 2001, after Asahi, *et al*. reported $TiO_{2-x}N_x$ films for enhanced photocatalytic activity in extended visible region [2]. Since then N-TiO_2 system is extensively researched all over the world. This study was later followed by other non-metal doped TiO_2 such as carbon [3] sulfur [4, 5], boron [6, 7], phosphorus [8, 9], fluorine [10] and iodine [11]. Carbon is also extensively studied like nitrogen because of its considerable effect on narrowing band-gap.

In spite of several advantages, non-metal doping shows a major drawback of decreasing dopant concentration during annealing process, which results in the decreased photocatalytic activity of these materials [12].

Cation doping, which include rare earth metals, noble metals, poor (p- block) metals and transition metals have been investigated in past [13]. Nobel metals such as Pt, Ag, Au, Pd, Ru, have shown enhanced photocatalytic activity [14-19]. Transition metals studied include Cu, Co, Ni, Cr, Mn, Mo, Nb, V, Fe [18-22].

The metal dopants are mainly responsible for widening of the light absorption range; increase the redox potential of the photo-generated radicals and enhancing quantum efficiency by inhibiting photo-generated electron-hole recombination. Transition metal ions alter the bulk electronic structure of the semiconductor by the interaction of the dopant with the matrix lattice. It mainly introduces the new energy level below the conduction band in TiO_2. Thus, it is widely studied for tuning of electronic structure of oxide and hence shifting the light absorption region from UV to visible light. This shift is caused by the charge-transfer transition between the d-electrons of the transition metals and the valence band of TiO_2. It is due to their unique d-electronic configuration and spectral characteristics, transition metals have gained much interest as an effective dopant for TiO_2 [23-25].

The transition metal dopants are reported mainly to exist in their oxide clusters rather than metal atoms within the surface of Ti cation matrices, in contrast to non-metal dopants which exists as isolated atoms within the surface. It is due to the difference in crystal nucleation behavior between dopants and TiO_2 [26].

Another interesting use of TiO_2 and metal doped TiO_2 is their antimicrobial activity to inactivate a wide range of pathogenic microorganisms including bacteria, viruses, fungi and algae. TiO_2 is a possible alternative to disinfect pathogenic microorganisms because of its strong oxidizing power and also due to its long term chemical and physical stability and non-toxicity. The Cu-TiO_2 system is reported for anti-bacterial and anti-viral activity. It is found

to be a very effective disinfectant for gram-positive as well as gram-negative bacteria under visible light [27-31]. Silver ions are also well known antibacterial agents. Silver doped TiO_2 shows enhanced photocatalytic inactivation of bacteria and viruses [31-35].

Among all the above mentioned transition metal dopants, Fe is the most studied transition metals as a dopant for TiO_2 with its different ion forms, which can act as traps for electron-hole pairs, thus inhibiting their recombination. It also showed to prevent agglomeration of the particles and in some cases the reduction in band-gap up to 2.6 eV and hence found to be the best candidate for increasing photocatalytic activity [36-39].

Considerable effects are shown in improving the properties of TiO_2 by copper and nickel doping into this material. Comparative studies of copper and nickel doping reveal that Ni-TiO_2 display slightly better photocatalytic efficiency and also a higher shift in visible light absorption, than that of Cu-TiO_2 [19, 40], though Cu-TiO_2 individually exhibit higher photo-activity and better shift in wavelength than the undoped material. Moreover, according to DFT calculations, the Ni-TiO_2 system is said to possess narrow band-gap, while Cu-TiO_2 is said to have no change in band-gap when compared with pure TiO_2 [41].

Incorporation of transition metals is also studied for their induced magnetic properties into the host semiconductor system. Recently these materials have attracted wide research interest as dilute magnetic semiconductors (DMS), due to their promising applications in spintronics. Various transition metal ions doped TiO_2 systems are known to attain room temperature ferromagnetism (RTFM), which is one of the important aspect of spintronic research. TiO_2 based DMS materials and existence of RTFM was first reported by Matsumoto *et al*. for Co-doped TiO_2 system [42].

The intrinsic semiconducting property of TiO_2 is altered from n-type to p-type on introducing Cu and Ni into this semiconductor lattice. It is mainly attributed to the newly introduced vacancies by the dopants [43].

Optimum concentration of dopant metal ion plays a significant role in catalytic activity of the host metal oxide. A remarkable shift in absorption wavelength is observed for M-TiO_2 with low doping concentration, while recombination of photo-generated charge carriers is commonly observed at higher metal dopant concentrations [44-45]. The literature study demonstrates that, among the metal ion dopants of the first transition series, Cu, Mn, Fe, ions can trap both electrons and holes, thus avoiding their recombination and hence contributing for better activity, whereas Cr, Co, Ni, ions can trap only one type of charge carriers [46].

Although mono-metal doping show significant role in improving the catalytic activity of host material, single metal doping also has several drawbacks. Such systems are often known to

suffer from thermal instability and partial blockage of surface sites. Furthermore, the metal centers in these materials sometimes tend to become electron traps to encourage the recombination of photo-generated electron–hole pairs, mostly at higher doping concentration (more than 5 wt %) [23,47].

In order to overcome these drawbacks of singly doped TiO_2, further advancement in this field of co-doping with complementary dopants is studied and found to rewarding. Various combinations with metal-metal, metal-non-metal or of two non-metals are studied in the past. Such metal composites are more effective due to the synergistic effect of these two dopants which can lead to increased visible light absorption by narrowing band-gap and also acting as an electron-hole trapping sites, thus decreasing the rate of recombination. Nano composites of these systems are reported to effectively improve the charge separation; also recently tri-doping has gained momentum. Tri-doping systems can have different combinations of metals and non-metals [23, 31, 44].

Moreover, the hybrid/ hetero-structured systems are more advantageous due to their significant effect in promoting the separation of charge carriers through interface charge transfer pathway which in turn results in extended visible light response range by coupling of suitable electronic structures in comparison to single component doping [26, 48].

In the overview of the above discussion and after the systematic study of template mediated TiO_2 nanoparticles (in Chapter 2), we then thought of introducing foreign elements into pure TiO_2 and study its effect on the catalytic properties of this material. At first, the incorporation of non-metal was analyzed. We then elaborated our research to co-doping with two metals, which was followed by tri-doping system of two metals with non-metal. Among the commonly studied non-metals, nitrogen is proven to be the most effective one in narrowing the band-gap of TiO_2 nanoparticles, by extending the absorption band edge to visible region and thus is found in most of the hybrid structures as a non-metal component.

This chapter is divided into three sections. In the first section, we studied the effect of nitrogen doping in TiO_2, using different N-precursors, *viz*, urea, semicarbazide and *N,N'*-dimethyl urea by varying the synthetic route. The second section deals with the study of bimetal combination with TiO_2, Cu-Ni-TiO_2 system. Followed by this, the third section is about analyzing the combined effect of these two systems. This section discusses the tri-doped system of TiO_2, Cu-Ni-N-TiO_2. The detailed discussion is carried on in coming sections.

3.2. General experimental procedure

Materials

Titanium tetraisopropoxide (TIP) (purity, 97%), $Ti(OC_3H_7)_4$, urea, semicarbazide, *N, N'*-dimethyl urea, $Cu_2(CH_3COO)_4$, $Ni(CH_3COO)_2.4H_2O$, were purchased from Spectrochem, methylene blue (MB) from Merck and rhodamine B (RhB) from Loba Chemicals. Isopropyl alcohol (IPA), supplied by Loba Chemicals was used as a solvent medium.

Synthetic procedure

For series F - By using decomposition route

Two different methods were followed with slight variation, for synthesizing TiO_2 nanoparticles.

In the first procedure, titanium (IV) isopropoxide mixed with urea in 1:2 ratio was heated at 100 °C with constant stirring. The solid obtained was calcined at 500 °C for 3 h. A dark yellow colored TiO_2 powder is obtained.

In the second method, titanium (IV) isopropoxide was heated at 100 °C with constant stirring. To the solid obtained urea was added in a 1:2 ratio (TIP: urea) and mixed by grinding. The mixture was further calcined at 500 °C for 3 h. A dark yellow colored TiO_2 powder was obtained.

Both the procedures were repeated with semicarbazide and *N,N'*-dimethyl urea in place of urea, where light yellow and light brown to ash colored powders were respectively obtained. The colors obtained are shown in Fig. 1. The samples prepared are accordingly grouped in pairs and labeled as F1, F2; F3, F4 and F5, F6 (Table 1).

Table 1 – Sample labeling for Series F

Precursor used	Sample code
Urea (1)	F1
Urea (2)	F2
Semicarbazide (1)	F3
Semicarbazide (2)	F4
N,N'-dimethylurea (1)	F5
N,N'-dimethylurea (2)	F6

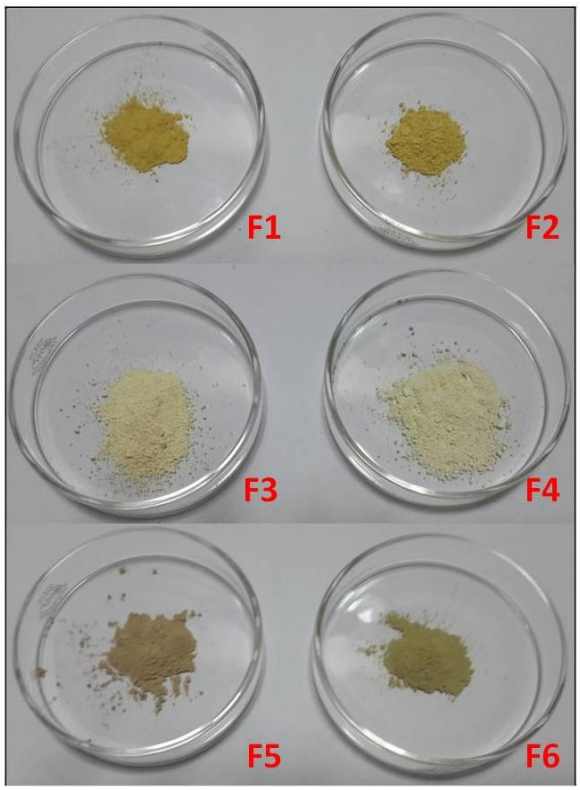

Fig. 1— *Colors obtained for samples F1- F6*

For series G and H

A set of photocatalysts - CuO-NiO co-doped TiO_2 were synthesized by using two different synthetic procedures. Anhydrous copper acetate [$Cu_2(CH_3COO)_4$] and nickel acetate tetrahydrate [$Ni(CH_3COO)_2.4H_2O$] were used as dopant metal precursor in 1:1 proportion. Further the Cu-Ni dopant concentration was varied from 0.01 to 5 wt %. The detailed procedure is described below.

a. By using non-aqueous sol-gel route (Series G)

In this method, a mixture of copper acetate and nickel acetate was dissolved in isopropyl alcohol by heating to 60 °C. This solution was then added drop wise to a solution of titanium isopropoxide in isopropyl alcohol with constant stirring. A colloidal gel with a greenish tinge was obtained. The intensity of the green color was found to deepen with increased metal concentration. The gel was heated to 100 °C to get a precursor powder which was then calcined at 500 °C for 3 h. TiO_2 nano powders with colors ranging from pale green to dark green were obtained (Fig. 2). These samples were coded as series G.

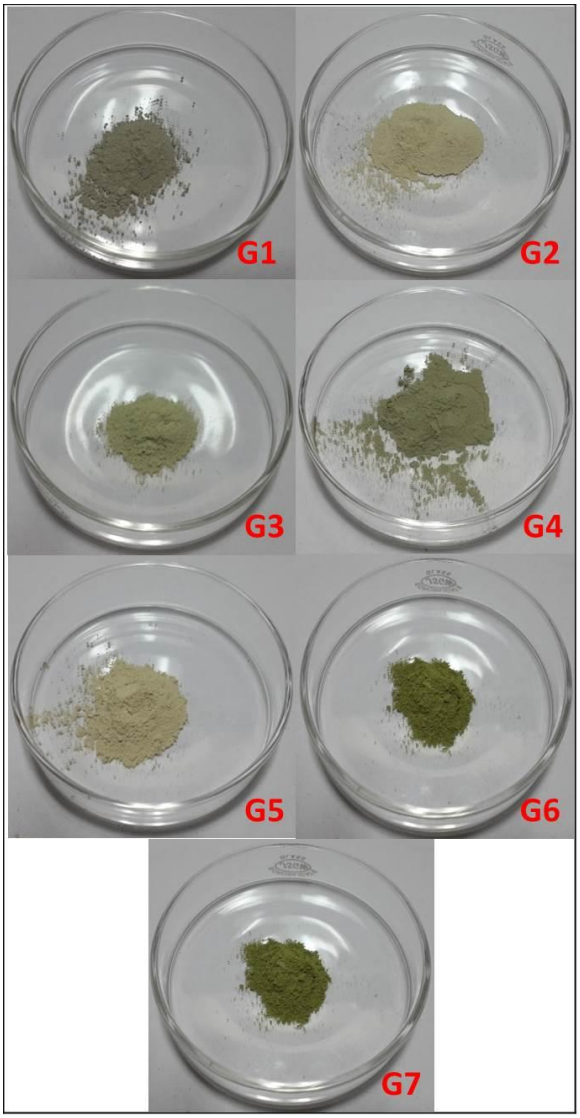

Fig. 2— *Colors obtained for samples G1-G7*

b. By using decomposition method (Series H)

In this procedure, titanium isopropoxide was first heated at 100 °C to an off-white powder. To this, a mixture of copper acetate and nickel acetate, dissolved in water was slowly added. The entire mixture was evaporated to dryness. The powdered precursor obtained was further calcined at 500 °C for 3 h, which resulted in off white to green colored TiO_2 nano powders (Fig. 3). The resultant samples were coded as series H.

A series of samples with varying (Cu + Ni) / Ti ratios, prepared by using both the methods separately, are coded accordingly as follows (Table 2).

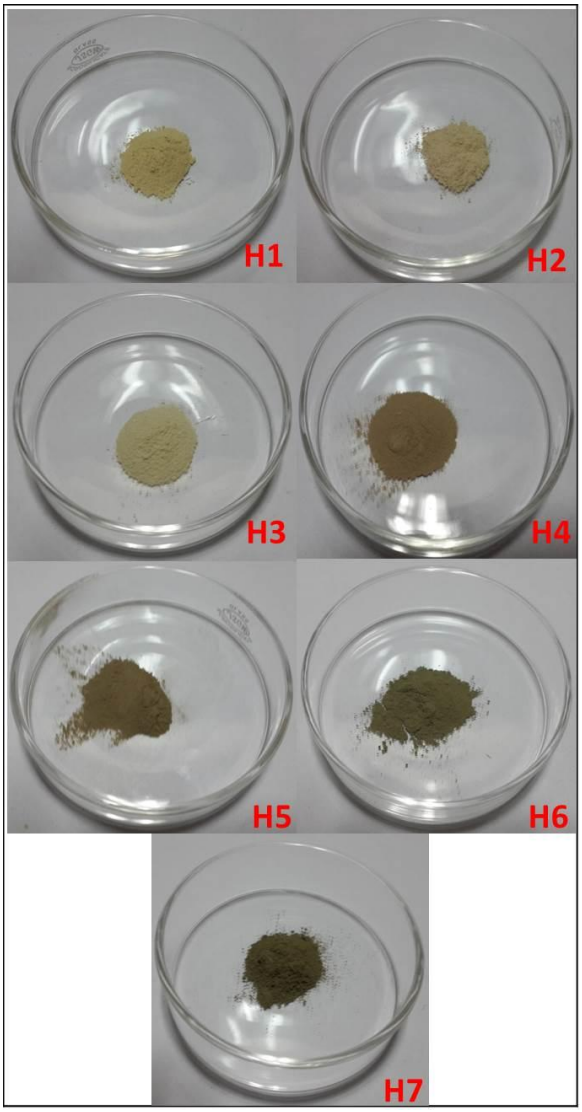

Fig. 3— *Colors obtained for samples H1- H7*

Table 2 – Sample labeling for Series G and H

(Cu + Ni)/Ti ratios (%)	Method 1	Method 2
0.01	G1	H1
0.05	G2	H2
0.10	G3	H3
0.50	G4	H4
1.00	G5	H5
2.00	G6	H6
5.00	G7	H7

For series I and J

A set of photocatalysts - CuO-NiO-N tri-doped TiO_2 were synthesized by employing two different synthetic procedures. Anhydrous copper acetate ($Cu_2(CH_3COO)_4$) and nickel

acetate tetrahydrate ($Ni(CH_3COO)_2.4H_2O$) were used as dopant metal precursors in 1:1 proportion and urea was used as nitrogen source. The Cu-Ni dopant concentration was varied from 0.01 to 5 wt %, while TIP: urea was maintained as 1:2 for entire experiment. The detailed procedure is as described below.

a. By using non-aqueous sol-gel route

In this method, a mixture copper acetate and nickel acetate was dissolved in isopropyl alcohol by heating to 60 °C. This solution was then added drop wise to a solution of titanium isopropoxide in isopropyl alcohol with constant stirring. To this mixture urea was added slowly, with constant stirring. The colloidal gel having a greenish tinge which becomes darker with increasing metal concentration was obtained. The gel was heated to 100 °C to get precursor powders with varying greenish shades, were calcined at 500 °C for 3 h. TiO_2 nano powders were obtained. The colors of the calcined powders were dark yellow in color for lower metal concentrations, which goes on fading while the appearance of green color becomes stronger at higher metal concentration (Fig. 4). These samples were coded as series I.

b. By using decomposition method

In this procedure, titanium isopropoxide was first heated at 100 °C to an off-white powder. To this, a mixture of copper acetate and nickel acetate, dissolved in water was slowly added. The entire mixture was evaporated to dryness, which resulted in off white to greenish colored powders depending upon the metal concentrations. The dried powder was then manually ground with urea in 1:2 proportions. This powder was further calcined at 500 °C for 3 h, which resulted in colored powders. For low metal concentration the color was yellow, while for high metal concentrations the color was green (Fig. 5). The resultant samples were coded as series H.

A series of samples with varying (Cu + Ni) / Ti ratios obtained by using both the methods separately are coded accordingly as shown below (Table 3).

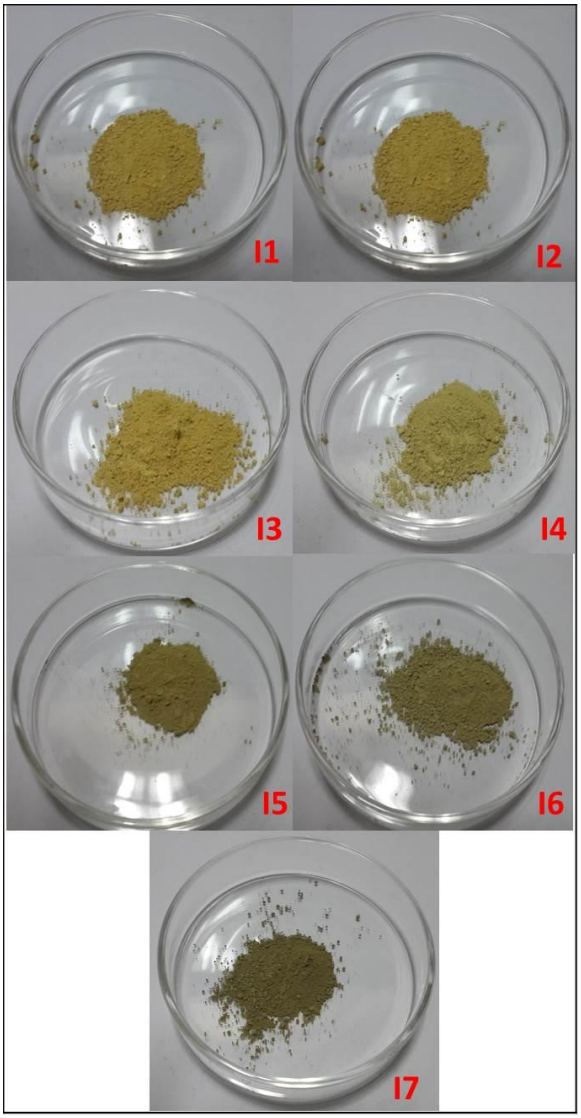

Fig. 4— *Colors obtained for samples I1- I7*

Table 3 – Sample labeling for Series I and J

(Cu + Ni)/Ti ratios (%)	Method 1	Method 2
0.01	I1	J1
0.05	I2	J2
0.1	I3	J3
0.5	I4	J4
1	I5	J5
2	I6	J6
5	I7	J7

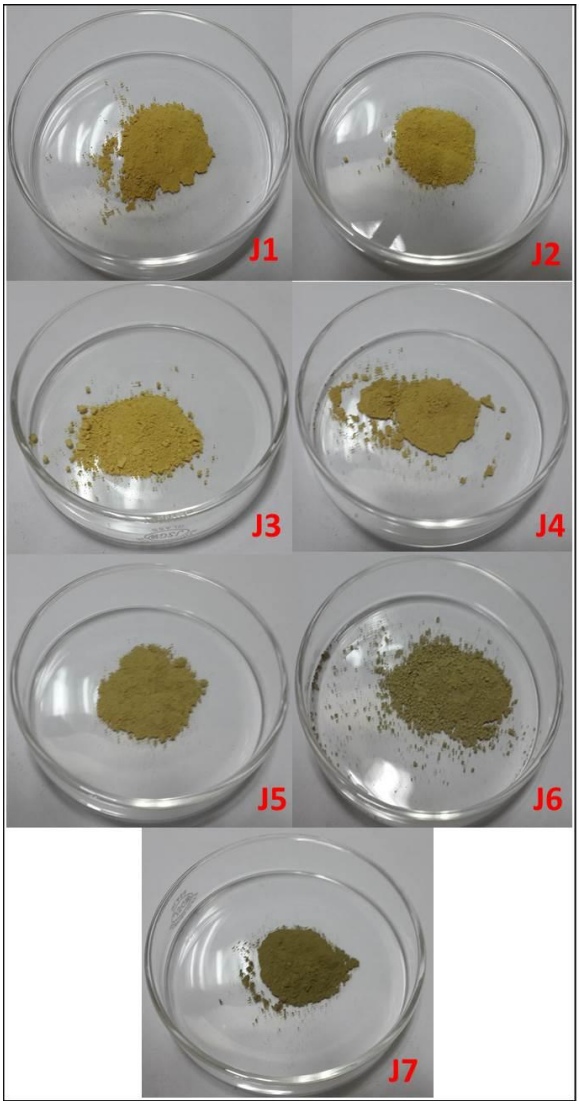

Fig. 5— *Colors obtained for samples J1- J7*

Characterization of TiO_2 nanoparticles

The crystal phase composition and crystallite size of TiO_2 nanoparticles were recorded using Bruker D8 ADVANCE X-ray diffractometer with Cu Kα radiation (1.5406 Å) in the 2θ scan range of 10-80°. The average crystallite size for the series of TiO_2 nanopowders were estimated according to the Scherrer's equation -

$$D = K\lambda / \beta \cos\theta \quad \text{- (eq. } \mathbf{1}\text{)}$$

Where, K is the Scherrer constant, λ is the X-ray wavelength, β is the peak width at half maximum and θ is the Bragg's diffraction angle.

Strain and number of dislocations are the influencing factors for the crystallite size of the sample. The broadening due to lattice strain in the material can be represented by the relationship

$$\varepsilon = \beta / 4 \tan\theta \quad \text{- (eq. } \mathbf{2}\text{)}$$

Where, ε is the strain in the material.

The percentage of anatase phase in the respective samples was calculated using the equation

$$\% A = 100 / (1 + 1.33 [I(R) / I(A)]) \quad \text{- (eq. 3)}$$

Where, I(A) and I(R) are the intensities of the major anatase (101) and rutile (110) peaks respectively.

Morphology of the sample was investigated by using Zeiss Avo18 scanning electron microscopy (SEM) along with Energy-dispersive X-ray Spectroscopy (EDX), which was further confirmed by transmission electron microscopy (TEM), which is also used to investigate the particle sizes of the sample. TEM images equipped with selected area electron diffraction (TEM/SAED) were obtained by using TECHNAI F30 and PHILIPS CM 200 field emission transmission electron microscope operating at 200 kV.

Nitrogen adsorption/desorption isotherms and surface area (S_{BET}) were obtained with a surface area and porosity analyzer (Micromeritics ASAP 2020 V3.00 H) and Quantachrome ASiQwin Instruments (ASIQC0100-4), at the temperature of liquid nitrogen. Before the analysis, samples were degassed at 150-300 °C for 0.5-12 h with continuous flow of nitrogen gas.

Band-gap energy, E_g and absorption edges of all the samples were determined using UV-Vis diffuse reflectance spectroscopy (UV-DRS) (Shimadzu UV-2450). $BaSO_4$ was used as background standard. Spectra were recorded at room temperature in the wavelength range of 200-800 nm. The minimum wavelength required to promote an electron depends upon the band-gap energy (E_g, eV) of the photocatalyst and can be estimated by determining the absorption wavelength (λ_{max}, nm) of each UV-Visible absorbance spectrum by the known relationship between the absorption band edge and the band-gap

$$E_g = 1239.8 / \lambda_{max} \quad \text{- (eq. 4)}$$

Where, E_g is the band-gap (eV) and λ (nm) is the wavelength of the absorption edges in the spectrum.

The IR studies were carried out on a Shimadzu IR Prestige-21 FTIR in the range of 4000-400 cm^{-1}.

Magnetic properties were studied as a function of applied field (M–H) using a vibrating sample magnetometer (VSM) on a Quantum Design-Versa Lab model.

Thin layer chromatography (TLC) was carried out on silica gel 60 F254 aluminium plates purchased from Merck.

^{1}H NMR (400 MHz) spectra were recorded on a Brucker AVANCE 400 instrument. Chemical shifts are expressed in δ relative to tetramethylsilane (TMS) which is expressed in ppm.

Photocatalytic activity testing

The photocatalytic activity was assessed by monitoring photo-decomposition of methylene blue and rhodamine B. Photo-decomposition of MB is a well known method for evaluating catalytic performance, commonly used over the world, and was first employed by Asahi *et al.* For comparison, commercial Degussa P25 was used as a reference material. These two dyes were selected due to their toxic effect when released in water from various industries.

In a typical degradation experiment, 10 mg of TiO_2 catalyst was suspended in 25 mL of the aqueous dye stock solutions (0.010 g/L – methylene blue and 0.020 g/L – rhodamine B), prepared in deionized water and were allowed to equilibrate for a given time (usually 15–30 min) in the dark before irradiation. The solution was then exposed to sunlight for the duration of 120 min between 10:00 am to 12:00 noon with intermittent swirling. Following the exposure of light at specified intervals of time, the decolorization of respective dyes was recorded at its absorption maximum (650 nm for MB and 450 nm for RhB), as a function of time against appropriate blanks.

The experiment was repeated for three times and the average of three readings was considered. The extent of photodegradation of dye was calculated using a calibrated relationship between the measured absorbance and concentration. The recyclability studies were also done for three cycles. The kinetic studies of the same were carried out from which the rate of dye degradation was determined.

Reduction of aromatic nitro compounds

The catalytic performance of the sample with highest Cu-Ni dopant (5 wt %) was tested for the reduction of *p*-nitrophenol to *p*-aminophenol in the presence of sodium borohydride as a reducing agent. In a typical catalytic test, 100 mg catalyst was first sonicated in 10 mL ethanol. To that, 100 mg of substrate (*p*-nitrophenol) was added, followed by 50 mg $NaBH_4$. The yellow color of *p*-nitrophenol was seen disappearing and changing to black. The progress of the reaction was monitored by TLC and the formation of *p*-aminophenol was confirmed by proton NMR spectroscopy. The catalytic activity was further tested for 3 consecutive cycles.

3.3. **Result and Discussion**

Section A – N-incorporated TiO_2

Introduction

This section deals with the study of the semiconductor material TiO_2, modified with the commonly employed non-metallic element nitrogen, using different N-precursors. Though TiO_2 is an effective photocatalyst for environmental remediation it has its limitation of poor utilization of visible light, owing to its wide band-gap, which is in abundance from direct sunlight. Nitrogen doping for TiO_2 has received wide attention due to its lowering of band-gap energies. Comparable atomic sizes, low ionization energy and stability make nitrogen most promising among the various non-metal doponants, though the position of nitrogen and nitrogen species in TiO_2 is still unclear. The nitrogen has been suggested to be present in the interstitial (between Ti-O-Ti bridges) and/or substitutional (replacing oxygen) positions. Several kinds of N species, including N_2, nitric monoxide (NO) and nitric dioxide (NO_2) are advocated.

Nitrogen doped TiO_2 because of its potential use in photocatalysis has attracted considerable interest. The synthesis of nitrogen doped materials is an important aspect taken into consideration by many researchers.

The effectivity of the catalyst for photo-degradation under visible light is assumed to dependent on the preparatory method used. Some of the preparative procedures reported in the literature include solution phase (sol-gel) method, mechanochemical, hydrothermal, pyrolysis, *etc.* It is well accepted that, sol-gel is a versatile method and commonly used for synthesizing doped TiO_2 nanomaterials. However, the use of simple decomposition method, because of its advantage of low cost, less time consuming and environment friendly, is also favored, though uncommon for such synthesis [49]. In addition to preparative method, the nitrogen source used is also considered to be an important factor which strongly affects the efficiency of the catalyst [50].

Various organic compounds as the nitrogen source are employed in the synthesis of N-doped titania include, urea, triethylamine, thiourea, hydrazine hydrate, guanidine derivative, *etc.* [51-52]. Doping with urea is claimed to produce an effective N-doped material [53-55]. However, with urea it is suggested that the melamine and its oligomerized products deposited on the surface are responsible for the photo-activity [56].

There are few reports available in literature with the use of decomposition method for synthesizing urea based N-TiO_2 material with discrete anatase and rutile phases showing

better photocatalytic activity [57-58]. Wormhole mesoporous TiO_2 is reported by combustion method with changing concentrations of urea to show high sunlight photocatalytic activity for the degradation of RhB [59].

However, no reports are available with the derivatives of urea such as, semicarbazide and *N,N'*-dimthyl urea. We have attempted for the first time the use of these two precursors as nitrogen source and compared the results with that of the well studied urea as nitrogen source.

The first section of this chapter discusses the results obtained by the synthesis of N-TiO_2 catalysts *via* the above mentioned N-precursors, using two different preparatory methods, for their effect on the catalytic properties. A typical schematic diagram for urea precursor is shown below (Scheme 1).

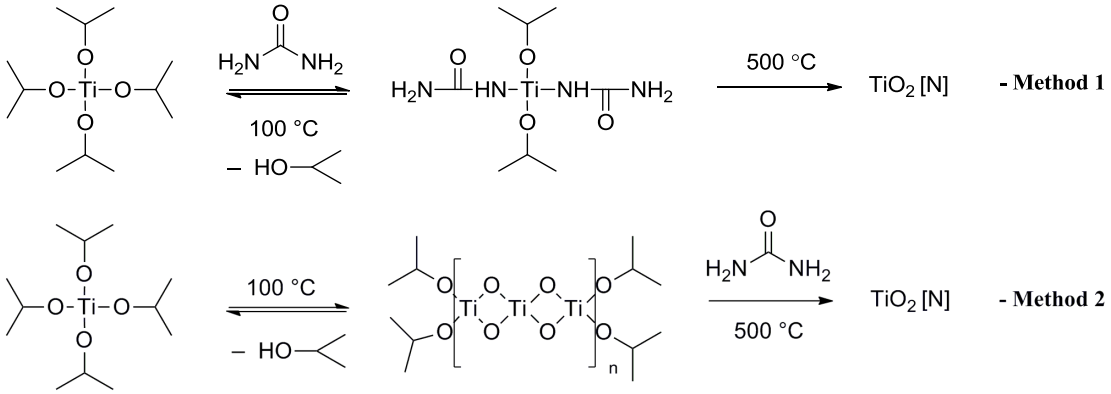

Scheme 1

In literature the N-TiO_2 samples are reported to be temperature sensitive and optimum temperature to synthesize crystalline material is 500 °C. The significant shift in absorption wavelength and improved photocatalytic activity is reported for the samples calcined at 500 °C, while high temperature treatment above 600 °C is claimed to result in reduced visible light absorption and poor photo-activity [60].

Considering the above observations, the calcination temperature for our experiments was selected as 500 °C, same as that of used for other experiments in previous chapter.

Surface, structural and optical properties

Powder X-ray studies

The phase composition and the crystallite size of the prepared TiO_2 samples were evaluated by X-ray powder diffraction analysis. Fig. 6a presents the XRD patterns of calcined TiO_2 powders. It shows sharp and well-defined peaks, indicating the crystallinity of the synthesized materials.

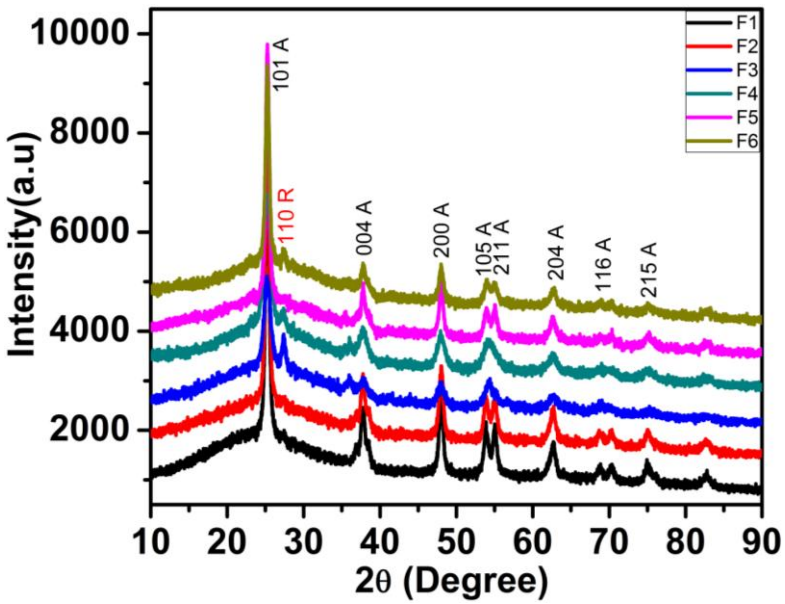

Fig. 6a—*XRD plots for samples calcined at 500 ºC*

From figure, it is clear that samples F1, F2 and F5 possess pure anatase phase, whereas for samples F3, F4 and F6 a slight presence of rutile phase is observed along with major anatase phase.

It is observed here that a slight rutile phase formation is shown by samples prepared from semicarbazide (F3 and F4) and *N,N'*-dimethyl urea (F6) (calcined at 500 °C), whereas urea gives only anatase phase.

In order to study the effect of these three precursors on the resultant phase formation and the intermediates involved, we heated separately urea, *N,N'*-dimethyl urea, and semicarbazide at 400 °C for 1 h. It was observed that, in case of urea, some whitish residue remained while in case of other two precursors no trace of any residue was seen. Further, the residue of urea was heated for 1 more h. still some residue remained. This suggested that, urea while decomposing forms intermediates like cynuric acid, ammelide, ammeline, *etc.*, which takes time to evaporate completely. Hence, in case of urea, because of its slow evaporation the resultant TiO_2 (anatase) formed do not get a chance to reorder to rutile phase. However, in case of *N,N'*-dimethyl urea and semicarbazide, no organic part remains as residue and hence one can see some rutile phase formation. In case of F5, being a bulk doping it takes more time for *N,N'*-dimethyl urea to evaporate, while in surface doping, sample F6, it evaporates faster and hence is the effect. Further the samples obtained at 500 °C are heated at 1000 °C for 1 h and XRD was recorded again, wherein it was found that all the samples were converted to rutile phase completely (Fig. 6b). Also, it was observed that EDX of these samples showed about 1 to 1.3 % nitrogen in samples with urea and semicarbazide, while it

was 0 % for sample obtained *via N,N'*-dimethyl urea (Table 4a). This suggests that nitrogen enters the lattice structure in the urea and semicarbazide samples while it is not in case of *N,N'*-dimethyl urea sample.

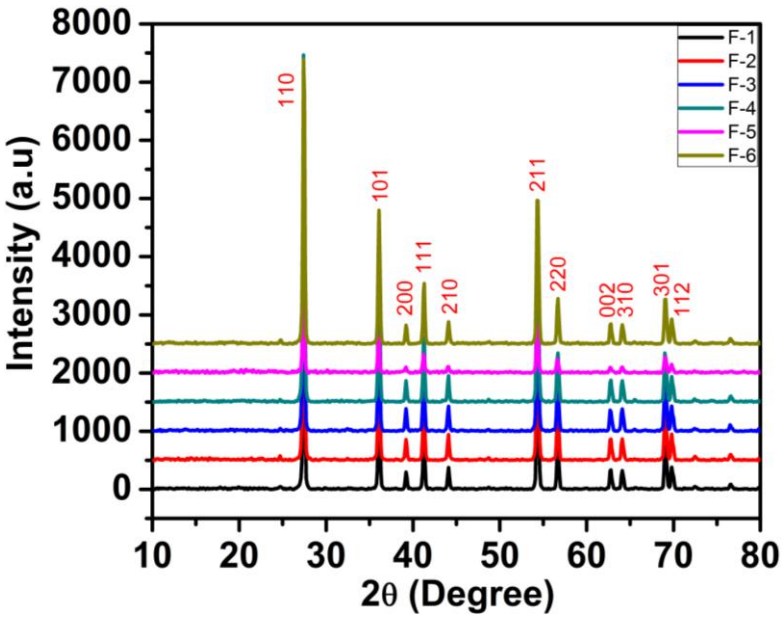

Fig. 6b—*XRD plots for samples calcined at 1000 ºC*

Table 4a – % N in samples calcined at 1000 °C

Sample	N content (wt %)
F1	1.3
F2	1.0
F3	1.3
F4	1.2
F5	0.0
F6	0.0

The literature reports says that, urea alters the condensation pathway, thereby extending the temperature at which rutile forms [61]. However the exact role of complexing agents or precursor material in phase transition and the ability to control TiO_2 polymorphs by a suitable preparation process is not fully understood, though the anatase-rutile ratio can be tuned to some extent by adjusting the factors such as synthetic method, precursor material or calcinations temperature [62].

The average crystallite sizes have been determined from (101) diffraction peak (the most predominant highest intensity peak), using Scherrer's formula (eq. **1**) and are found to be in the range of 6-12 nm (Table 4b). The synthesized samples were found to be smaller in size as compared to Degussa P25 (25 nm).

Relatively smaller values of crystallite sizes are observed for the samples F3, F4 and F6 (obtained with a slight rutile phase). Thus we can say that, for N-doped samples, the presence of slight rutile phase is responsible for reduced crystallite sizes. This is an interesting observation since normally the presence of rutile phase leads to increase in the crystallite size.

Table 4b – Crystallite sizes

Sample	Crystallite size (nm)
F1	11.9
F2	12.5
F3	7.8
F4	6.6
F5	10.9
F6	6.2
P25	25.0

UV-DRS studies

The absorption spectra of TiO_2 nanoparticles are shown in Fig. 7.

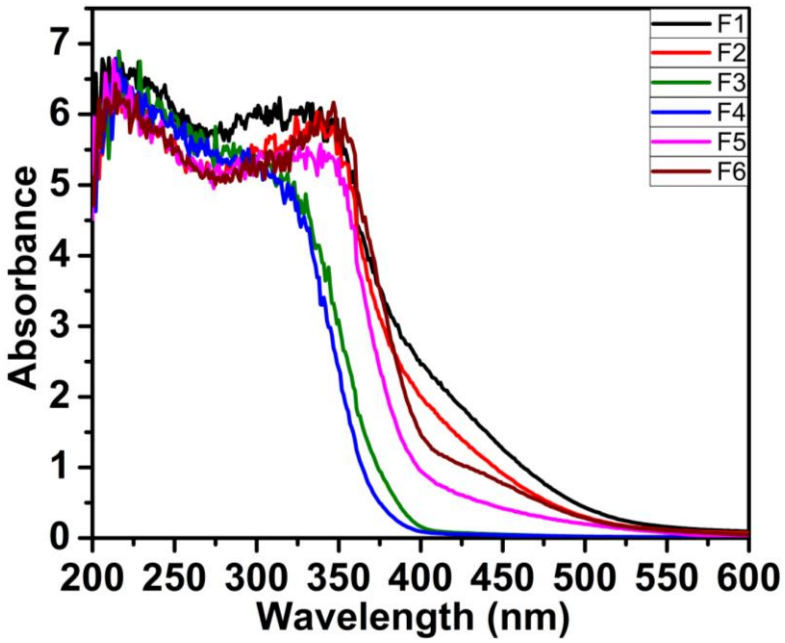

Fig. 7—*UV-DRS spectra of calcined samples*

DRS spectra of these samples show strong absorption in the region 390-400 nm, due to intrinsic properties of TiO_2.

In addition, samples F1, F2 and F5, F6 are observed to be remarkably red shifted. These observations are in accordance with the previous reports where urea was used as a nitrogen

source. The observed red shift in absorption edge can be attributed to the formation of the new electron state above the valence band by N- doping, which facilitates the promotion of electron to the conduction band and hence allowing visible light absorption or decrease in band-gap energy [63].

The samples F3 and F4, though having a pale yellow color exhibit slightly lower shift in absorption wavelength compared to other samples, probably because of smaller particle size and also a small amount of mixed rutile phase. Presence of rutile mixture in lower concentration (<15%) is reported in literature to exhibit an unexpected blue shift of absorption edge, and is attributed to band-filling mechanism, based on increasing n-type doping level by N-incorporation into TiO_2 lattice [64].

Further red shifts in anatase and blue shifts in rutile, as a significance of N-doping is explained based on a contraction of O-2p band in rutile upon doping due to lowering of top of the valence band. It is elucidated based on theoretical studies that, the nitrogen doping is expected to create localized impurity levels near or above valence band, which may result in a decrease in band-gap and hence allowing visible light absorption [65].

The band-gap energies (E_g) as calculated from λ_{max} values (eq. **4**) are found to be in the range 2.7 to 3.1 eV (Table 5).

Table 5 – Band-gap energies

Sample	Band-gap (eV)
F1	2.70
F2	2.88
F3	3.00
F4	3.14
F5	2.69
F6	2.79
P25	3.35

BET analysis

The typical plots of N_2 adsorption-desorption isotherm and corresponding pore size distribution curves (inset) of the catalysts prepared are shown in Fig. 8.

According to IUPAC classification, the isotherm curves are typical of a mesoporous material of the type IV, associated with capillary condensation taking place in mesopores. The Hysteresis loops in the BJH adsorption analysis are observed to be of intermediate between H2- and H3-type for samples F1, F2 (prepared from urea), starting at a relative pressure of 0.4 P/P_0 and slight leveling off near the saturation vapor pressure ($P = P_0$).

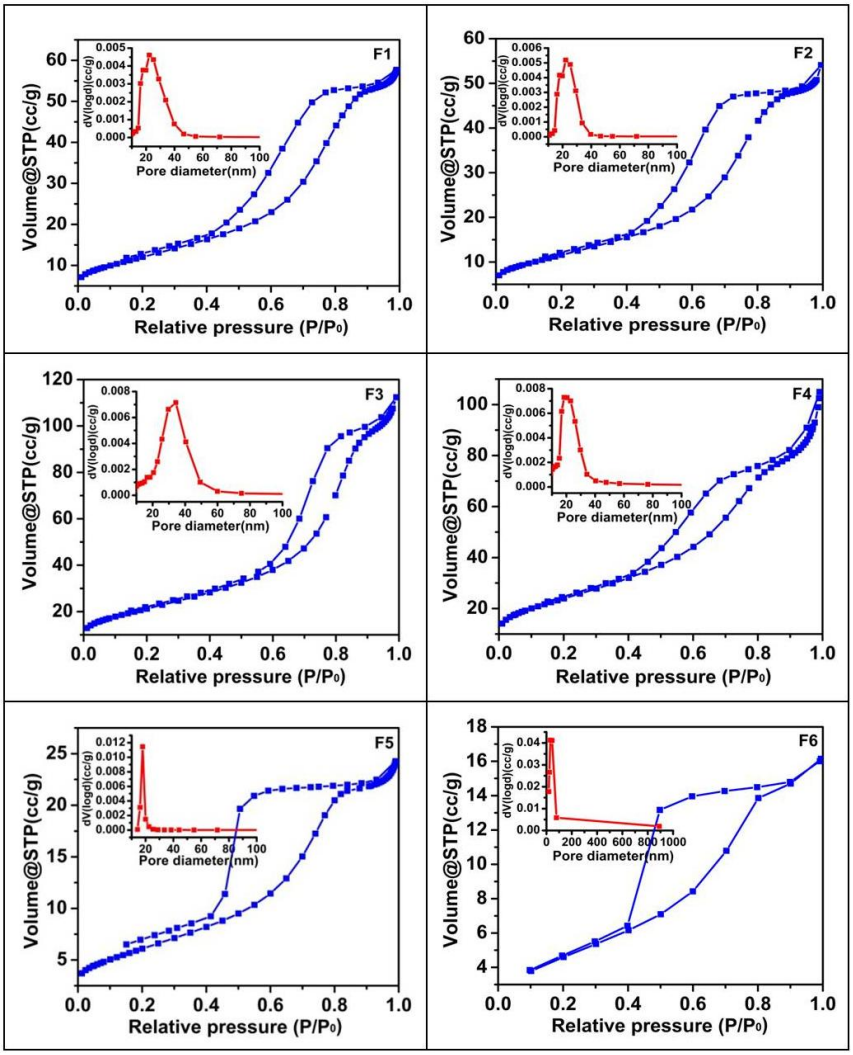

Fig. 8—*Nitrogen adsorption-desorption isotherms and pore size distribution (inset) of N-TiO_2 nanoparticles*

The pronounced hysteresis loop of these samples is a characteristic of the mesoporous materials arise out of agglomeration of nanoparticles with slit shaped pores. Samples F3, F4 (prepared from semicarbazide) depict similar nature of H3-type hysteresis loop with the absence of plateau at high relative pressure and starting at a relatively higher value (~0.5 P/P_0). The observed shape of isotherm curves designates the non-rigid nature of the mesopores in this case. The mesoporous nature of these four samples (F1-F4) is also supported by their broad pore size distribution curves.

Whereas for samples F5, F6 (synthesized from *N,N'*-dimethyl urea precursor), H2-type hysteresis loop with a well defined plateau at high P/P_0 values is observed indicating the presence of virtually rigid structures among the particles. Broad shape of hysteresis loop of both the samples and open lower end in the case of sample F5 is also noticed in this case. The lack of closure of the hysteresis loop below a relative pressure of 0.45 is assumed to be

caused by swelling of particles. This can also be attributed to the lower value of surface area and which probably may be the reason for comparatively lower photocatalytic activity of these samples. The rigid pore structure is further supported by their narrow pore size distribution [66, 67].

The observed difference in the nature of the hysteresis loop, the pore size distribution curve and other surface properties may be ascribed to the variable starting precursor materials employed for the synthesis of these samples. However, there is no such difference observed for the catalysts obtained from different synthetic methods. These results imply that, the slight variation of synthetic method in this case does not contribute to alter the surface properties of the catalysts obtained, but it is more dependent on the starting precursor material used.

BET surface area of all the samples is given in Table 6. It can be seen that the higher surface area is obtained for the samples F3 and F4, showing better photocatalytic activity, while the lower values are seen for the sample F6 (with poor photocatalytic activity).

Therefore, we can say that the surface area results have a direct impact on the catalytic properties and higher values of surface area results in enhanced absorption of reactant molecules on the surface of the catalyst, which in turn results in better photo-degradation ability.

Table 6 – Surface properties

Sample	BJH surface area (m^2/g)	Pore volume (cc/g)
F1	43.6	0.089
F2	41.5	0.084
F3	76.0	0.174
F4	85.8	0.162
F5	22.0	0.038
F6	16.9	0.028
P25	56.0	0.250

Morphological studies

The surface morphology of the catalysts prepared was carried out by using scanning electron microscopy (SEM). Fig. 9a shows the SEM images of the synthesized samples. As seen from the figure, most of the nanoparticles are well separated, although some of them are partially aggregated, consisting of smaller groups formed by finer primary particles. All the samples display similar morphology exhibiting uniform spherical shape of particles. The effective particle size is difficult to measure due to their existence in cluster form.

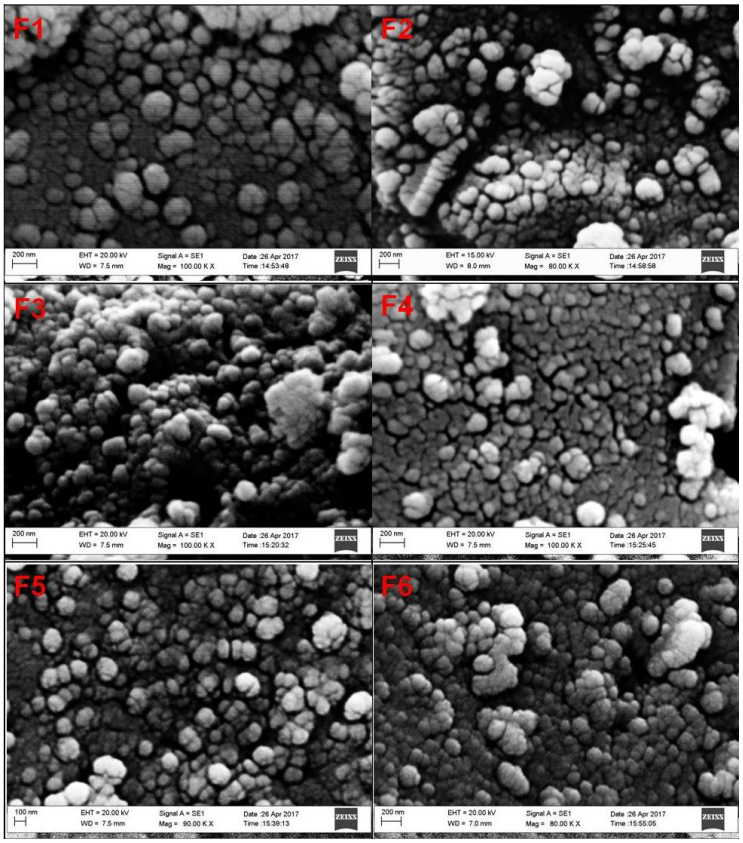

Fig. 9a— *SEM images of TiO_2 nanoparticles for samples F1- F6*

The surface morphology of these nanoparticles is further confirmed by TEM images. Micrographs in Fig. 9b display randomly packed particles with spherical morphology and pore channels formed from the particle packing, which is in support of the observation drawn from the SEM images. Shadow regions in the picture indicate that the particles may have agglomerated. It is also seen that the higher agglomeration is observed for samples F5 and F6, and the finer particles are seen in aggregated form to produce larger clusters. The average particle size was found to be in the range 6-12 nm (Table 7), which is in good agreement with the XRD data. Comparatively poor activity of sample F6 though having smaller particle size, might be as a result of the observed agglomeration. The detailed structure and crystallinity of TiO_2 nanoparticles was further investigated by the selected area electron diffraction pattern (SAED), as shown in the inset of Fig. 9b.

The SAED shows the apparent concentric ring diffraction patterns indexes to anatase phase, which confirms the polycrystalline nature of the prepared samples. The corresponding d-spacings are assigned as (101), (004), (200), (211), (204), (220), (215), of anatase and are in accordance with the XRD results.

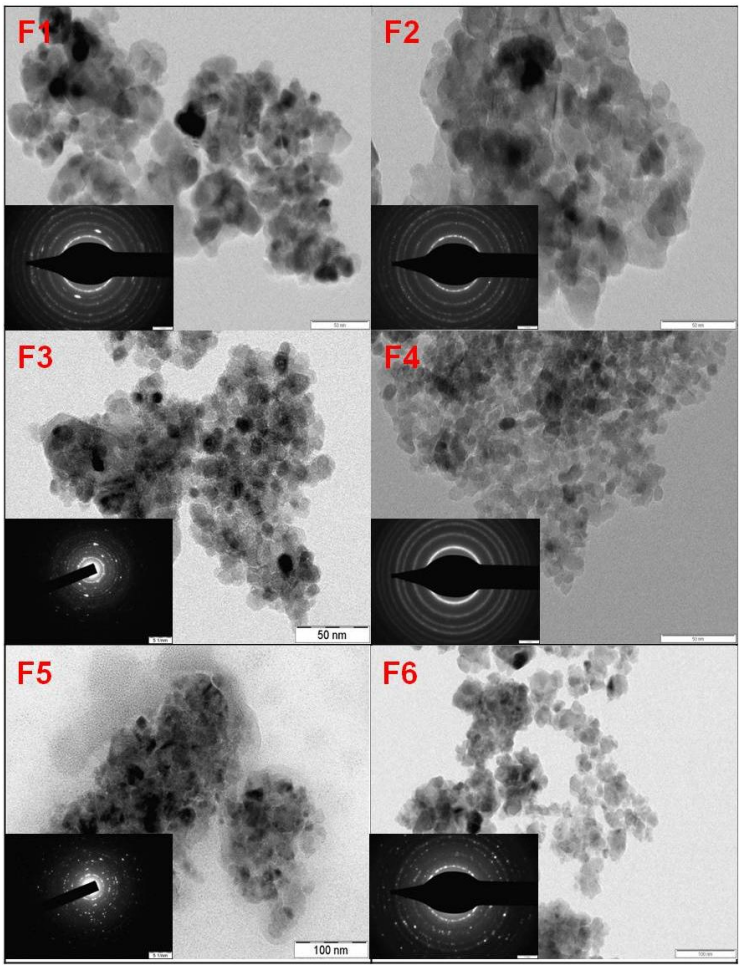

Fig. 9b— *TEM images with corresponding SAED patterns (inset) of TiO_2 nanoparticles for samples F1- F6*

Table 7 – Particle sizes

Sample	Particle size (nm)
F1	11.4
F2	12.5
F3	7.4
F4	6.5
F5	11.4
F6	6.8
P25	21.0

IR studies

The IR spectra of all calcined TiO_2 samples are shown in Fig. 10a. The broad band at around 3400 cm^{-1} and another weak band at around 1623 cm^{-1}, originates from surface adsorbed water and the surface hydroxyl groups [68-69]. In the spectra of precursor (uncalcined) samples (Fig. 10b), the strong broad band at 3500-2500 cm^{-1} could be attributed to Ti-OH stretching and -NH_2 stretching of urea and semicarbazide. The other strong bands in the

region of 1600-1100 cm^{-1} were due the amide bond and C-O, C-N bonds of organic precursors. The detailed study of calcined samples reveal that, the considerable shift of absorption band for Ti-O-Ti stretching frequencies to higher energy is observed in all the samples, and a clear peak is seen at 570 cm^{-1}. The observed shifts to higher energy can be assigned to the formation of O-Ti-N and N-Ti-N bonds in N-doped TiO_2, which is further confirmed from the observed additional peak at 415 cm^{-1} in the spectra of samples heated at 1000 °C, which can be assigned to N-Ti-N bonds (Fig. 10c and enlarged image inset) [70, 71].

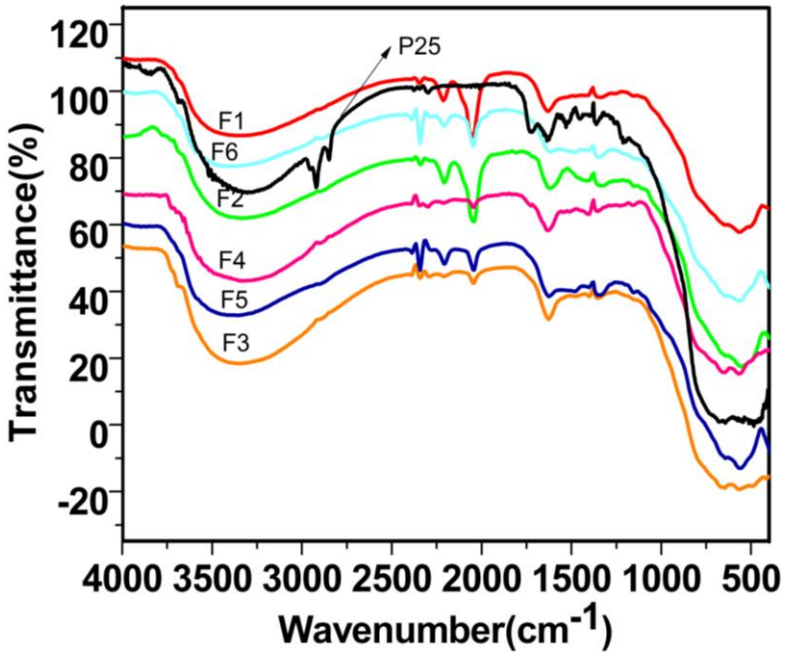

Fig. 10a—*IR spectra of calcined samples*

Additional band at 2340 (Ti-N=C=O), 2207 (Ti-NH-CN) and 2044 (Ti-O-CN) cm^{-1} were seen in all the six samples. This could arise from the linkage of isocyanic acid or cynuric acid units to the Ti *via* oxygen or nitrogen during initial decomposition of precursors. It is suggested that the TiO_2 surface appears yellow when heated with urea because of the melam, melom, melon, and graphitic carbon nitride present on the surface of the TiO_2 [72]. In our case though the samples appeared yellow in color in case of urea and semicarbazide, the corresponding multiple strong bands in the region 1640-1200 cm^{-1} due to these intermediates were not seen. IR spectrum of decomposed urea (see XRD discussion) displayed a band at 1734 cm^{-1} in the carbonyl stretching region suggesting formation of ammelide intermediate (Fig. 10d). This band was also seen when Degussa sample was milled with urea and heated at 400 °C for 1 h. This suggests that urea follows the same decomposition pathway over TiO_2.

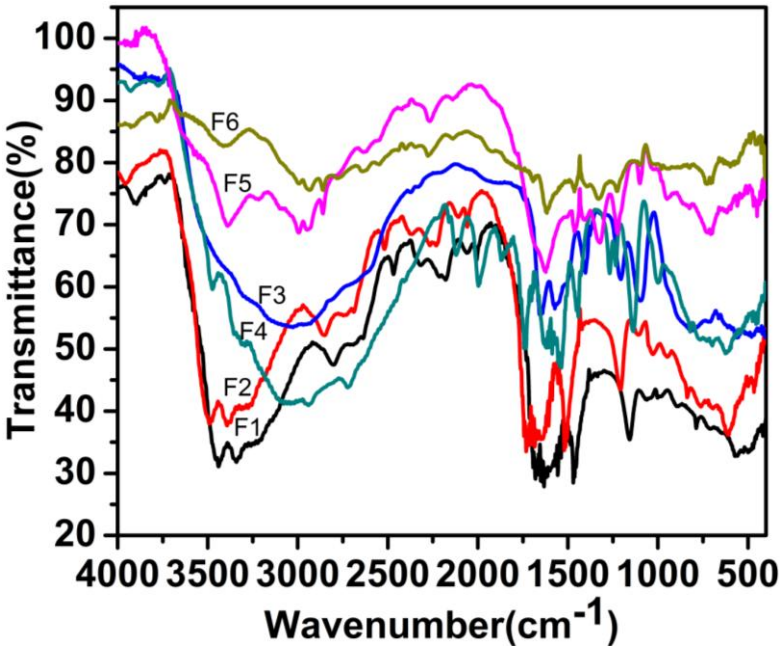

Fig. 10b—*IR spectra of precursor samples*

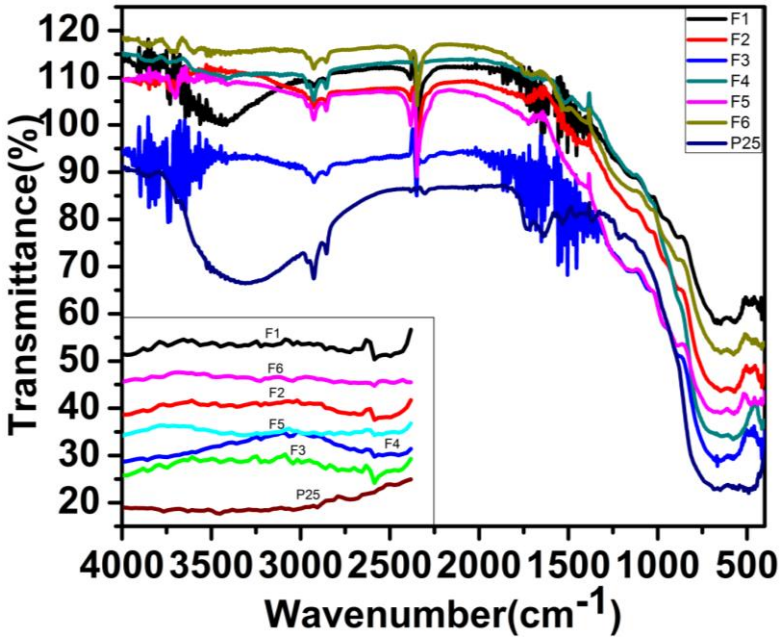

Fig. 10c—*IR spectra of samples heated at 1000 °C*

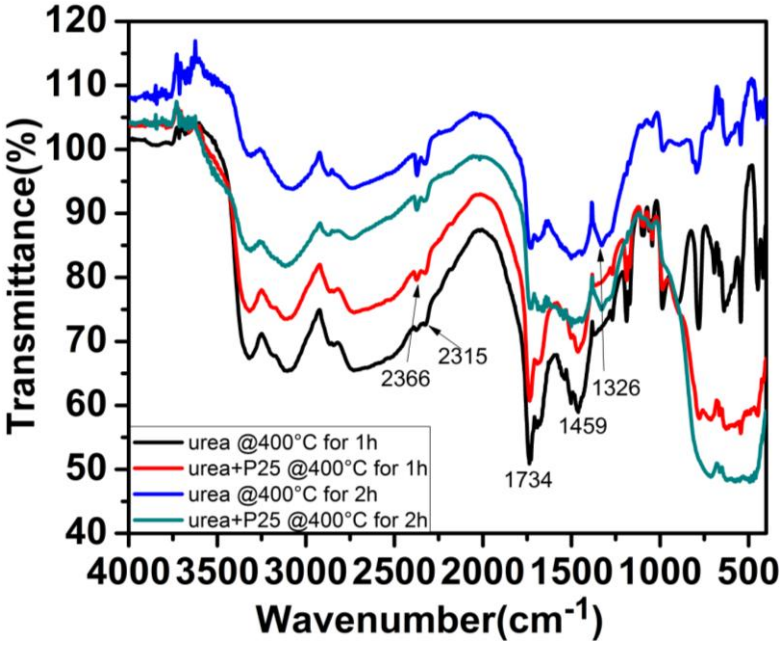

Fig. 10d—*IR spectra of urea and @P25*

Overall IR studies of precursor samples and the final samples suggested that, all the three precursors decompose in a similar pathway to lead to the formation of isocyanic/ cynuric acid [72-74]. A probable schematic route for the formation of various intermediates during the decomposition of the precursors on the surface of TiO_2 is depicted in Schemes 2-4.

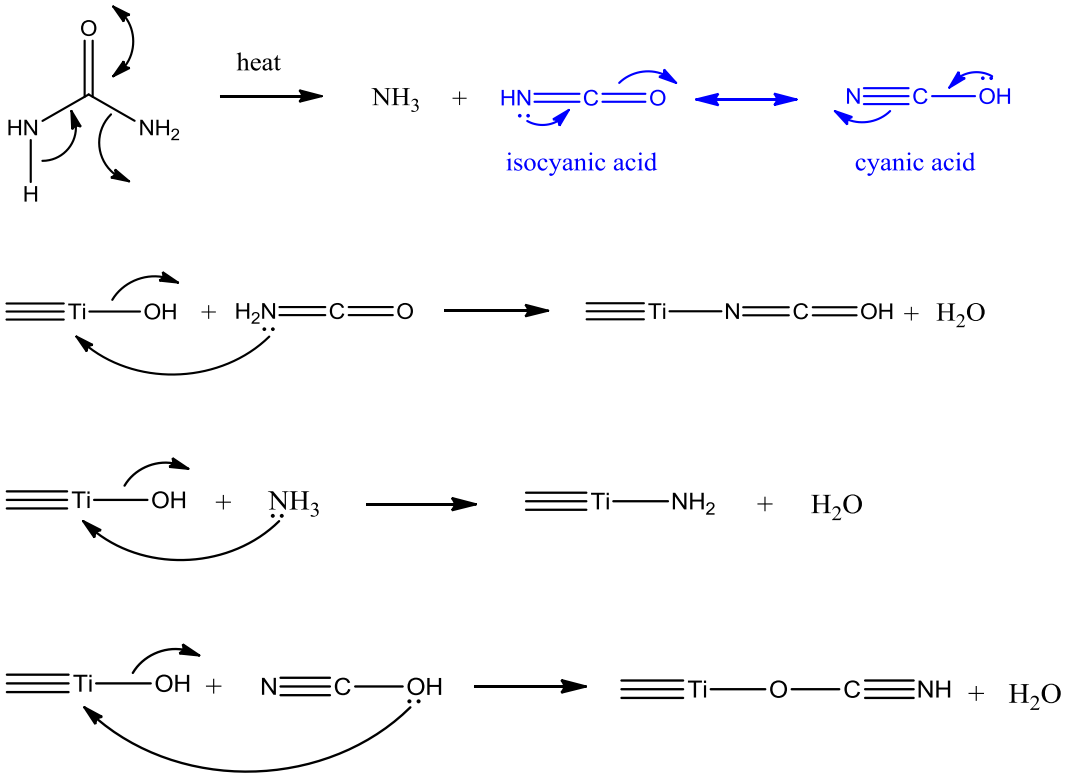

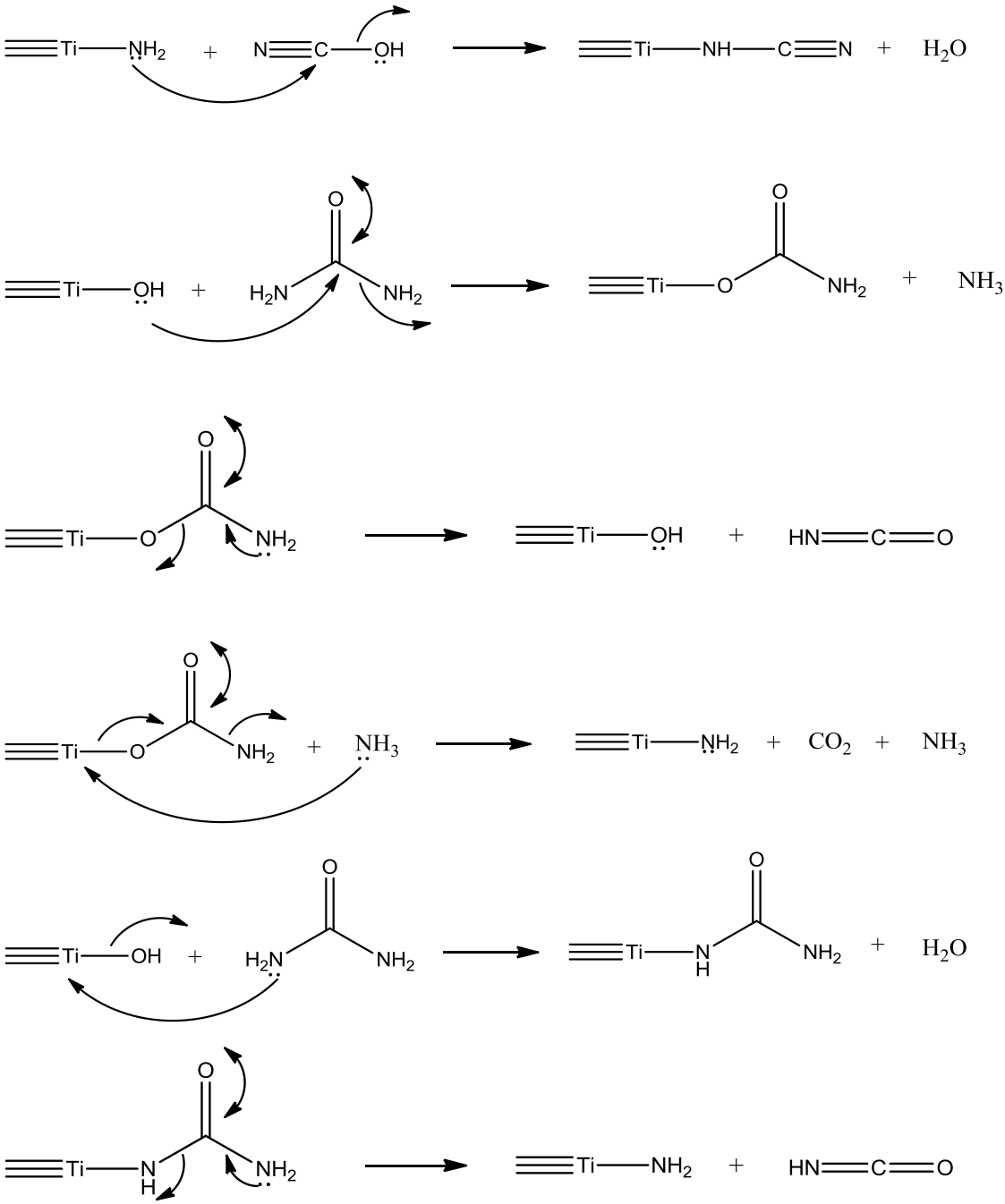

Scheme 2–*The myriad possibilities of decomposition of urea on TiO_2 surface*

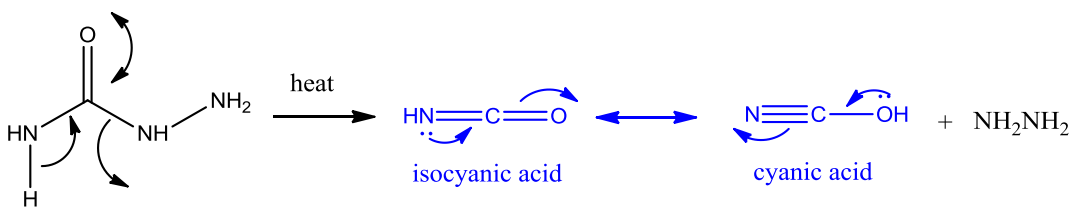

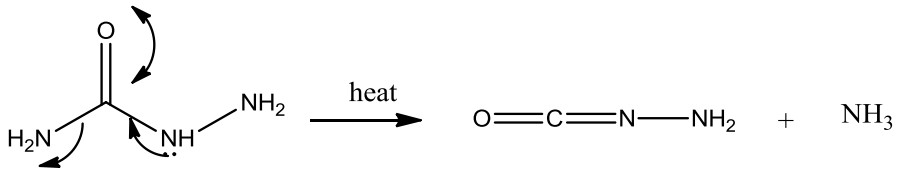
O
H2N
NH
NH2
heat
O=C=N—NH2
+
NH3

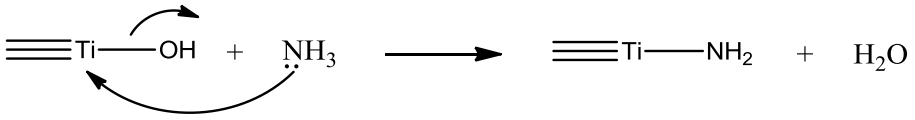
Ti—OH
+
NH3
Ti—NH2
+
H2O

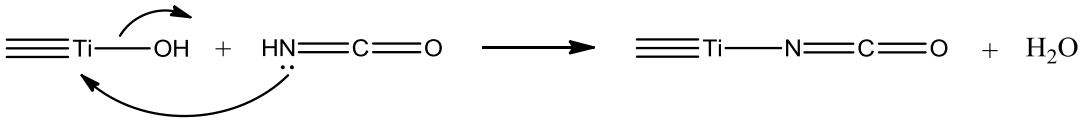
Ti—OH
+
HN=C=O
Ti—N=C=O
+
H2O

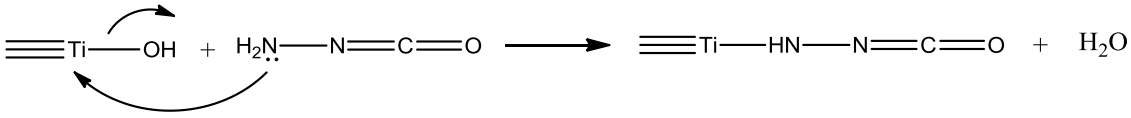
Ti—OH
+
H2N—N=C=O
Ti—HN—N=C=O
+
H2O

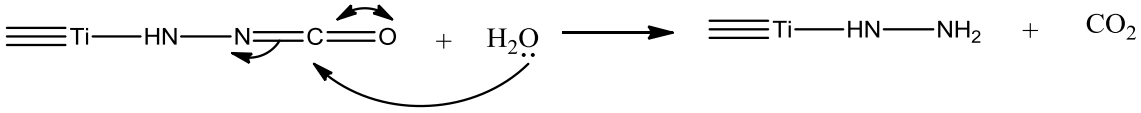
Ti—HN—N=C=O
+
H2O
Ti—HN—NH2
+
CO2

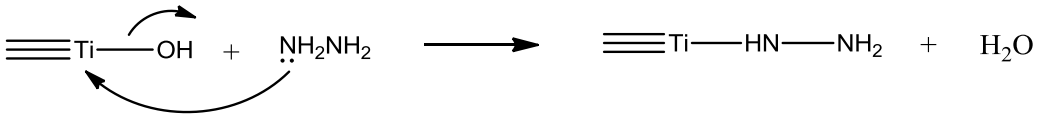
Ti—OH
+
NH2NH2
Ti—HN—NH2
+
H2O

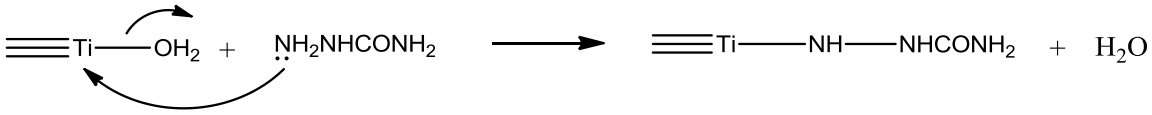
Ti—OH2
+
NH2NHCONH2
Ti—NH—NHCONH2
+
H2O

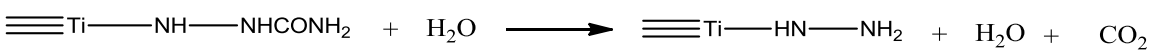
Ti—NH—NHCONH2
+
H2O
Ti—HN—NH2
+
H2O
+
CO2

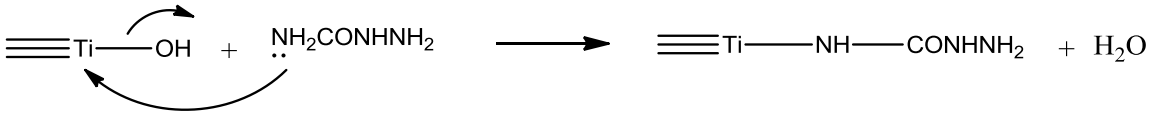
Ti—OH
+
NH2CONHNH2
Ti—NH—CONHNH2
+
H2O

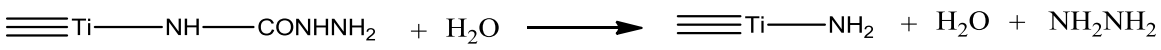

Scheme 3–*The myriad possibilities of decomposition of semicarbazide on TiO_2 surface*

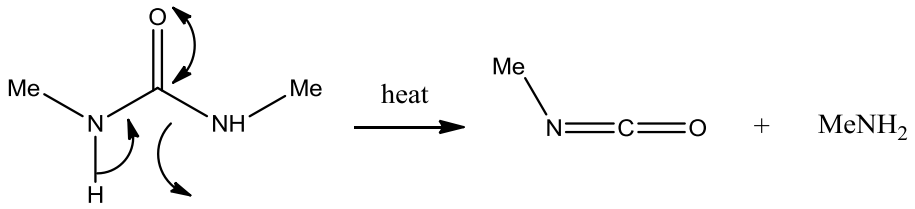

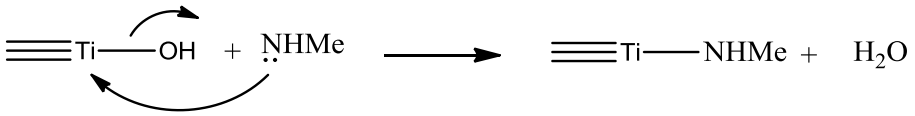

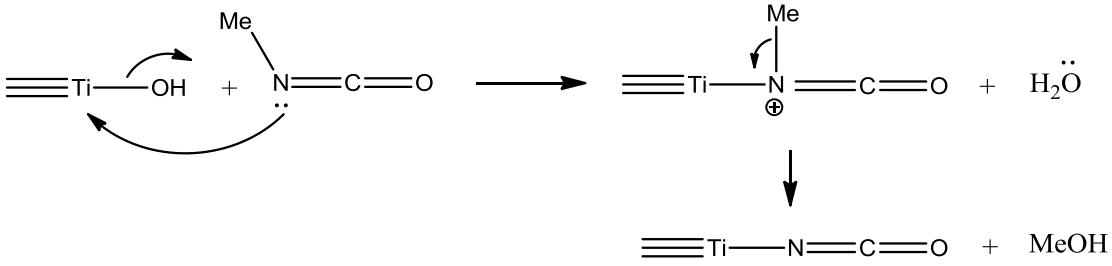

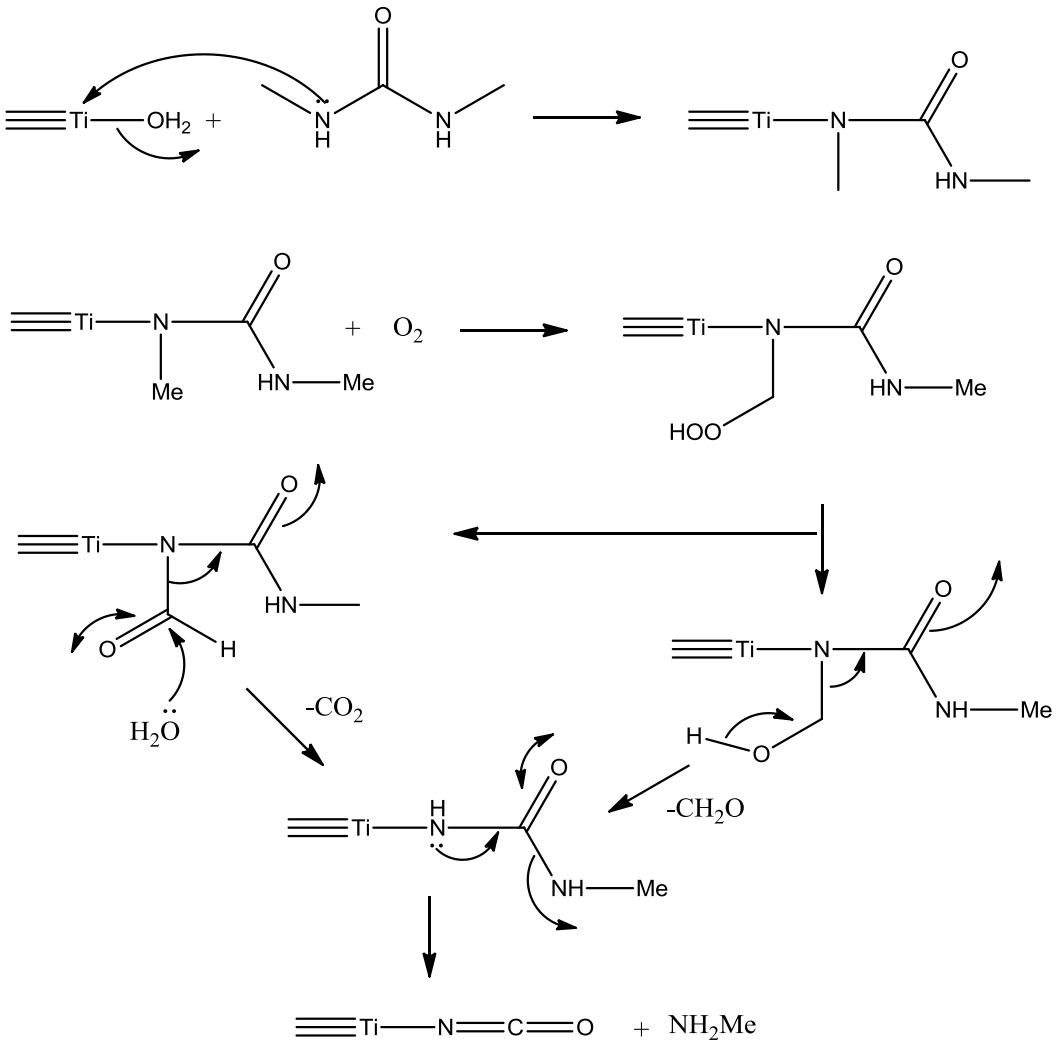

Scheme 4–*The probable decomposition of N,N'-dimethyl urea on TiO_2 surface*

Photocatalytic activity testing

To explore the photocatalytic activity of the prepared nanoparticles, the degradation of methylene blue was investigated under natural sunlight irradiation in comparison with Degussa P25. The results obtained are shown in graphical form given below (Fig. 11a). All the samples except F6, shows rapid degradation than Degussa P25. As stated in the literature, introduction of nitrogen in TiO_2 lattice may be responsible for the improvement of photocatalytic activity of these samples. The detailed degradation studies revealed that, among the six samples, those prepared using semicarbazide precursor (samples F4 and F3) showed the highest photo-decomposition rate and the sample F4 being the most active of all. Furthermore, the samples prepared from urea (F1, F2), though having more visible light absorbance, show activity lower than that of samples F3 and F4.

Since photocatalysis is a heterogeneous process which involves photo-excitation, bulk diffusion and surface transfer of carriers, the surface properties and large exposure of surface area are prime factors in this regard. Other factors likely to affect the surface structure of TiO_2 include particle size, crystallinity, phase purity, dopant type and its bonding form [75].

Co-existence of a small amount of rutile with anatase phase is responsible for the efficient electron transfer, promoted by the interface between anatase and rutile. The highest photocatalytic activity of the samples F3 and F4 could be attributed to the presence of optimum anatase-rutile composition, smaller size, large surface area and efficient charge separation at the anatase-rutile interface of these samples [70].

This has also been explained as, the generation of oxygen vacancies due to anatase-rutile phase transformation, which lead to an overall contraction of oxygen structure, shrinkage in volume and breakage of two of the six Ti-O bonds in TiO_6 octahedra [76].

Moreover, high crystallinity and smaller particle size favors the fast diffusion of the charge carriers to the surface for rapid reaction with adsorbed dye molecules and hence effective utilization of charge carriers for oxidation. The low surface area of the two samples F5 and F6 are responsible for the poor adsorption of the reactant molecules on the catalytic surface, thus resulting in comparatively lower activity.

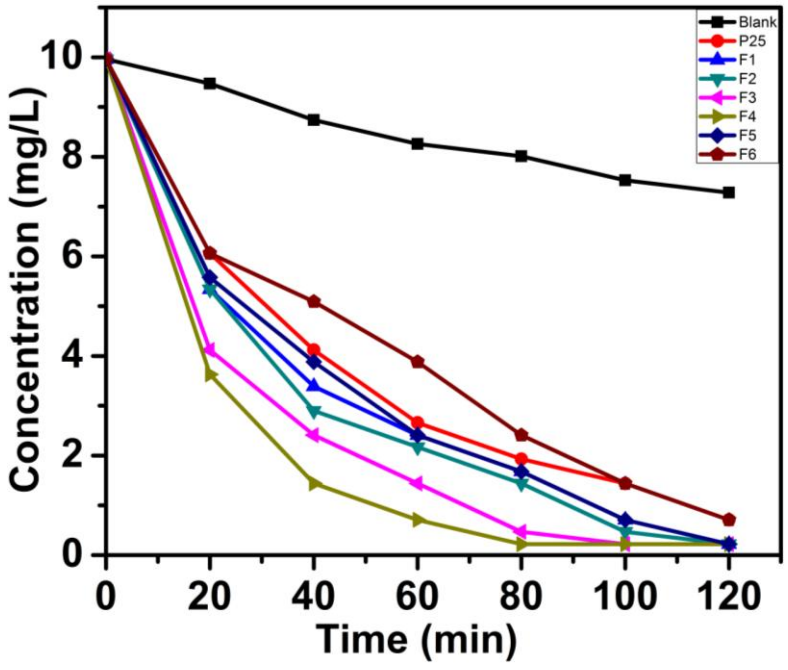

Fig. 11a— *Sunlight degradation plots for MB*

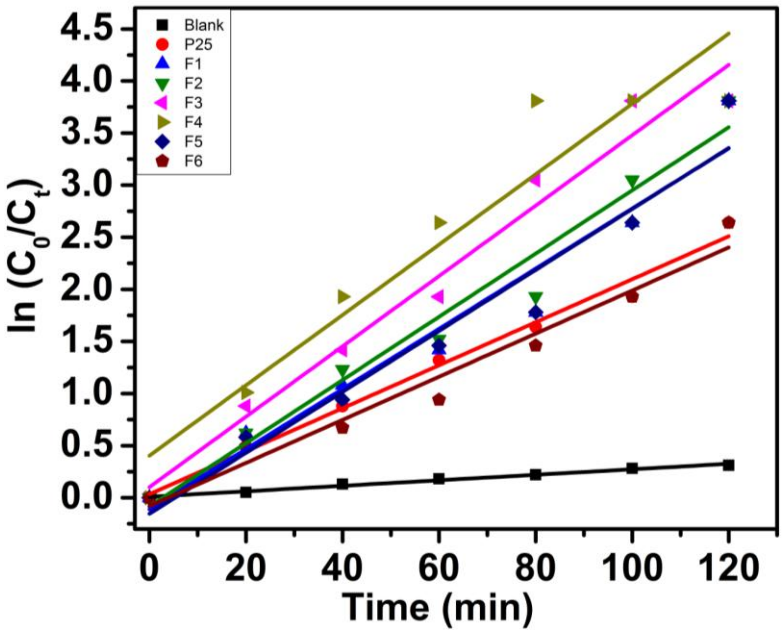

Fig. 11b—*Kinetics of MB degradation*

Furthermore, the catalytic activity of the samples was also confirmed by photo-degradation of rhodamine B. Similar degradation behaviors were obtained with slower degradation rate compared to that of methylene blue. The results are displayed in Fig. 11c.

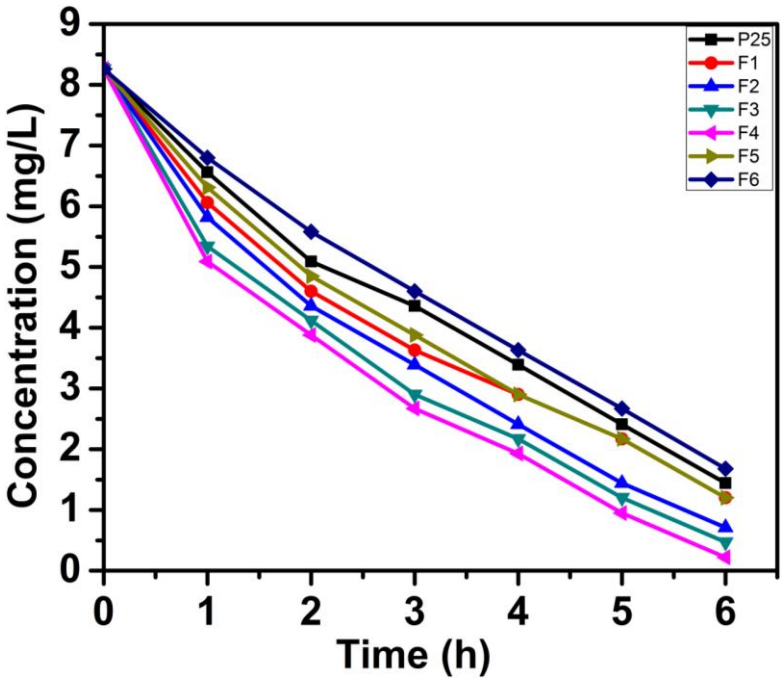

Fig. 11c— *Sunlight degradation plots for RhB*

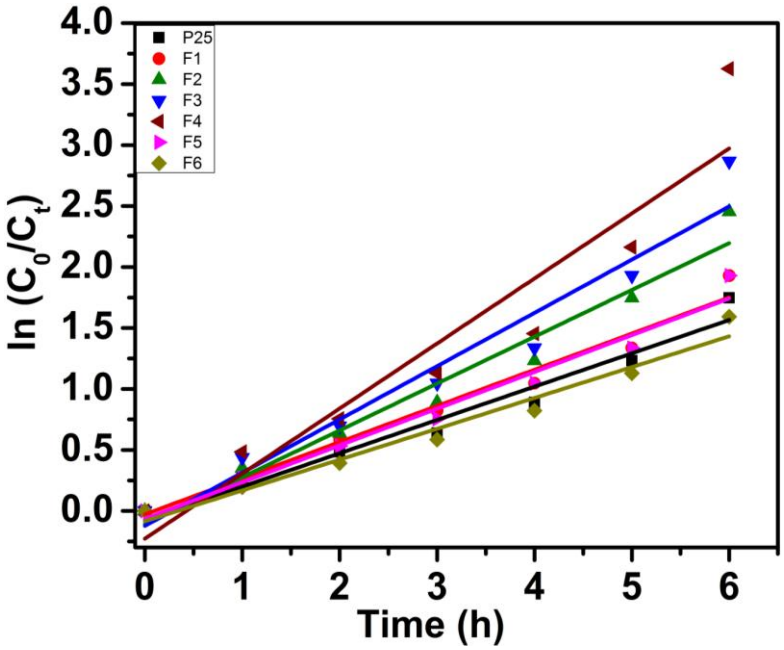

Fig. 11d—*Kinetics of RhB degradation*

The kinetics of the photocatalytic degradation reaction was studied under optimized conditions by using Langmuir–Hinshelwood kinetic model- ln (C_0/C_t) = kt, and thus calculated rate constant k values for both the dyes, are given in Table 8, which is in accordance with the other results.

Here C_0 in the equation is the initial concentration of dye solution at time t = 0, C is the concentration of dye solution after different time interval of photocatalytic reaction and slope k is the apparent rate constant.

The respective plots of ln (C_0/C_t) versus time for MB and RhB (Fig. 11b & 11d respectively) represents straight line, which indicates the photocatalytic degradation follows a pseudo first order kinetics in both the cases. Linear relationships for all the photocatalysts is seen, from which it can be observed that the apparent reaction rate constant is highest for sample F4.

Table 8 – Rate constants

Sample	**Rate constant k**	
	MB (min^{-1})	**RhB (h^{-1})**
F1	0.0289	0.2965
F2	0.0303	0.3838
F3	0.0338	0.4366
F4	0.0342	0.5333
F5	0.0293	0.3013
F6	0.0207	0.2528
P25	0.0206	0.2732

Recyclability studies were done up to three cycles for all the samples and the results obtained are shown in Fig. 11e and 11f respectively for MB and RhB dyes. The catalyst was recovered by centrifugation and drying. All the samples could be reused for degradation with negligible loss in activity.

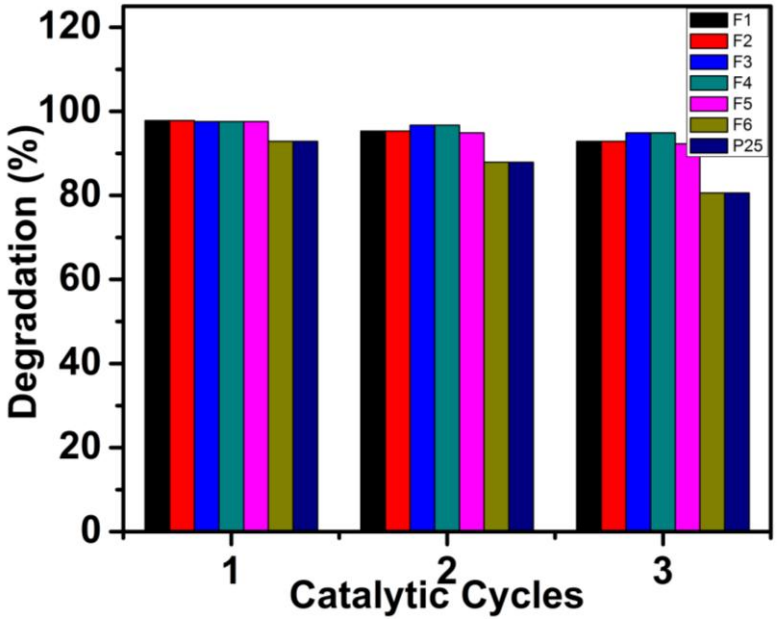

Fig. 11e—*Recyclability studies*

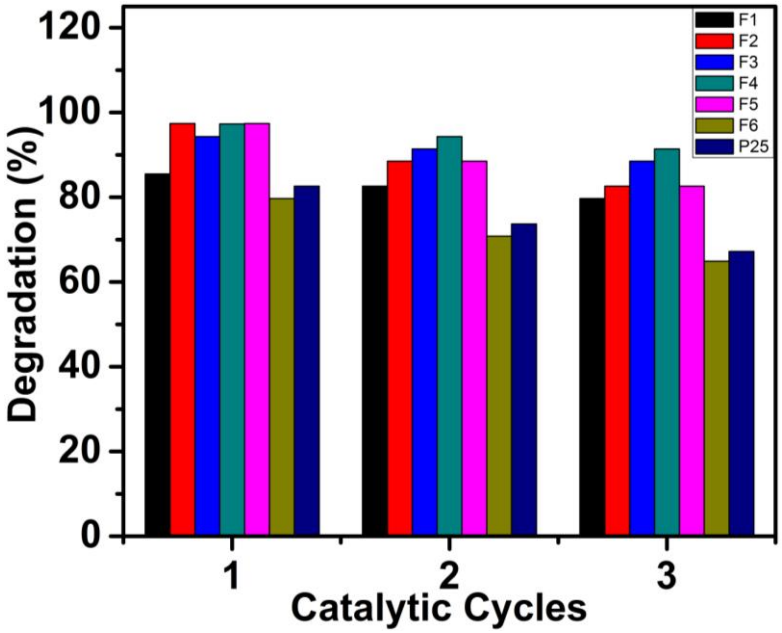

Fig. 11f—*Recyclability studies*

Summary and Conclusion

Nitrogen doped TiO_2 samples using urea and two urea derivatives as N-precursors were prepared by employing two different preparation methods. The two urea derivatives

semicarbazide and *N,N*-dimethyl urea are being tried for the first time as nitrogen source for doping studies. Of all the samples the samples prepared using semicarbazide as a precursor gave the best catalysts for photo-degradation studies. From the degradation studies of these samples it can be said that, photo-degradation efficiency of the catalysts is mainly related to its crystalline and surface properties. Phase purity and the surface properties of the catalysts prepared are primarily decided by the N-source used, rather than the variability of the synthetic method. It is observed that large surface area and a slight percentage of rutile in anatase in the sample are key factors affecting photocatalytic activity. The properties of catalysts are summarized in Table 9.

Table 9 – Summary of the properties of TiO_2 nanoparticles

Sample	**Cryst. size (nm)**	**Particle size (nm)**	**BET surf. area (m^2/g)**	**Pore vol. (cc/g)**	**λ_{max} (nm)**	**Rate constant k MB (min^{-1})**	**RhB (h^{-1})**
F1	11.9	11.4	43.6	0.089	460	0.0289	0.2965
F2	12.5	12.1	41.5	0.084	430	0.0303	0.3838
F3	7.8	7.4	76.0	0.174	414	0.0338	0.4366
F4	6.6	6.5	85.8	0.162	395	0.0342	0.5333
F5	10.9	11.4	22.0	0.038	461	0.0293	0.3013
F6	6.2	6.8	16.9	0.028	444	0.0207	0.2528
P25	25.0	21.0	56.0	0.250	370	0.0206	0.2732

Section B – CuO-NiO-incorporated TiO_2

After studying the effect of nitrogen incorporation into TiO_2, we further thought of modifying TiO_2 using transition metals. Transition metals and metal oxide doped TiO_2 systems are of prime importance for a number of catalytic applications. Late transition metals of 3d series are more valuable dopants, since they render the combined effect of magnetic and semiconducting properties into the parent metal oxide.

Cu/Ni doping to TiO_2 is gaining interest in recent years in the photocatalysis field due to their relative scavenging effect on photo-generated charge carriers. In addition Cu and Ni individually serve as efficient doping ions for TiO_2, due to their ability to introduce magnetic properties into this oxide in addition to improving its intrinsic semiconductor properties, thus making the material useful in electrical devices. The relative studies of these two systems in terms of optical and magnetic properties seem to be very promising.

Coupling of narrow band-gap semiconductor with TiO_2 has been proposed for potential application to induce an oxidation process under visible light. In this context, CuO (1.4 eV) having a high absorption coefficient can be effectively coupled with TiO_2. CuO-TiO_2 nanocomposites represent one of the most appealing systems for the synergistic combination. This combination has demonstrated to be stable with improved photocatalytic properties [77-78].

As discussed earlier, the optimum dopant concentration plays a crucial role in photocatalytic activity. Cu is reported to be more effective with low dopant concentration (< 1%), for photocatalytic applications. For example, copper in 0.06 M % is found to be optimum for degradation of rhodamine B [79], 0.1 wt % of CuO was proved to be the best for degradation of methylene blue [80] and optimum loading of 0.5 M % copper ion in sulfated TiO_2 for phenol oxidation [81]. Other than photo-degradation of toxic chemicals, it has found applications in hydrogen generation [82-83].

Doping of NiO in TiO_2 system has been studied for several properties, including photocatalytic reactions such as dye degradation and hydrogen production, since low valance Ni^{2+} doping is generally considered to improve the photo-activity of titania [84-85]. Literature study reveals that, 0.5 % Ni doped TiO_2 shows better photocatalytic degradation of methylene blue [86]. In another study 1.5 M % Ni was found to be optimum for MO degradation [87].

Room temperature ferromagnetism has been illustrated in both Ni and Cu doped TiO_2 systems. Cu-TiO_2 is reported to show ferromagnetism below 10 % concentration, above which it is observed to quench the magnetic moments to 0 μ_B [88], while for Ni-TiO_2,

ferromagnetism is shown to exist at very low concentration, up to 2 % or even lower than that [43, 89]. It is shown increasing up to 8 wt % of Ni, however above that, the increase in paramagnetic phases is observed [90]. Paramagnetic phases are also seen co-existing with ferromagnetism, at a high Cu concentration (above 5 %) [91].

Considering the above properties of individual Ni and Cu doping, we thought it would be interesting to study the co-dopant system for their possible synergistic properties.

Bimetallic Ni-Cu-TiO_2 was first reported by Gao *et al.* in 2004 [92] for the reduction of nitrate. They employed various mono-metallic, Cu/TiO_2, Ni/TiO_2, Pd/TiO_2 and Pt/TiO_2, and bi-metallic, Ni-Cu/TiO_2, Pd-Cu/TiO_2, Pt-Cu/TiO_2, combinations for this reaction. Among all these catalyst systems studied, Ni-Cu/TiO_2 was found to show the maximum photocatalytic activity. The promoting effect of bimetal was attributed by the authors to the more effective separation of photo-generated spatial charges in tiny TiO_2 semiconductor particles. For tiny metal-modified TiO_2 semiconductor particles, supported bimetal Cu and Ni behaves as short-circuited photoelectron chemical cell, where both cathodic and anodic reactions can occur at the same particle.

Prior to that, Liu and Liu [93] had reported Cu-Ni/Al_2O_3 catalyst for carbon dioxide hydrogenation in 1999. The same system was also studied earlier by Hierl *et al.* in 1981 [94]. Later in 2006, Haung and Jhao [95] reported Ni-Cu/ samaria-doped ceria for steam reformation of methane in the presence of carbon dioxide. Decomposition of methane over Ni-Cu/SiO_2 was reported by Lazaro *et al.* in 2007 [96]. A similar report was published earlier by Wang *et al.* in the year 2004, for decomposition of methane over a Ni-Cu-MgO Catalyst [97].

In the year 2009, Li *et al.* described *in situ* preparation of Ni-Cu/TiO_2 bimetallic catalysts [98]. In 2012 and 2013, Riaz *et al.* have claimed 100 % degradation of organic II dye by doping Cu-Ni (1:9) on commercial Degussa P25, while Cu-TiO_2 and Ni-TiO_2 could only degrade 55 and 48 % respectively of the dye [99-100]. Singh *et al.* in 2014 [101] have used 10 % Cu:Ni (9:1)/ TiO_2 for solar hydrogen production from water. Riaz and coworkers have demonstrated the photocatalytic degradation of DIPA using this bimetallic system [102]. Hierarchical structure Cu-Ni/TiO_2 nanocomposites as an electrode for lithium ion batteries were studied by Yue *et al.* in 2017 [103], and for reduction of HMF and furfural to methylated furans by Seemala *et al.* [104]. In this report, the authors claimed that, Ni in a combined system of Cu-Ni-TiO_2 act as a supportive metal dopant to promote Cu-reactivity, to further enhance its properties. This was proposed to be due to the strong interaction

between Ni and TiO_2, which reduces the concentration of Ni at the catalyst surface and thus serves as an anchoring site for Cu on TiO_2 to enhance its stability.

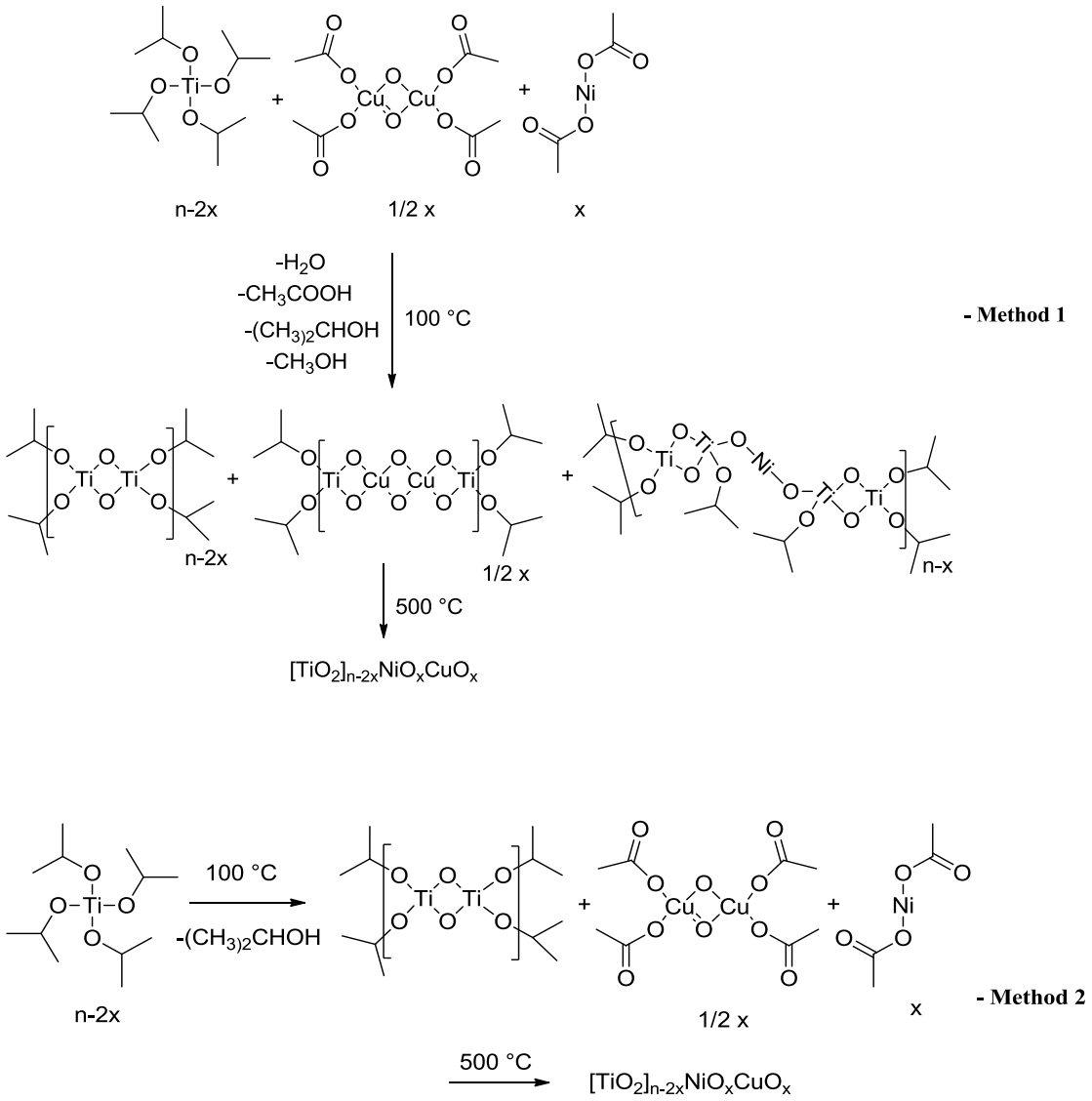

Scheme 5

From the above studies, it is clear that the bimetallic Cu-Ni/TiO_2 is a promising system for catalytic applications. In most of the studies the preparation involved use of commercial Degussa P25 as a support material. It was to be noted that though Cu-Ni/TiO_2 catalyst was mentioned, there were actually two types of catalysts. One was Cu-Ni metallic alloy on TiO_2 and the second was a combination of metal oxides *i.e.* NiO, Cu_2O, CuO on TiO_2. The first catalyst system was good for reduction studies while the second catalyst was for photocatalytic studies. The advantage of the second catalyst system was that it could be conveniently converted to the first catalyst system by reduction. Thus we chose to synthesize the second catalyst system. This was done in two ways. In the first procedure different percentage of Ni:Cu precursor (1:1) were mixed with titanium precursor and then gelled to

form a powder, which was calcined at 500 °C for 3 h to obtain the desired product. In the second procedure, TiO_2 powder was first obtained from titanium precursor and then dopant precursors were added.

It was expected that in the first procedure the dopant species would get uniformly distributed in the TiO_2 matrix (Method 1) while in the second, they were to be more on the surface (Method 2) as shown below (Scheme 5).

Structural and morphological properties

Powder X-ray studies

Analysis of phase composition, crystalline nature and crystallite size of the prepared catalysts was carried out using X-ray powder diffraction technique. Fig. 12a and 12b presents the respective powder XRD pattern of calcined TiO_2 samples of series G and H. Sharp and well-defined peaks, indicates the highly crystalline nature of these catalysts.

The peak positions and their relative intensities for both series clearly suggests the presence of anatase as a major phase, as indicated by the consistent powder diffraction patterns (JCPDS card # 21-1272), with the main peak at 25.27° corresponding to the (101) plane. Samples of series G are obtained with pure anatase phase, whereas for series H, samples H5 and H7 contain a slight rutile phase (marked as R) (8.3 and 5.9 %, respectively), as calculated using eq. **3**, while other samples have pure anatase phase. With the increase in metal concentration in case of series G, two small peaks at 32.8 and 35.6 (marked with *) are observed for sample G7, corresponding to (110) and (111) respective planes of CuO monoclinic crystalline phase (ICDD file no. 80- 1916). No such peaks due to NiO crystalline phase are observed, though both the dopants are in equal concentration. This could be due to higher ionic radius of Cu^{2+} (0.87 Å) than Ti^{4+} (0.74 Å) which causes slight distortion of the perfect lattice of TiO_2 when doped, while Ni^{2+} being of similar radius (0.72 Å) do no cause such a distortion [19, 105]. These results are also supported by the literature reports for Ni-TiO_2, which shows absence of peaks due to Ni species, even at 12 wt % of Ni doping [90], whereas for Cu-TiO_2, CuO peaks were seen even for 2 % Cu doping [106]. The absence of any of the segregate crystalline phases for various Cu or Ni species for series H suggests the presence of highly dispersed metal particles onto TiO_2 surface.

The incorporation of CuO/NiO into TiO_2 lattice can be further confirmed by studying the details of intensity of peaks (004) and (200). Incorporation of Cu into TiO_2 is reported to cause preferential growth along (004) direction, thus increasing the intensity of (004) peak and corresponding decrease in (200) peak, which in turn results in a decreased intensity ratio

of I_{101}/I_{004} and I_{101}/I_{200}, with increasing Cu concentration [91]. Such variation of intensity ratio is observed for series G, which shows an initial increase from 0.1 to 1 wt % of metal and later remains constant at higher metal concentration indicating the lattice incorporation of metal species in this series.

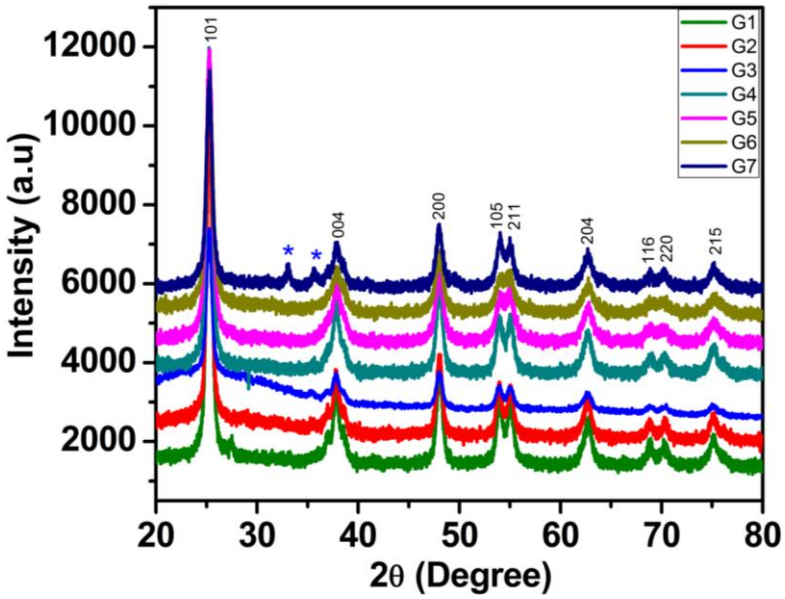

Fig. 12a—*XRD plots for calcined samples of series G*

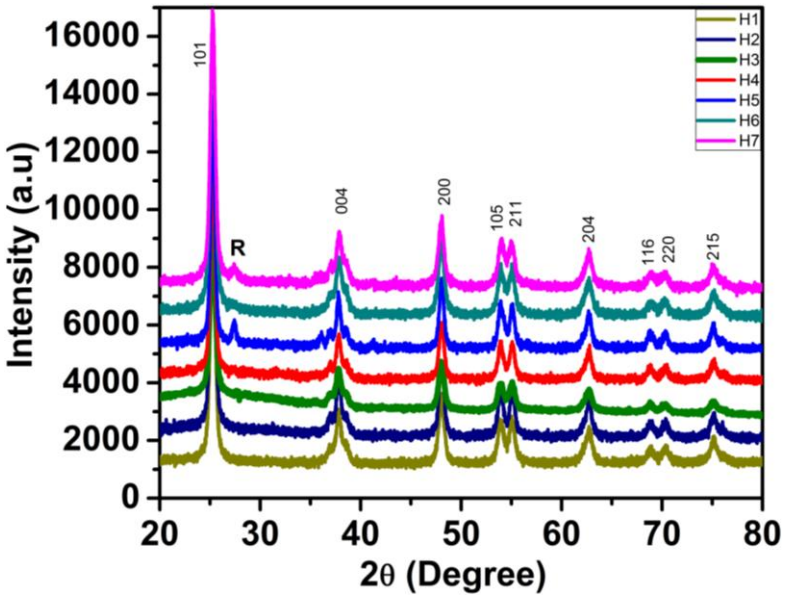

Fig. 12b—*XRD plots for calcined samples of series H*

Slight fluctuations from the observed trend are seen for low metal concentrations (< 1 wt %), which may be attributed to the combined effect of CuO-NiO species. However, for series H, the intensity ratio is observed to be almost constant for all samples, which suggest that, the

metal species might have remained spread on the surface of TiO_2. This prediction is further supported by the absence of peak for Cu/Ni species in the XRD pattern even at 5 wt % metal concentrations for this series. The average crystallite size for both the series as determined from (101) diffraction peak (the most predominant highest intensity peak), according to the Debye-Scherrer equation (eq. **1**), is found to be in the range of 11-14 nm for series G (Table 10a) and 13-19 nm for series H (Table 10b). The synthesized samples were found to be smaller in size as compared to Degussa P25 (25nm).

It can be noticed that, the samples of series H are found to be higher in size compared to that of series G. Moreover, a linear decrease in size with increasing metal content is observed for series G with the exception of sample G7, whereas, random variation in size is seen in the samples of series H. The fluctuations observed in sizes can be considered as the effect of the lattice strain produced during synthesis [43]. The lesser value of strain and dislocation density enhances free carrier mobility in the host lattice. Strain is inversely proportional to the crystallite size. The corresponding strain for these samples is calculated using eq. **2**.

Here the linear increase in strain is observed from 0.0113 to 0.0121 for samples of series G with increasing metal percentage (Table 10a). Increasing value of strain indicates the increasing degree of imperfections with a corresponding increase in Cu-Ni % into TiO_2 lattice. However, for series H, random value of strain is observed, with highest strain value (0.0120) and corresponding lowest crystallite size (13.85 nm) for sample H3 (1 wt % Cu-Ni) (Table 10b). The random variation of the crystallite size and strain for series H is in support of inferences drawn from the intensity ratio, that the CuO-NiO species might have remained spread on the surface, while the linear decrease in size or increase in strain for series G suggests the incorporation of metal species into the TiO_2 lattice.

Table 10a – Crystallite studies for series G

Sample	Crystallite size (nm)	Lattice strain	Peak intensities ratios I_{101}/I_{004}	I_{101}/I_{200}
G1	14.65	0.0113	6.905	4.302
G2	14.38	0.0115	6.918	4.255
G3	14.48	0.0114	3.601	3.977
G4	12.93	0.0128	5.844	3.946
G5	11.88	0.0139	6.181	4.413
G6	11.15	0.0148	6.435	4.530
G7	13.73	0.0121	6.357	3.831
P25	25.0			

Table 10b – Crystallite studies for series H

Sample	Crystallite size (nm)	Lattice strain	Peak intensities ratios I_{101}/I_{004}	I_{101}/I_{200}
H1	17.05	0.0097	6.413	3.838
H2	17.52	0.0094	6.786	4.066
H3	13.85	0.0120	6.707	4.277
H4	17.58	0.0094	6.694	4.080
H5	19.51	0.0085	6.238	3.826
H6	15.84	0.0104	6.577	4.224
H7	16.33	0.0101	6.937	4.378
P25	25.0			

UV studies

The absorption spectra of series G and H samples are respectively shown in Fig. 13a and 13b. Significant absorption peaks in the wavelength region shorter than 400 nm can be assigned to the intrinsic band-gap of TiO_2, while enhanced absorption in the visible region extending up to 800 nm can be attributed to the successful insertion of Cu-Ni in TiO_2 matrix. It is observed that the red shift in absorption wavelength goes on increasing with increase in dopant concentration, which suggests that the shift is clearly due to presence of CuO-NiO in TiO_2.

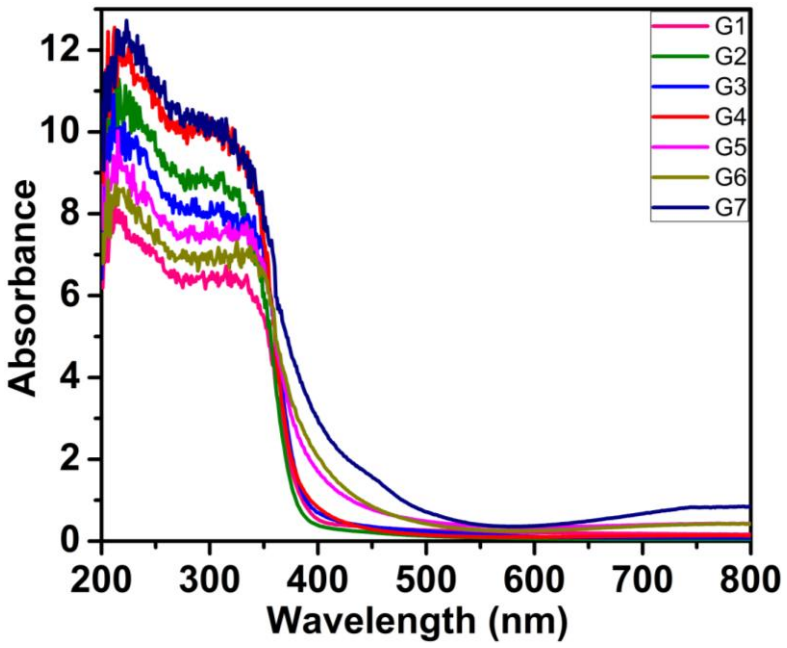

Fig. 13a—*UV-DRS spectra of calcined samples of series G*

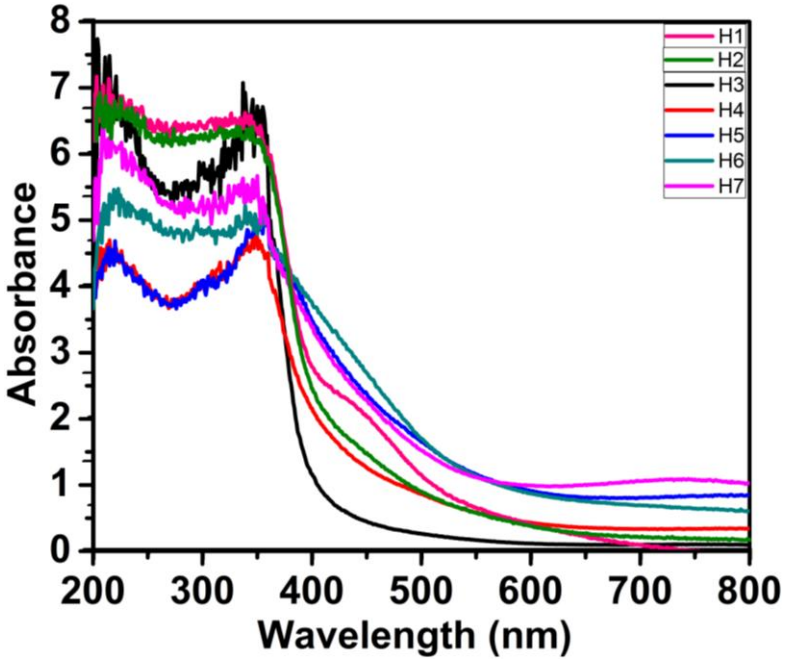

Fig. 13b—*UV-DRS spectra of calcined samples of series H*

An additional peak is clearly seen in this region from 550-800 nm for all the samples, which matches with the corresponding peak for individual Cu/Ni doping, as reported in the literature. These weak absorption peaks can be attributed to the d-d transitions of the dopant ions in the crystalline environment of TiO_2 [107]. The intensity of this peak is observed to increase with increasing dopant concentration, with the exception of the sample with 0.01 wt %, which display slightly higher intensity compared to samples with 0.05 and 0.1 wt %. A considerable increase in the visible light absorption is attributed to the creation of new energy levels in the band-gap of TiO_2 and thus causes electronic transitions between the valence band and these intra-band energy levels [91].

Table 11 – Band-gap energies

Sample	Band-gap (eV)	λ_{max} (nm)	Sample	Band-gap (eV)	λ_{max} (nm)
G1	3.16	392.2	H1	2.32	534.9
G2	3.20	387.9	H2	2.52	492.0
G3	3.13	395.6	H3	3.01	411.3
G4	3.12	397.2	H4	2.59	479.4
G5	2.90	427.9	H5	2.24	554.2
G6	2.73	453.9	H6	2.13	582.6
G7	2.67	464.2	H7	2.27	546.8
P25	3.35	370.7	P25	3.34	370.7

It is also observed that, overall comparison of absorbance wavelength of the two series indicates a higher shift of the wavelength for series H than that of the series G. This might be due to the presence of dopant species on the surface of TiO_2 in case of series H, which are responsible for greater shift in absorption wavelength.

The values of λ_{max} and corresponding band-gap values as calculated using eq. **4** for all samples are summarized in Table 11. The band-gap values are found to be in the range 2.7 to 3.2 eV for series G and 2.1 to 3.0 eV for series H.

BET analysis

The typical plots of N_2 adsorption-desorption isotherm for series G and H are respectively shown in Fig. 14a and 14b with the corresponding pore size distribution curves (inset).

The isotherm curves can be classified as typical of a mesoporous material of the type IV associated with capillary condensation taking place, as per the IUPAC classification. The hysteresis loops in the BJH adsorption analysis are observed to be of H2-type for samples G1-G4, with the leveling off the loop at saturation vapor pressure ($P = P_0$) for the sample G1 (0.01 wt % Cu-Ni). While with the increasing metal % (G2, G3, G4), the loop does not level off even at saturation vapor pressure ($P = P_0$), is a characteristic of the mesoporous materials arising out of agglomeration of nanoparticles, with slit shaped pores. The mesoporous nature of these samples is also confirmed by the pore size distribution curve extended up to 40 nm. With further increase in metal %, for sample G5 (1 wt %), H3-type hysteresis loop with the absence of plateau at high relative pressure and starting at a slightly higher value (~0.5 P/P_0) is obtained, designating the non-rigid nature of the mesopores, which is also supported from the broad pore size distribution. For the samples G6 and G7, the intermediate of H2- and H3-type hysteresis loops, with distinctly observed pronounced plateau region for sample G6, indicates the presence of ink bottle shaped pores [66] and which is found to be reflected in their poor photocatalytic activity. The unusual shape of the pore size distribution curve is seen in these samples. The shape of isotherm and pores size distribution curves has a direct impact on the photocatalytic activity in this series.

However, for series H, clear H2-type hysteresis loop with a well-defined plateau at high P/P_0 values is observed for samples H1, H4, H6 and H7, indicating the presence of virtually rigid structures of these samples. Whereas, slightly broader hysteresis loops, intermediate of H2- and H3-type are observed for samples H2, H3 and H5. The very narrow shape of pore size distribution curves is observed for almost all samples.

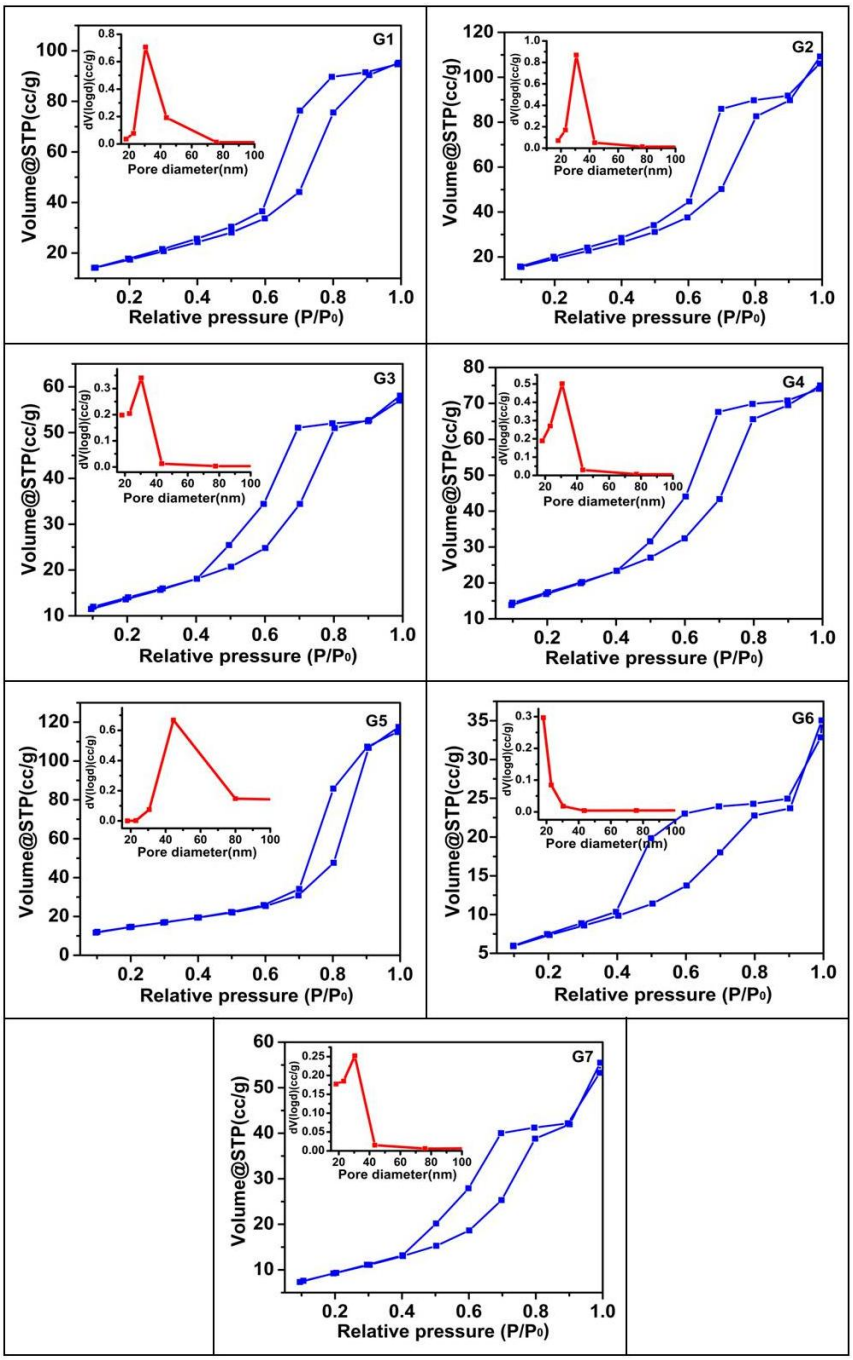

Fig. 14a—*Nitrogen adsorption-desorption isotherms and pore size distribution (inset) of CuO-NiO-TiO_2 nanoparticles of series G*

It is observed that, the nature of hysteresis loop and pore size distribution curve does not significantly affect the photocatalytic properties in this case.

The BJH surface area and pore volume of these samples are given respectively, for series G and H, in Table 12a and 12b. For series G, it can be seen that, the surface area goes on increasing with metal concentration up to 0.5 wt %, whereas become random after that. The similar linear increasing trend is also observed for pore volume, which decreases at 1 wt %

metal insertion and again increases up to 5 wt %. The obtained results can be attributed to the synergistic effect of the combined system of Cu-Ni doping into TiO_2 lattice. For series H, slightly fluctuating and comparatively lower values of surface area and pore volumes are observed than that of series G. This might be the effect of the metal species remaining spread on the surface, which is in agreement with the strain values observed in the XRD results.

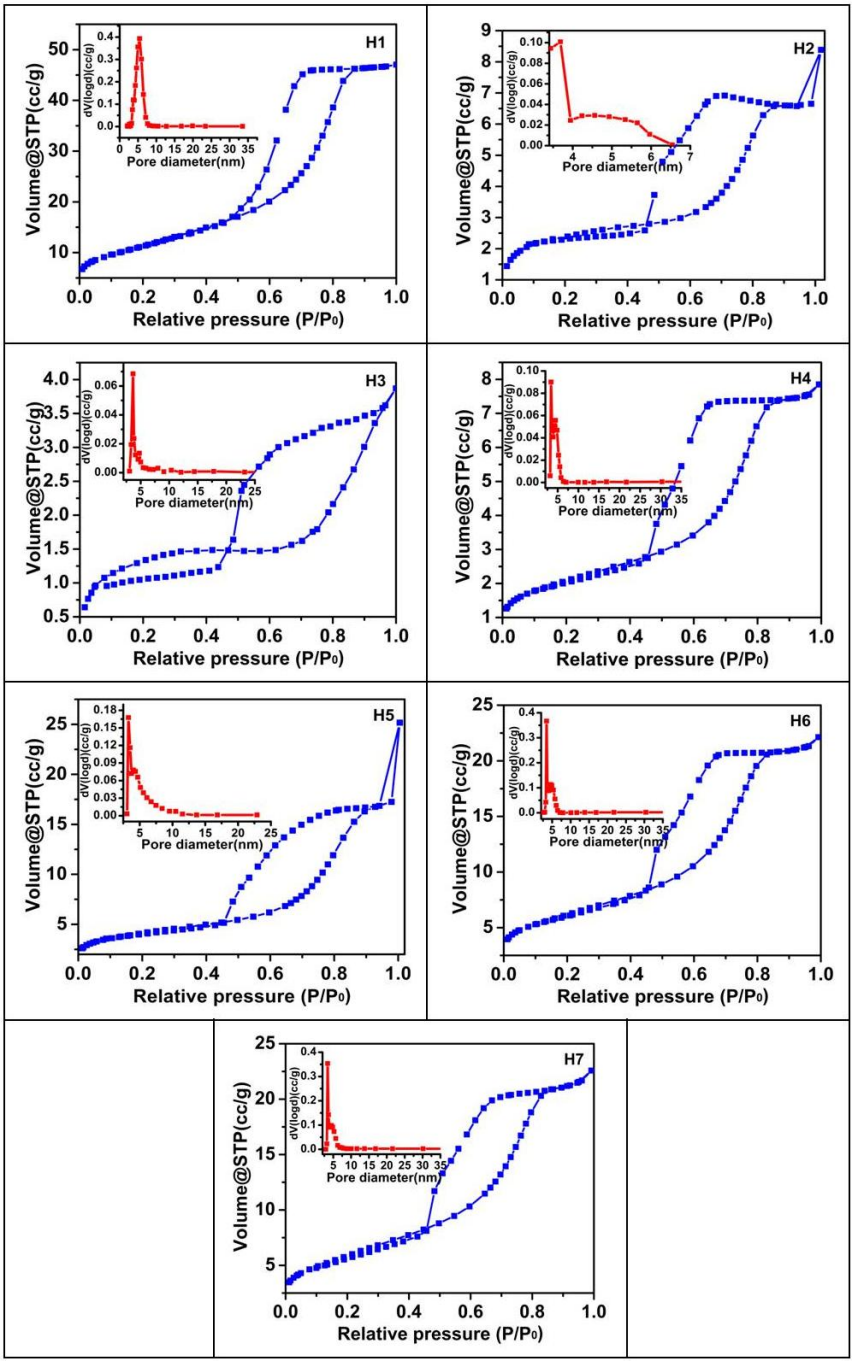

Fig. 14b—*Nitrogen adsorption-desorption isotherms and pore size distribution (inset) of CuO-NiO-TiO_2 nanoparticles of series H*

Table 12a – Surface properties for series G

Sample	BJH surface area (m^2/g)	Pore volume (cc/g)
G1	43.50	0.059
G2	60.00	0.096
G3	93.95	0.156
G4	101.93	0.177
G5	70.70	0.097
G6	90.58	0.126
G7	72.23	0.191
P25	56.00	0.250

Table 12b – Surface properties for series H

Sample	BJH surface area (m^2/g)	Pore volume (cc/g)
H1	31.90	0.035
H2	32.02	0.036
H3	58.50	0.076
H4	11.03	0.011
H5	5.31	0.006
H6	11.55	0.012
H7	24.31	0.027
P25	56.00	0.250

Morphological studies

The surface morphology of these nanoparticles is studied by SEM analysis. SEM micrographs and corresponding EDX images of series G and H are respectively shown in Fig. 15a and 15c. It is observed that fine granular and densely packed nanoparticles of spherical shape are seen in almost all the samples of series G. Particles are seen to be uniformly distributed and are of similar morphology for varying metal concentration. Slight aggregation of particles is also observed with a lesser degree of agglomeration. Slightly higher agglomeration is observed among the particles of the sample with 5 wt % Cu-Ni loading.

For series H, randomly placed spherical particles of different size and aggregated in groups are seen. Smaller sized particles densely packed, with slight agglomeration are observed for samples with lower metal concentration (H1-H4), whereas slightly bigger sized particles closely spaced are seen in samples H5 and H7, while randomly spaced particles forming clusters are seen for the sample H6. Slight agglomeration is also observed among these

particles. The difference in morphology of samples H5 and H7 may be due to the presence of slight rutile phase.

The chemical composition of the prepared nanoparticles is further confirmed from EDX images. From these images, Ti and O are observed to be major constituents with a slight presence of C, which may be due to the supporting material used. Traces of Cu and Ni species are also seen in all the samples signifying the incorporation of these species into TiO_2 matrix.

The samples with lower metal loading (0.01-0.1 wt %) of both the series, displaying higher photo-degradation rate were further investigated with TEM analysis. TEM micrographs (Fig. 15b and 15d) displayed well distributed tiny nanoparticles of nearly spherical shape. Slight agglomeration is observed for samples with 0.01 wt % metal loading.

The average particle sizes of these catalysts were obtained to be in the range of 13-14 nm for series G and 13-17 nm for series H. These values are consistent with the XRD results.

The corresponding SAED images (inset of Fig. 15b and 15d) are used to study the polycrystalline nature of these samples, which shows concentric ring patterns of small spots. The observed patterns are consistent with Bragg's reflections observed in XRD pattern. The interplanar spacings could be indexed according to anatase TiO_2 as (101), (004), (200), (211), (204), (220) and (215), matching with the XRD results (JCPDF no. 21-1272).

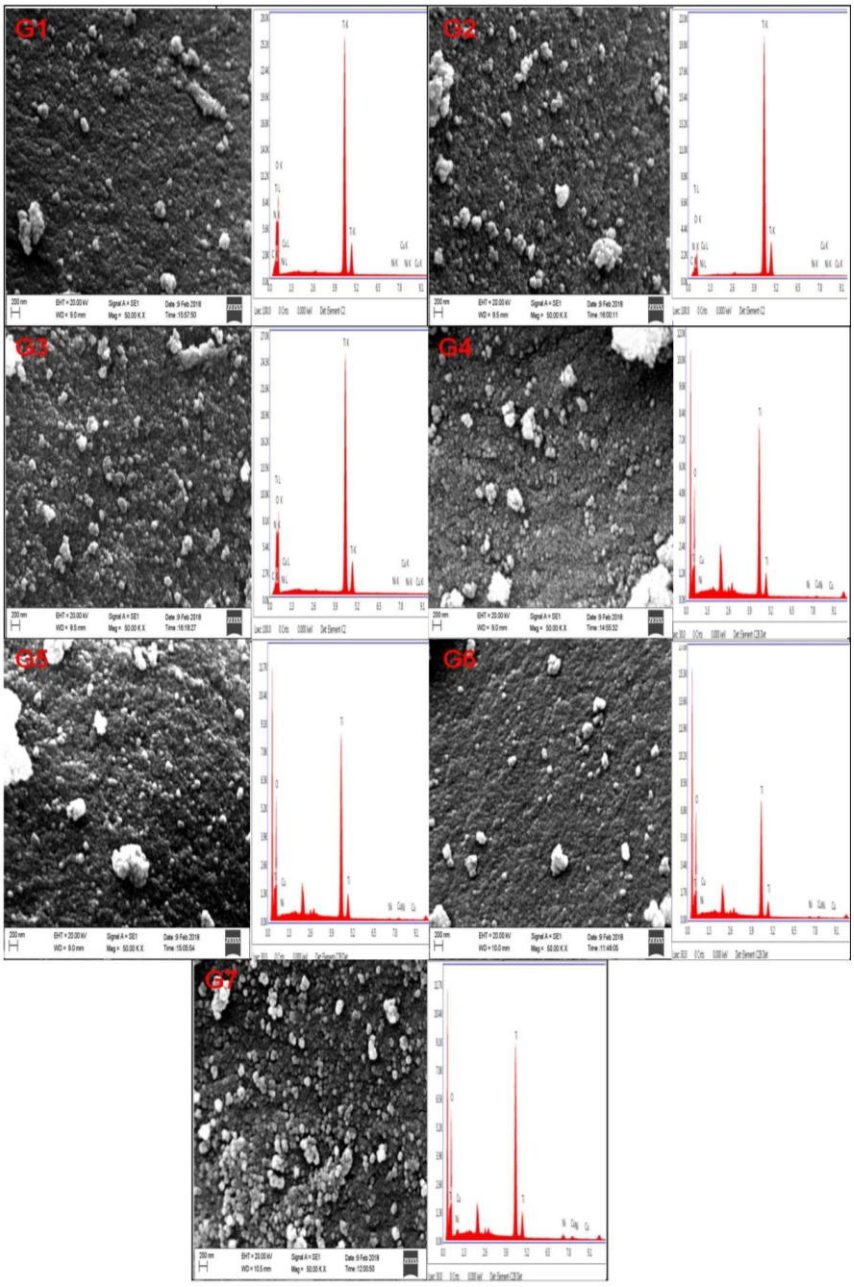

Fig. 15a— *SEM micrographs and corresponding EDX images of CuO-NiO-TiO_2 nanoparticles of series G*

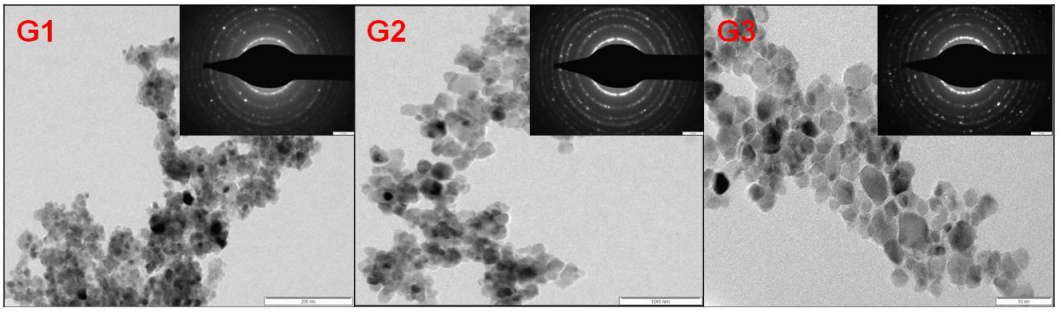

Fig. 15b— *TEM micrographs and corresponding SAED images (inset) of CuO-NiO-TiO_2 nanoparticles with lower metal % loading of series G*

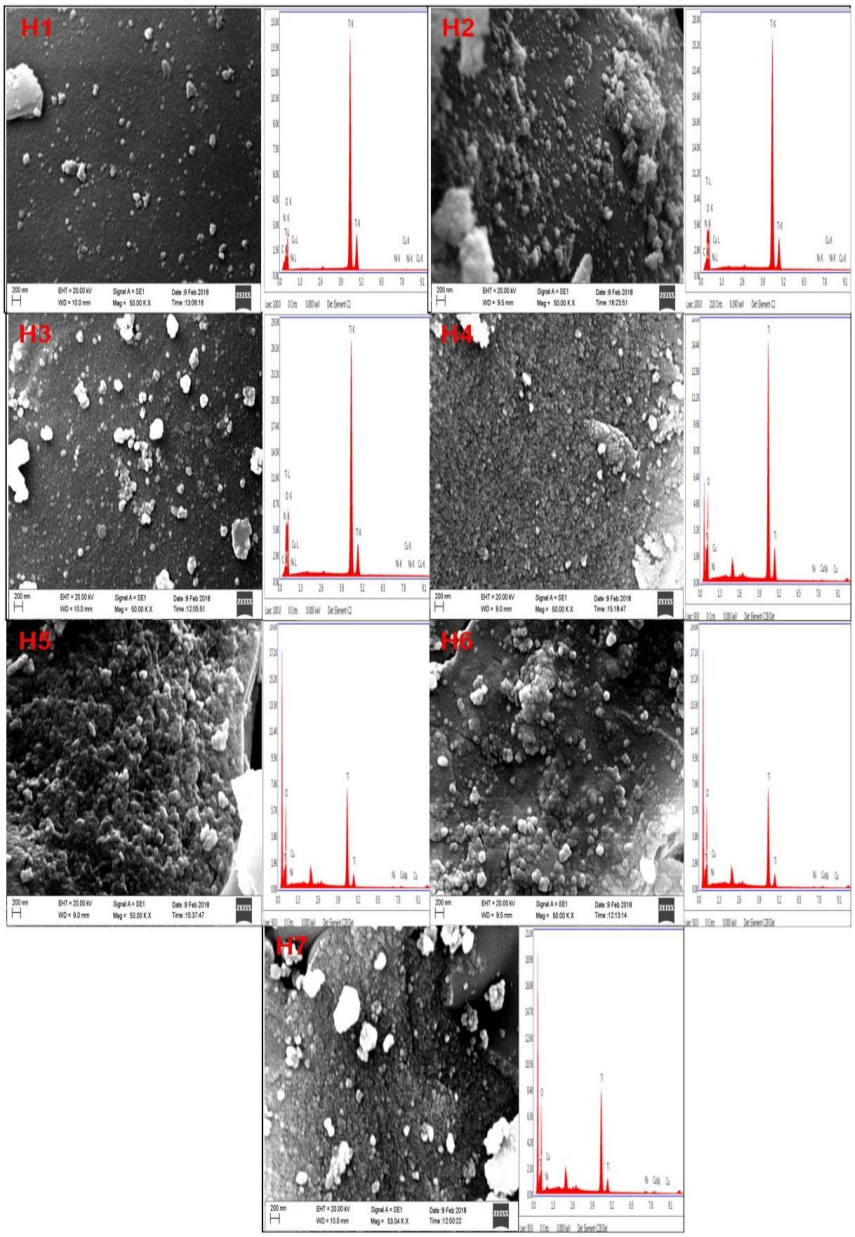

Fig. 15c— *SEM micrographs and corresponding EDX images of CuO-NiO-TiO_2 nanoparticles of series H*

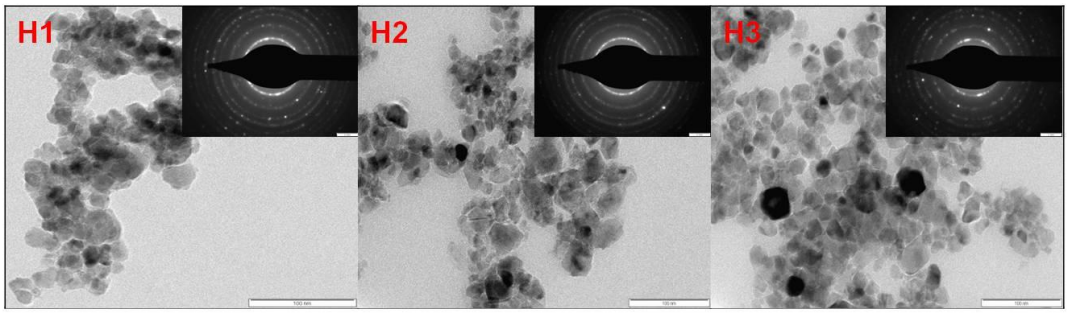

Fig. 15d— *TEM micrographs and corresponding SAED images (inset) of CuO-NiO-TiO_2 nanoparticles with lower metal % loading of series H*

Magnetic studies

The magnetic behaviors of CuO-NiO-TiO_2 samples were investigated with Vibrating Sample Magnetometry (VSM). *M-H* plots for the series G and H are given in Fig. 16a and 16b respectively, and the inset of figures shows the enlarged view of these curves. From the graph, very low hysteresis (inset) is observed, exhibiting the lower value of coercivity and remanence in all the samples. The linear variation of magnetization at higher values of the applied field, with no saturation of hysteresis loop indicates the presence of large paramagnetic moment co-existing with ferromagnetism [42,91]. The paramagnetic character is further confirmed by the low value of remanence field (M_r), suqareness in *M-H* loops [90]. The highest magnetization values observed at 3T, the values of remanent magnetization M_r and coercivity H_c for series G and H are given in Table 13a and 13b respectively.

It is observed that, the coercivity and remanent magnetization goes on decreasing with increase in metal content for series G, with abnormal increase for sample G6 (2 wt % Cu-Ni), whereas for series H, random values of M_r and H_c are seen. In this case, two decreasing trends are observed, first up to 0.1 wt % Cu-Ni and then from 0.5 to 5 wt % Cu-Ni. However, the values of magnetization are found to increase with increasing metal content, for both the series. The overall values of coercivity measured for these samples are in the range 60-246 Oe for series G and 102-228 Oe for series H, which suggest the soft magnetic behavior in these samples. The obtained values signify the existence of ferromagnetic ordering at room temperature, indicating the presence of room temperature ferromagnetism (RTFM) in theses samples [42, 108].

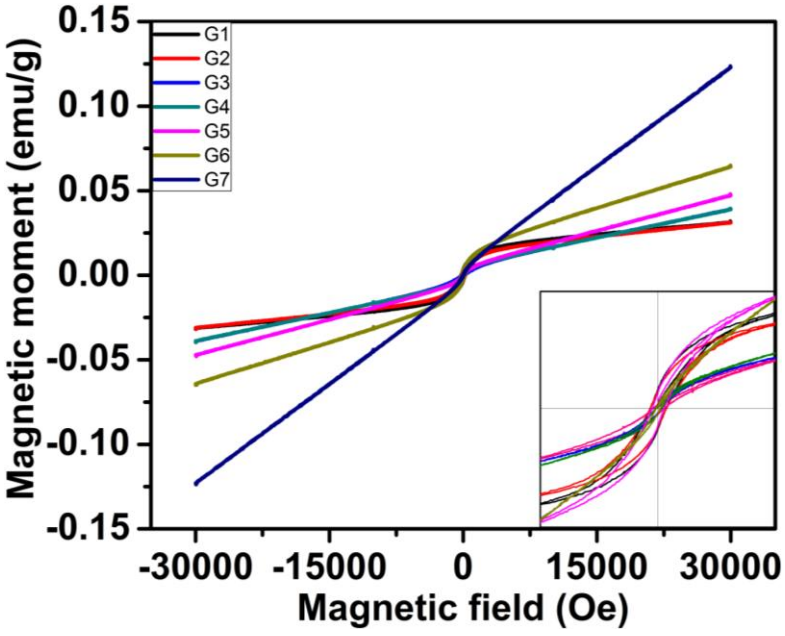

Fig. 16a— *M-H curves of CuO-NiO-TiO_2 nanoparticles at RT with enlarged view (inset) of series G*

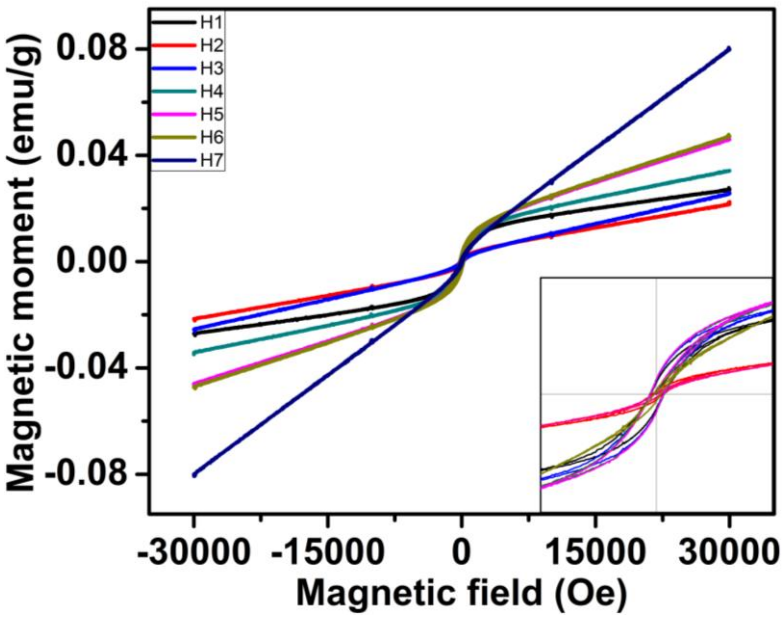

Fig. 16b— *M-H curves of CuO-NiO-TiO_2 nanoparticles at RT with enlarged view (inset) of series H*

In literature, it is reported to rise in magnetization for Ni-TiO_2 up to 2 wt % doping, while it decreases with further increase in Ni content [109]. This disappearance of magnetization nature at a higher dopant concentration could be due to the ionic interactions of the neighboring metal ions.

Both the individual doped systems, Cu-TiO_2 and Ni-TiO_2, are reported with the co-existence of ferro- and paramagnetic components, and the dominating paramagnetic phase over ferromagnetism is observed for Cu-TiO_2 systems with increasing Cu concentrations [90-91].

It is observed that the individual magnetic properties of these dopant species (antiferromagnetic nature of CuO and NiO) are not displayed on incorporation into TiO_2, which suggest that, the observed RTFM is an intrinsic property of the sample due to the incorporation of these dopants, which could possibly have exchange interactions on substituting Ti in the lattice [89 ,91].

Table 13a – Magnetic properties for series G

Sample	Unsaturation magnetisation (emu/g)	Remanance magnetisation (emu/g)	Coercivity (Oe)
G1	0.032	0.0035	246.57
G2	0.031	0.0032	242.16
G3	0.039	0.0009	171.08
G4	0.039	0.0006	84.98
G5	0.048	0.0007	84.98
G6	0.065	0.0029	179.62
G7	0.125	0.0006	59.62

Table 13b – Magnetic properties for series H

Sample	Unsaturation magnetisation (emu/g)	Remanance magnetisation (emu/g)	Coercivity (Oe)
H1	0.028	0.0020	184.40
H2	0.023	0.0007	161.96
H3	0.026	0.0004	110.64
H4	0.034	0.0030	203.96
H5	0.046	0.0029	227.72
H6	0.048	0.0028	221.28
H7	0.081	0.0009	101.98

IR studies

The IR spectra of all calcined TiO_2 samples show the presence of surface hydroxyl groups and /or adsorbed water for both the series (Fig. 17a and 17b). The characteristic stretching frequency of –OH group can be seen between 3000-3500 cm^{-1} and the corresponding bending vibrations at 1600 cm^{-1}. The metal oxide bands seen at 500 cm^{-1} are of Ti-O stretching. No bands are seen corresponding to the isopropyl group and also the acetate group suggesting, complete removal of the organic part.

IR spectra of precursor samples for both the series displayed distinct bands at 3000-3500 cm^{-1} and ~1600 cm^{-1} of the metal hydroxide and water (Fig. 17c and 17d). In addition to this, the bands at around 1100-1600 cm^{-1} are seen, clearly indicating the presence of organic functionality, *i.e.* isopropyl group and acetate group.

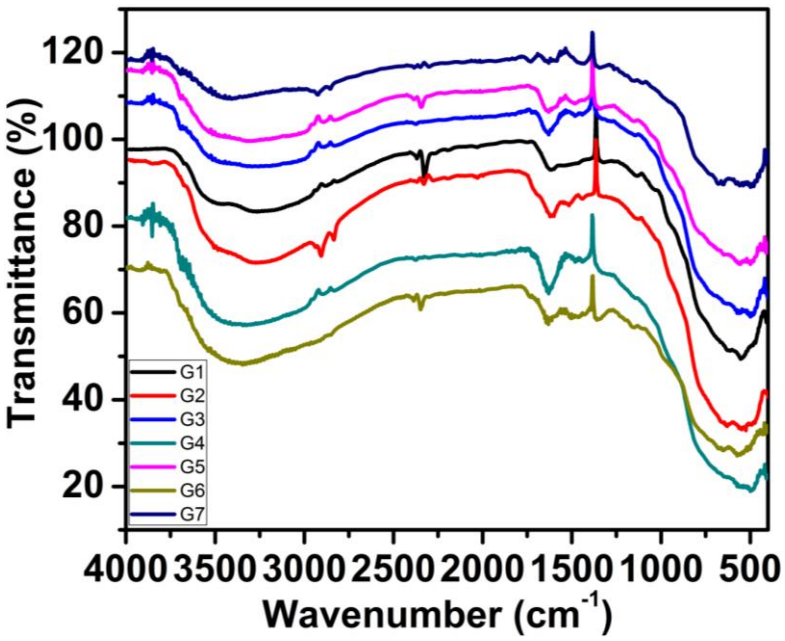

Fig. 17a—*IR spectra of calcined samples of series G*

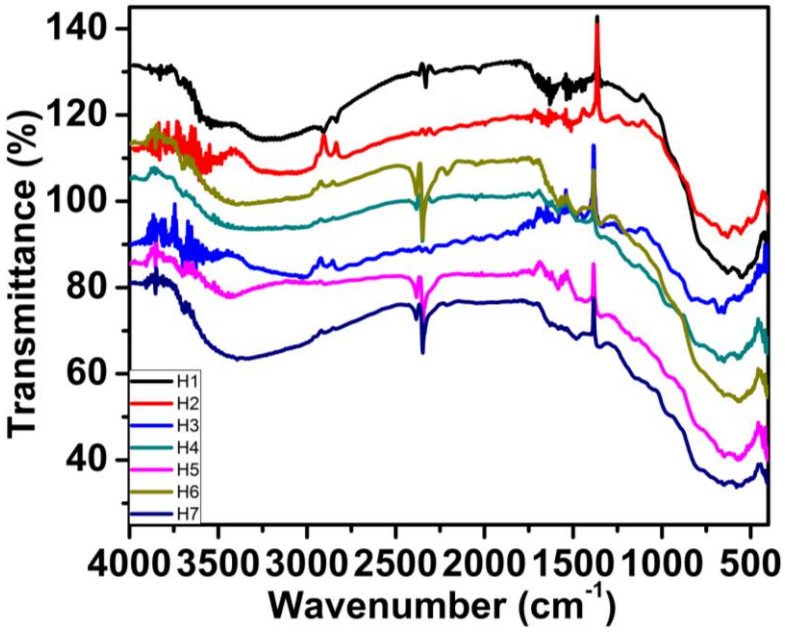

Fig. 17b—*IR spectra of calcined samples of series H*

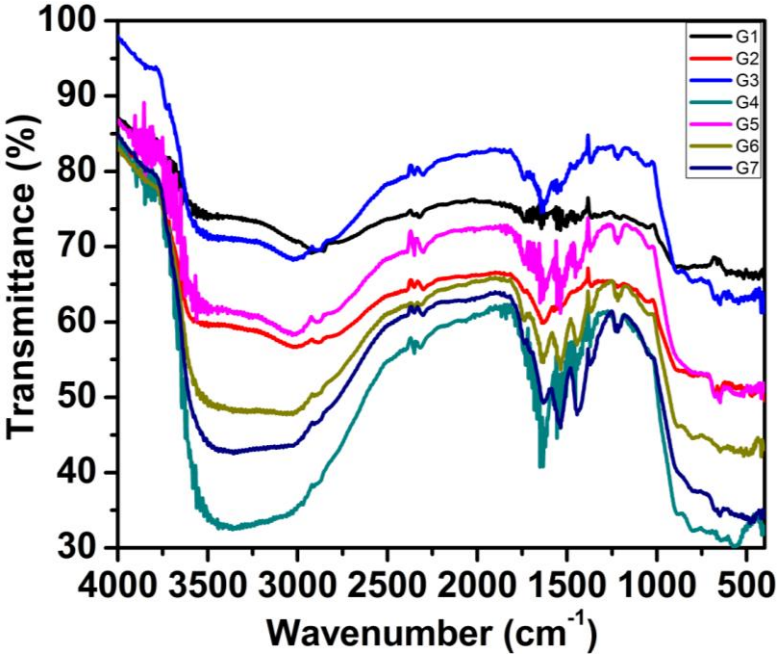

Fig. 17c—*IR spectra of precursor samples of series G*

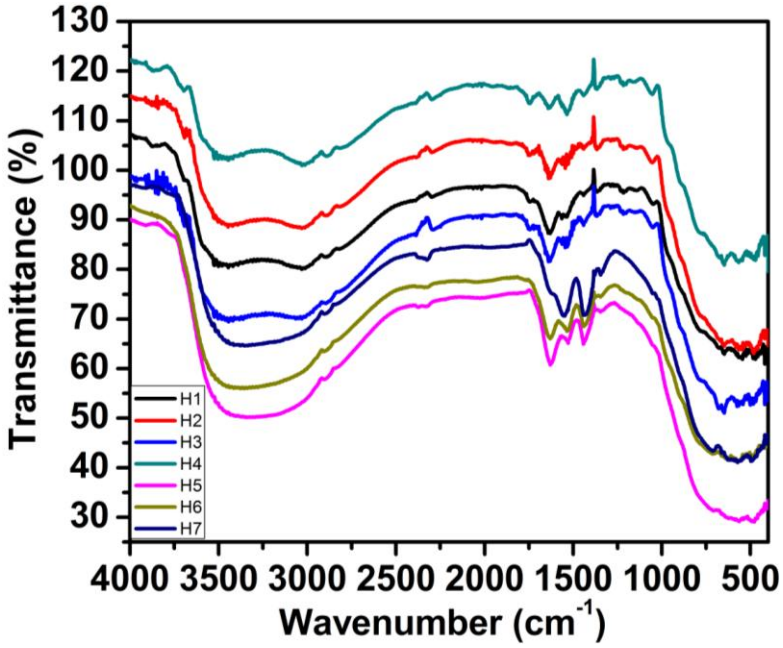

Fig. 17d—*IR spectra of precursor samples of series H*

Photocatalytic activity testing

The photocatalytic activity of the obtained samples was studied by the degradation of methylene blue, which is the most studied azo dye for comparing catalytic activity. Fig. 18a and 18b respectively displays the comparative catalytic activity under natural sunlight irradiation for samples of series G and H, in comparison with Degussa P25 as a standard.

It can be seen that, the samples G1, G2, G3 of series G and H1, H2, H3 of series H display better photocatalytic activity compared to Degussa. The highest degradation rate is observed for samples G2 and H2 (0.05 wt % Cu-Ni). Thus, we can say that the catalysts with lower metal insertion (0.01-0.1 wt Cu-Ni) are the suitable candidate for degradation of MB. It can be seen that, these samples though have bigger crystallite sizes with lesser absorption wavelengths and lower values of the magnetization, are more photo-active among respective series. The random values of surface area and pore volume cannot be related to photo-degradation results. Hence the observed photocatalytic activity can be solely attributed to the low Cu-Ni dopant concentration of these catalysts.

It is observed that, the bimetallic dopant species, CuO-NiO, efficiently improves the properties of host TiO_2 material. The increased magnetization values, greater shift in absorption wavelength and decreasing crystallite sizes are clearly seen with increasing metal concentration. The decrease in degradation rate with increasing metal concentration can be accounted for surface blocking of active sites of the catalyst at higher metal concentration. Also, Cu/Ni at higher concentration may themselves act as recombination center, thus reducing the photocatalytic efficiency of the catalyst [110].

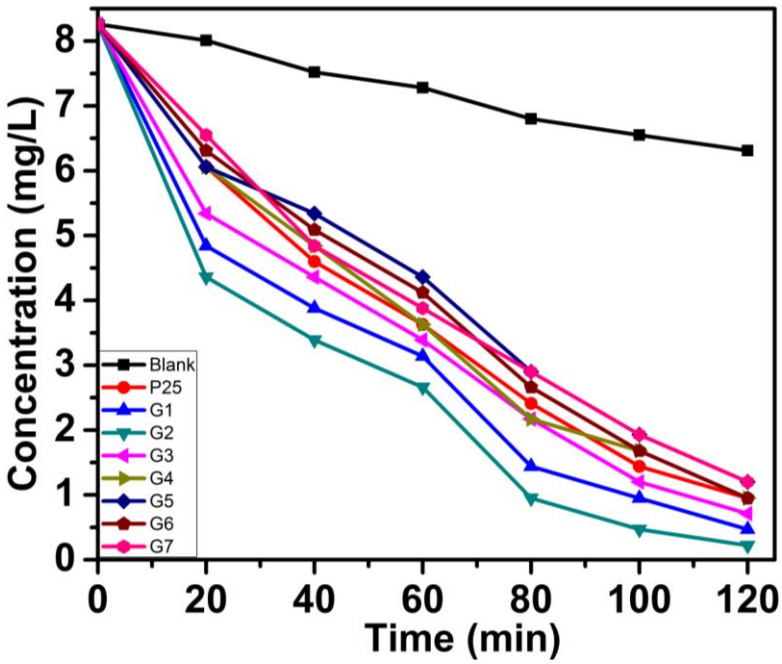

Fig. 18a— *Methylene blue degradation plots for series G*

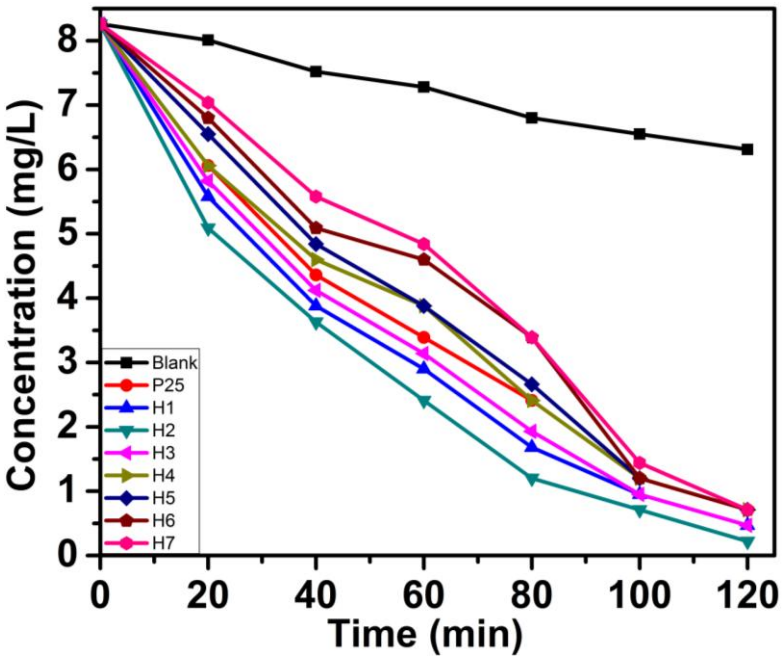

Fig. 18b— *Methylene blue degradation plots for series H*

A plot of ln (C_0/C_t) versus time for both the series (Fig. 18c and 18d), represents a straight line which indicates the photocatalytic degradation follows a pseudo first order kinetics. The rate constants derived from the plot are given in Table 14. The apparently higher rate of degradation is observed for samples G2 and H2, and is further goes on decreasing with increasing metal concentration. The observed data are in accordance with the other results.

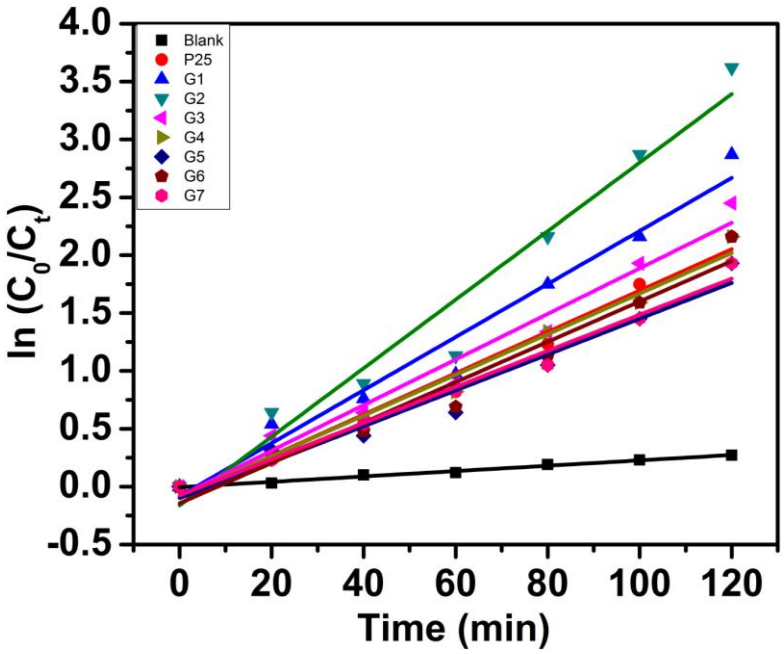

Fig. 18c—*Kinetic studies MB degradation for series G*

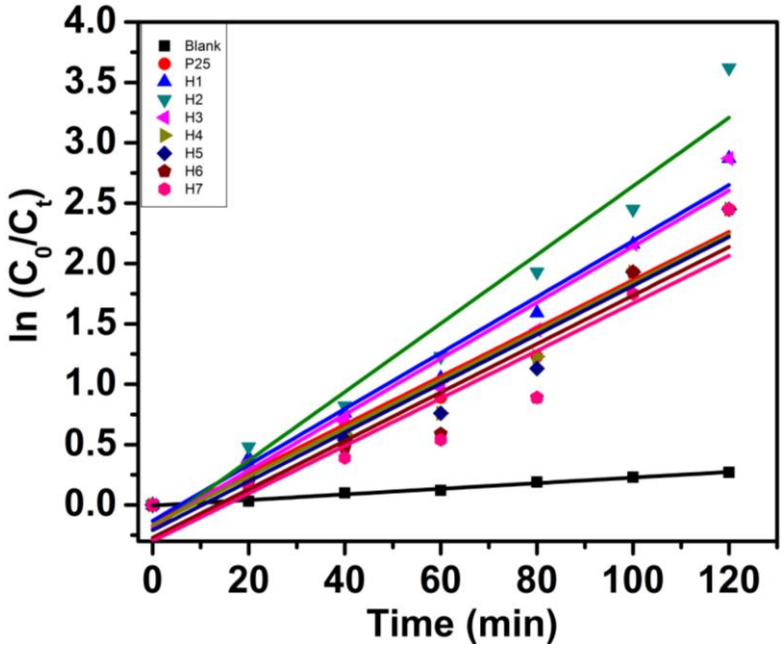

Fig. 18d—*Kinetic studies MB degradation for series H*

Recyclability studies were done for three cycles for the samples showing better degradation results, of both the series, after separating the catalyst by centrifugation. The graphical results are displayed in Fig. 18e and 18f respectively, for series G and H. All the samples could be reused for degradation with negligible loss in activity.

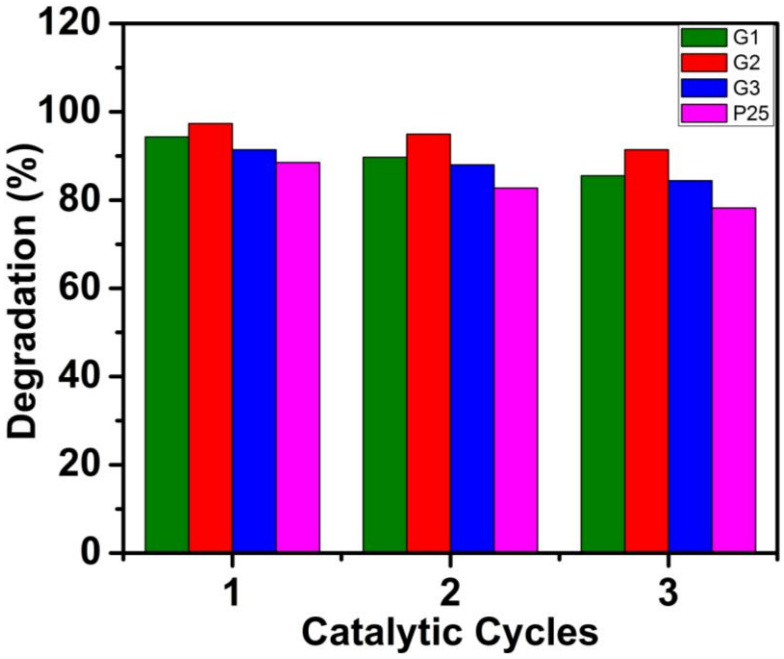

Fig. 18e—*Recyclability studies for the samples showing better results for series G*

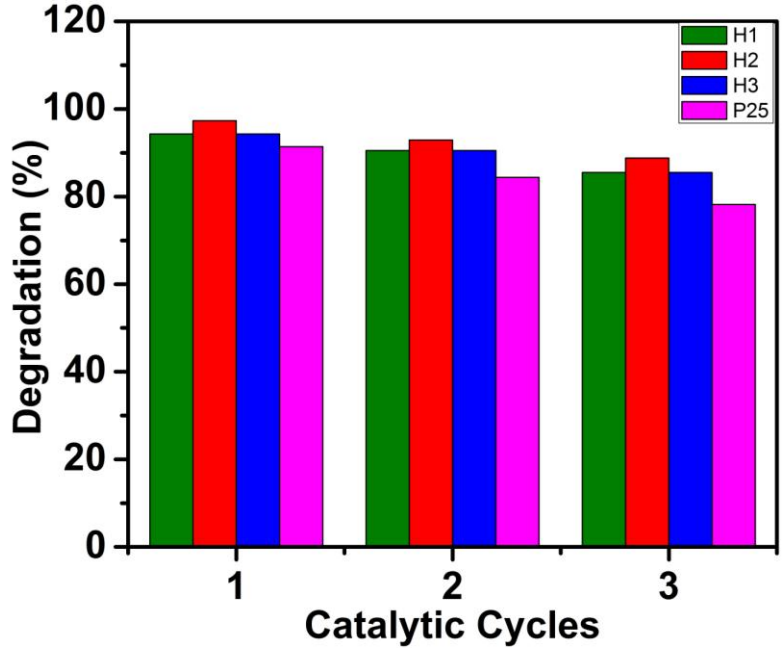

Fig. 18f—*Recyclability studies for the samples showing better results for series G*

Table 14 –Kinetic studies

Sample	Rate constant k (min-1)	Sample	Rate constant k (min-1)
G1	0.0229	H1	0.02318
G2	0.0296	H2	0.02841
G3	0.0197	H3	0.02320
G4	0.0176	H4	0.02005
G5	0.0155	H5	0.02025
G6	0.0174	H6	0.02007
G7	0.0156	H7	0.01970
P25	0.0179	P25	0.01996

Catalytic Reduction

The sample with higher metal loading (5 wt %) was studied for the sodium borohydride mediated reduction reaction. *p*-Nitrophenol is an industrial pollutant discharged by pesticide, herbicide, insecticide and dye industries [111]. Hence, the reduction of it to *p*-aminophenol which gets degraded faster is very important in the effluent treatment strategies. Also, *p*-aminophenol is an industrially important raw material in many industries. Hence *p*-nitrophenol was chosen as a substrate for the reductions studies. Efficient conversion of *p*-nitrophenol to *p*-amino phenol was observed in 5 min. The recyclability was studied up to 3 cycles, with a slight increase in reduction time for subsequent reduction. The product obtained was monitored by TLC and further confirmed by NMR spectroscopy. The obtained spectra for *p*-nitro phenol (substrate) and *p*-amino phenol (product) is given in Fig. 19a and 19b respectively.

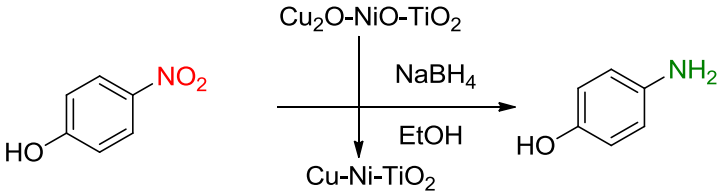

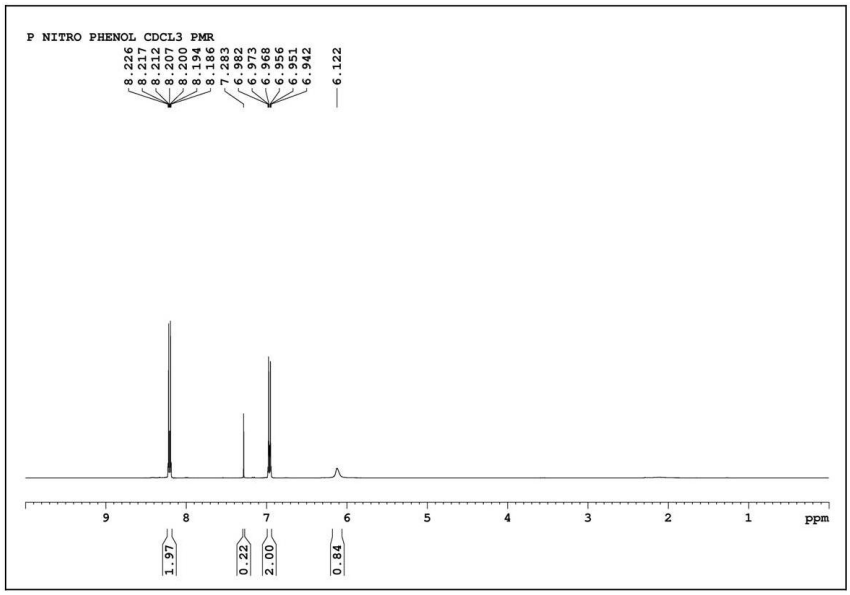

Fig. 19a—*NMR spectra for p-nitro phenol (substrate)*

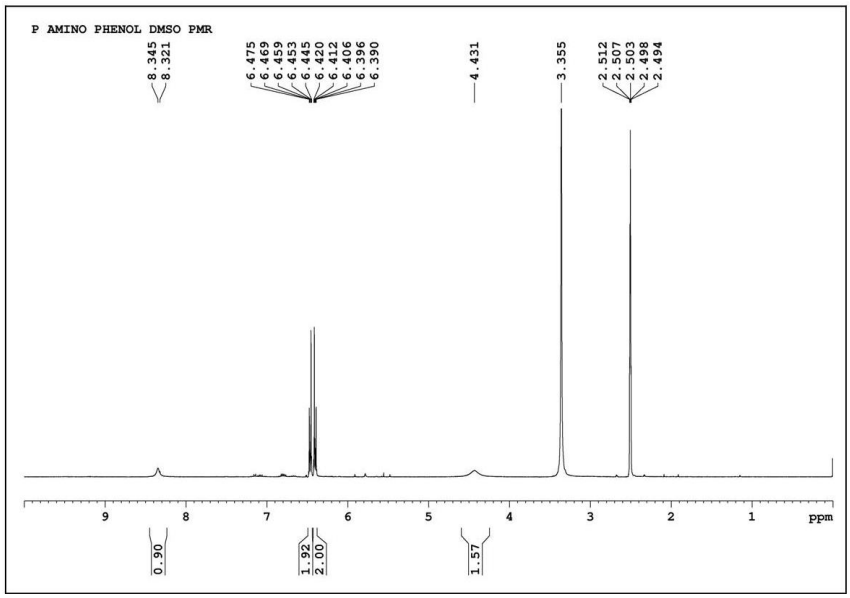

Fig. 19a—*NMR spectra for p-amino phenol (product)*

Summary and Conclusion

CuO-NiO-TiO_2 nanoparticles with 1:1 Cu:Ni ratio and varying M:Ti concentration, were prepared by employing two different preparation methods. The degradation studies reveal that, photo-degradation efficiency of these catalysts is solely depends on the percentage of Cu-Ni dopants, irrespective of the other properties and catalyst with low metal dopants are observed to display better photocatalytic activity. The optimum doping concentration for photo-degradation is observed to be 0.05 wt %. Further the catalyst with higher of metal loading (5 wt %) was efficiently used for nitro reduction.

Magnetic studies show that the samples exhibit room temperature ferromagnetism (RTFM) co-existing with paramagnetism, which in turn is responsible for the observed unsaturation of the hysteresis loop. A linear increase in magnetization values (at 3T) is observed with increasing metal doping concentration. The properties of the catalysts for series G and H are summarized respectively in Table 15a and 15b.

Table 15a – Summary of the properties of CuO-NiO-TiO_2 nanoparticles for series G.

Sample	Cryst. size (nm)	BJH surf. area (m^2/g)	Pore vol. (cc/g)	High. mag. value (emu/g)	M_R (emu/g)	H_c (Oe)	λ_{max} (nm)	Rate const. k (min^{-1})
G1	14.65	43.50	0.059	0.032	0.0035	246.57	392.2	0.0229
G2	14.38	60.00	0.096	0.031	0.0032	242.16	387.9	0.0296
G3	14.48	93.95	0.156	0.039	0.0009	171.08	395.6	0.0197
G4	12.93	101.93	0.177	0.039	0.0006	84.98	397.2	0.0176
G5	11.88	70.70	0.097	0.048	0.0007	84.98	427.9	0.0155
G6	11.15	90.58	0.126	0.065	0.0029	179.62	453.9	0.0174
G7	13.73	72.23	0.191	0.125	0.0006	59.98	464.2	0.0156
P25	25.00	56.00	0.250	---	---	---	370.7	0.0179

Table 15b – Summary of the properties of CuO-NiO-TiO_2 nanoparticles for series H.

Sample	Cryst. size (nm)	BJH surf. area (m^2/g)	Pore vol. (cc/g)	High. mag. value (emu/g)	M_R (emu/g)	H_c (Oe)	λ_{max} (nm)	Rate const. k (min^{-1})
H1	17.05	31.90	0.035	0.028	0.0020	184.40	534.9	0.02318
H2	17.52	32.02	0.036	0.023	0.0007	161.96	492.0	0.02841
H3	13.85	58.50	0.073	0.026	0.0004	110.64	411.3	0.02320
H4	17.58	11.03	0.011	0.034	0.0030	203.96	479.4	0.02005
H5	19.51	5.31	0.006	0.046	0.0029	227.72	554.2	0.02025
H6	15.84	11.55	0.012	0.048	0.0028	221.28	582.6	0.02007
H7	16.33	24.31	0.027	0.081	0.0009	101.98	546.8	0.01970
P25	25.00	56.00	0.250	---	---	---	370.7	0.01996

Section C – CuO-NiO-N-incorporated TiO_2

After studying non-metal doped and bi-metallic co-doped TiO_2 systems we thought of studying tri-doped system, with bi-metal and a non-metal combination. Such combinations seem to be more promising due to the cooperative impact of three individual species on the parent support material and are therefore in high demand in recent years for improving catalytic activity.

Wide literature work is available with metal and non-metal combination with TiO_2. Nitrogen is claimed to be an effective non-metal dopant even for a combined system, mainly because of its similarity in size with the oxygen atom and low ionization energy.

Recently, many reports demonstrating various strategies to synthesize the co-doped TiO_2 with nitrogen and transition metal as the modifying substances and their applications in photocatalytic dye degradation or H_2 generation have been published [112-120].

According to theoretical studies, the transition metal doping alters the density of electronic states below the conduction band edge, and introduces impurity levels at the top of the VB which help reduce the recombination rate of charge carriers, while the p-orbitals of nitrogen populate the gap just above the valence band edge [112]. The combination of N with these metals is thought to be effective due to the synergistic effect of these two elements. Moreover, the simultaneous incorporation of n- and p-type dopants with unequal charge states helps in stabilizing these dopants due to electrostatic attraction between them [119].

The combined system of nitrogen with copper [121-125] or nickel [126-128] for high photocatalytic activity is reported in literature.

Comparative results of co-doped systems of nitrogen with various transition metal ions for dye degradation reveal that, N-Cu-TiO_2 displays much higher photo-activity than N-Ni-TiO_2. This may be due to the difference in the exhibited band-gap energies of the two systems of these two metals. However, the shift in absorbance in the visible region is observed to increase by increasing nickel doping concentration [113]. The optimum doping concentration for M-N co-doping is reported to be 2.5 %, above which the photocatalytic activity, is found to decrease in comparison with the N-doped samples [114].

In this section, we have discussed the mutual effect of combining the earlier two systems, bimetallic CuO-NiO and N with TiO_2 and investigated this reconstructed tri-doped system for photocatalytic performance. This newly designed system was expected to be more rewarding in terms of photocatalytic effectivity. So far, no reports are available in the literature for this combined system.

Structural, optical and morphological analysis

Powder X-ray studies

For the analysis of phase composition, crystalline nature and crystallite size of the prepared TiO_2 samples, X-ray powder diffraction technique was used. Fig. 20a and 20b presents the XRD pattern of calcined TiO_2 powders of series I and J respectively. Sharp and well-defined peaks, indicates the highly crystalline nature of these catalysts.

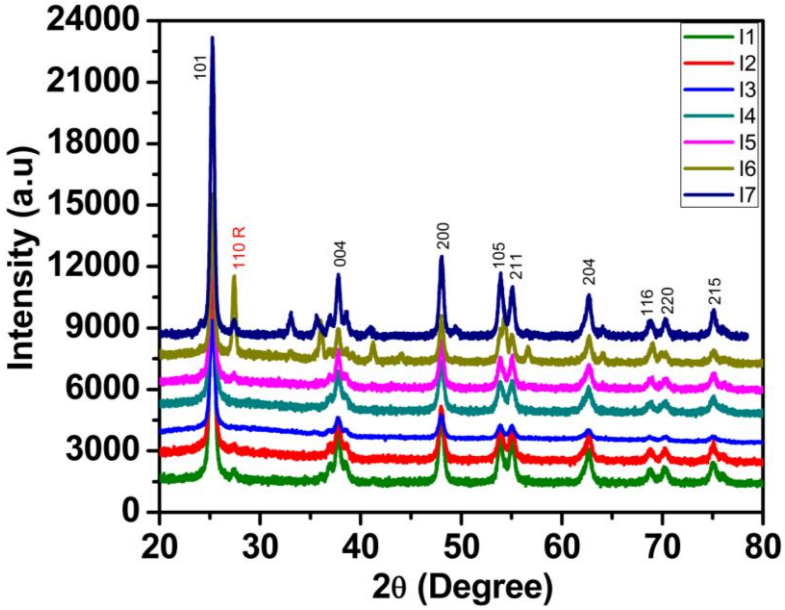

Fig. 20a—*XRD plots for the calcined samples of series I*

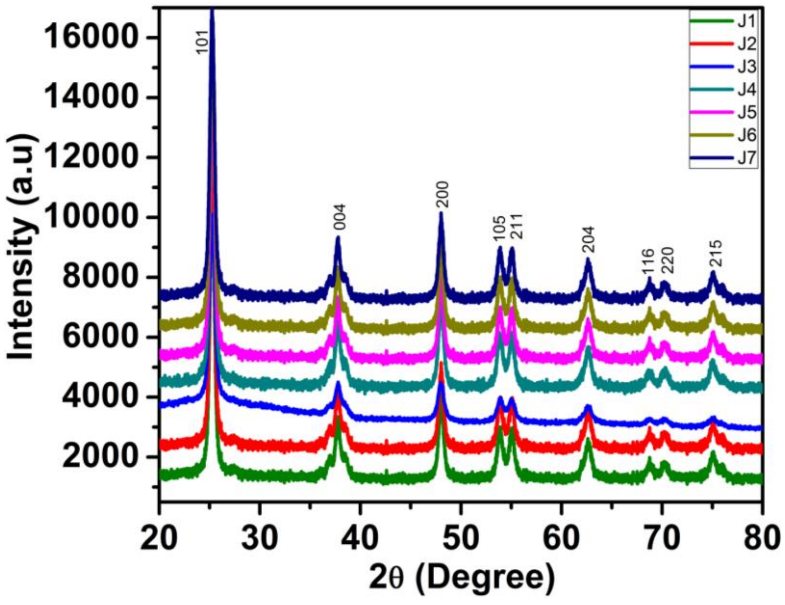

Fig. 20b—*XRD plots for the calcined samples of series J*

The peak positions and their relative intensities for these samples suggest the presence of anatase as a major phase. Pure anatase phase with the consistent powder diffraction patterns (JCPDS card # 21-1272), is clearly seen for series J, with the main peak at 25.27° corresponding to the (101) plane. While, for series I, sample I6 (2 wt % Cu-Ni) show anatase-rutile, mixed phases with 34.05 % of rutile content, as calculated using eq. **3**.

Moreover, for series I, sample I7 with highest metal concentration (5 wt %), shows the appearance of two small peaks at 32.8 and 35.6 (marked with *), corresponding to (110) and (111) respective planes of CuO monoclinic crystalline phase (ICDD file no. 80- 1916). However, peaks due to the Ni species were not seen, though both the dopants are in equal concentration. This observation is identical to that of CuO-NiO doped TiO_2 system discussed in the earlier section. Since Cu^{2+} is reported to distort TiO_2 lattice to some extent due to the differences in their ionic radius (Cu^{2+} - 0.87 Å and Ti^{4+} - 0.74 Å), the peak visible at higher metal concentration (5 wt %) is an evidence for successful incorporation of Cu metal ions into TiO_2 lattice. The absence of any additional peak corresponding to Ni species, may be attributed to the similar ionic radius of these species (Ni^{2+} - 0.72 Å), thus imparting no such distortion to the perfect lattice structure of TiO_2. These observations are also noted for individual M-ion doping from the literature reports [19, 105].

No additional peaks other than of TiO_2 due to Cu/Ni species are observed for series J suggests that, the metal particles are well scattered on the surface of TiO_2.

In order to confirm the lattice incorporation of CuO/NiO into TiO_2, the details of intensity of peaks (004) and (200) are studied. The increasing intensity of (004) peak and corresponding decrease in (200) peak due to Cu^{2+} incorporation into TiO_2 resulting in a decreased intensity ratios of I_{101}/I_{004} and I_{101}/I_{200}, as the Cu concentration is increased, is already mentioned in the literature [91]. In our case, the varying intensity ratios are observed for series I, while almost constant values of ratio are seen in series J. For series I, the expected decrease in the intensity ratios of I_{101}/I_{004} is observed for increasing metal doping from 0.1 to 5 wt %, clearly indicating the incorporation of CuO-NiO species into TiO_2 lattice in this series. The exceptions observed for samples with low metal content may be due to the presence of N-dopant species, which seems to dominate when the metal content is very low. Almost constant values of intensity ratio are observed in series J, with the exception for sample J3 (0.1 wt %), which further supports the surface dispersion of CuO-NiO on TiO_2 matrix. This prediction is in agreement with the observed absence of peaks of Cu/Ni species in the XRD pattern of this series even with 5 wt % metal concentrations.

The average crystallite sizes for both the series as determined from (101) diffraction peak (the most predominant highest intensity peak), as calculated using Scherrer formula (eq. **1**), are found to be in the range of 14-20 nm for series I (Table 16a) and 12-18 nm for series J (Table 16b). The synthesized samples were found to be smaller in size as compared to Degussa P25 (25 nm).

It is observed that, the crystallite size goes on increasing with increase in metal concentration from 0.1 to 5 wt % Cu-Ni doping, with the exception of samples with low metal content (0.01 and 0.05 wt %) for both the series. The observed anomalous behavior to that of Cu-Ni co-doped TiO_2 series (Section 2) can be attributed to the presence of nitrogen as a dopant element. Also, similarity in sizes is observed for the samples prepared by the two different methods indicate that the presence of nitrogen species may be stabilizing the surface to bulk interactions.

The corresponding values of strain responsible for fluctuations observed in crystallite sizes [43], are calculated using the eq. **2**. Strain is inversely proportional to the crystallite size and has direct impact on mobility of charge carriers and hence photo-activity of the catalyst. The lesser value of strain accelerates free carrier mobility in the host lattice. In this case, the strain values are found decreasing with corresponding increase in size from 0.1 to 5 wt % metal loading, whereas slight increase is observed for initial low metal content samples. This anomaly is corresponding to the decrease in crystallite sizes for these samples with low metal concentration. The strain values for series I and J are respectively given in Table 16a and 16b.

Table 16a – Crystallite studies for series I

Sample	**Crystallite size (nm)**	**Lattice strain**	**Peak intensities ratios** I_{101}/I_{004}	I_{101}/I_{200}
I1	18.49	0.0090	6.962	4.080
I2	17.12	0.0097	6.875	4.164
I3	14.69	0.0113	8.205	5.323
I4	15.41	0.0108	6.702	4.113
I5	17.36	0.0095	6.685	3.916
I6	19.83	0.0084	5.966	4.174
I7	20.75	0.0080	5.630	3.846
P25	25.00	--	--	--

Table 16b – Crystallite studies for series J

Sample	Crystallite size (nm)	Lattice strain	Peak intensities ratios I_{101}/I_{004}	I_{101}/I_{200}
J1	17.12	0.0097	6.519	3.924
J2	16.55	0.0100	6.449	3.840
J3	12.15	0.0140	7.340	5.584
J4	14.92	0.0110	6.645	3.966
J5	17.12	0.0097	6.836	3.877
J6	17.15	0.0097	6.769	3.887
J7	18.10	0.0091	6.941	3.972
P25	25.00	--	--	--

UV-DRS studies

The absorption spectra of series I and J samples are respectively shown in Fig. 21a and 21b. From the graphs, the extended absorption peaks in the visible region up to 800 nm are observed almost for all samples, which can be ascribed to the successful insertion of Cu-Ni in TiO_2 matrix, whereas the significant absorption peaks are seen in the lower region below 400 nm can be assigned to the intrinsic band-gap of TiO_2. The red shift observed in absorption wavelength found increasing with increased dopant concentration, which is considered to be the effect of presence of CuO-NiO in TiO_2, with the exception of sample I2 (0.05 wt %) of series I and J1 (0.01 wt %) and J2 (0.05 wt %) of series J.

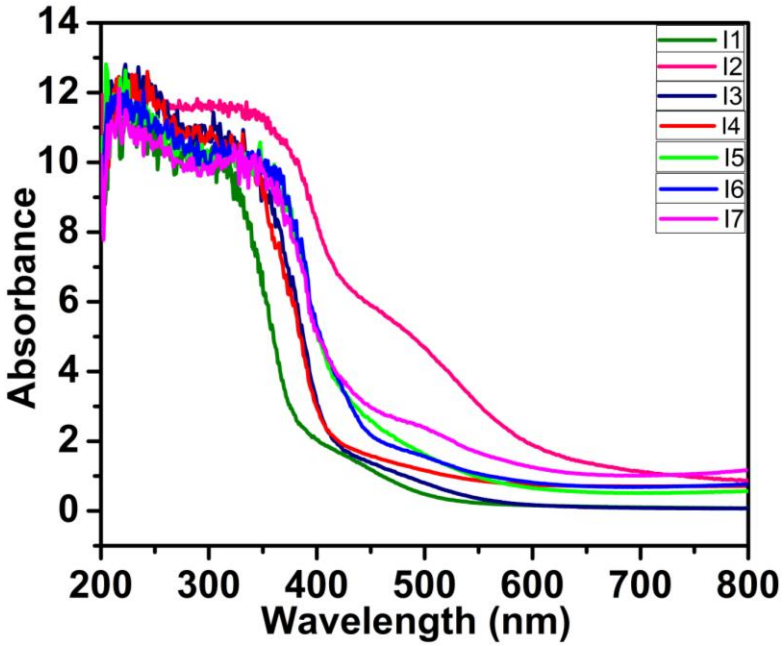

Fig. 21a—*UV-DRS spectra of calcined samples of series I*

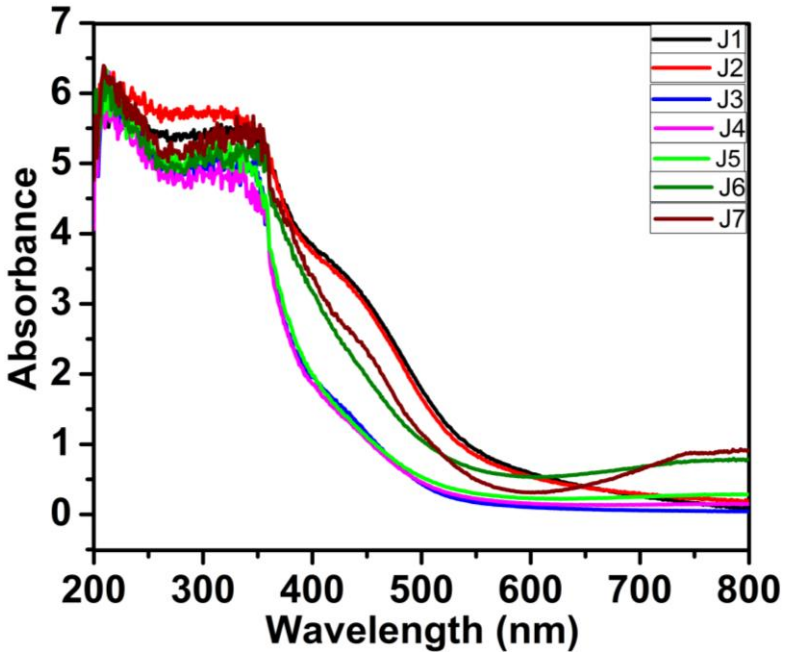

Fig. 21b—*UV-DRS spectra of calcined samples of series J*

The fluctuating and random values of absorption wavelength can be seen in both the series, while the exceptional huge shift in absorption wavelength is observed for sample I2, J1 and J2. The lowest value of λ_{max} is observed for sample I4 (0.5 wt %) and thereafter increases till 5 wt % metal loading, in case of series I. For series J, the lowest value of λ_{max} is observed for sample J5 (1 wt %). From these results, it can be said that, initially, at lower metal doping, N is responsible for enhanced red shift observed. While at higher metal loading, the effect of N is slightly lowered by equally effective metal ions. The XRD analysis of these samples also showed different behavior *(vide supra).*

An additional peak is also observed in the region of 600-800 nm for all the samples, which is purely due to CuO-NiO incorporation and is in accordance with that reported in the literature for individual Cu/Ni doping. The weak absorption peaks in this region are considered to be the effective interaction of d-d transitions of the dopant ions with the crystalline environment of TiO_2 [107]. The dopant concentration is found to show a direct impact on the intensity of this peak, which goes on increasing with the increase in dopant concentration. The exception is seen for sample I2 (0.05 wt %), which display slightly higher intensity for these bands compared to samples with 0.05 and 0.1 wt % of dopants in series I. A similar trend is also seen for samples J1 and J2 of series J, in comparison with sample J3.

This observed enhanced visible light absorption can be assigned to the electronic transitions resulted due to the formation of new energy level in the band-gap of TiO_2, between the valence band and these intra-band energy levels [91].

In addition to this a slight bulge is observed in the region 400-550 nm which may be attributed to N-dopant in the sample. A similar trend of bulging intensity with increasing metal concentration is observed in this case, with the exception of samples I2, J1 and J2. These observations suggest that the effect of nitrogen predominates and probably suppresses the effect Cu-Ni species when they are present in very low concentrations.

An overall higher shift in absorbance wavelength is observed for series J, compared to that of the series I, with abnormally higher shift for samples J1 and J2 (up to 600 nm) and can be attributed to the layer formation of dopant species on the surface of TiO_2 in case of series J, whereas that of incorporation CuO-NiO into N-TiO_2 lattice in case of series I. This observation further supports the observations drawn from the XRD analysis.

The band-gap energies (*Eg*) of these samples were calculated by the eq. **4** and are found to be in the range 2.6 to 3.1 eV for series I and 2.0 to 2.7 eV for series J (Table 17).

Table 17 – Band-gap energies

Sample	**Band-gap (eV)**	**λ_{max} (nm)**	**Sample**	**Band-gap (eV)**	**λ_{max} (nm)**
I1	3.09	401.2	J1	2.03	610.8
I2	2.59	477.8	J2	2.04	606.4
I3	3.05	406.3	J3	2.71	457.4
I4	3.14	394.8	J4	2.59	478.7
I5	2.84	436.1	J5	2.64	470.3
I6	2.81	440.3	J6	2.23	556.9
I7	2.71	457.4	J7	2.19	567.0
P25	3.35	370.7	P25	3.34	370.7

BET analysis

The typical plot of N_2 adsorption-desorption isotherm for series I and J respectively are shown in Fig. 22a and 22b with corresponding pore size distribution curves (inset).

The isotherm curves can be classified as typical of a mesoporous material of the type IV associated with capillary condensation taking place within mesopores, as per the IUPAC classification. Further, the BJH adsorption/ desorption analysis reveal that, the hysteresis loop is of H3-type with broad pore size distribution curve in the mesoporous region (2-50 nm), for all the samples of series I. This observation indicates the highly mesoporous nature of these nanoparticles, forming slit-like pores. The nature of hysteresis loops with limiting uptake over a range of high P/P_0 reaching up to 1, an upward deviation can be attributed to capillary condensation in mesopores. A slightly unusual behavior is noticed for samples I6 and I7 at a low relative pressure (P/P_0 <0.6) after the lower closure point, which imparts the

low value of surface areas for these samples. For series J, H2-type hysteresis loop with narrow pore size distribution is observed, indicating the presence of well-defined ink-bottle shaped pores, in all the samples except J2 and J7, for which H3-type loop is seen. This type of hysteresis loop further reveals the existence of hierarchically structured porous materials with a filled pore neck of smaller diameter [129].

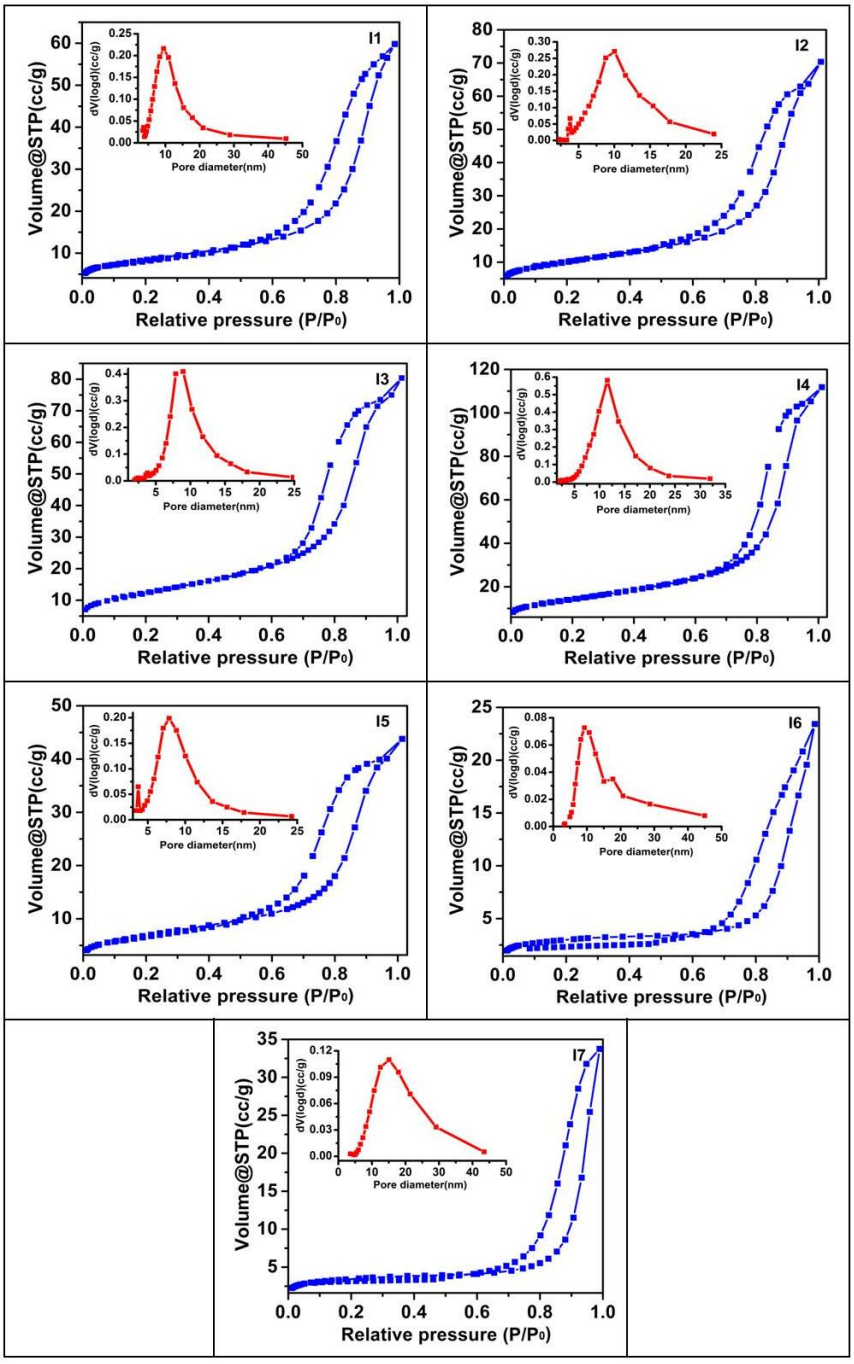

Fig. 22a—*Nitrogen adsorption-desorption isotherms and pore size distribution (inset) of CuO-NiO-TiO_2 nanoparticles of series I*

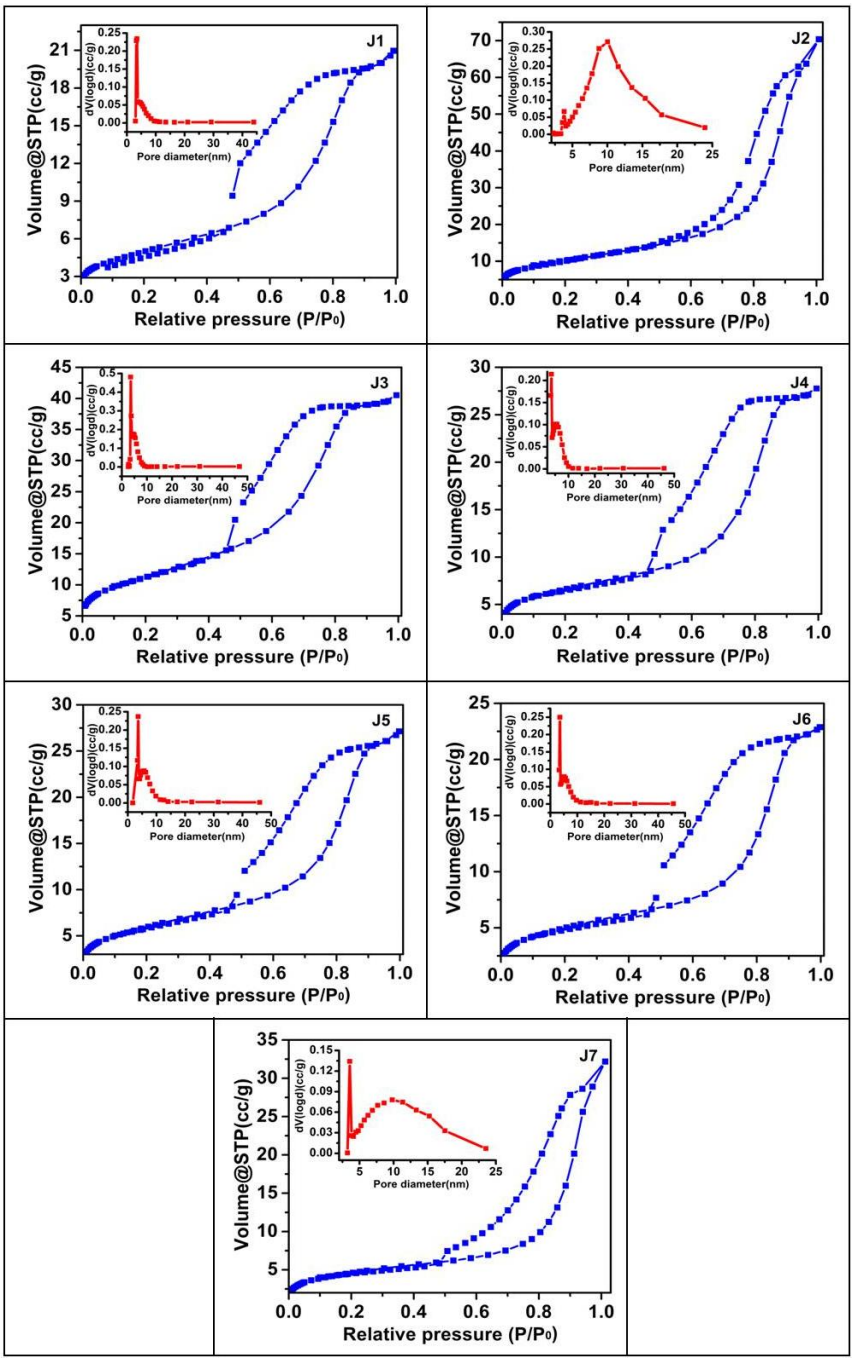

Fig. 22b—*Nitrogen adsorption-desorption isotherms and pore size distribution (inset) of CuO-NiO-TiO_2 nanoparticles of series J*

While for samples J2 and J7, the presence of mesoporosity is indicated by the nature of the hysteresis loop. The broad pore size distribution curve is obtained for sample J2 confirms the mesoporous nature of this sample, and the same is the additional feature for its better photocatalytic activity. However, for sample J7, though having a similar nature of the hysteresis loop, the observed poor photocatalytic activity can be attributed to the bimodal nature of the pore size distribution curve with a sharp peak at lower value indicating the presence of amorphous nature. In addition, for sample J1, an extraneous effect is observed

having open hysteresis loop below the relative pressure of 0.45, can be interpreted to the swelling of particles [67]. The similar observation is also noticed in case of N-doped sample (Section 1).

The BJH surface area and pore volume of series I and J are given respectively in Table 18a and 18b. From the table, it can be seen that, the surface area and pore volume goes on increasing with metal concentration up to 0.5 %, whereas found to decrease after that for both the series.

Moreover, similar values of surface area and pore volume are observed for both the series. The results are at variance with that of the Cu-Ni doped series, wherein a difference in surface area data is seen. This may be attributed to the presence of nitrogen as dopant species, which probably stabilizes the pore structures and surface properties of the material.

Table 18a – Surface properties for series I

Sample	BJH surface area (m^2/g)	Pore volume (cc/g)
I1	39.27	0.093
I2	44.38	0.098
I3	55.04	0.115
I4	62.65	0.162
I5	32.47	0.062
I6	12.41	0.036
I7	14.49	0.052
P25	56.00	0.250

Table 18b – Surface properties for series J

Sample	BJH surface area (m^2/g)	Pore volume (cc/g)
J1	29.46	0.033
J2	44.38	0.098
J3	56.05	0.064
J4	35.68	0.044
J5	32.65	0.042
J6	29.69	0.036
J7	23.59	0.045
P25	56.00	0.250

Morphological studies

The surface morphology for both the series is studied by SEM analysis. Fig. 23a and 23c display SEM images and corresponding EDX images of respective series I and J.

It can be observed that densely packed spherical shaped particles with smaller granular size and uniformly distributed are obtained for the samples I1-I5 and I7 of series I, while sample I6 is observed with spherical particles grouped together, forming slightly bigger clusters. Slight agglomeration is also seen among the particles. Small difference in morphology observed for the sample I6, can be attributed to the presence of rutile-anatase mix phase in the sample.

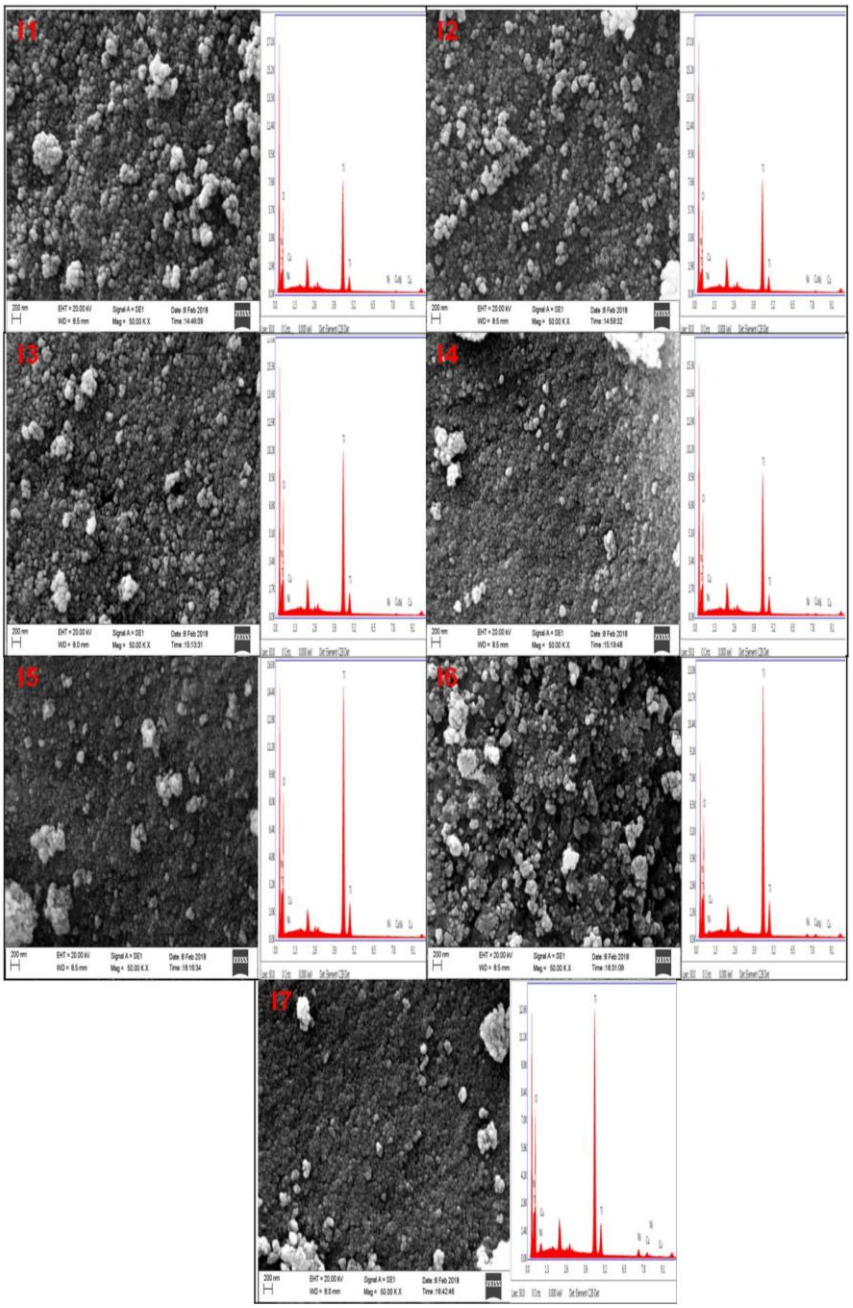

Fig. 23a— *SEM micrographs and corresponding EDX images of CuO-NiO-N-TiO_2 nanoparticles - series I*

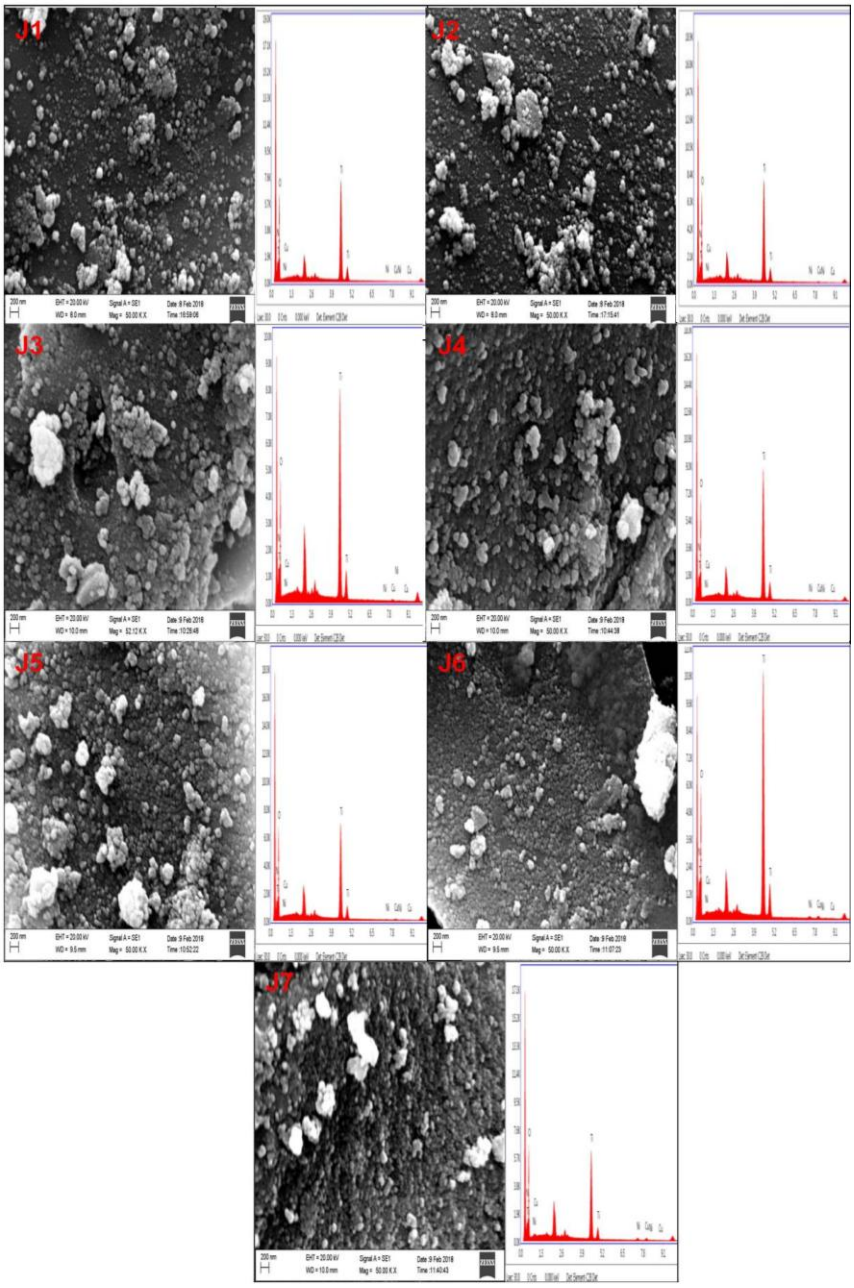

Fig. 23b— *SEM micrographs and corresponding EDX images of CuO-NiO-N-TiO_2 nanoparticles- series J*

Whereas for series J, randomly placed tiny spherical particles in highly dispersed form are observed for samples J1 and J2 (with lower metal loading), slightly bigger particles grouped together are obtained for samples J3, J4 and densely packed spherical particles of smaller size are observed for samples J5, J6 and J7, with higher metal loading. Slight agglomeration is also observed for higher metal loaded samples.

The chemical composition of the prepared nanoparticles is further detected from EDX images. From these images, Ti and O are observed to be major components along with a slight presence of C, which may be due the supporting material used. Traces of Cu, Ni and N are also seen indicating the successful incorporation of these species in the samples.

IR Studies

The IR spectra of all calcined TiO_2 samples show the presence of surface hydroxyl groups and /or adsorbed water for both the series (Fig. 24a and 24b). The characteristic stretching frequency can be seen between 3000-3500 cm^{-1} and the bending vibrations at 1600 cm^{-1}. The metal oxide bands are seen at 500 cm^{-1} is of Ti-O stretching. No bands are seen corresponding to the isopropyl group and also the acetate groups suggesting complete removal of organic part.

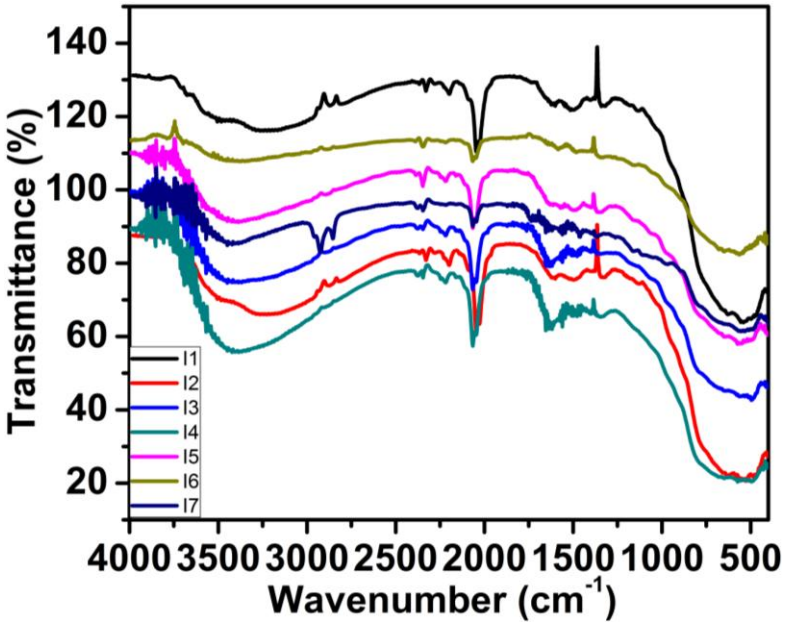

Fig. 24a—*IR spectra of calcined samples of series I*

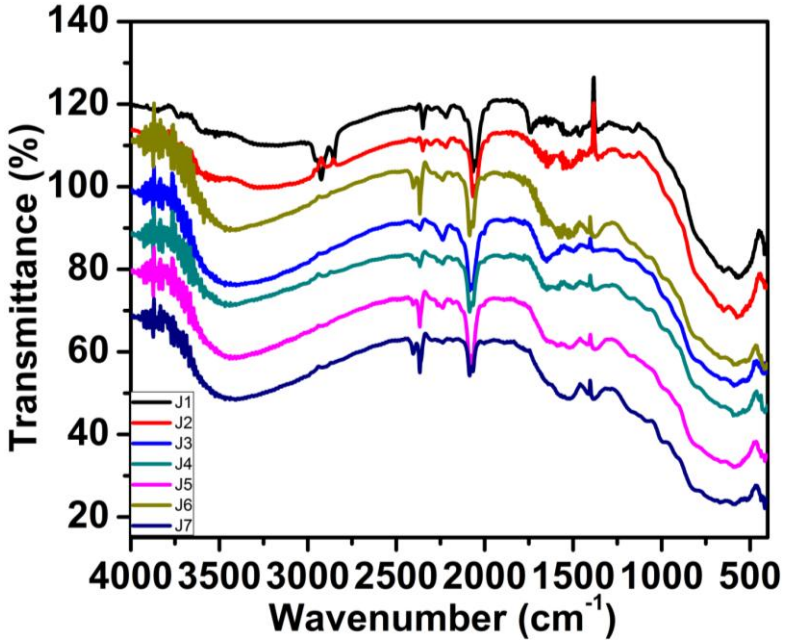

Fig. 24b—*IR spectra of calcined samples of series J*

IR spectra of precursor (uncalcined) samples of both the series displayed distinct bands at 3000-3500 cm^{-1} and ~1600 cm^{-1} of the metal hydroxide and water (Fig. 24c and 24d). Also, bands at around 1100-1600 cm^{-1} were seen, clearly indicates the presence of organic functionality, *i.e.* isopropyl group and acetate group. Additional bands at 2340, 2207 and 2044 cm^{-1} were seen in all the six samples. This could arise from the linkage of isocyanic acid or cynuric acid units to the Ti *via* oxygen or nitrogen as described earlier in Section 1.

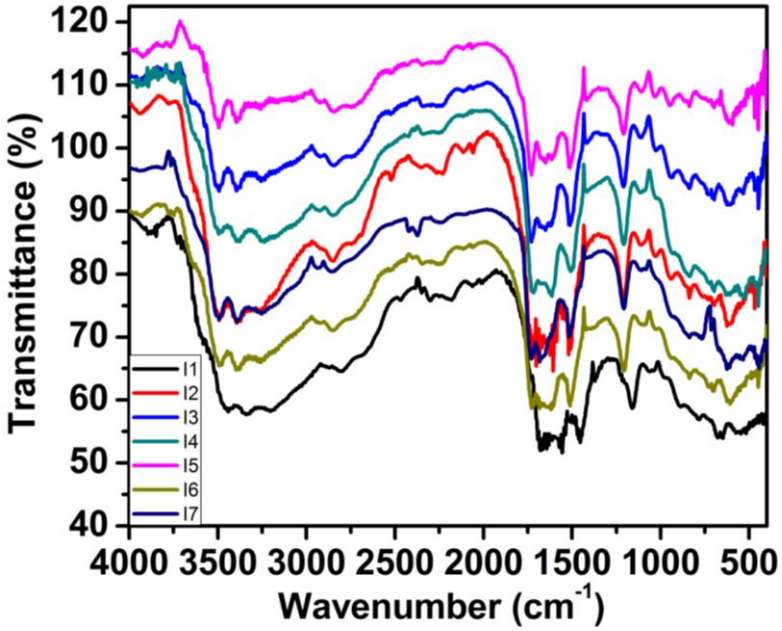

Fig. 24c—*IR spectra of precursor samples of series I*

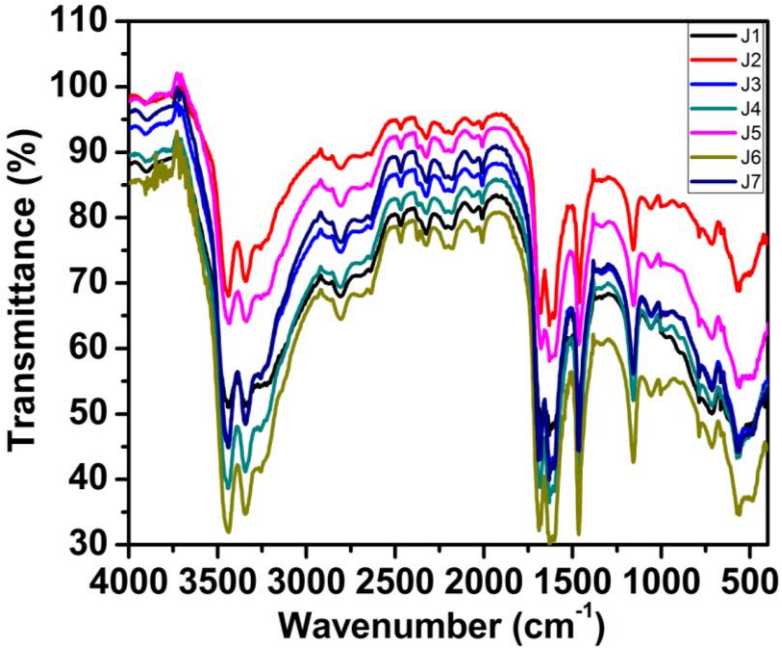

Fig. 24b—*IR spectra of precursor samples of series J*

Photocatalytic activity testing

The photocatalytic activity of the obtained samples was studied by the degradation of methylene blue, the most studied azo dye for comparing catalytic activity. Fig. 25a and 25b displays the comparative catalytic activity under natural sunlight irradiation for samples of series I and J respectively, in comparison with Degussa P25 as a standard.

It can be seen that, the samples with lower metal loading, I1, I2, I3 for series I and J1, J2, J3 for series J display better photocatalytic activity compared to Degussa. The highest degradation rate is observed for sample I2 and J2 (0.05 wt % Cu-Ni). Thus, we can say that the catalysts with lower metal insertion (0.01-0.1 wt %) shows better degradation compared to Degussa for both the series, with 0.05 wt % to be optimum metal concentration for effective photocatalytic activity. These samples (I2 and J2) show exceptionally greater shift in absorption wavelength. The other factors such as crystallite size and surface area show less effect on photocatalytic activity. Hence the observed photocatalytic activity can be mainly attributed to the lower Cu-Ni dopant concentration of these catalysts. Also, it can be accounted for higher visible light absorption power due to the presence of nitrogen, which increases the harvesting of electron-hole charge carriers by inhibiting recombination effect, which is the major barrier for enhancement of quantum efficiency [112]. Moreover, the reduced photo-activity of the catalyst with higher metal loading might be due to the fact that, higher content of Cu-Ni act as recombination center, thus retarding the degradation rate.

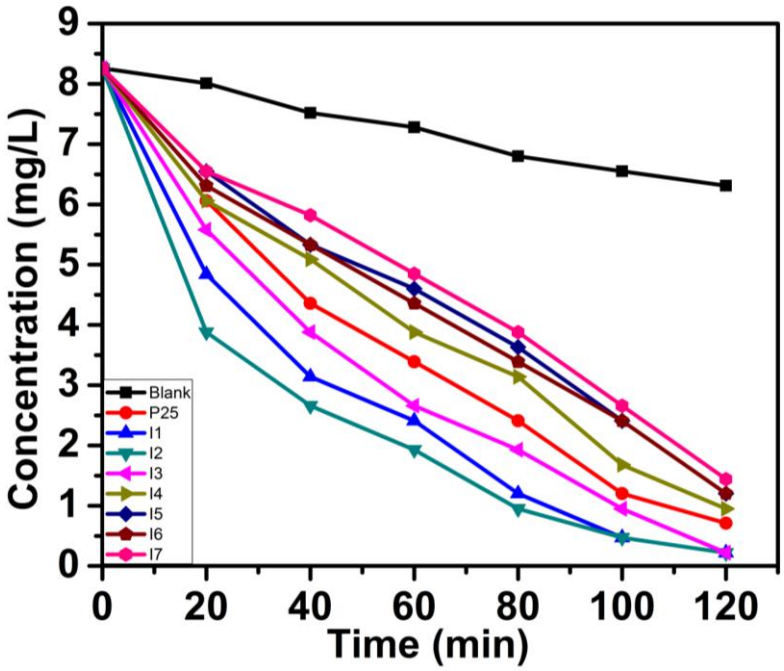

Fig. 25a-*Methylene blue degradation plots for series I*

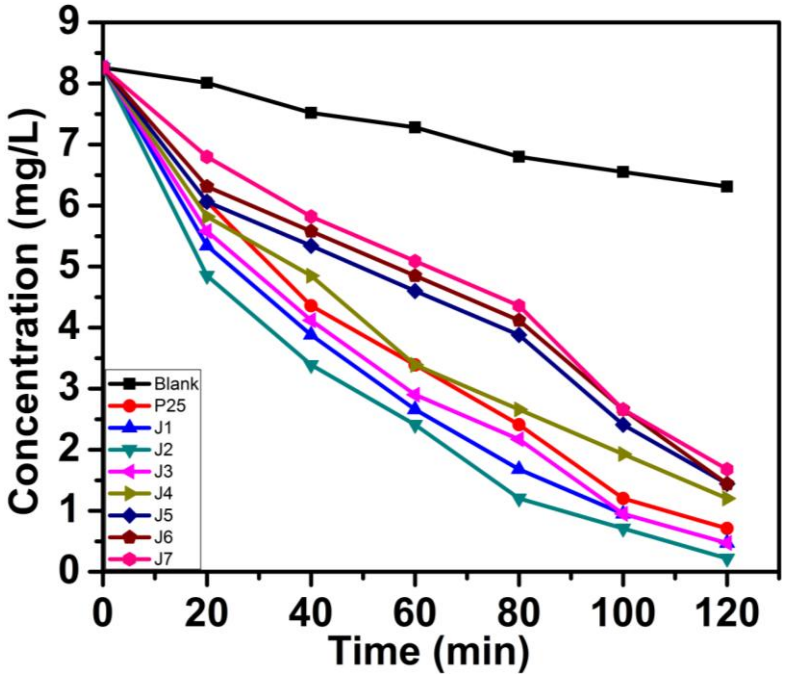

Fig. 25b- *Methylene blue degradation plots for series J*

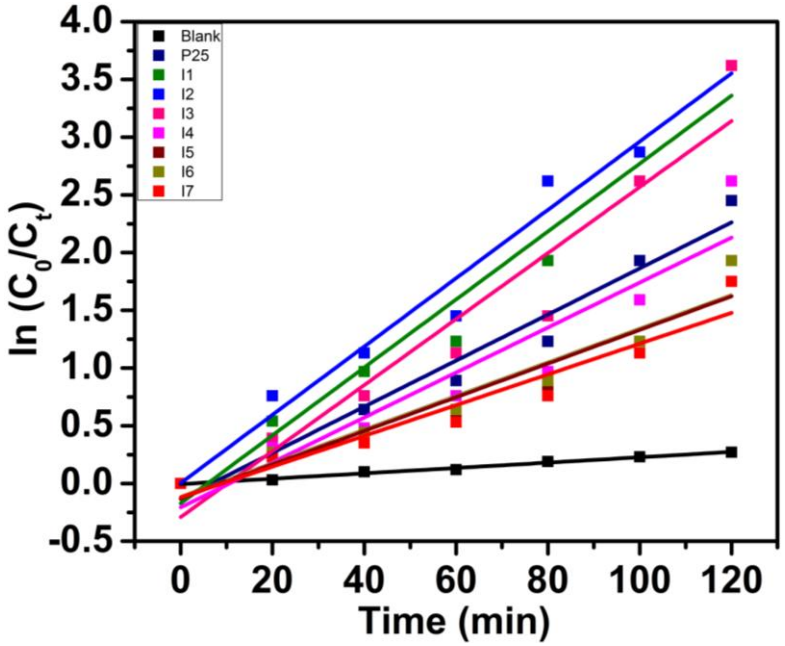

Fig. 25c-*Kinetic studies MB degradation for series I*

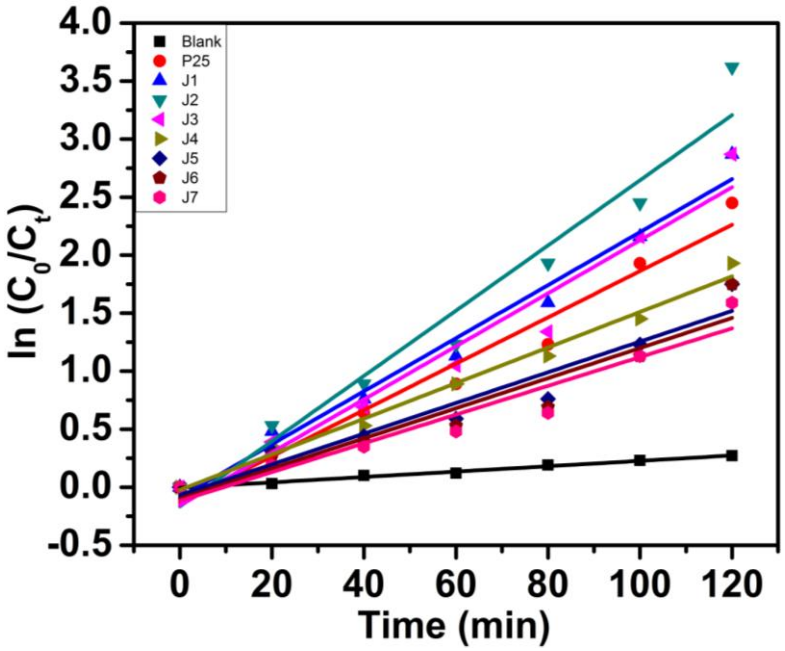

Fig. 25d—*Kinetic studies MB degradation for series J*

A plot of ln (C_0/C_t) versus time for series I and J (Fig. 25c and 25d) represents a straight line which indicates the photocatalytic degradation follows a pseudo first order kinetics. The rate constant derived from the plot is given in Table 19 which is in accordance with the other results.

Table 19 –Kinetic studies

Sample	Rate constant k (min^{-1})	Sample	Rate constant k (min^{-1})
I1	0.02943	J1	0.02286
I2	0.02959	J2	0.02811
I3	0.02859	J3	0.02286
I4	0.01948	J4	0.01534
I5	0.01459	J5	0.01323
I6	0.01457	J6	0.01298
I7	0.01332	J7	0.01239
P25	0.01996	P25	0.01996

Recyclability studies for the samples showing better degradation results than Degussa of series I and J were carried out for three cycles after separating the catalyst by centrifugation and are respectively showed in Fig. 25e and 25f. All the samples showed good reusability for degradation in comparison with Degussa.

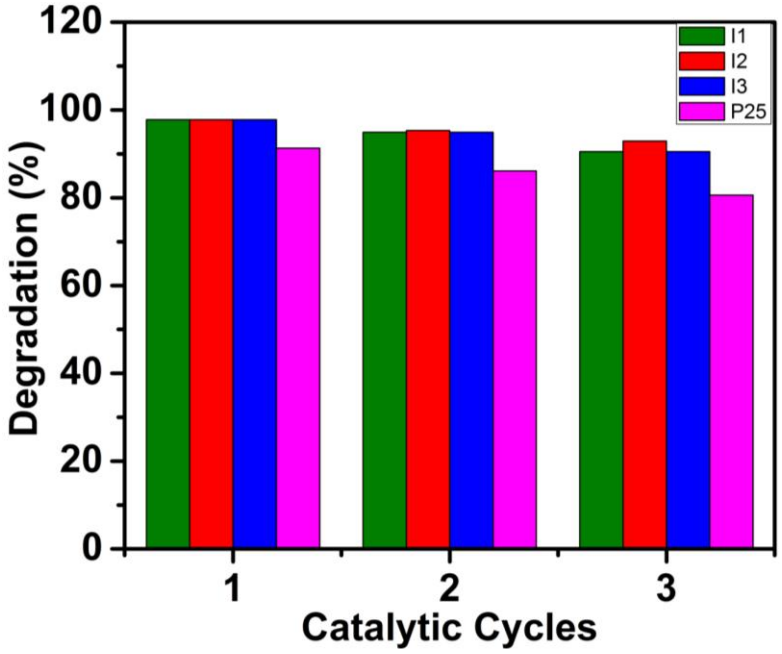

Fig. 25e-*Recyclability studies for the samples showing better results for series I*

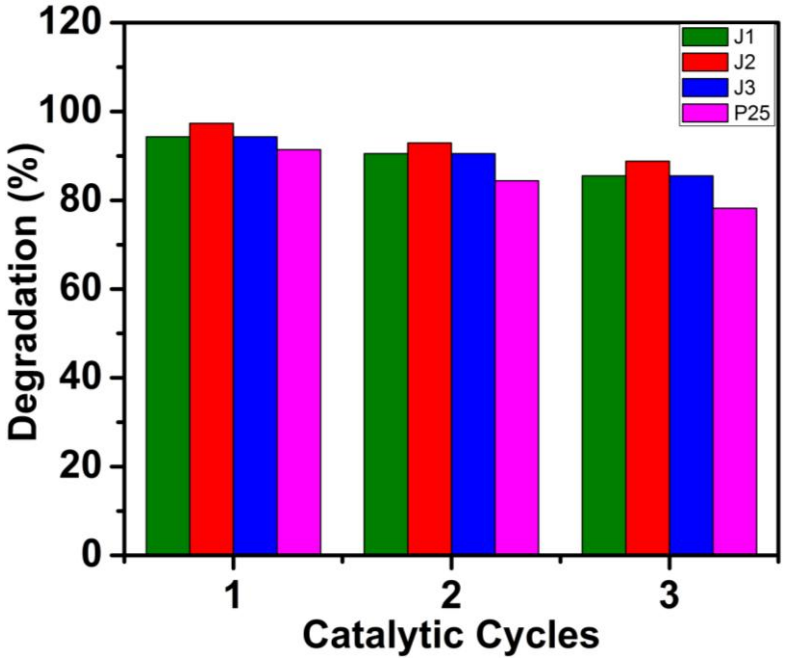

Fig. 25f-*Recyclability studies for the samples showing better results for series J*

Summary and Conclusion

CuO-NiO-N-TiO_2 nanoparticles were successfully prepared with 1:1 Cu:Ni ratio and varying M:Ti concentration, by using two different preparation methods. The ratio of TIP:urea was maintained as 1:2 throughout the experiment. The degradation studies reveal that, photo-degradation efficiency of these catalysts is solely depending on the concentration of Cu-Ni

dopants. The catalysts with lower metal dopants are observed to display better photocatalytic activity and optimum doping concentration for photo-degradation is observed to be 0.05 wt %, irrespective of the other properties. Presence of nitrogen in the samples with lower metal concentration showed an unusual shift in absorption wavelength. The properties of the catalysts are summarized in Table 20a and 20b respectively for series I and J.

Table 20a – Summary of the properties of CuO-NiO-N-TiO_2 nanoparticles for series I.

Sample	**Cryst. size (nm)**	**BJH surf. area (m^2/g)**	**Pore vol. (cc/g)**	**λ_{max} (nm)**	**Rate const. k (min^{-1})**
I1	18.49	39.27	0.093	401.2	0.02943
I2	17.12	44.38	0.098	477.8	0.02959
I3	14.69	55.04	0.115	406.3	0.02859
I4	15.41	62.65	0.162	394.8	0.01948
I5	17.36	32.47	0.062	436.1	0.01459
I6	19.83	12.41	0.036	440.3	0.01457
I7	20.75	14.49	0.052	457.4	0.01332
P25	25.00	56.00	0.250	370.7	0.01996

Table 20b – Summary of the properties of CuO-NiO-N-TiO_2 nanoparticles for series J.

Sample	**Cryst. size (nm)**	**BJH surf. area (m^2/g)**	**Pore vol. (cc/g)**	**λ_{max} (nm)**	**Rate const. k (min^{-1})**
J1	17.12	29.46	0.033	610.8	0.02286
J2	16.55	44.38	0.098	606.4	0.02811
J3	12.15	56.05	0.064	457.4	0.01286
J4	14.92	35.68	0.044	478.7	0.01534
J5	17.12	32.65	0.042	470.3	0.01323
J6	17.15	29.69	0.036	556.9	0.01298
J7	18.10	23.59	0.045	567.0	0.01239
P25	25.00	56.00	0.250	370.7	0.01996

References

1. S. Sato, Photocatalytic Activity of NO_x-Doped TiO_2 in the Visible Light Region, Chem. Phys. Lett. 123 (1986) 126-128.
2. R. Asahi, T. Morikawa, T. Ohwaki, K. Aoki,Y. Taga, Visible-Light Photocatalysis in Nitrogen-Doped Titanium Dioxide, Science 293 (2001) 269-271.
3. S. Sakthivel, H. Kisch, Daylight Photocatalysts by Carbon-Modified Titanium Dioxide, Angew. Chem. Int. Ed. 42 (2003) 4908-4911.
4. T. Umebabayashi, T. Yamaki, H. Itoh, K. Asai, Band Gap Narrowing of Titanium Dioxide by Sulfur Doping, Appl. Phys. Lett. 81 (2002) 454-456.
5. T. Ohno, T. Mitsui, M. Matsumura, Photocatalytic Activity of S Doped TiO_2 Photocatalyst under Visible Light, Chem. Lett. 32 (2003) 364-365.
6. A. Zaleska, J.W. Sobczak, E. Grabowska, J. Hupka, Preparation and Photocatalytic Activity of Boron-Modified TiO_2 under UV and Visible Light, Appl. Catal., B 78 (2007) 92-100.
7. S.C. Moon, H. Mametsuka, S. Tabata, E. Suzuki, Photocatalytic Production of Hydrogen from Water using TiO_2 and B/TiO_2, Catal. Today 58 (2000) 125-132.
8. L. Korosi, I. Dekany, Preparation and Investigation of Structural and Photocatalytic Properties of Phosphate Modified Titanium Dioxide, Colloids Surf., A 280 (2006) 146-154.
9. J.C. Yu, L. Zhang, Z. Zheng, J. Zhao, Synthesis and Characterization of Phosphated Mesoporous Titanium Dioxide with High Photocatalytic Activity, Chem. Mater. 15 (2003) 2280 -2286.
10. J.C. Yu, J. Yu, W. Ho, Z. Jiang, L. Zhang, Effects of F- Doping on the Photocatalytic Activity and Microstructures of Nanocrystalline TiO_2 Powders, Chem. Mater. 14 (2002) 3808-3816.
11. X. Hong, Z. Wang, W. Cai, F. Lu, J. Zhang, Y. Yang, N. Ma, Y. Liu, Visible-Light-Activated Nanoparticle Photocatalyst of Iodine-Doped Titanium Dioxide, Chem. Mater. 17 (2005) 1548-1552.
12. Q. Chen, D. Jiang, W. Shi, D. Wu, Y. Xu, Visible-Light-Activated Ce–Si co-Doped TiO_2 Photocatalyst, Appl. Surf. Sci. 255 (2009) 7918-7924.
13. A.A. Ismail, D.W. Bahnemann, Mesoporous Titania Photocatalysts: Preparation, Characterization and Reaction Mechanisms, J. Mater. Chem. 21 (2011) 11686-11707.
14. A.V. Rupa, D. Divakar, T. Sivakumar, Titania and Noble Metals Deposited Titania catalysts in the Photodegradation of Tartrazine, Catal. Lett. 132 (2009) 259-267.

15. J. Papp, H.-S. Shen, R. Kershaw, K. Dwight, A. Wold, Titanium (IV) Oxide Photocatalysts with Palladium, Chem. Mater. 5 (1993) 284-288.
16. K.R. Thampi, J. Kiwi, M. Grätzel, Methanation and Photomethanation of Carbon Dioxide at Room Temperature and Atmospheric Pressure, Nature 327 (1987) 506-508.
17. C. He, Y. Yu, X. Hu, A. Larbot, Influence of Silver Doping on the Photocatalytic Activity of Titania Films, Appl. Surf. Sci. 200 (2002) 239-247.
18. W.K. Wong, M.A. Malati, Doped TiO_2 for Solar Energy Applications, Sol. Energy 36 (1986) 163-168.
19. J. Choi, H. Park, M.R. Hoffmann, Effects of Single Metal-Ion Doping on the Visible-Light Photoreactivity of TiO_2, J. Phys. Chem. C 114 (2010) 783-792.
20. A. Fuerte, M. D. Hernández-Alonso, A.J. Maira, A. Martínez-Arias, M. Fernández-García, J.C. Conesa, J. Soria, Visible Light-Activated Nanosized Doped-TiO_2 Photocatalysts, Chem. Commun. 24 (2001) 2718-2719.
21. H. Yamashita, M. Harada, J. Misaka, M. Takeuchi, Y. Ichihashi, F. Goto, M. Ishida, T. Sasaki, M. Anpo, Application of Ion Beam Techniques for Preparation of Metal Ion-Implanted TiO_2 Thin Film Photocatalyst Available under Visible Light Irradiation: Metal Ion Implantation and Ionized Cluster Beam Method, J. Synchrotron Radiat. 8 (2001) 569-571.
22. K. Melghit, O.S. Al-Shukeili, I. Al-Amri, Effect of M-doping (M = Fe, V) on the Photocatalytic Activity of Nanorod Rutile TiO_2 for Congo Red Degradation under the Sunlight, Ceram. Int. 35 (2009) 433-439.
23. C.M. Teh, A.R. Mohamed, Role of Titanium Dioxide and Ion Doped Titanium Dioxide on Phtotocatalytic Degradation of Organic Pollutants (Phenol Compounds and Dyes) in Aqueous Solutions: A review, J. Alloys Compd. 509 (2011) 1648-1660.
24. H. Zhang, G. Chen, D.W. Behnemann, Photo-electrocatalytic Materials for Environmental Applications, J. Mater. Chem. 19 (2009) 5089-5121.
25. D. Robert, Photosensitization of TiO_2 by M_xO_y and M_xS_y Nanoparticles for Heterogeneous Photocatalysis Applications, Catal. Today 122 (2007) 20-26.
26. G. Liu, L.Z. Wang, H.G. Yang, H.M. Cheng, G.Q. Lu, Titania-based Photocatalysts-Crystal Growth, Doping and Heterostructuring, J. Mater. Chem. 20 (2010) 831-843.
27. S. Chen, Y. Guo, S. Chen, Z. Ge, H. Yang, J. Tang, Fabrication of Cu/TiO_2 Nanocomposite: Toward an Enhanced Antibacterial Performance in the Absence of Light, Mater. Lett. 83 (2012) 154-157.

28. H. Ishiguro, Y. Yao, R. Nakano, M. Hara, K. Sunada, K. Hashimoto, J. Kajioka, A. Fujishima, Y. Kubota, Photocatalytic Activity of Cu^{2+}/TiO_2-coated Cordierite Foam Inactivates Bacteriophages and *Legionella Pneumophila*, Appl. Catal., B 129 (2013) 56-61.
29. C. Karunakaran, G. Abiramasundari, P. Gomathisankar, G. Manikandan, V. Anandi, Cu-doped TiO_2 Nanoparticles for Photocatalytic Disinfection of Bacteria under Visible Light, J. Colloids Interface. Sci. 352 (2010) 68-74.
30. H.M. Yadav, S.V. Otari, V.B. Koli, S.S. Mali, C.K. Hong, S.H. Pawar, S.D. Delekar, Preparation and Characterization of Copper-Doped Anatase TiO_2 Nanoparticles with Visible Light Photocatalytic Antibacterial Activity, J. Photochem. Photobiol., A 280 (2014) 32-38.
31. S. Yadav, G. Jaiswar, Review on Undoped/Doped TiO_2 Nanomaterial; Synthesis and Photocatalytic and Antimicrobial Activity, J. Chin. Chem. Soc. 64 (2017) 103-116.
32. A. Zielinska, E. Kowalska, J.W. Sobczak, I. Lack, M. Gazd, B. Ohtanie, J. Hupka, A. Zaleska, Silver-doped TiO_2 Prepared by Microemulsion Method: Surface Properties, Bio- and Photoactivity, Sep. Purif. Technol. 72 (2010) 309-318.
33. A.A. Ashkarran, Antibacterial Properties of Silver-doped TiO_2 Nanoparticles under Solar Simulated Light, J. Theor. Appl. Phys. 4-4 (2011) 1-8.
34. B. Yu, K.M. Leung, Q. Guo, W.M. Lau, J. Yang, Synthesis of Ag–TiO_2 Composite Nano Thin Film for Antimicrobial Application, Nanotechnology 22 (2011) 115603:1-9.
35. K. Ubonchonlakate, L. Sikong, F. Saito, Photocatalytic Disinfection of P.aeruginosa Bacterial Ag-doped TiO_2 Film, Proc. Eng. 32 (2012) 656-662.
36. B. Xin, Z. Ren, P. Wang, J. Liu, L. Jing, H. Fu, Study on the Mechanisms of Photoinduced Carriers Separation and Recombination for Fe^{3+}-TiO_2 Photocatalysts, App. Surf. Sci. 253 (2007) 4390-4395.
37. L. Sun, J. Li, C.L. Wang, S.F. Li, H.B. Chen, C.J. Lin, An Electrochemical Strategy of Doping Fe^{3+} into TiO_2 Nanotube Array Films for Enhancement in Photocatalytic Activity, Sol. Energy Mater. Sol. Cells. 93 (2009) 1875-1880.
38. M.C. Wang, H.J. Lin, T.S. Yang, Characteristics and Optical Properties of Iron Ion (Fe^{3+})-doped Titanium Oxide Thin Films Prepared by Sol-Gel Spin Coating, J. Alloys Compd. 473 (2009) 394-400.

39. M. Asiltürk, F. Sayilkan, E. Arpaç, Effect of Fe^{3+} ion Doping to TiO_2 on the Photocatalytic Degradation of Malachite Green Dye under UV and Vis-Irradiation, J. Photochem. Photobiol., A 203 (2009) 64-71.
40. J.-Y. Park, K.-II Choi, J.-H. Lee, C.-H. Hwang, D.-Y. Choi, J.-W. Lee, Fabrication and Characterization of Metal-Doped TiO_2 Nanofibers for Photocatalytic Reactions, Mater. Lett. 97 (2013) 64-66.
41. N. Fajariaha, W.A.E. Prabowob, F. Fathurrahmanb, A. Melatia, H.K. Dipojono, The Investigation of Electronic Structure of Transition Metal Doped TiO_2 for Diluted Magnetic Semiconductor Applications: A First Principle Study, Procedia Eng. 170 (2017) 141-147.
42. Y. Matsumoto, M. Murakami, T. Shono, T. Hasegawa, T. Fukumura, M. Kawasaki, P. Ahmet, T. Chikyow, S. Koshihara, H. Koinuma, Science 291 (2001) 854-856.
43. B. Parveen, M. Hassan, Z. Khalid, S. Riaz, S. Naseem, Room-Temperature Ferromagnetism in Ni-doped TiO_2 diluted Magnetic Semiconductor Thin Films, J. Appl. Res. Technol. 15 (2017) 132-139.
44. S.M. Gupta, M. Tripathi, A Review of TiO_2 Nanoparticles, Chin. Sci. Bull. 56 (2011) 1639-1657.
45. W. Choi, A. Termin, M.R. Hoffmann, The Role of Metal Ion Dopants in Quantum-Sized TiO_2: Correlation between Photoreactivity and Charge Carrier Recombination Dynamics, J. Phys. Chem. 98 (1994) 13669-13679.
46. M. Ni, M.K.H. Leung, D.Y.C. Leung, K. Sumathy, A review and Recent Developments in Photocatalytic Water-Splitting using TiO_2 for Hydrogen Production, Renewable and Sustainable Energy Rev. 11 (2007) 401-425.
47. R. Daghrir, P. Drogui, D. Robert, Modified TiO_2 for Environmental Photocatalytic Applications: A Review, Ind. Eng. Chem. Res. 52 (2013) 3581-3599.
48. W. Li, Z. Wu, J. Wang, A.A. Elzatahry, D. Zhao, A Perspective on Mesoporous TiO_2 Materials, Chem. Mater. 26 (2014) 287-298.
49. F. Dong, W. Zhao, Z. Wu, S. Guo, Band Structure and Visible Light Photocatalytic Activity of Multi-Type Nitrogen Doped TiO_2 Nanoparticles Prepared by Thermal Decomposition, J. Hazard. Mater. 162 (2009) 763-770.
50. N. Kometani, A. Fujita, Y. Yonezawa, Synthesis of N-doped Titanium Oxide by Hydrothermal Treatment, J. Mater. Sci. 43 (2008) 2492-2498.

51. Y. Cong, J. Zhang, F. Chen, M. Anpo, Synthesis and Characterization of Nitrogen-Doped TiO_2 Nanophotocatalyst with High Visible Light Activity, J. Phys. Chem. C 111 (2007) 6976-6982.
52. Y. Nosaka, M. Matsushita, J. Nishino, A.Y. Nosaka, Nitrogen-Doped Titanium Dioxide Photocatalysts for Visible Response Prepared by using Organic Compounds, Sci. Technol. Adv. Mater. 6 (2005) 143-148.
53. K. Kobayakawa, Y. Murakami, Y. Sato, Visible-Light Active N-Doped TiO_2 Prepared by Heating of Titanium Hydroxide and Urea, J. Photochem. Photobiol., A 170 (2005) 177-179.
54. D. Kusano, M. Emori, H. Sakama, Influence of Electronic Structure on Visible Light Photocatalytic Activity of Nitrogen-Doped TiO_2, RSC Adv. 7 (2017) 1887-1898.
55. J. Yuan, M. Chen, J. Shi, W. Shangguan, Preparations and Photocatalytic Hydrogen Evolution of N-Doped TiO_2 from Urea and Titanium Tetrachloride, Int. J. Hydrog. Energy 31 (2006) 1326-1331.
56. D. Mitoraj, H. Kisch, The Nature of Nitrogen-Modified Titanium Dioxide Photocatalysts Active in Visible Light, Angew. Chem. Int. Ed. 47 (2008) 9975-9978.
57. A.R. Gandhe, J.B. Fernandes, A Simple Method to Synthesize Visible Light Active N-Doped Anatase (TiO_2) Photocatalyst, Bull. Catal. Soc. India 4 (2005)131-134.
58. A.R. Gandhe, J.B. Fernandes, A Simple Method to Synthesize N-Doped Rutile Titania with Enhanced Photocatalytic Activity in Sunlight, J. Solid State Chem. 178 (2005) 2953-2957.
59. K. Sivaranjani, C.S. Gopinath, Porosity Driven Photocatalytic Activity of Wormhole Mesoporous $TiO_{2-x}N_x$ in Direct Sunlight, J. Mater. Chem. 21 (2011) 2639-2647.
60. N.T. Nolana, D.W. Synnott, M.K. Seery, S.J. Hinder, A.V. Wassenhoven, S.C. Pillai, Effect of N-Doping on the Photocatalytic Activity of Sol–Gel TiO_2, J. Hazard. Mater. 211-212 (2012) 88-94.
61. S.C. Pillai, P. Periyat, R. George, D.E. McCormack, M.K. Seery, H. Hayden, J. Colreavy, D. Corr, S.J. Hinder, Synthesis of High-Temperature Stable Anatase TiO_2 Photocatalyst, J. Phys. Chem. C 111 (2007) 1605-1611.
62. S. Girish Kumar, K.S.R. Koteswara Rao, Polymorphic Phase Transition Among the Titania Crystal Structures using a Solution-Based Approach: from Precursor Chemistry to Nucleation Process, Nanoscale 6 (2014) 11574-11632.

63. Z. Wu, F. Dong, W. Zhao, S. Guo, Visible Light Induced Electron Transfer Process over Nitrogen Doped TiO_2 Nanocrystals Prepared by Oxidation of Titanium Nitride, J. Hazard. Mater. 157 (2008) 57-63.
64. O. Diwald, T.L. Thompson, E.G. Goralski, S.D. Walck, J.T. Yates, Jr., The Effect of Nitrogen Ion Implantation on the Photoactivity of TiO_2 Rutile Single Crystals, J. Phys. Chem. B 108 (2004) 52-57.
65. C.D. Valentin, E. Finazzi, G. Pacchioni, A. Selloni, S. Livraghi, M.C. Paganini, E. Giamello, N-doped TiO_2: Theory and Experiment, Chem. Phys. 339 (2007) 44-56.
66. K.S.W. Sing, R.T. Williams, Physisorption Hysteresis Loops and the Characterization of Nanoporous Materials, Adsorption Science & Technology, 22 (2004) 773-782.
67. S.J. Gregg, K.S.W. Sing, Adsorption, surface area and porosity, 2nd ed., New York: Academic Press, (1982) pgs. 303.
68. Y. Suda, T. Morimoto, Molecularly Adsorbed H_2O on the Bare Surface of TiO_2 (Rutile), Langmuir 3 (1987) 786-788.
69. K. Tanaka, J.M. White, Characterization of Species Adsorbed on Oxidized and Reduced Anatase, J. Phys. Chem. 86 (1982) 4708-4714.
70. V. Etacheri, M.K. Seery, S.J. Hinder, S.C. Pillai, Highly Visible Light Active $TiO_{2-x}N_x$ Heterojunction Photocatalysts, Chem. Mater. 22 (2010) 3843-3853.
71. A.W. Jackson, O. Shebanova, A.L. Hector, P.F. McMillan, Amorphous and Nanocrystalline Titanium Nitride and Carbonitride Materials Obtained by Solution Phase Ammonolysis of $Ti(NMe_2)_4$, J. Solid State Chem. 179 (2006) 1383-1393.
72. D. Mitoraj, H. Kisch, On the Mechanism of Urea-Induced Titania Modification, Chem. Eur. J. 16 (2010) 261-269.
73. N.E.A. El-Gamel, L. Seyfarth, J. Wagler, H. Ehrenberg, M. Schwarz, J. Senker, E. Kroke, The Tautomeric Forms of Cyameluric Acid Derivatives, Chem. Eur. J. 13 (2007) 1158-1173.
74. A. Sattler, S. Pagano, M. Zeuner, A. Zurawski, D. Gunzelmann, J. Senker, K. Müller-Buschbaum, W. Schnick, Melamine–Melem Adduct Phases: Investigating the Thermal Condensation of Melamine, Chem. Eur. J. 15 (2009) 13161-13170.
75. G. Liu, X. Wang, Z. Chen, H.-M. Cheng, G.Q. (Max) Lu, The Role of Crystal Phase in Determining Photocatalytic Activity of Nitrogen Doped TiO_2, J. Colloid Interface Sci. 329 (2009) 331-338.

76. R.D. Shannon, J.A. Pask, Kinetics of the Anatase-Rutile Transformation, J. Am. Ceram. Soc. 48 (1965) 391-398.
77. S.S. Lee, H. Bai, Z. Liu, D.D. Sun, Novel-structured Electrospun TiO_2/CuO Composite Nanofibers for High Efficient Photocatalytic Cogeneration of Clean Water and Energy From Dye Wastewater, Water Res. 47 (2013) 4059-4073.
78. A. Ajmal, I. Majeed, R.N. Malik, M. Iqbal, M.A. Nadeem, I. Hussain, S. Yousuf, Zeshan, G. Mustafa, M.I. Zafar, M.A. Nadeem, Photocatalytic Degradation of Textile Dyes on Cu_2O-CuO/TiO_2 Anatase Powders, J. Environ. Chem. Eng. 4 (2016) 2138-2146.
79. B. Xin, P. Wang, D. Ding, J. Liu, Z. Ren, H. Fu, Effect of Surface Species on Cu-TiO_2 Photocatalytic Activity, Appl. Surf. Sci. 254 (2008) 2569-2574.
80. G. Li, N.M. Dimitrijevic, L. Chen, T. Rajh, K.A. Gray, Role of Surface/Interfacial Cu^{2+} Sites in the Photocatalytic Activity of Coupled CuO-TiO_2 Nanocomposites, J. Phys. Chem. C 112 (2008) 19040-19044.
81. G. Colón, M. Maicu, M.C. Hidalgo, J.A. Navío, Cu-doped TiO2 systems with improved photocatalytic activity, Appl. Catal., B 67 (2006) 41-51.
82. W.-T. Chen, V. Jovic, D. Sun-Waterhouse, H. Idriss, G.I.N. Waterhouse, The role of CuO in Promoting Photocatalytic Hydrogen Production over TiO_2, Int. J. Hydrog. Energy 38 (2013) 15036-15048.
83. J. Yu, Y. Hai, M. Jaroniec, Photocatalytic Hydrogen Production over CuO-modified Titania, J. Colloid Interface Sci. 357 (2011) 223-228.
84. J.-Z. Chen, T.-H. Chen, L.-W. Lai, P.-Y. Li, H.-W. Liu, Y.-Y. Hong, D.-S. Liu, Preparation and Characterization of Surface Photocatalytic Activity with NiO/TiO_2 Nanocomposite Structure, Materials 8 (2015) 4273-4286.
85. T. Sreethawong, Y. Suzuki, S. Yoshikawa, Photocatalytic Evolution of Hydrogen over Mesoporous TiO_2 Supported NiO Photocatalyst Prepared by Single-Step Sol–Gel Process with Surfactant Template, Int. J. Hydrog. Energy 30 (2005) 1053-1062.
86. I. Ganesh, A.K. Gupta, P.P. Kumar, P.S.C. Sekhar, K. Radha, G. Padmanabham, G. Sundararajan, Preparation and Characterization of Ni-Doped TiO_2 Materials for Photocurrent and Photocatalytic Applications, Sci. World J. 2012 (2012) 1-16.
87. D. Zhang, Chemical synthesis of Ni/TiO_2 Nanophotocatalyst for UV/Visible Light Assisted Degradation of Organic Dye in Aqueous Solution, J. Sol-Gel Sci. Technol. 58 (2011) 312-318.

88. S. Li, P. Jena, Origin of the Anatase to Rutile Conversion of Metal-doped TiO_2, Phys. Rev. B 79 (2009) 201204(R):1-4.
89. S.A. Ahmed, Ferromagnetism in Cr-, Fe-, and Ni-doped TiO_2 samples, J. Magn. Magn. Mater. 442 (2017) 152-157.
90. Y.R. Uhm, S.H. Woo, W.W. Kim, S.J. Kim, C.K. Rhee, The Characterization of Magnetic and Photo-catalytic Properties of Nanocrystalline Ni-doped TiO_2 Powder Synthesized by Mechanical Alloying, J. Magn. Magn. Mater. 304 (2006) e781-e783.
91. B. Anitha, M.A. Khadar, Dopant Concentration Dependent Magnetism of Cu-doped TiO_2 Nanocrystals, J. Nanopart. Res. 18 (2016) 149:1-14.
92. W.Gao, R. Jin, J. Chen, X. Guang, H. Zheng, F. Zhang, N. Guan, Titania-supported Bimetallic Catalysts for Photocatalytic Reduction of Nitrate, Catal. Today 90 (2004) 331-336.
93. Y. Liu, D. Liu, Study of Bimetallic Cu-Ni/γ-Al_2O_3 Catalysts for Carbon Dioxide Hydrogenation, Int. J. Hydrog. Energy 24 (1999) 351-354.
94. R. Hierl, H. Knözinger, H.-P. Urbach, Surface Properties and Reduction Behavior of Calcined CuO/ Al_2O_3 and CuO-NiO/ Al_2O_3 Catalysts, J. Catal. 69 (1981) 475-486.
95. T.-J. Huang, S.-Y. Jhao, Ni–Cu/Samaria-doped Ceria Catalysts for Steam Reforming of Methane in the Presence of Carbon Dioxide, Appl. Catal., A 302 (2006) 325-332.
96. M.J. Lázaro, Y. Echegoyen, I. Suelves, J.M. Palacios, R. Moliner, Decomposition of Methane over Ni-SiO_2 and Ni-Cu-SiO_2 Catalysts: Effect of Catalyst Preparation Method, Appl. Catal., A 329 (2007) 22-29.
97. H. Wang, R.T.K. Baker, Decomposition of Methane over a Ni–Cu–MgO Catalyst to Produce Hydrogen and Carbon Nanofibers, J. Phys. Chem. B 108 (2004) 20273-20277.
98. P. Li, J. Liu, N. Nag, P.A. Crozier, *In situ* Preparation of Ni–Cu/TiO_2 Bimetallic Catalysts, J. Catal. 262 (2009) 73-82.
99. N. Riaz, F.K. Chong, B.K. Dutta, Z.B. Man, M.S. Khan, E. Nurlaela, Photodegradation of Orange II under visible light using Cu–Ni/TiO_2: Effect of Calcination Temperature, Chem. Eng. J. 185-186 (2012) 108-119.
100. N. Riaz, F.K. Chong, Z.B. Man, M.S. Khan, B.K. Dutta, Photodegradation of Orange II under Visible Light Using Cu−Ni/TiO_2: Influence of Cu:Ni Mass Composition, Preparation, and Calcination Temperature, Ind. Eng. Chem. Res. 52 (2013) 4491-4503.

101. B. Singh, M. Singh, F.K. Chong, E. Nurlaela, Simulation of Solar Hydrogen Production from Water in the Presence of TiO_2 -Supported Bimetallic Cu-Ni Photocatalyst, World Appl. Sci. J. 30 (2014) 370-374.
102. N. Riaz, M.A.Bustam, F.K. Chong, Z.B.Man, M.S. Khan, A.M. Shariff, Photocatalytic Degradation of DIPA Using Bimetallic Cu-Ni/TiO_2 Photocatalyst under Visible Light Irradiation, Sci. World J. 2014 (2014) 1-8.
103. Y. Yue, D. Juarez-Robles, Y. Chen, L. Ma, W.C.H. Kuo, P. Mukherjee, H. Liang, Hierarchical Structured Cu/Ni/TiO_2 Nanocomposites as Electrodes for Lithium-Ion Batteries, ACS Appl. Mater. Interfaces 9 (2017) 28695-28703.
104. B. Seemala, C.M. Cai, C.E. Wyman, P. Christopher, Support Induced Control of Surface Composition in Cu−Ni/TiO_2 Catalysts Enables High Yield Co-Conversion of HMF and Furfural to Methylated Furans, ACS Catal. 7 (2017) 4070-4082.
105. D.L. Hou, R.B. Zhao, H.J. Meng, L.Y. Jia, X.J. Ye, H.J. Zhou, X.L. Li, Room-Temperature Ferromagnetism in Cu-doped TiO_2 Thin Films, Thin Solid Films 516 (2008) 3223-3226.
106. N. Wongpisutpaisan, N. Vittayakorn, A. Ruangphanit, W. Pecharapa, Cu-Doped TiO_2 Nanopowders Synthesized by Sonochemical-Assisted Process, Sains Malaysiana 42 (2013) 175-181.
107. O.V. Komova, A.V. Simakov, V.A. Rogov, D.I. Kochubei, G.V. Odegova, V.V. Kriventsov, E.A. Paukshtis, V.A. Ushakov, N.N. Sazonova, T.A. Nikoro, Investigation of the State of Copper in Supported Copper–Titanium Oxide Catalysts, J. Mol. Catal. A: Chem. 161 (2000) 191-204.
108. H. Gao, J. Tian, H. Zheng, F. Tan, W. Zhang, Effects of Fe Doping on the Optical and Magnetic Properties of TiO_2 Films Deposited on Si Substrates by a Sol–Gel Route, J. Sol-Gel Sci. Technol. 74 (2015) 521-527.
109. N. Bahadur, R. Pasricha, Govind, S. Chand, R.K. Kotnala, Effect of Ni doping on the Microstructure and High Curie Temperature Ferromagnetism in Sol–Gel Derived Titania Powders, Mater. Chem. Phys. 133 (2012) 471-479.
110. W. Xu, H. Wang, X. Zhou, T. Zhu, CuO/TiO_2 Catalysts for Gas-phase Hg^0 Catalytic Oxidation, Chem. Eng. J. 243 (2014) 380-385.
111. S. Panigrahi, S. Basu, S. Praharaj, S. Pande, S. Jana, A. Pal, S.K. Ghosh, T. Pal, Synthesis and Size-Selective Catalysis by Supported Gold Nanoparticles: Study on Heterogeneous and Homogeneous Catalytic Process, J. Phys. Chem. C 111 (2007) 4596-4605.

112. R. Zhang, Q. Wang, J. Liang, Q. Li, J. Dai, W. Li, Optical Properties of N and Transition Metal R(R=V, Cr, Mn, Fe, Co, Ni, Cu, and Zn) co-doped Anatase TiO_2, Physica B 407 (2012) 2709-2715.
113. N. Kaur, S.K. Shahi, V. Singh, Choline Chloride Assisted Synthesis of N and Metal co-doped TiO_2 and their Photocatalytic Activity under Visible Light, Photochem. Photobiol. 92 (2016) 69-75.
114. J.E. Mathis, J.J. Lieffers, C. Mitra, F.A. Reboredo, Z. Bi , C.A. Bridges, M.K. Kidder, M.P. Paranthaman, Increased Photocatalytic Activity of TiO_2 Mesoporous Microspheres from co-doping with Transition Metals and Nitrogen, Ceram. Int. 42 (2016) 3556-3562.
115. J.E. Mathis, M.K. Kidder, Y. Li, J. Zhang, M.P. Paranthaman, Controlled Synthesis of Mesoporous co-doped Titania Nanoparticles and Their Photocatalytic Activity, Adv. Nano Res. 4 (2016) 157-165.
116. Z. Yang, L. Qin, P. Tian, Y. Zhang, Review of N and Metal co-Doped TiO_2 for Water Purification under Visible Light Irradiation, IPCBEE 78 (2014) 31-40.
117. K.S. Rane, R. Mhalsiker, S. Yin, T. Sato, K. Cho, E. Dunbar, P. Biswas, Visible Light-Sensitive Yellow $TiO_{2-x}N_x$ and Fe–N co-doped $Ti_{1-y}Fe_yO_{2-x}N_x$ Anatase Photocatalysts, J. Solid State Chem. 179 (2006) 3033-3044.
118. M.Z. Selcuk, M.S. Boroglu, I. Boz, Hydrogen Production by Photocatalytic Water-Splitting Using Nitrogen and Metal co-Doped TiO_2 Powder Photocatalyst, Reac. Kinet. Mech. Catal. 106 (2012) 313-324.
119. W. Zhu, X. Qiu, V. Iancu, X.-Q. Chen, H. Pan, W. Wang, N.M. Dimitrijevic, T. Rajh, H.M. Meyer III, M.P. Paranthaman, G.M. Stocks, H.H. Weitering, B. Gu, G. Eres, Z. Zhang, Band Gap Narrowing of Titanium Oxide Semiconductors by Noncompensated Anion-Cation co-doping for Enhanced Visible-Light Photoactivity, Phys. Rev. Let. 103 (2009) 226401:1-4.
120. H. Sun, G. Zhou, S. Liu, H.M. Ang, M. O Tadé, S. Wang, Visible Light Responsive Titania Photocatalysts co-doped by Nitrogen and Metal (Fe, Ni, Ag, or Pt) for Remediation of Aqueous Pollutants, Chem. Eng. J. 231 (2013) 18-25.
121. R. Jaiswal, J. Bharambe, N. Patel, A. Dashora, D.C. Kothari, A. Miotello, Copper and Nitrogen co-doped TiO_2 Photocatalyst with Enhanced Optical Absorption and Catalytic Activity, Appl. Catal., B 168-169 (2015) 333-341.
122. M.B. Fishera, D.A. Keaneb, P. Fernández-Ibáñez, J. Colreavy, S.J. Hinder, K.G. McGuigan, S.C. Pillai, Nitrogen and Copper Doped Solar Light Active

TiO_2 Photocatalysts for Water Decontamination, Appl. Catal., B 130-131 (2013) 8-13.

123. H. Liu, M. Zou, B.V. Hakala, R.S. Abolaji, M. Yang, Synthesis, Characterization of Cu, N co-doped TiO_2 Microspheres with Enhanced Photocatalytic Activities, Adv. Mater. Sci. 2 (2017) 1-7.
124. K. Song, J. Zhou, J. Bao, Y. Feng, Photocatalytic Activity of (Copper, Nitrogen)-co-doped Titanium Dioxide Nanoparticles, J. Am. Ceram. Soc. 91 (2008) 1369-1371.
125. S.M. Reda, M. Khairy, M.A. Mousa, Photocatalytic Activity of Nitrogen and Copper Doped TiO_2 Nanoparticles Prepared by Microwave-Assisted Sol-Gel Process, Arabian J. Chem. (2017) doi.org/10.1016/j.arabjc.2017.02.002.
126. M. Nurdin, L.O.A.N. Ramadhan, D. Darmawati, M. Maulidiyah, D. Wibowo, Synthesis of Ni, N co-doped TiO_2 using Microwave-Assisted Method for Sodium Lauryl Sulfate Degradation by Photocatalyst, J. Coat. Technol. Res. 15 (2018) 395-402.
127. S. Priatmoko, Triyono, I. Kartini, Roto, Preparation, Characterization and Activity of Ni and N co-doped TiO_2 Photocatalyst in Degradation of Methylene Blue, Asian J. Chem. 28 (2016) 1697-1702.
128. Y. Zhang, C. Li, C. Pan, N + Ni co-doped Anatase TiO_2 Nanocrystals with Exposed {001} Facets through Two-Step Hydrothermal Route, J. Am. Ceram. Soc. 95 (2012) 2951-2956.
129. K.A. Cychosz, R. Guillet-Nicolas, J. García-Martínez, M. Thommes, Recent Advances in the Textural Characterization of Hierarchically Structured Nanoporous Materials, Chem. Soc. Rev. 46 (2017) 389-414.

Chapter 4 – Synthesis and applications of mixed metal nano composites for hydrogen generation

4.1. Introduction

Depleting petroleum source and pollution problems associated with its use in the automobile industry has led to search for an alternate source of energy. Transportation economy based on hydrogen fuel has attracted considerable interest. One of the problems associated to use of hydrogen as a fuel for automobiles is the storage to run at least 500 km without need to refill. Presently it is almost impossible to store that much amount of hydrogen required for a more efficient car. In view of this many materials of high volumetric and/or gravimetric hydrogen densities are studied. Metal hydrides and borane compounds of amines/ ammonia are explored as potential storage materials. One borane compound, ammonia borane (AB = NH_3BH_3) has attracted significant interest due to its stability and commercial availability. AB is a solid at room temperature, stable to moisture and air and contain 1902 / kg (100-140 g/ L) hydrogen. Various methods have been employed to harness H_2 from AB. Some of these are mentioned below.

1. Solid state thermal decomposition
2. Ionic liquid catalysed dehydrogenation
3. Solution phase decomposition
4. Nano-phase ammonia borane encapsulated in SBA-15
5. Transition metal catalysed dehydrogenation

Solid state thermal decomposition

In this method, hydrogen is obtained by thermal decomposition of AB. High temperatures (around 110, 150 and 1400 °C for the first, second and third equivalent of H_2), are required for the release of hydrogen. However, higher heating rates results in volatile product such as borazine. Such unwanted volatile products may be detrimental to PEM fuel cells.

Dehydrogenation of AB in ionic liquids

AB can be dehydrogenated in ionic liquids more efficiently than by thermal heating and at much lower temperatures. The role of ionic liquids in dehydrogenating AB may be related to its ability to induce formation of ionic species. However, this method has not been explored to that extent.

Solution phase thermal dehydrogenation

The thermal decomposition of AB in ethereal solutions like glyme, diglyme, THF and 2-methyl THF has shown to release hydrogen by forming solvent borane adducts.

Nano-phase ammonia borane encapsulated in SBA-15

Preparation of nanophase AB by incorporating AB into the channels of mesoporous silica SBA-15 is reported [1]. This has resulted in lowering of dehydrogenation temperature from 114 °C to 85 °C, which has helped decrease the release of the borazine side product.

Transition metal (TM) catalysed dehydrogenation

Dehydrogenation of ammonia borane in the presence of a suitable TM catalyst under aqueous conditions can give 3 molecules of hydrogen (eq. 1)

$$NH_3BH_3\ (aq) + 2H_2O \xrightarrow{TM} NH^{4+}\ (aq) + BO^{2-}\ (aq) + 3H_2\ (g) \qquad \text{(eq. 1)}$$

Numerous transition metals have been explored for this reaction and the quantity and rate of hydrogen release is found to be depended on the catalyst. Also, hydrogen can be released *via* alcoholysis in the presence of a transition metal catalyst (eq. 2)

$$NH_3BH_3 + 4CH_3OH \xrightarrow{TM} NH_4\ B(OCH_3)_4\ (sol) + 3H_2\ (g) \qquad \text{(eq. 2)}$$

Hydrolysis or methanolysis of AB can produce 3 equivalents of H_2. AB is quite stable in water and methanol under neutral and weakly basic medium. When proper catalysts are used, hydrogen release can take place at ambient temperature. Hence, efficient, economical, recyclable and easily accessible catalysts are desirable from the solvolysis reaction. Till date significant progress has been made in the development of heterogeneous nano catalyst. Several comprehensive review articles are published [2-5] and more and more articles are being published. Monometallic and heterometallic reagents are pursued in search of better efficiency. Numerous studies have been carried out using noble metals, which show mostly extremely high activity of hydrolytic dehydrogenation of AB. However the cost of the catalyst and recyclability are the two issues to be addressed. To overcome the recyclability issue and increase the efficiency, many solid supports such as carbon material, SiO_2, γ-Al_2O_3, metal-organic frameworks *etc.* have been used. The solid supports also help in dispersing the noble metal nanoparticles, prevention of agglomeration and controlling the size and morphology. Introduction of magnetic materials into the support has greatly addressed the recovery problems.

For practical applications nanocatalyst based on first row transition metals such as Fe, Co, Ni and Cu have also been successfully applied for hydrolysis of AB [6]. However the stability of

this non-noble catalyst has to be taken into account as they readily oxidize. Polymer, dendrimer, capping, is used to stabilize these metals.

Another approach pursued is introduction of metalloid elements like boron and phosphorous. They seem to be effective in improving the stability of these metals.

Recently heterometallic catalyst has attracted people working in this field. Bimetallic and multimetallic catalyst due to synergistic effect can enhance the catalytic performance of the individual metals. Bimetallic nanoparticles on supported materials are reported in literature to display distinctly improved catalytic efficiency [7-10]. Also, some of the transition metal alloys based on Pt and Ni are studied for comparative hydrogen generations. Alloys of Pt were shown for decreasing activity of H_2-generation in the order of PtRu>Pt_3Au>PtIr>PtCo> Pt_3Ni>PtCu>PtSn~Pt/C, whereas NiSn and NiAu is reported to show higher activity among Ni based alloys [11-13].

Bimetallic nanoparticles with core-shell architecture have gained much interest due to their unique and novel characteristic properties and catalytic applications [14]. Some of the core-shell nanoparticles *viz.*, Ni@Ru, Au@Co, *etc.*, are claimed to exhibit better catalytic activity compared to alloys and other monometallic catalysts [12, 15]. Other bimetallic and trimetallic core-shell nanoparticles are also reported to show higher activities than that of corresponding monometallic counterparts [16-27].

Among the first transition series, Fe, Co and Ni are of special interest for such reactions because of their magnetic nature, which makes them easily recyclable. Some of these like, NiCu, NiCo, CuCo, CuFe, FeCo, CoNi, FeNi combinations are already being shown to be effective in AB dehydrogenation [11, 28-32].

Catalytic activities at ambient temperature of some selected first transition series monometallic and bimetallic catalyst for the dehydrogenation of AB are shown below (Table 1).

From our laboratory, Co.Co_2.B as an efficient magnetically recoverable catalyst was reported for hydrolysis of $NaBH_4$ in generating H_2 [53]. Prior to that, Co-Ni-B nanocomposite was proved to be efficient bimetallic combination compared to individual metal-metal boride nanocomposites, for dehydrogenation of AB in methanol [54].

Continuing the studies in this field, we were interested in studying the bimetallic system stabilized by boron for H_2-generation. For this we chose iron and nickel as the two metal components. Limited literature is known for the combination of these two metals. Fe-Ni (1:1) alloy was found to be very efficient for dehydrogenation of AB [55]. Fe-Ni (1:1) nanoparticles on plolythyleneimone-decorated graphine oxide were found to be very

effective for dehydrogenation of AB [56]. Ni-Fe-B with Ni-Fe (1:1) was reported for hydrolysis of sodium borohydride [57]. We chose Fe-Ni-B system for this study. The required composite in varying ratio of Fe:Ni was to be synthesized from reduction of the corresponding salts of the metals by ammonia-borane. Xu and co-workers [47] have reduced Fe^{2+} with $NaBH_4$ in presence of AB. In literature Fe nanoparticles hydrolysis with AB releases 3 moles of hydrogen in 8 min [47], Ni-B with $NaBH_4$ takes 18 min [57], while Ni-Ni_3-B with $NaBH_4$ takes 6 min [53].

Table 1: *Catalytic activities at ambient temperature of some selected first transition series monometallic and bimetallic catalyst for the dehydrogenation of AB*

Catalyst	**Catalyst/AB molar ratio**	**TOF (min^{-1})**	**Ref.**
Cu/SiO_2-$CoFe_2O_4$	0.0031	40.0	33
Ni@3D-(N)GF	0.0090	41.7	34
Skeletal Ni	--	5.3	35
Ni@MCM-41	0.0160	30.7	36
Ni/CNT	0.0254, -	26.2, 23.53	37, 38
Ni@mesoSiO_2	0.00425	18.5	39
Ni/ZIF-8	0.0160	14.2	40
Ni NPs/C	0.0425	8.8	41
Co/PEI-GO	0.1110	39.9	42
Co/PSMA	0.0200	25.7	43
Co/graphene	0.0130	13.9	44
Co@N-C 700	--	5.6	45
G6-OH(Co60)	0.0130	10.0	46
Amorphous Fe	0.1200	3.125	47
PEG stabilized Fe	0.1250	6.4	48
CuNi/ CMK-1	0.0720	54.8	49
CuCo@MIL-101	0.0340	19.6	50
NiMo/ graphene	0.0500	66.7	51
CoNi/ RGO	0.0500	19.54	52
CoNi/ graphene	0.0200	13.49	32

4.2. General experimental procedure

Materials

$Fe(NO_3)_3.9H_2O$, $Ni(NO_3)_2.6H_2O$, were purchased from Molychem and methanol from Runa chemicals. Ammonia borane was synthesized from $(NH_4)_2SO_4$ and $NaBH_4$ in 70-80 % yields in 4 h of reaction time, using the literature procedure [58].

Preparation of Fe-Ni-B nanocomposites

To a methanol solution (2 mL) of $Ni(NO_3)_2.6H_2O$ (26.72 mg, 0.09 mM) and $(Fe(NO_3)_3.9H_2O$ (4.04 mg, 0.01 mM), excess of ammonia borane was added in a test tube connected to a gas burette. The reaction started with the continuous evolution of hydrogen gas and a black colored powder was formed. After the evolution of H_2 ceases, a black powder formed was made to settle at the bottom of the test tube by attracting with an external magnet. The supernatant was syringed out. The obtained nano powder was washed with methanol several times. The x value of $Ni_{1-x}Fe_x$ was changed from 0 to 1 (0, 0.05, 0.1, 0.25, 0.5, 0.75 and 1).

Catalyst characterization

The prepared nanocomposite was characterized by various techniques. For investigating morphology and particle size of the sample, transmission electron microscopy (TEM), High resolution TEM and selective area electron diffraction (SAED) patterns were obtained by using TECHNAI F30 field emission transmission electron microscope operating at 200 kV. Scanning electron microscopy (SEM) was cone by using ESEM Quanta 200, FEI instrument. Structural characterization was performed by conventional X-Ray powder diffraction using Bruker D8 ADVANCE X-ray diffractometer with Cu Kα radiation (1.5406A°) in the 2θ scan range of 10-80°. Multiple point BET surface areas and pore structures were measured with a surface area and porosity analyzer (Micromeritics Tristar 3000, USA), at the temperature of liquid nitrogen. Before the analysis, samples were degassed at 200 °C for 8 h with continuous flow of nitrogen gas. Magnetic properties were studied as a function of applied field (M–H) using a vibrating sample magnetometer (VSM) on a Quantum Design-Versa Lab model. The XPS measurements were carried out by employing a Mg KR source at room temperature at a base pressure of 3 × 10-10 Torr, using a custom-built high-resolution photoelectron spectrometer.

Measurement of Hydrogen generation

For catalytic H_2-production, 1 mL of methanol solution of AB (16 mg, 0.5 mM), was added to Shlenk tube containing the above prepared catalyst. This solution (in a water bath) was stirred/ swirled manually throughout the experiment. Catalytic activity for this reaction was determined by measuring H_2-generation by an analytical gas burette containing copper sulfate solution. The final volume was recorded by equalizing the levels in the burette and the reservoir. All the experiments were conducted three times and the constructed graphs are presented with standard deviation.

Kinetic studies

Initially the prepared catalyst was studied for H_2-production at different pH range *viz.* pH 5 (using citrate buffer), pH 7.4 and 8 (using phosphate buffer), to see whether it affects the rate of hydrogenation. Further, different solvents (H_2O, DMSO and THF) were screened as a medium and methanol.

The kinetics of this reaction was studied by varying different parameters, such as, Fe/(Fe + Ni) ratio, solution temperature, catalyst concentration and ammonia borane concentration. Initially Fe/(Fe+Ni) ratio was varied and the corresponding rate of hydrogen generation was studied for these samples. The sample giving good results was chosen for further experiment. The methanolysis reaction was carried out at different temperatures ranging from 9 ℃ to 49 °C to find the activation energies. To know the order of reaction the catalyst concentration and AB concentration were varied keeping other parameters constant.

Recyclability

To evaluate the utility of the catalyst, catalyst recyclability was studied for more than 5 cycles. Recovery of the catalyst was achieved by magnetic separation and removal of the supernatant by syringe.

4.3. Result and discussion

Effect of Fe/(Fe + Ni) ratio variation

Initially equivalent quantities of Ni and Fe were mixed together and reduced with AB. A rapid stream of hydrogen generation was noticed. The catalyst formed was separated with the help of a magnet and a fresh AB solution was added. Again, rapid generation of hydrogen was seen. Encouraged by these results a systematic study by varying the ratio of Fe/(Fe + Ni) from 0, 5, 10, 25, 75 and 100% Fe concentration was undertaken. For each concentration the catalyst formed was studied for the volume and the rate of H_2-generation and is plotted against time as shown Fig. 1.

It is observed that the reaction catalyzed by Ni alone (0% Fe) takes 18 min for completion of reaction with lower rate of reaction (54 mL/min/g), which increases with Fe concentration up to 10 % Fe (Fe:Ni = 0.01:0.09), for which the highest rate was obtained of 2198.49 mL/min/g and with the further increase in Fe concentration, the rate drastically falls down. At 75 % and 100% Fe, catalyst formed is non-magnetic and does not show H_2-generation. As the highest rate of H_2-generation was for the concentration 10 % Fe (Fe:Ni = 0.01:0.09), this concentration was used for further studies.

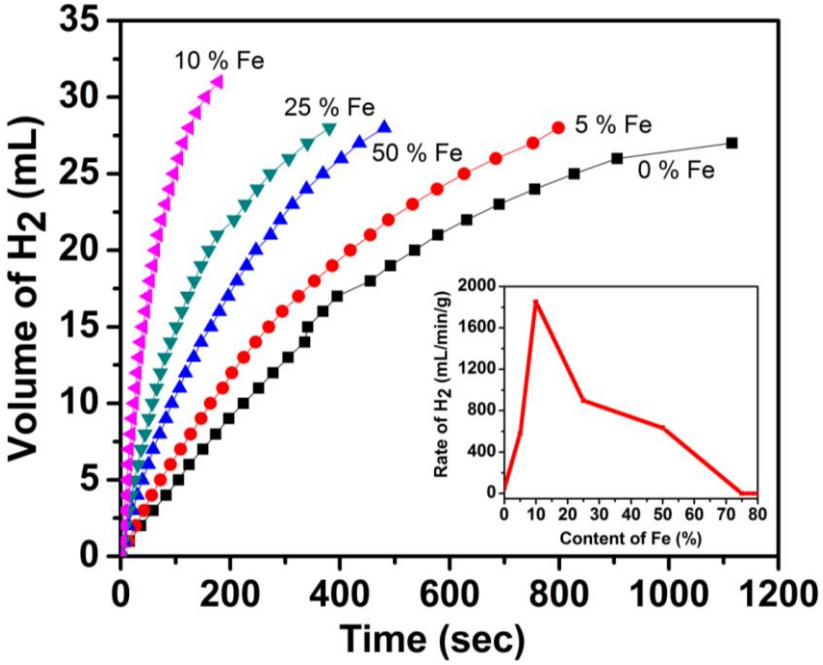

Fig. 1– *H_2-generation rate for varying molar ratio of Fe-Ni-B catalyst and corresponding comparative graph (inset)*

To check whether such bimetallic system can also be synthesized by sequential reduction instead of tandem reductions, we attempted reduction of Fe^{3+} and Ni^{2+} salts separately with AB. In case of Fe^{3+} no reduction was observed while Ni^{2+} salts got reduced. Hence, to this

reduced Ni (Ni-Ni_2B), Fe^{3+} salts were added, followed by a fresh bout of AB. However the materials formed were found to be poor generator of H_2.

Effect of solvent variation

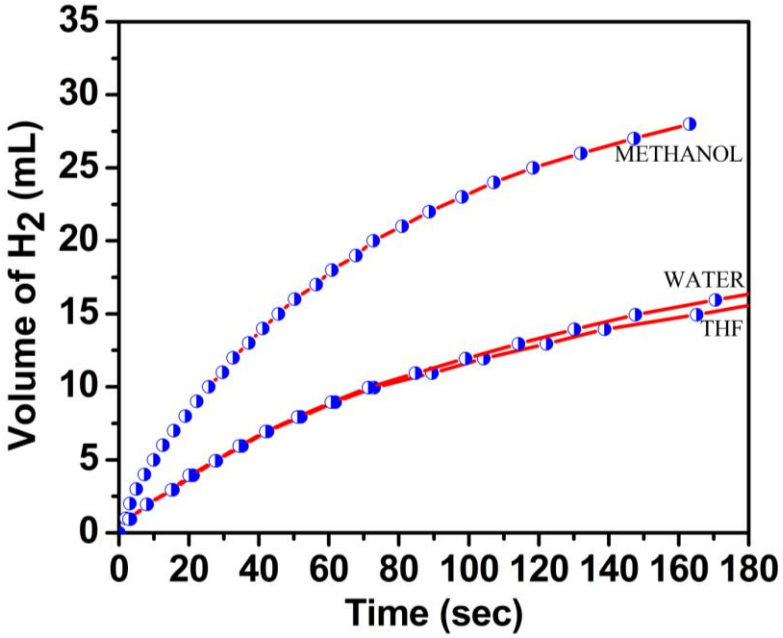

Fig. 2a– *Rate of H_2-generation with varying solvents*

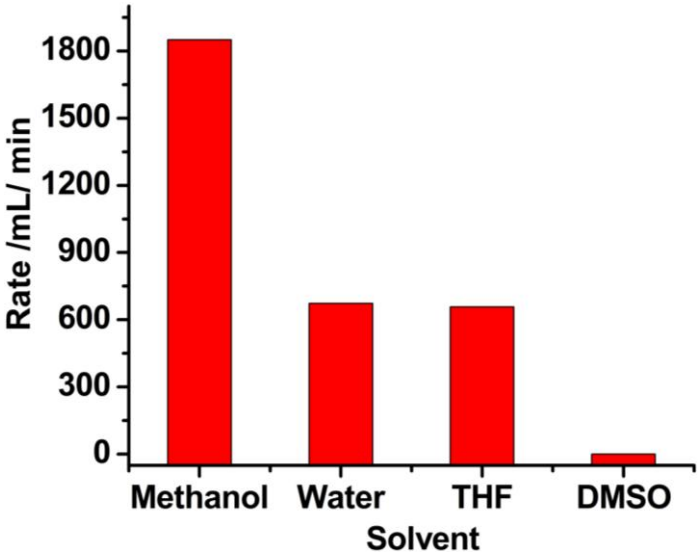

Fig. 2b– *Comparative study of H_2-generation with varying solvents*

The effect of a change in solvents on H_2-generation was studied with water, THF and DMSO solvents in comparison with methanol. The observed rate of hydrogenation is given in Fig. 2a. It can be seen that methanol was found to be a better solvent giving highest rate, while water and THF is found to give lower rate. When DMSO was used as a solvent, no H_2-generation was observed (Fig. 2b). Hence methanol was chosen as the reaction medium.

Catalyst activity measurement

The volume of H_2 generated was measured as a function of time by methanolysis of AB (0.5 mM) with Fe-Ni-B catalyst (0.01 mM) at RT (29 °C) and neutral pH. The plot of H_2-generation versus time is given in Fig. 3. The excellent catalytic activity of this catalyst was revealed by completion of reaction in a short period of 2.7 min.

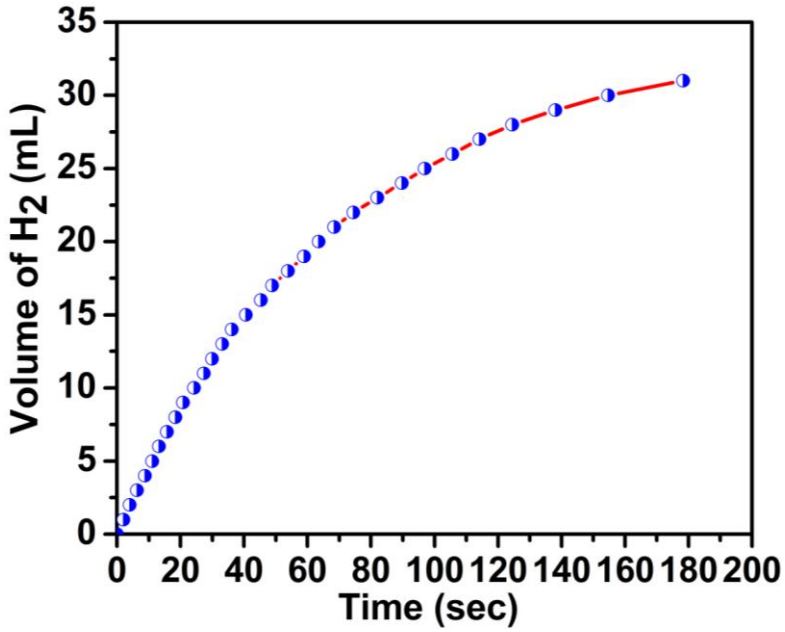

Fig. 3– *H_2-generation rate of Fe-Ni-B catalyst with Fe:Ni molar ratio 0.01:0.09*

Effect of pH

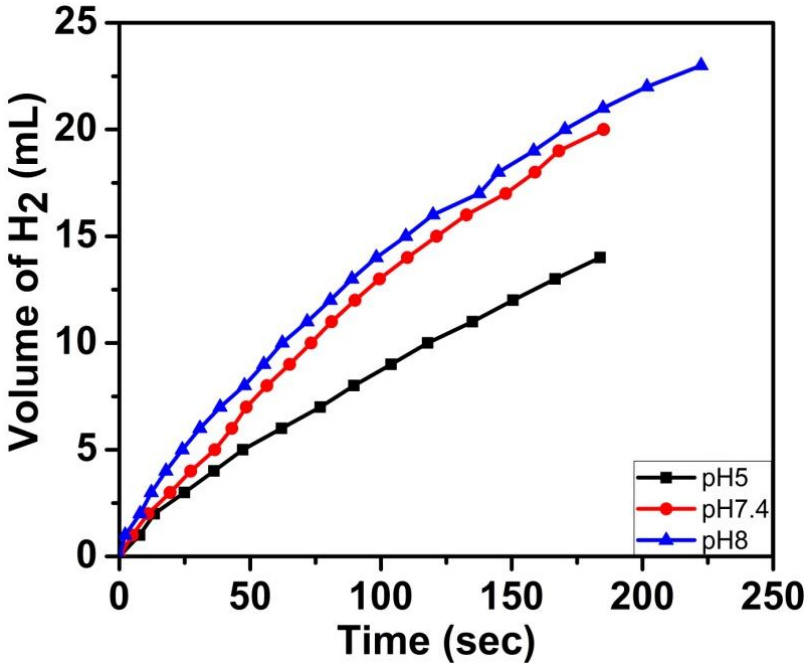

Fig. 4– *Effect pH variation on H_2-generation rate of Fe-Ni-B catalyst*

To study the buffer activity, the effect of variation of pH was studied and the corresponding rate was compared. It was found that, with the change in pH from 5 to 7.4 to 8, the rate is observed to decrease (Fig. 4).

Structural and morphological properties

Powder X-ray studies

XRD plot for as prepared sample, display broad peaks indicating the amorphous nature of the sample (Fig. 5a). This is also true for reported Fe-Ni/ Fe-Ni-B nano alloys [57, 59], where it is claimed that amorphous catalyst show better activity.

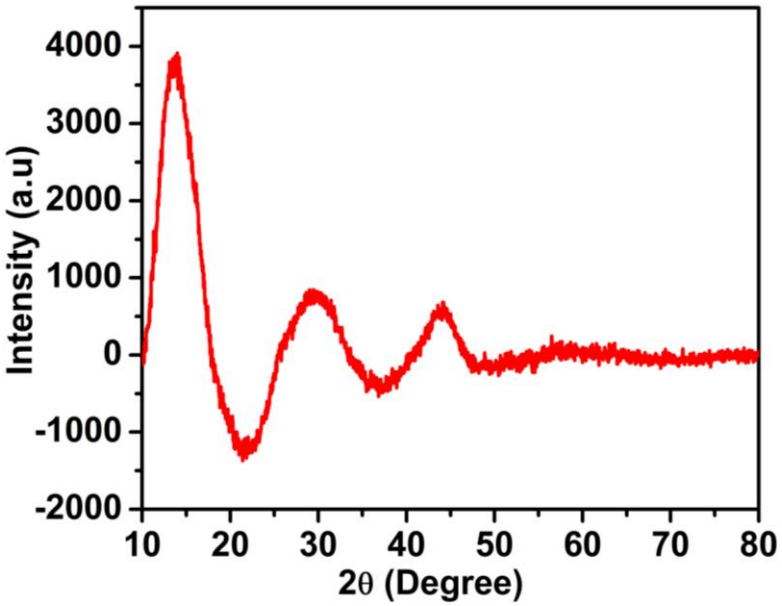

Fig. 5a— *XRD plots for as prepared sample*

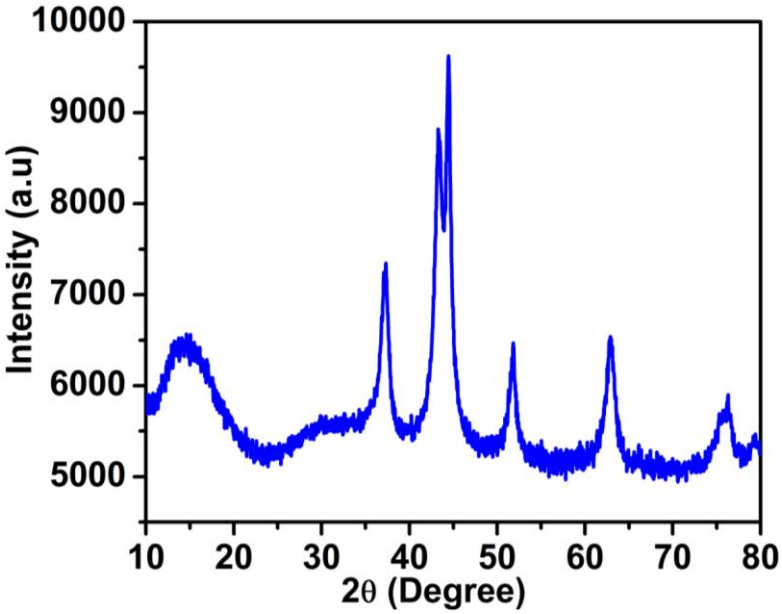

Fig. 5b— *XRD plots for annealed sample of Fe-Ni-B*

To further analyze the phase and crystallite size of the catalyst, X-ray powder diffraction study of the annealed sample, at 350 °C for 12 h under nitrogen atmosphere, was carried out and the pattern obtained is shown in Fig. 5b. Crystalline peaks obtained, clearly indicate the formation of Fe-Ni-B nano alloy and the peaks can be marked as (112), (022), (210), (212) and (042), of the composition Fe_3Ni_3B orthorhombic (ICDD File Card No. 36- 979).
The mean crystallite size of the highest intensity peak in annealed sample, was estimated by using Scherrer's formula $D = K\lambda / \beta \cos\theta$, where, K is the Scherrer constant, λ is the X-ray wavelength, β is the peak width at half maximum and θ is the Bragg's diffraction angle. It is found to be approximately 14 nm.

BET analysis of annealed catalyst

Further the surface area and other related details of the annealed Fe-Ni-B catalyst were studied by using the BET method and are compared with Ni-B sample. The isotherm plots for Fe-Ni-B and Ni-B samples are respectively shown in Fig. 6a and 6b, with corresponding pore size distribution curves (inset). The surface area data of Ni-B and Fe-Ni-B is observed to be similar as that of reported in previous data [57, 59]. The comparative values of surface area, pore volume and pore diameter of Ni-B and Fe-Ni-B are displayed in Table 2. The surface area value was found to increase from 19.64 m^2/g to 24.66 m^2/g, on introducing Fe in Ni-B sample. This observation is in accordance with the literature report, which states that the introduction of Fe is responsible for the increase of surface area of Ni-B catalyst. The observed lower value of surface area for both the samples could be possibly due to partial aggregation of metal during the annealation process [59].
The isotherm curves are more resembling to type II, indicating non-porous or macroporous nature of the sample. The intermediate flat region in the isotherms corresponds to unrestricted monolayer-multilayer adsorption up to high P/P_0 value. The H3-type hysteresis pattern with characteristic lower closure point, in case of Fe-Ni-B sample, is indicative of slit-like pores. Slight adsorption at very low-relative pressure ($P/P_0 < 0.01$) for this sample, is indicative of the existence of micropores in the catalyst. However, for sample Ni-B, the comparatively higher value of closure point at $P/P_0 = 0.5$, reflects the interconnected blocked pores with condensation of surface necks, due to neck closing of bottle-neck pores.
Extremely narrow pore size distribution from 3-4 nm is seen for both the samples, tells about the existence of micropores. The additional small peak at lower value for Ni-B sample further suggests the slight amorphous nature of the sample [60-63].

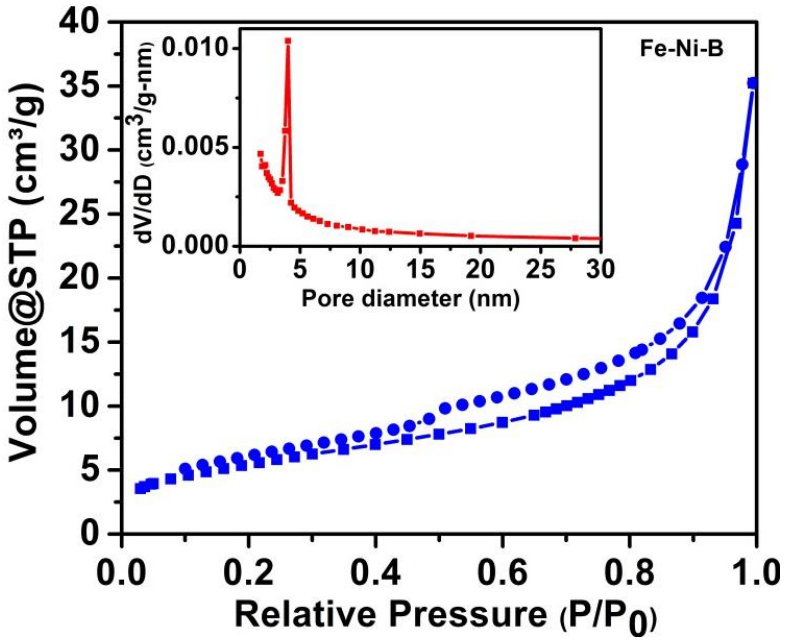

Fig. 6a— *N_2 adsorption-desorption isotherms and pore size distribution (inset) of Fe-Ni-B catalysts*

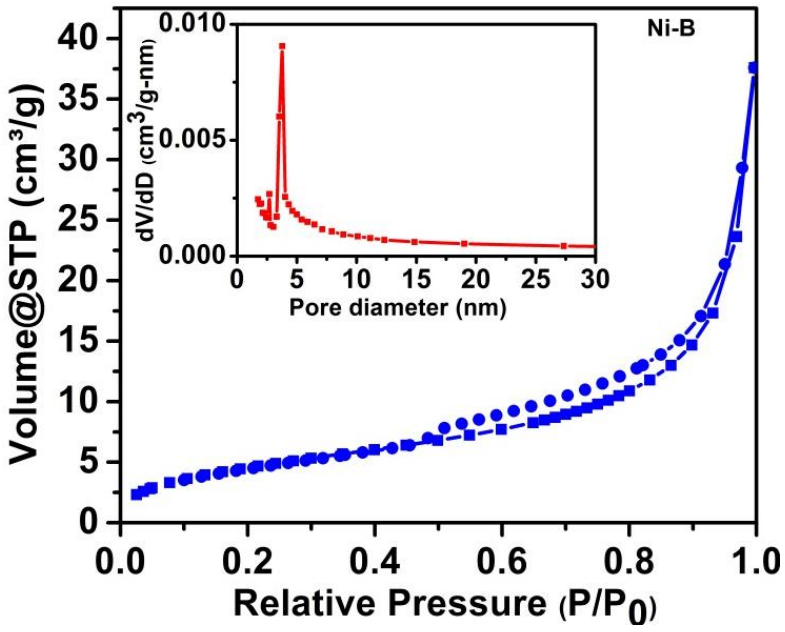

Fig. 6b-*N_2 adsorption-desorption isotherms and pore size distribution (inset) of Ni-B catalysts*

Table 2 – Surface area values of Ni-B and Fe-Ni-B catalysts

Sample No	BET Surface Area (m^2/g)	BJH Desorption cumulative surface area of pores (m^2/g)	BJH Desorption cumulative volume of pores (cm^3/g)	BJH Desorption average pore diameter (nm)
Ni-B	17.26	19.64	0.058	11.81
Fe-Ni-B	19.65	24.65	0.056	9.03

SEM analysis

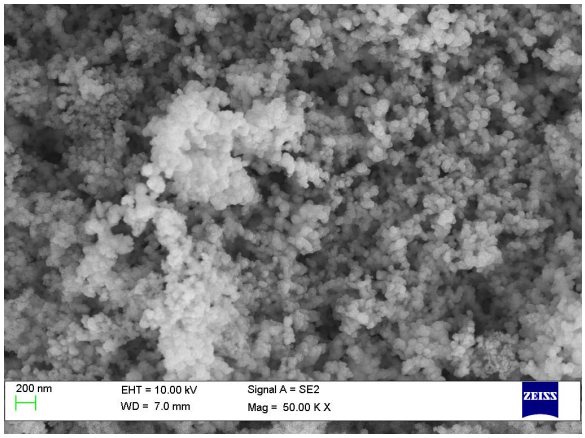

Fig. 7a—*SEM image of Fe-Ni-B catalyst*

The morphology of the annealed sample was studied by using SEM analysis (Fig. 7a). It can be seen that the sample is obtained with similar particle-like morphology, homogeneously distributed and are nearly spherical in shape. Smaller particles are found aggregated in clusters, may be due to higher surface energy. A lower degree of agglomeration is also seen among the particles.

TEM analysis

The particle morphology and shape is further confirmed by TEM analysis (Fig. 7b). TEM micrograph (Fig. 7b (p)) display nearly spherical nanoparticles dispersed in the form of agglomerates. Some self-aggregation is also seen which results in a sponge like particles, and hence the exact determination of size is difficult. This self-aggregation is may be due to the high specific surface energy for the nanosized particles, and is in accordance with the SEM results [59].

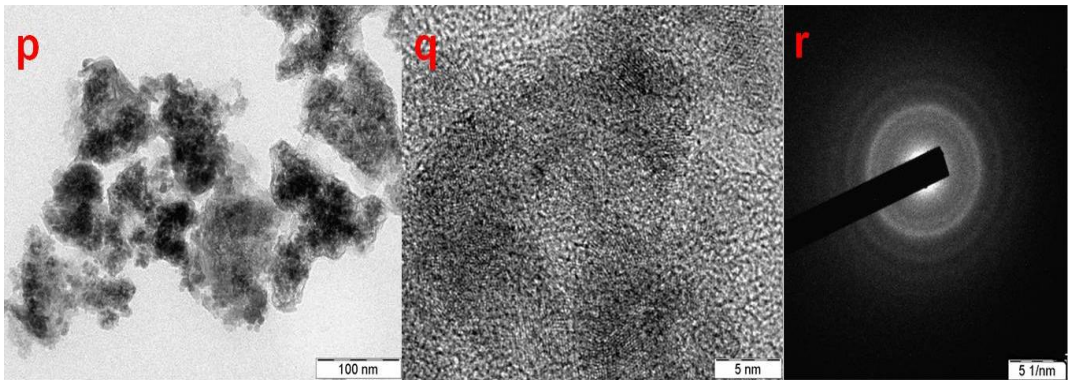

Fig. 7b—*TEM image (p), corresponding HRTEM image (q) and SAED pattern (r) of Fe-Ni-B catalyst*

HRTEM further tells about the details of the particles (Fig. 7b (q)). The small grains of amorphous nanoparticles with absence of lattice fringes are observed from the picture.

TEM micro diffraction of the alloy particles (SAED) (Fig. 7b (r)) shows diffuse ring pattern of cloud like nature which is a characteristic of amorphous material. Also a very blurred polycrystalline ring pattern is observed outside the cloudy region, indicating the presence of some crystallinity along with amorphous mixture. This may have arisen during annealation of the sample.

XPS analysis of annealed catalyst

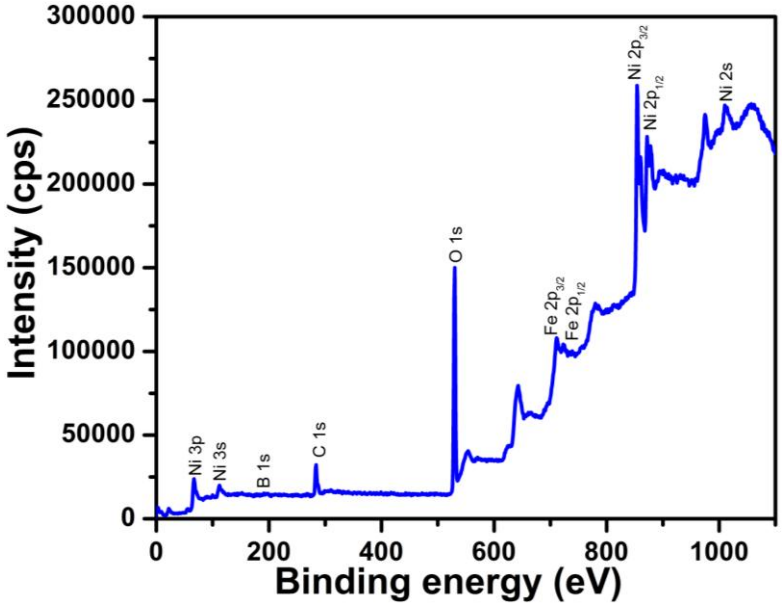

Fig. 8— *XPS full scan spectra for Fe-Ni-B catalyst*

XPS analysis was employed to further verify the chemical states of elements of the catalyst prepared. The XPS full scan spectrum of the prepared samples is shown in Fig. 8. Major peaks due to Ni 2p, Fe 2p and B 1s are clearly seen in the spectra along with the peaks due to Ni 3p, 3s, and 2s. Several additional peaks are also seen to appear, which can be attributed to the oxidation of these metals during handling of the catalyst and XPS sampling procedure [59]. Moreover, since XPS is a surface technique, some oxide peaks are expected to appear in the spectra.

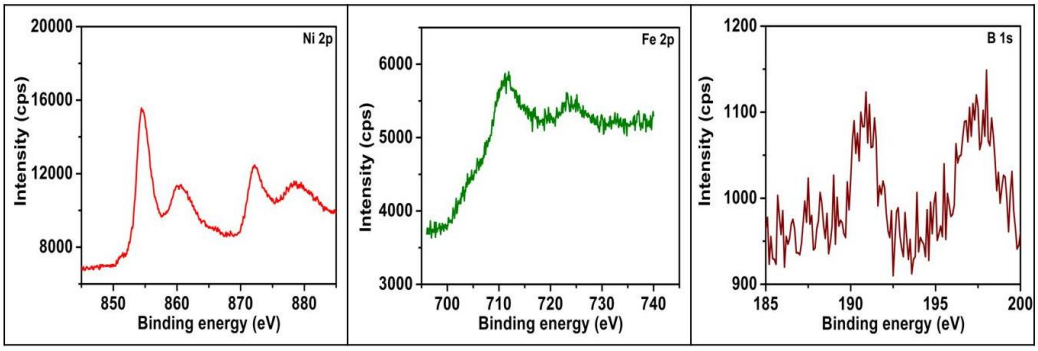

Fig. 9— *XPS spectra for Fe-Ni-B catalyst – for Ni 2p, Fe 2p and B 1s*

Detailed study of XPS spectra shows 2 peaks at 854.5 eV and 872.2 eV, are due to spin-orbit doublet splitting of Ni 2p orbital, which gives Ni $2p_{3/2}$ and Ni $2p_{1/2}$ respectively. Small peaks at 710.6 eV and 722.9 eV, are due to spin-orbit splitting of Fe 2p to Fe $2p_{3/2}$ and Fe $2p_{1/2}$ respectively. The peaks of B 1s at 190.9 eV and 198 eV correspond to elemental boron and oxidized boron respectively. Main peaks for Ni 2p, Fe 2p and B 1s, after carbon correction are shown in detail (Fig. 9). The shift in binding energy of elemental boron in comparison with the pure boron (187.1 eV), indicates the partial electron donation of boron to the alloying nickel and hence confirming the formation of Fe-Ni-B alloy.

Magnetic studies (VSM)

The coercivity and magnetic moment of the catalyst sample was measured by vibrating sample magnetometer as a function of milling time in magnetic field with the maximum induction of 3 T at 50 K and 300 K (RT) (Fig. 10).

The magnetization parameters are displayed in Table 3. It is observed that the magnetization values decreases with increasing temperature, may be due to increase in randomness of spins at higher temperature.

Further the analysis of hysteresis loop indicates the presence of a non-saturating component in the sample, which is found to be of a higher degree at low temperature. The highest value of magnetization at 3T, is found to be 0.058 and 0.124 emu/g, and the corresponding M_r value is 0.0025 and 2.629 emu/g respectively at 300 K and 50 K. Also the comparatively narrow hysteresis loop is observed at higher temperature near the coercive field region as seen from the inset of Fig. 10. As it is stated in the literature, at lower temperature, the surface spin fluctuations are minimized and short range interactions are developed between them, resulting in frozen disordered surface spin states due to formation of magnetically correlated spins of growing size, which is further responsible for nonsaturation of the magnetization [64-65]. Further the observed change of the coercive field can be attributed to the interactions of frozen surface spins with core spins *via* interface-exchange coupling, which affect the actual anisotropy of the particle [66]. As reported earlier, H_c value of Fe-Ni alloy goes on decreasing with the addition of other elements, which may be due to its reduction. H_c value for the catalyst sample was found to be 6.264 Oe (0.5 kA/m), which is observed to be higher than the reported value for Fe-Ni-B sample (up to 0.16 kA/m) [67].

This observed value of coercivity and highest magnetization value at 3 T, may be due to smooth, nano-granular clusters and presence of amorphous nature of the sample.

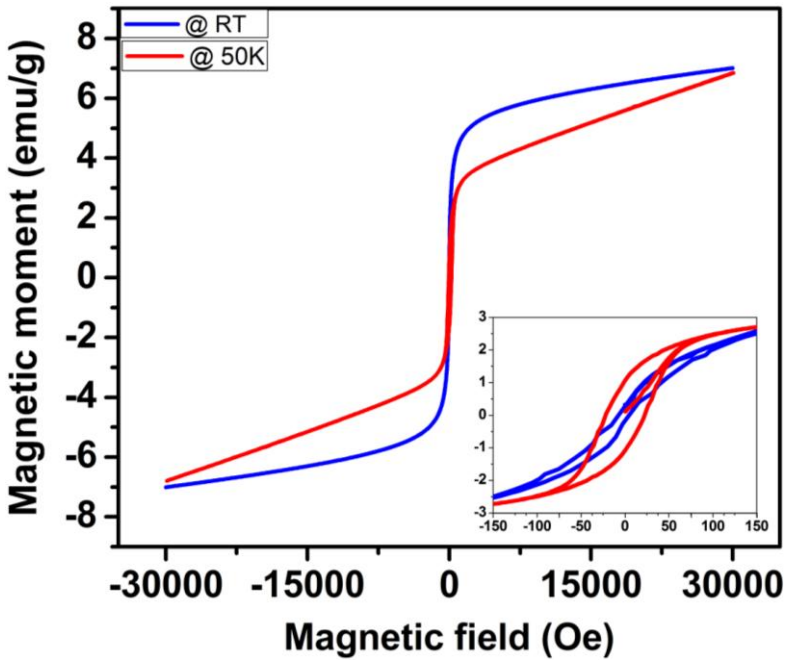

Fig. 10— *M-H curves of Fe-Ni-B catalyst at RT and at 50 K with enlarged view (inset)*

Table 3 – Magnetic properties of Fe-Ni-B catalysts at 50 K and 300 K

Temperature (K)	Highest magnetisation at 3 T (emu/g)	Remanance magnetisation (emu/g)	Coercivity (Oe)
300	6.93	0.0025	6.3
50	15.24	2.6290	145.3

Kinetic studies

Effect of temperature

The methanolysis of AB is supposed to be a temperature sensitive reaction. Thus, in order to inspect the effect of temperature on H_2-generation rate, the temperature range was chosen as 282-322 K with 10 K increments. The fixed temperature was maintained by using a water bath (either cooling with ice or heating using electric heater). Then the dehydrogenation reaction was carried out with the same concentration of catalyst and AB. It is observed that the H_2-generation rate rises rapidly with the increasing temperature as expected. The maximum rate was observed to be 333.2 mL/min/g at 282 K and 3235.8 mL/min/g at 322 K, while other parameters were kept constant.

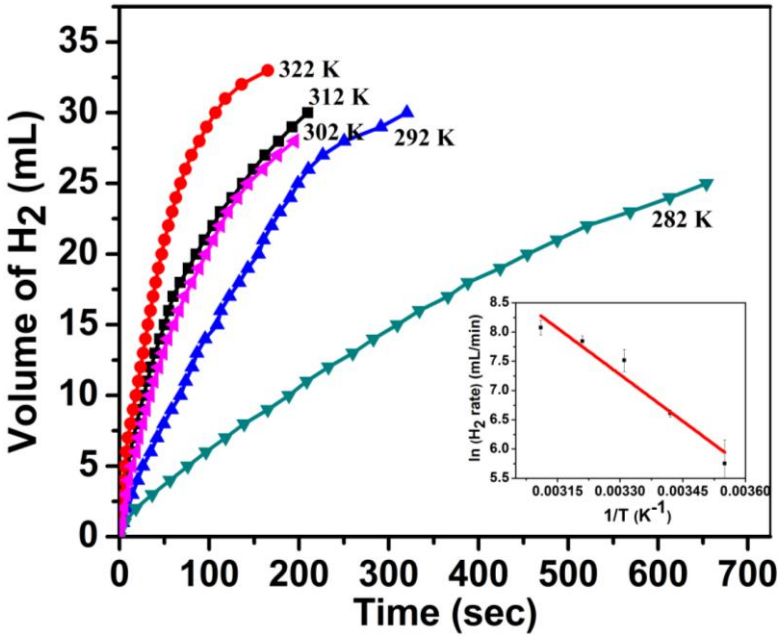

Fig. 11 – *Effect of temperature on H_2-generation rate and corresponding activation plot (inset)*

The activation energy (Ea) was calculated by using well known Arrhenius equation from the chart, ln (rate) as a function of 1/T. The rate of H_2-generation at different temperatures is shown in Fig. 12 with corresponding Arrhenius plot (inset). The activation energy as calculated from the plot is found to be 44 kJ/mol, which is found lower than that of reported values for p(AMPS)-M catalyst system of AB (47.7 kJ/mol for Co, 48.8 kJ/mol for Cu and 52.8 kJ/mol for Ni) [68], for $NaBH_4$ reduction using Fe-Ni-B catalyst (57kJ/mol) [57] and also by using other monometallic catalyst systems (Co – 75 kJ/mol, Ni - 71 kJ/mol and Raney Ni - 63kJ/mol) [69].

Effect of catalyst concentration

In order to identify the order of the reaction, the hydrogen production was affected by changing the concentration of catalyst used, from the initial concentration 0.1 mM. For this, five different concentrations, 0.05, 0.1, 0.15, 0.2 and 0.25 mM were studied for their effect on hydrogen generation rate and the same is plotted as a function of time in Fig. 12. All other parameters were kept constant. It is illustrated from the figure that the linear relationship is maintained here and the rate of H_2 generation is found to increase with increasing catalyst concentration. The fairly good linear correlation is observed from the straight line graph of ln (rate) versus ln (catalyst concentration) with slope 1.15 (inset of Fig. 12), indicates the reaction is of first order with respect to catalyst concentration. However, the slight deviation from the linear behavior is seen, which can be attributed to the interaction of the catalyst

nanoparticles (due to their highly magnetic nature) with each other, which may hinder the reaction when used in large amounts [68]. Hence it can be said that the rate is proportional to the catalyst concentration.

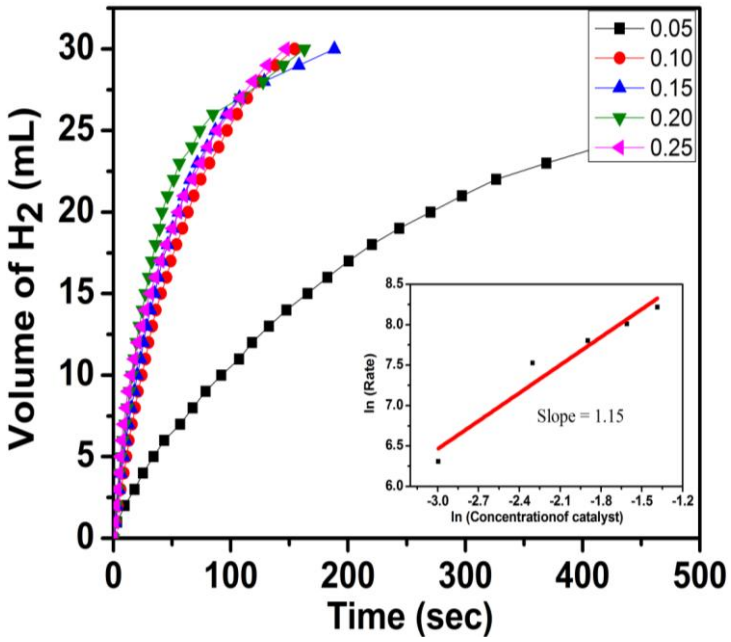

Fig. 12 – *Effect of catalyst concentration on H_2-generation rate and corresponding kinetics plot (inset)*

Effect of AB concentration (Enzyme-like kinetics)

The effect of AB concentration on dehydrogenation experiment was studied by employing Fe-Ni-B catalyst with 10 % Fe. A series of experiments were carried out using eight different concentrations of AB from 0.25 to 2.0 mM, with a difference of 0.25 mM. The other parameters were kept constant. The resulted rate of H_2-generation as a function of time, for each AB concentration is plotted as shown in Fig. 13, with corresponding kinetic studies (inset). The kinetic studies reveal that the rate of H_2-generation initially increases from concentration 0.25 mM to 0.75 mM, however it remains almost constant after that. This indicates that the H_2-generation rate is almost independent at higher concentrations of AB. Further the enzyme-like kinetics can be predicted for this system and is studied by Lineweaver-Burk plot (Fig. 14).

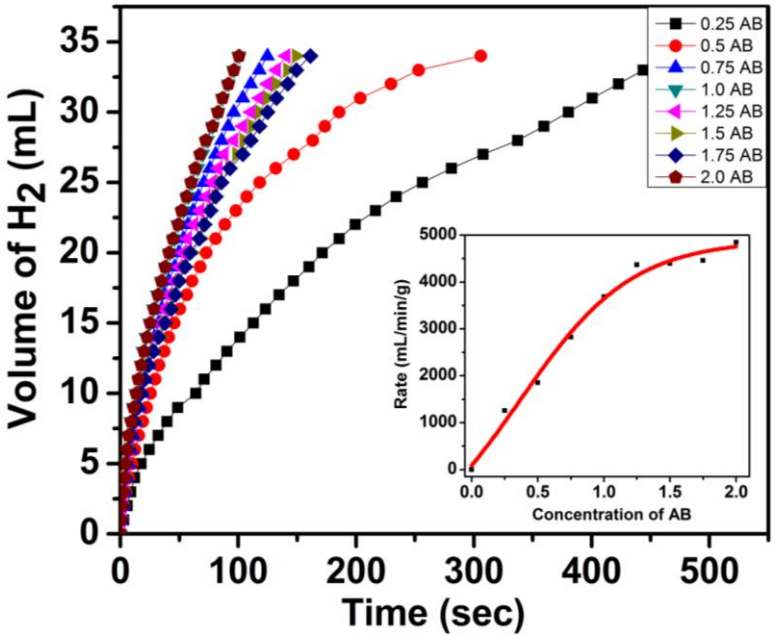

Fig. 13 – *Effect of AB concentration on H_2-generation rate and corresponding kinetic study (inset)*

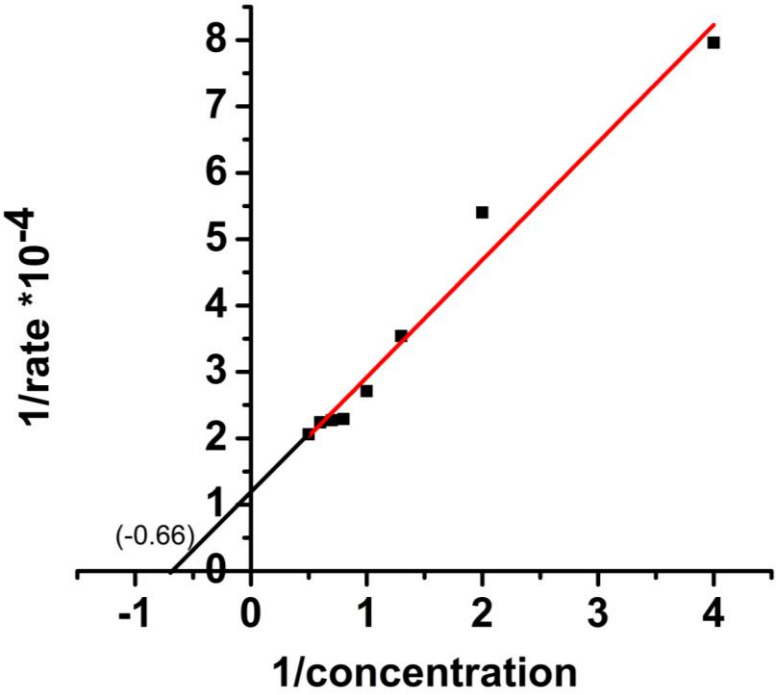

Fig. 14 – *Lineweaver-Burk plot of Fe-Ni-B catalyst*

From the Lineweaver-Burk plot, the Michaelis Menten constant, KM, of the dehydrogenation reaction was found to be 1.55 M, which is sufficiently high. Although this high value indicates that the nanocomposites have some affinity towards ammonia borane, it also indicates the rapid release of hydrogen from the surface of the catalyst after the dehydrogenation of ammonia borane. This is in agreement with the high hydrogen generation rate. The other parameter, maximum velocity, V_{max} was calculated to be around 8617.77

ml/min/g, which is higher than actually observed V_{max} value and in accordance with the principle of enzyme catalysis. These catalytic parameters explain the enzyme-like catalysis of Fe-Ni-B nanocomposites and the corresponding robust ammonia borane dehydrogenase-like activity.

The TOF was found to be 18.51/min for the ratio of 50 at room temperature.

Effect of use of support material

It is well known that metal catalyst when loaded on support materials like silica, carbon, alumina, TiO_2 *etc.* shows more efficiency. This is due to decrease in size, more surface availability, less agglomeration and better recovery. Hence, we thought of immobilizing the catalyst on TiO_2. For this we chose the TiO_2 material A7 with high surface area (see chapter 2). The same quantity of catalyst was prepared on varied amount of TiO_2 (10 mg, 25 mg and 50 mg) and this supported system was tested for H_2-generation. The rate of H_2-generation is plotted as a function of time, which is found to be 851 mL/min/g, 578 mL/min/g and 454 mL/min/g respectively (Fig 15). This rate is observed to be much lower than that of results obtained without supporting material. This could be due the catalyst getting adsorbed in the pores of the supporting material and not being available for reaction with AB and also the supporting material not having any positive effect on the catalytic reaction.

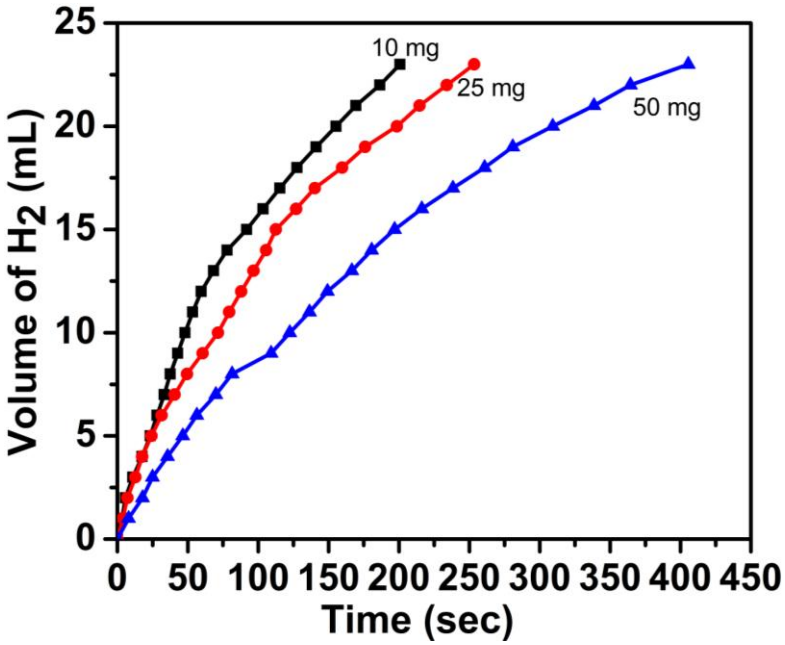

Fig. 15 – *Effect of use of support material catalyst*

Recyclability studies

To determine the recyclability of the catalyst, the same catalyst was used for more than five times for H_2-generation with the same conditions of AB concentration, temperature and solvent. The catalyst was recovered by magnetic separation.

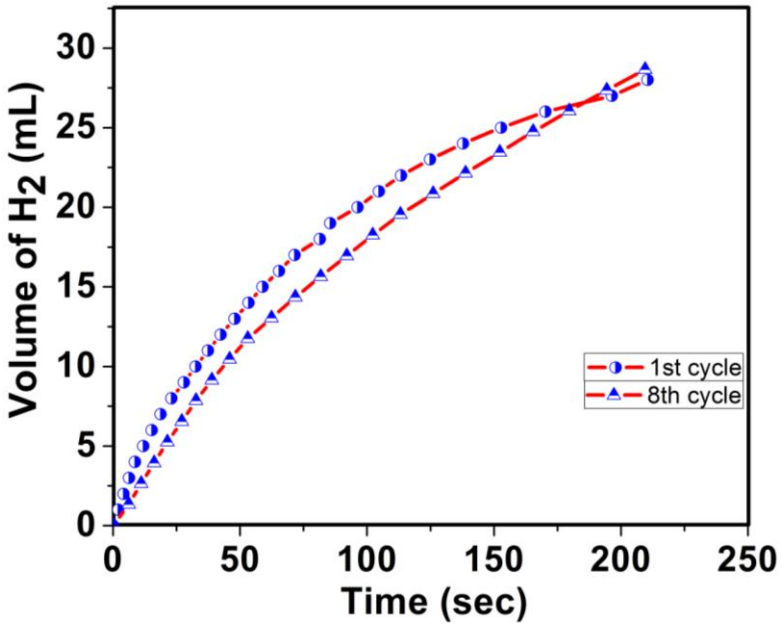

Fig. 16 – *Recyclability studies of Fe-Ni-B catalyst*

Fig. 16 shows the catalytic activity of the 1st and 8th cycle. Negligible decrease in catalytic activity can be seen from the plot and thus the catalyst Fe-Ni-B nanocomposite can be effectively used up to 8 cycles. The catalyst prepared was highly magnetic in nature. The magnetic behavior is shown in Fig. 17.

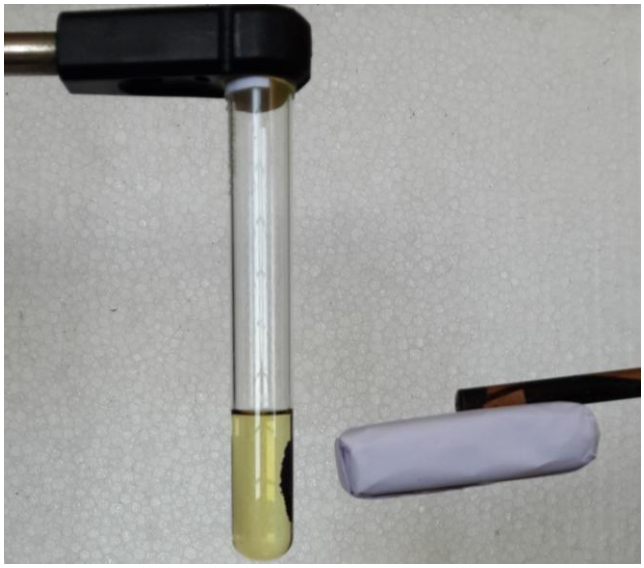

Fig. 17 – *Fe-Ni-B nanocomposites showing magnetic behaviour*

Summary and Conclusion

Fe-Ni-B nanocomposite was successfully prepared by reduction of metal salts of Fe and Ni using ammonia borane in methanol solution. The prepared catalyst was exploited for catalytic hydrogen generation from ammonia borane. The kinetics of H_2-generation was studied by varying different parameters such as Fe/Ni ratio, temperature, catalyst concentration and AB concentration. The catalytic efficacy was found by the observed rate of H_2-generation to be 2198.49 mL/min/g in 2.7 min, at room temperature, and in neutral conditions. The prepared nanoparticles possess enzyme-like catalytic activity.

The present system shows synergistic effect of Fe on Ni-B system. The catalyst's magnetic property was demonstrated for recyclability studies. However, immobilization of the catalyst on TiO_2 surfaces showed reduced activity. Interestingly, it was observed that, though iron salts do not get reduced by AB, in the presence of Ni-B they do get reduced.

References

1. J.-H. Park, S.-K. Kim, H.S. Kim, Y.J. Cho, J. Park, K.E. Lee, C.W. Yoon, S.W. Nam, S.O. Kang, Convenient Metal Embedment into Mesoporous Silica Channels for High Catalytic Performance in AB Dehydrogenation, Chem. Commun. 49 (2013) 10832-10834.
2. Q. Xu, M. Chandra, Portable Hydrogen Generation System: Catalytic Hydrolysis of Ammonia-Borane, J. Alloys Compd. 446-447 (2007) 729-732.
3. H.-L. Jiang, Q. Xu, Catalytic Hydrolysis of Ammonia Borane for Chemical Hydrogen Storage, Catal. Today 170 (2011) 56-63.
4. M. Zahmakiran, S. Özkar, Transition Metal Nanoparticles in Catalysis for the Hydrogen Generation from the Hydrolysis of Ammonia-Borane, Top. Catal. 56 (2013) 1171-1183.
5. W.-W. Zhan, Q.-L. Zhu, Q. Xu, Dehydrogenation of Ammonia Borane by Metal Nanoparticle Catalysts, ACS Catal. 6 (2016) 6892-6905.
6. Q. Xu, M. Chandra, Catalytic Activities of Non-noble Metals for Hydrogen Generation from Aqueous Ammonia–Borane at Room Temperature, J. Power Sources 163 (2006) 364-370.
7. Z.-H. Lu, H.-L. Jiang, M. Yadav, K. Aranishi, Q. Xu, Synergistic Catalysis of Au-Co@SiO_2 Nanospheres in Hydrolytic Dehydrogenation of Ammonia Borane for Chemical Hydrogen Storage, J. Mater. Chem. 22 (2012) 5065-5071.
8. H.-L. Jiang, T. Umegaki, T. Akita, X.-B. Zhang, M. Haruta, Q. Xu, Bimetallic Au-Ni Nanoparticles Embedded in SiO_2 Nanospheres: Synergetic Catalysis in Hydrolytic Dehydrogenation of Ammonia Borane, Chem. Eur. J. 16 (2010) 3132-3137.
9. G.P. Rachiero, U.B. Demirci, P. Miele, Bimetallic RuCo and RuCu Catalysts Supported on γ-Al_2O_3. A Comparative Study of their Activity in Hydrolysis of Ammonia-Borane, Int. J. Hydrog. Energy 36 (2011) 7051-7065.
10. J.M. Yan, Z.L. Wang, H.L. Wang, Q. Jiang, Rapid and Energy-Efficient Synthesis of a Graphene-CuCo Hybrid as a High Performance Catalyst, J. Mater. Chem. A 22 (2012) 10990-10993.
11. C.F. Yao, L. Zhuang, Y.L. Cao, X.P. Ai, H.X. Yang, Hydrogen Release from Hydrolysis of Borazane on Pt- and Ni- based Alloy Catalysts, Int. J. Hydrog. Energy 33 (2008) 2462-2467.

12. G. Chen, S. Desinan, R. Nechache, R. Rosei, F. Rosei, D. Ma, Bifunctional Catalytic/Magnetic Ni@Ru Core-shell Nanoparticles, Chem. Commun. 47 (2011) 6308-6310.
13. F. Cheng, H. Ma, Y. Li, J. Chen, $Ni_{1-x}Pt_x$ (x = 0–0.12) Hollow Spheres as Catalysts for Hydrogen Generation from Ammonia Borane, Inorg. Chem. 46 (2007) 788-794.
14. Z.-H. Lu, Q. Yao, Z. Zhang, Y. Yang, X. Chen, Nanocatalysts for Hydrogen Generation from Ammonia Borane and Hydrazine Borane, J. Nanomater. 2014 (2014) 1-11.
15. J.-M. Yan, X.-B. Zhang, T. Akita, M. Haruta, Q. Xu, One-step Seeding Growth of Magnetically Recyclable Au@Co, Core-shell Nanoparticles: Highly Efficient Catalyst for Hydrolytic Dehydrogenation of Ammonia Borane, J. Am. Chem. Soc. 132 (2010) 5326-5327.
16. H.-L. Jiang, T. Akita, Q. Xu, A One-pot Protocol for Synthesis of Non-noble Metal-based Core-shell Nanoparticles under Catalysts for Hydrolytic Dehydrogenation of NH_3BH_3, Chem. Commun. 47 (2011) 10999-11001.
17. J. Wang, Y.L. Qin, X. Liu, X.B. Zhang, *In situ* Synthesis of Magnetically Recyclable Graphene-Supported Pd@Co Core–shell Nanoparticles as Efficient Catalysts for Hydrolytic Dehydrogenation of Ammonia Borane, J. Mater. Chem. 22 (2012) 12468-12470.
18. L. Yang, W. Luo, G.Z. Cheng, Graphene-supported Ag Based Core-shell Nanoparticles for Hydrogen Generation in Hydrolysis of Ammonia Borane and Methylamine Borane, ACS Appl. Mater. Interfaces 5 (2013) 8231-8240.
19. N. Cao, J. Su, W. Luo, G.Z. Cheng, Hydrolytic Dehydrogenation of Ammonia Borane and Methylamine Borane Catalyzed by Graphene Supported Ru@Ni Core-shell Nanoparticles, Int. J. Hydrog. Energy 39 (2014) 426-435.
20. K. Aranishi, H.-L. Jiang, T. Akita, M. Haruta, Q. Xu, One-step Synthesis of Magnetically Recyclable Au/Co/Fe Triple Layered Core-shell Nanoparticles as Highly Efficient Catalysts for the Hydrolytic Dehydrogenation of Ammonia Borane, Nano Res. 4 (2011) 1233-1241.
21. H.-L. Wang, J.-M. Yan, Z.-L. Wang, Q. Jiang, One-step Synthesis of Cu@FeNi Core-shell Nanoparticles: Highly Active Catalyst for Hydrolytic Dehydrogenation of Ammonia Borane, Int. J. Hydrog. Energy 37 (2012) 10229-10235.

22. X.Y. Meng, L. Yang, N. Cao, C. Du, K. Hu, J. Su, W. Luo, G. Cheng, Graphene-Supported Trimetallic Core-shell Cu@CoNi Nanoparticles for Catalytic Hydrolysis of Amine Borane, ChemPlusChem 79 (2014) 325-332.
23. F.Y. Qiu, Y.L. Dai, L. Li, C. Xu, Y. Huang, C. Chen, Y. Wang, L. Jiao, H. Yuan, Synthesis of Cu@FeCo Core–shell Nanoparticles for the Catalytic Hydrolysis of Ammonia Borane, Int. J. Hydrog. Energy 39 (2014) 436-441.
24. X.C. Shen, M. Dai, M. Gao, Z.B. Wang, B. Zhao, W.P. Ding, Core-shell Structured Cu@CoCr Catalyst: Synthesis and Catalytic Performance for Hydrolysis of Ammonia Borane Aqueous Solution, Chin. J. Inorg. Chem. 29 (2013) 999-1006.
25. L. Yang, J. Su,W. Luo, G.Z. Cheng, Strategic Synthesis of Graphene Supported Trimetallic Ag-based Core–shell Nanoparticles Toward Hydrolytic Dehydrogenation of Amine Boranes, Int. J. Hydrog. Energy 39 (2014) 3360-3370.
26. L. Yang, J. Su, X.Y. Meng, W. Luo, G.Z. Cheng, *In situ* Synthesis of Graphene Supported Ag@CoNi Core-shell Nanoparticles as Highly Efficient Catalysts for Hydrogen Generation from Hydrolysis of Ammonia Borane and Methylamine Borane, J. Mater. Chem. A 1 (2013) 10016-10023.
27. F.Y. Qiu, G. Liu, L. Li, Y. Wang, C. Xu, C. An, C. Chen, Y. Xu, Y. Huang, Y. Wang, L. Jiao, H. Yuan, Synthesis of Triple-layered Ag@Co@Ni Core-shell Nanoparticles for the Catalytic Dehydrogenation of Ammonia Borane, Chem. Eur. J. 20 (2014) 505-509.
28. C.M. Li, J.Y. Zhou, W. Gao, J. Zhao, J. Liu, Y. Zhao, M. Wei, D.G. Evans, X. Duan, Binary Cu-Co Catalysts Derived from Hydrotalcites with Excellent Activity and Recyclability Towards NH_3BH_3 Dehydrogenation, J. Mater. Chem. A 1 (2013) 5370-5376.
29. Z.-H. Lu, J. Li, A. Zhu, Q. Yao, W. Huang, R. Zhou, R. Zhou, X. Chen, Catalytic Hydrolysis of Ammonia Borane *via* Magnetically Recyclable Copper Iron Nanoparticles for Chemical Hydrogen Storage, Int. J. Hydrog. Energy 38 (2013) 5330-5337.
30. J.-M. Yan, X.-B. Zhang, S. Han, H. Shioyama, Q. Xu, Magnetically Recyclable Fe-Ni Alloy Catalyzed Dehydrogenation of Ammonia Borane in Aqueous Solution Under Ambient Atmosphere, J. Power Sources 194 (2009) 478-481.
31. F.Y. Qiu, Y.J. Wang, Y.P. Wang, L. Li, G. Liu, C. Yan, L.F. Jiao, H.T. Yuan, Dehydrogenation of Ammonia Borane Catalyzed by *in situ* Synthesized Fe-Co Nanoalloy in Aqueous Solution, Catal. Today 170 (2011) 64-68.

32. W.Q. Feng, L. Yang, N. Cao, C. Du, H. Dai, W. Luo, G. Cheng, *In situ* facile Synthesis of Bimetallic CoNi Catalyst Supported on Graphene for Hydrolytic Dehydrogenation of Amine Borane, Int. J. Hydrogen Energy 39 (2014) 3371-3380.
33. M. Kaya, M. Zahmakiran, S. Özkar, M. Volkan, Copper(0) Nanoparticles Supported on Silica-Coated Cobalt Ferrite Magnetic Particles: Cost Effective Catalyst in the Hydrolysis of Ammonia-Borane with an Exceptional Reusability Performance, ACS Appl. Mater. Interfaces 4 (2012) 3866-3873.
34. M. Mahyari, A. Shaabani, Nickel Nanoparticles Immobilized on Three Dimensional Nitrogen-doped Graphene as a Superb Catalyst for the Generation of Hydrogen from the Hydrolysis of Ammonia Borane, J. Mater. Chem. A 2 (2014) 16652-16659.
35. A. Nozaki, Y. Tanihara, Y. Kuwahara, T. Ohmichi, K. Mori, T. Nagase, H.Y. Yasuda, H. Yamashita, Skeletal Ni Catalysts Prepared from Amorphous Ni–Zr Alloys: Enhanced Catalytic Performance for Hydrogen Generation from Ammonia Borane, ChemPhysChem 17 (2016) 412-417.
36. P.-Z. Li, A. Aijaz, Q. Xu, Highly Dispersed Surfactant-Free Nickel Nanoparticles and Their Remarkable Catalytic Activity in the Hydrolysis of Ammonia Borane for Hydrogen Generation, Angew. Chem. Int. Ed. 51 (2012) 6753-6756.
37. J. Zhang, C. Chen, W. Yan, F. Duan, B. Zhang, Z. Gao, Y. Qin, Ni Nanoparticles Supported on CNTs with Excellent Activity Produced by Atomic Layer Deposition for Hydrogen Generation from the Hydrolysis of Ammonia Borane, Catal. Sci. Technol. 6 (2016) 2112-2119.
38. G. Zhao, J. Zhong, J. Wang, T.-K. Sham, X. Sun, S.-T. Lee, Revealing the Synergetic Effects in Ni Nanoparticle-Carbon Nanotube Hybrids by Scanning Transmission X-ray Microscopy and their Application in the Hydrolysis of Ammonia Borane, Nanoscale 7 (2015) 9715-9722.
39. H. Liu, C. Cao, P. Li, Y. Yu, W. Song, Core-shell Structured Nanospheres with Mesoporous Silica Shell and Ni Core as a Stable Catalyst for Hydrolytic Dehydrogenation of Ammonia Borane, J. Energy Chem. 23 (2014) 50-56.
40. P.-Z. Li, K. Aranishi, Q. Xu, ZIF-8 Immobilized Nickel Nanoparticles: Highly Effective Catalysts for Hydrogen Generation from Hydrolysis of Ammonia Borane, Chem. Commun. 48 (2012) 3173-3175.
41. Ö. Metin, V. Mazumder, S. Özkar, S. Sun, Monodisperse Nickel Nanoparticles and Their Catalysis in Hydrolytic Dehydrogenation of Ammonia Borane, J. Am. Chem. Soc. 132 (2010) 1468-1469.

42. J. Hu, Z. Chen, M. Li, X. Zhou, H. Lu, Amine-Capped Co Nanoparticles for Highly Efficient Dehydrogenation of Ammonia Borane, ACS Appl. Mater. Interfaces 6 (2014) 13191-13200.
43. Ö. Metin, S. Özkar, Water Soluble Nickel (0) and Cobalt (0) Nanoclusters Stabilized by Poly(4-styrenesulfonic acid-co-maleic acid): Highly Active, Durable and Cost Effective Catalysts in Hydrogen Generation from the Hydrolysis of Ammonia Borane, Int. J. Hydrogen Energy 36 (2011) 1424-1432.
44. L. Yang, N. Cao, C. Du, H. Dai, K. Hu, W. Luo, G. Cheng, Graphene Supported Cobalt (0) Nanoparticles for Hydrolysis of Ammonia Borane, Mater. Lett. 115 (2014) 113-116.
45. H. Wang, Y. Zhao, F. Cheng, Z. Tao, J. Chen, Cobalt Nanoparticles Embedded in Porous N-doped Carbon as Long-life Catalysts for Hydrolysis of Ammonia Borane, Catal. Sci. Technol. 6 (2016) 3443-3448.
46. K. Aranishi, Q.-L. Zhu, Q. Xu, Dendrimer-Encapsulated Cobalt Nanoparticles as High Performance Catalysts for the Hydrolysis of Ammonia Borane, ChemCatChem 6 (2014) 1375-1379.
47. J.-M. Yan, X.-B. Zhang, S. Han, H. Shioyama, Q. Xu, Iron-Nanoparticle-Catalyzed Hydrolytic Dehydrogenation of Ammonia Borane for Chemical Hydrogen Storage, Angew. Chem. Int. Ed. 47 (2008) 2287-2289.
48. M. Dinc, Ö. Metin, S. Özkar, Water Soluble Polymer Stabilized Iron (0) Nanoclusters: A Cost-effective and Magnetically Recoverable Catalyst in Hydrogen Generation from the Hydrolysis of Sodium Borohydride and Ammonia Borane, Catal. Today 183 (2012) 10-16.
49. H. Yen, Y. Seo, S. Kaliaguine, F. Kleitz, Role of Metal−Support Interactions, Particle Size, and Metal−Metal Synergy in CuNi Nanocatalysts for H_2 Generation, ACS Catal. 5 (2015) 5505-5511.
50. J. Li, Q.-L. Zhu, Q. Xu, Non-noble Bimetallic CuCo Nanoparticles Encapsulated in the Pores of Metal–organic Frameworks: Synergetic Catalysis in the Hydrolysis of Ammonia Borane for Hydrogen Generation, Catal. Sci. Technol. 5 (2015) 525-530.
51. Q. Yao, Z.-H. Lu, W. Huang, X. Chen, J. Zhu, High Pt-like Activity of the Ni–Mo/graphene Catalyst for Hydrogen Evolution from Hydrolysis of Ammonia Borane, J. Mater. Chem. A 4 (2016) 8579-8583.

52. Y. Yang, F. Zhang, H. Wang, Q. Yao, X. Chen, Z.-H. Lu, Catalytic Hydrolysis of Ammonia Borane by Cobalt Nickel Nanoparticles Supported on Reduced Graphene Oxide for Hydrogen Generation, J. Nanomater. 2014 (2014) 294350:1-10.
53. A.A. Vernekar, S.T. Bugde, S. Tilve, Sustainable Hydrogen Production by Catalytic Hydrolysis of Alkaline Sodium Borohydride Solution using Recyclable Co-Co_2B and Ni-Ni_3B Nanocomposites, Int. J. Hydrog. Energy 37 (2012) 327-334.
54. S.B. Kalidindi, A.A. Vernekar, B.R. Jagirdar, Co–Co_2B, Ni–Ni_3B and Co–Ni–B Nanocomposites Catalyzed Ammonia–Borane Methanolysis for Hydrogen Generation, Phys. Chem. Chem. Phys. 11 (2009) 770-775.
55. J.-M. Yan, X.-B. Zhang, S. Han, H. Shioyama, Q. Xu, Magnetically Recyclable Fe–Ni Alloy Catalyzed Dehydrogenation of Ammonia Borane in Aqueous Solution under Ambient Atmosphere, J. Power Sources 194 (2009) 478-481.
56. X. Zhou, Z. Chen, D. Yan, H. Lu, Deposition of Fe–Ni Nanoparticles on Polyethyleneimine-decorated Graphene Oxide and Application in Catalytic Dehydrogenation of Ammonia Borane, J. Mater. Chem. 22 (2012) 13506-13516.
57. M. Nie, Y.C. Zou, Y.M. Huang, J.Q. Wang, Ni-Fe-B Catalysts for $NaBH_4$ Hydrolysis, Int. J. Hydrog. Energy 37 (2012) 1568-1576.
58. P.V. Ramachandran, P.D. Gagare, Preparation of Ammonia Borane in High Yield and Purity, Methanolysis, and Regeneration, Inorg. Chem. 46 (2007) 7810-7817.
59. Y.-W. Chen, N. Sasirekha, Preparation of NiFeB Nanoalloy Catalysts and Their Applications in Liquid-Phase Hydrogenation of p-Chloronitrobenzene, Ind. Eng. Chem. Res. 48 (2009) 6248-6255.
60. M. Thommes, K. Kaneko, A.V. Neimark, J.P. Olivier, F.R.-Reinoso, J. Rouquerol, K.S.W. Sing, Physisorption of Gases, with Special Reference to the Evaluation of Surface Area and Pore Size Distribution (IUPAC Technical Report), Pure Appl. Chem. 87 (2015) 1051-1069.
61. K.S.W. Sing, R.T. Williams, Physisorption Hysteresis Loops and the Characterization of Nanoporous Materials, Adsorpt. Sci. Technol. 22 (2004) 773-782.
62. M. Thommes, Physical Adsorption Characterization of Nanoporous Materials, Chem. Ing. Tech. 82 (2010) 1057-1073.

63. B. Coasne, A. Galarneau, R.J.M. Pellenq, F. Di Renzo, Adsorption, Intrusion and Freezing in Porous Silica: the View from the Nanoscale, Chem. Soc. Rev. 42 (2013) 4141-4171.
64. E.D. Biasi, C.A. Ramos, R.D. Zysler, H. Romero, Large Surface Magnetic Contribution In Amorphous Ferromagnetic Nanoparticles, Phys. Rev. B 65 (2002) 144416:1-8.
65. R.D. Zysler, H. Romero, C.A. Ramos, E.D. Biasi, D. Fiorani, Evidence of Large Surface Effects in Co–Ni–B Amorphous Nanoparticles, J. Magn. Magn. Mater. 266 (2003) 233-242.
66. E.D. Biasi, R.D. Zysler, C.A. Ramos, Surface Anisotropy and Surface-core Interaction in Co-Ni-B and Fe-Ni-B Dispersed Amorphous Nanoparticles, Phys. Rev. B 71 (2005) 104408:1-6.
67. C. Liang, C.P. Gooneratne, Q.X. Wang, Y. Liu, Y. Gianchandani, J. Kosel, Magnetic Properties of FeNi-Based Thin Film Materials with Different Additives, Biosensors 4 (2014) 189-203.
68. O. Ozay, E. Inger, N. Aktas, N. Sahiner, Hydrogen Production from Ammonia Borane *via* Hydrogel Template Synthesized Cu, Ni, Co Composites, Int. J. Hydrog. Energy 36 (2011) 8209-8216.
69. C.M. Kaufman, B. Sen, Hydrogen Generation by Hydrolysis of Sodium Tetrahydroborate: Effects of Acids and Transition Metals and their Salts, J. Chem. Soc., Dalton Trans. 2 (1985) 307-313.